Locomotor patterns and persistent activity in self-organizing neural models

Thomas Henry Cooke

Centre for Theoretical and Computational Neuroscience

University of Plymouth

A thesis submitted to the University of Plymouth in partial fulfilment of the requirements for the degree of

Doctor of Philosophy

November 2008

Thomas Henry Cooke

Locomotor patterns and persistent activity in self-organizing neural models

The thesis investigates principles of self-organization that may account for the observed structure and behaviour of neural networks that generate locomotor behaviour and complex spatiotemporal patterns such as spiral waves, metastable states and persistent activity. This relates to the general neuroscience problem of finding the correspondence between the structure of neural networks and their function. This question is both extremely important and difficult to answer because the structure of a neural network defines a specific type of neural dynamics which underpins some function of the neural system and also influences the structure and parameters of the network including connection strengths. This loop of influences results in a stable and reliable neural dynamics that realises a neural function.

In order to study the relationship between neural network structure and spatiotemporal dynamics, several computational models of plastic neural networks with different architectures are developed. Plasticity includes both modification of synaptic connection strengths and adaptation of neuronal thresholds. This approach is based on a consideration of general modelling concepts and focuses on a relatively simple neural network which is still complex enough to generate a broad spectrum of spatio-temporal patterns of neural activity such as spiral waves, persistent activity, metastability and phase transitions.

Having considered the dynamics of networks with fixed architectures, we go on to consider the question of how a neural circuit which realizes some particular function establishes its architecture of connections. The approach adopted here is to model the developmental process which results in a particular neural network structure which is relevant to some particular functionality; specifically we develop a biologically realistic model of the tadpole spinal cord. This model describes the self-organized process through which the anatomical structure of the full spinal cord of the tadpole develops. Electrophysiological modelling shows that this architecture can generate electrical activity corresponding to the experimentally observed swimming behaviour.

Contents

List of Figures

ACKNOWLEDGEMENTS

I would like to take this opportunity to thank several people whose support has been crucial to me throughout my work on this thesis.

Firstly, and primarily I must acknowledge my supervisor, Professor Roman Borisyuk who gave me the opportunity to study within this fascinating area and has been consistently encouraging, supportive, and patient at all stages, not to mention extremely generous with his time. His amazing energy and passion for neuroscience is an inspiration.

Thanks must also go to Professor Alan Roberts at the University of Bristol, who provided enormous experience on all aspects of *Xenopus* tadpole swimming and spinal cord anatomy. The intriguing anatomical data which formed the basis for our investigation of tadpole spinal cord architecture were largely collected by Dr. Wen-Chang Li.

I have enjoyed many fruitful discussions with my colleagues and friends at CTCN which helped me to develop the ideas that eventually formed the basis for this work. They have been a pleasure to spend time with. Martin Coath encouraged me to write the thesis in LaTeX and provided helpful advice on getting the best results from it.

My examiners, Professor Stephen Coombes and Dr. Thomas Wennekers suggested corrections and changes that significantly improved the thesis.

My parents, Eric and Diana Cooke have provided a great deal of support and were always prepared to listen and offer encouragement. My brother Daniel has also been a source of optimism and good cheer.

Finally, I would like to thank my wonderful wife Sana for her apparently inexhaustible patience and good humour, for which I will always be grateful.

AUTHOR'S DECLARATION

At no time during the registration for the degree of Doctor of Philosophy has the author been registered for any other University award.

Relevant scientific seminars and conferences were regularly attended at which work was presented on several occasions. Three research papers and one book review have been published in refereed journals. Two abstracts have also been published.

Refereed journal articles:

Borisyuk, R., **Cooke, T.**, & Roberts, R. (2008) *Stochasticity and functionality of neural systems: mathematical modelling of axon growth in the spinal cord of tadpole.* Biosystems, **93** (1-2):101-114

Li, W-C., **Cooke, T.**, Sautois, B., Soffe, S., Borisyuk, R., & Roberts, A. (2007), *Axon and dendrite geography predict the specificity of synaptic connections in a functioning spinal cord network.* Neural Development, **2**:17. **URL:** http://dx.doi.org/10.1186/1749-8104-2-17

Borisyuk, R. & **Cooke, T.** (2007) *Metastable states, phase transitions, and persistent neural activity.* Biosystems, **89**, 30-37

Borisyuk, R. & **Cooke, T.** (2006), *Book review: "Bursting: The Genesis of Rhythm in the Nervous System", S. Coombes and P. Bressloff, eds., (2005)*, Journal of Integrative Neuroscience **5**:3,483-488

Abstracts:

Borisyuk, R. & **Cooke, T.** (2007) *How tadpoles swim: simple but realistic biological model.* 2007 SIAM conference on applications of dynamical systems, Snowbird, final program and abstracts, pp 77.

Borisyuk, R. & **Cooke, T.** (2007) *Stochasticity and functionality of neural systems.* BIOCOMP 2007, Italy, abstracts pp 26-27.

Posters and conference presentations:

2006: Neural Mechanisms of Locomotion Workshop, Plymouth. Oral presentation: *Computational Simulation of the Development of the Xenopus Swimming Circuit.*

2006: CNS 2006 Workshop on Structural Plasticity and Development, Edinburgh. Oral presentation: *Computational Simulation of the Development of the Xenopus Swimming Circuit.*

2006: Theoretical Neuroscience Network Annual Meeting, Bristol. Oral presentation: *Metastable States, Phase Transitions and Persistent Activity.*

2004: Neural Computation and Psychology Workshop, Plymouth. Poster presentation: *Evolution of Neural Network Structures for Adaptive Mating Call Generation and Mate Location in a Population of Breeding Agents.*

Other conferences attended:

2007: Non-Linear Neurodynamics Workshop, Exeter.

2005: Workshop on Mathematical Neuroscience, Edinburgh.

2005: Theory and Applications of Coupled Cell Networks, Cambridge.

2004: Simulation of Adaptive Behaviour, Santa Monica.

Word count for the main body of this thesis: 34670

Signed: Thomas Cooke

Date: 9/12/08

Chapter 1

Introduction

The thesis investigates principles of self-organization that may account for the observed structure and behaviour of neural networks that generate locomotor behaviour and complex spatiotemporal patterns such as spiral waves and persistent activity. The general natural science problem which the thesis addresses is to study interrelations between structure and function. This classical problem will be studied in the neuroscience context of finding the correspondence between the structure of neural networks and their function. This question is both extremely important and difficult to answer because the structure of a neural network defines a specific type of neural dynamics (which underpins some function of the neural system) and this dynamics also influences the structure and parameters of the network including connection strengths. This loop of influences results in a stable and reliable neural dynamics that realises a neural function.

The thesis includes the study of spatio-temporal patterns of neural activity in plastic neural networks with different architectures. Plasticity includes both modification of synaptic connection strengths and adaptation of neuronal thresholds. The study of threshold adaptations seems to be a promising approach because the number of adjustable parameters increases linearly with the number of network elements (as opposed to the number of possible connections which increases quadratically with the number of neurons). This approach is based on a consideration of

general modelling concepts and focuses on a relatively simple neural network which is still complex enough to generate a broad spectrum of spatio-temporal patterns of neural activity such as spiral waves, persistent activity, metastability and phase transitions. Although we study these models using a computational approach, these relatively simple models also permit the use of mathematical methods such as phase plane analysis and bifurcation theory, which can provide boundaries between different dynamical regimes and allows the determination of parameter values that realise neural functions. Part I of the dissertation is devoted to this study.

The question of how the neural circuit which can realize some particular function establishes its architecture of connections is under intensive investigation in neuroscience. Despite this, it is not yet clear how a particular neuronal structure relates to a specific function. It seems that a promising approach is to model the developmental process which results in a particular neural network structure which is relevant to some particular functionality. To demonstrate this approach in operation, we develop a biologically realistic model of the tadpole spinal cord. This model describes the self-organized process through which the anatomical structure of the full spinal cord of the tadpole develops. We produce the anatomical model to describe connections between spiking elements in the tadpole spinal cord and demonstrate that this new model can generate electrical activity corresponding to the experimentally observed swimming behaviour. Part II of the dissertation is devoted to this study.

1.1 General discussion of research topics

The following three sections contain discussion of the basic topics of this thesis: 1) Development of anatomical structure of neural circuits, 2) Activity dependent modification of neural parameters, and 3) Structure and function of neuronal networks.

1.1.1 Development of anatomical structure of neural circuits

Self-organizing principles are in operation in all aspects of the development of the nervous system. A helpful overview of principles implicated in the development of

brain structure can be found in (Price and Willshaw, 2000; Bayer and Altman, 2001; Wolpert, 2002). Important mechanisms include cell proliferation, differentiation, and migration; the growth of axons and dendrites; axon guidance and synaptogenesis; programmed cell death; and modification of synaptic connections by activity. We do not consider the early stages of this process which are primarily driven by genetic and molecular factors, instead we concentrate on the later stages which include in particular axon growth and the formation of synaptic contacts. Important aspects of synaptogenesis include distribution of synapses along the dendrites and development of appropriate neurotransmitters which can control the relative influences of excitation and inhibition. It is clear that these processes are activity driven and the result of synaptogenesis is dependent on neural activity.

Axon growth and formation of neural architecture

It is difficult to study axon growth and development of neural structure in cortical microcircuits (Price and Willshaw, 2000). A more workable approach is to concentrate on a simpler neural structure such as the spinal cord. In particular, in this dissertation we consider the spinal cord of the *Xenopus* tadpole, which is a very simple neuronal circuit which includes only about 2000 neurons of less than 10 cell types.

In the core, axial parts of the vertebrate nervous system, like the spinal cord and brainstem, neurons, dendrites and longitudinal axons are laid out in a dorsoventrally ordered array on each side of the body. At early stages in development a major factor influencing primary synapse formation in such regions may be the physical proximity or separation of axons and dendrites. If axons can recognise and contact dendrites, then synapses may form.

So, in the frog tadpole spinal cord, dorsally located sensory axons mainly excite the dorsal dendrites emerging from the cell bodies of dorsal sensory pathway neurons but the very ventral central axons of motoneurons will virtually never contact these

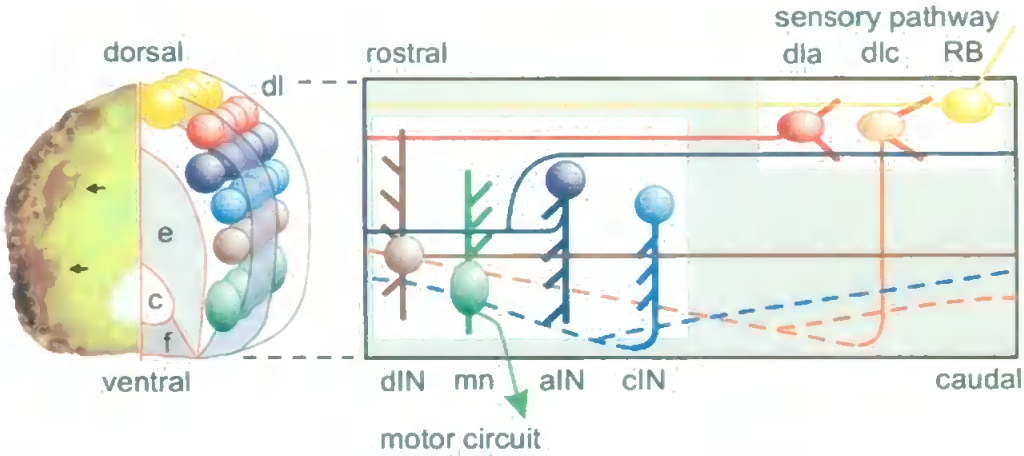

Figure 1.1: Organization of neurons in *Xenopus* spinal cord. Left part of figure shows transverse section of the spinal cord with the left side stained to show glycine immunoreactive cell bodies (arrows) and axons (in the marginal zone). Diagrammatic right side shows the main regions: neural canal (c) bounded by ventral floor plate (f) and ependymal cell layer (e), lateral marginal zone of axons (mauve), layer of differentiated neuron cell bodies arranged in longitudinal columns (coloured circles) lying inside the marginal zone except in dorso-lateral (dl) and dorsal positions. Right part of figure shows a diagrammatic view of the spinal cord seen from the left side showing characteristic position and features of 7 different neuron types. Each has a cell body (solid ellipse), dendrites (thick lines) and axon(s) (thin lines). Commissural axons projecting on the opposite right side are dashed.

dendrites, so synapses will not be made. At this early, primary stage of development neurons may need only to be able to distinguish neuronal dendrites from axons and non-neuronal processes. Detailed cellular recognition and other more subtle processes to specify correct connections may, therefore, not be necessary for the formation of primary functional networks during spinal cord development.

If the dorso-ventral distribution of axons and dendrites is an important determinant of spinal network connectivity, then what are the factors that control these distributions? Fortunately, this is a very active area of biological research. Different dorso-ventral distributions of axons and dendrites originate with the specification of soma positions. In the chick and mouse, a large body of work is defining the transcriptional networks that regulate the formation of an ordered dorso-ventral series of longitudinal neuron columns identified by the transcription factors that they express (Jessell, 2000; Helms and Johnson, 2003; Goulding and Pfaff, 2005; Zhuang

and Sockanathan, 2006). Fundamentally, around 12 neuron types are arranged in a consistent sequence of columns from dorsal to ventral: sensory, sensory related interneurons, motor related interneurons and motoneurons.

The same basic plan is seen in the tadpole spinal cord (Figure 1.1). Once formed into these columns, neurons are polarized (de Anda et al., 2005) and grow processes in very distinct orientations. In frogs, most neurons grow axons ventrally. Growth cones immediately come under the influence of attractive and repulsive chemical gradients that control their direction of growth, for example, whether they turn or grow straight across the ventral surface to the opposite side before turning (Dickson, 2002; Dickson and Gilestro, 2006; Chilton, 2006; Bourikas et al., 2005; Kennedy et al., 2006). In the tadpole all axons eventually grow in a longitudinal direction, starting in a characteristic dorso-ventral region for each neuron type. Meanwhile, dendrites grow from the soma or initial segment of the axon and, like the axons, come to lie in dorso-ventral positions characteristic for each neuron type. In contrast to extensive studies on dendrite development in brain neurons (Cline, 2003), there is little work on the mechanisms determining their growth in spinal cord. Evidence from zebrafish shows that dendrites play an active role in extending very short distances (approximately 10 μm) towards longitudinal axons to form en-passant synapses (Jontes et al., 2000).

The hypothesis examined in (Li et al., 2007) is that axons can recognise and make synapses with any dendrites that they contact, so the connections formed will depend primarily on the distribution of axons and dendrites. If this is correct, then synapse formation will occur where axons and dendrites lie in the same dorso-ventral regions of the spinal cord. Axons make synapses with the dendrites they chance to contact rather than making synapses preferentially by recognising specific chemical markers on particular synaptic targets. The main result of the paper (Li et al., 2007) states that simple factors such as morphogen gradients controlling dorso-ventral soma, dendrite and axon positions may sufficiently constrain the synaptic

connections made between different types of neuron as the spinal cord first develops and allow functional networks to form. Detailed cellular recognition between spinal neuron types may not be necessary for the reliable formation of functional networks to generate early behaviour like swimming. We will consider this topic in more detail in part II of the thesis.

Synaptogenesis and homeostatic neural activity

Recently, significant discoveries in neuroscience have been made which demonstrate the important role of homeostatic pressures in determining the development of neural structure. For example, studies of the developmental shift from excitatory to inhibitory actions of GABA suggest an activity-driven feedback mechanism that produces a proper balance between excitation and inhibition in the developing brain. At early stages of development of neural circuits, there are only a limited number of synapses with connection strengths that are not yet adjusted. Therefore, the neural activity is low and irregular. This might prevent further synaptic development which seems to be an activity-driven process. This suggests that a higher proportion of excitatory synapses is required at this stage of development. This can be achieved by having synapses that initially have an excitatory effect, and switch to having an inhibitory effect at a later stage of development.

Accounts from Spitzer and Ben-Ari (Ben Ari, 2002) suggest the following line of reasoning:

1. GABA is excitatory in the developing brain, and GABA-releasing synapses are formed before glutamatergic synapses across a wide range of species and structures. This may be what allows developing neurons to be sufficiently excited for growth while avoiding a mismatch between excitation and inhibition in the developed network.

2. Giant Depolarizing Potentials (GDP), a primitive network-driven pattern of activity, generate large oscillations of intracellular calcium even in cells with

few synapses, allowing activity-dependent growth and synapse formation.

3. Once a sufficient density of glutamate and GABA-ergic synapses has been generated, a chloride-extruding system (the KCC2 transporter) becomes operative which allows GABA to assume its conventional inhibitory effect. Evidence (Rohrbough and Spitzer, 1999) points to this transition being activity-dependent, specifically that GABA itself promotes the transition from excitation to inhibition through $GABA_A$-receptor mediated PSCs.

This line of reasoning suggests an elegant mechanism where excitatory GABA promotes growth and synapse formation until it exists in sufficient concentrations to activate KCC2 and cause the switch to inhibitory action. This represents a kind of self-limiting positive feedback, a very powerful developmental mechanism.

The GABA transition is not the only example of developmental processes apparently seeking to maintain a balance between excitation and inhibition. There is also strong evidence that transmitter expression at individual synapses is activity-dependent in a homeostasis-directed manner; recent papers (Spitzer et al., 2004; Borodinsky et al., 2004) demonstrate convincingly the ability to influence transmitter expression in the neural tube of developing *Xenopus* embryos through pharmacological and electrical manipulation. Particularly noteworthy is that these manipulations can cause excitatory and inhibitory transmitters to be expressed in the same cell, a phenomenon that is not observed in the unmanipulated animal.

Another example of the anatomical structure of a neural network changing in response to the level of activity is given in Kirov et al. (2004). They demonstrate that homeostatic regulation of spine number in mature hippocampal neurons results in more dendritic spines when synaptic transmission is blocked, providing a mechanism to compensate for diminished synaptic input. It is unsettled whether blockade of synaptic transmission also elevates spine number during development. Work by Muller et al. (1993) has demonstrated a complementary effect; chronic

epilepsy in hippocampal slice cultures produces a reversible loss of dendritic spines. It is worth noting that activity can also promote dendritic morphogenesis (Maletic-Savatic et al., 1999), suggesting the idea that some activity level exists where these constraints balance each other, and that the network actively seeks this level. This idea is further supported by work by Lauri et al. (2003) which demonstrates that activity blockade (with TTX) increases the number of functional synapses in the hippocampus of newborn rats.

No discussion of the role of spontaneous activity in development would be complete without a mention of the long-studied role of retinal waves in the organization of the early visual system. A well-known paper (Katz and Shatz, 1996) presents the idea that correlations in retinal waves drive the formation of ocular dominance columns, and determining the precise mechanism through which this occurs remains an active research area, for example see recent work by Torborg et al. (2005). It has also been suggested that electrotonic coupling is involved in developing the proper innervation of motor neurons (Kandler and Katz, 1995).

To summarize, a compelling body of recent work suggests that the level of network activity in developing circuits has a strong influence on the development of those circuits. Of course, those developmental changes influence the level of activity, creating a powerful mutual feedback loop. To investigate this loop, we study spatiotemporal activity of simple neural models with synaptic plasticity and adaptable thresholds (Chapter 4).

1.1.2 Activity dependent modification of neural parameters

Adaptation of cell membrane properties to regulate activity level

It has long been known that some neurons appear to modulate their own excitability, exhibiting an increasing threshold when stimulated repeatedly. This effect was described in (Hill, 1936), in which a mathematical model of accommodation is developed that characterizes the dynamics of the threshold U as being dependent on

two factors: a tendency to rise at a rate proportional to $V - V_0$ (where V represents "local potential" and V_0 represents resting potential) and a tendency to decay back to its original value U_0 in an exponential manner. The time constant for U is much greater than the time constant for V and so U reflects the recent history of V. This model was able to reproduce the experimental finding that the threshold is greater for a slowly increasing current than for a quickly increasing one, and this type of accommodation also provides one possible explanation for the fact that a nerve can be repeatedly excited by high-frequency stimulation but eventually fail to respond after this stimulation has persisted for some time.

Another phenomenon relating to the adaptation of neuronal excitability is Spike Frequency Adaptation (SFA), in which the spiking rate in response to a stimulus declines over time. Experiments described in Madison and Nicoll (1984) demonstrated firing rate accommodation in CA1 pyramidal cells. Reductions in SFA in the absence of calcium and the presence of carbachol suggest that this accommodation is partly due to a calcium-activated potassium current, and partly due to the M-current, a non-inactivating, voltage-sensitive potassium current. (Hemond et al., 2008) report that some pyramidal cells in the CA3b subregion of the hippocampus exhibit spike frequency adaptation in response to strong stimuli. In an accompanying modelling study they also found that this adaptation was dependent on the M-current. Henze and Buzsáki (2001) show that decreased excitability (depolarized threshold) of hippocampal pyramidal cells is associated with spiking activity in the 1 second time window previous to an action potential. They suggest that this may be due to sodium channel inactivation that decays with approximately a 1 second time constant.

Spike frequency adaptation has also been used in computational models. For example, Coombes and Owen (2005) have shown that a neural field model with SFA can exhibit rich spatiotemporal phenomena including bumps, breathers, and waves. In chapters 2 and 4, we examine the use of a very simple threshold accommodation

rule in a network of locally coupled binary Hopfield-type neurons.

Homeostatic synaptic plasticity and STDP learning rule

Generally speaking a learning rule provides conditions for increasing or decreasing the strength of synaptic connections. Multiple applications of a learning rule might result in unlimited growth of the synaptic strength; this is quite likely in commonly used paradigms like Hebbian plasticity and STDP because synaptic strengthening makes subsequent strengthening more likely, creating a positive feedback effect. Therefore, a learning rule should be accompanied by some additional constraints to keep synaptic strength within specified bounds; this can be considered a normalization of the learning rule (see, for example, the normalization procedure in Grossberg's ART).

Theoretically speaking, the normalization is a nontrivial and delicate procedure because from one side the learning rule is local and depends only on the activities of pre- and postsynaptic neurons, but from the other side, global activity of the sub-population of neurons should be taken into account for normalisation. This is because the incoming signal to a neuron depends on both the connection strengths and activities of active neurons that provide input to the postsynaptic cell. Hence, to provide a substantial input signal to the considered neuron in the case of a few active neurons, connection strength normalization should provide large values for connection strengths. In the opposite case where many neurons are active, the connection strengths should be sufficiently small that the cell is not saturated.

Turrigiano (Turrigiano et al., 1998; Turrigiano, 1999; Turrigiano and Nelson, 2000, 2004) and others have explored cell-level mechanisms such as synaptic scaling that may mitigate the potentially pathological effects of STDP. However, such local mechanisms may not be sufficient to prevent deleterious effects of STDP at the network level, for example over-excitability of neural assemblies.

Synaptic plasticity is difficult to study and many unanswered questions remain

about its mechanisms, however, a number of rules have been proposed that appear to capture important characteristics. The most well known of these are Hebbian plasticity and Spike-Timing Dependent Plasticity (STDP). Hebbian learning is often summed up by the phrase, "Cells that fire together, wire together", in other words, simultaneous pre- and postsynaptic firing causes synaptic strengthening. STDP refines this principle by stipulating that a pair of pre- and postsynaptic spikes may result in synaptic strengthening or weakening depending on their relative timing.

A very important feature of these learning rules, especially STDP, is that synaptic strengthening reinforces the pattern of activity that produced the strengthening, which in turn makes further strengthening more likely. This creates a destabilizing positive feedback (Turrigiano and Nelson, 2004) which has led some researchers to ask what prevents this effect leading to a pathological condition.

One possible answer is synaptic scaling (Turrigiano et al., 1998; Turrigiano, 1999; Turrigiano and Nelson, 2000, 2004; van Rossum et al., 2000; Yeung et al., 2004). Under synaptic scaling, the strengths of a cell's afferent synapses are scaled by a cell-autonomous process in order to maintain some homeostatic level of synaptic input. It has also been argued that STDP can naturally stabilize postsynaptic firing rates while maintaining the sensitivity of the postsynaptic cell to the timing of presynaptic inputs (Song et al., 2000; Kempter et al., 2001).

So far we have discussed homeostatic activity in terms of mean activity levels. However, we would also like to consider how variability in neuronal dynamics can be maintained under STDP-like learning rules, and this will be discussed in the next section.

Interplay between synaptic strengths and network dynamics

Is is well-known that the functioning of a neuronal network depends not only on the pattern of connections between neurons, but also on synaptic strengths, and further, that synaptic strengths are demonstrably plastic in many systems. Having

established that spontaneous activity is important in the development of structure, it is natural to ask what effects it may have in plastic networks.

A number of studies have demonstrated a link between slow-wave sleep and task performance (Tononi and Cirelli, 2003; Huber et al., 2004; Derégnaucourt et al., 2005). Sleep slow oscillations are travelling waves that sweep the human cerebral cortex up to once per second during slow-wave sleep. Tononi and Cirelli (2003) suggests that these patterns may induce a generalized synaptic downscaling that acts in opposition to the general tendency towards synaptic potentiation during wakefulness. It is further suggested that the amount of slow-wave sleep experienced is regulated by the amount of synaptic potentiation during wakefulness through a natural network effect, which would explain the fact that slow-wave sleep has been demonstrated to be more intense in areas of the brain that have been heavily used in experimental tasks. Several recent studies have provided further evidence which may support this hypothesis (Massimini et al., 2004; Ferri et al., 2008; Vajda et al., 2008; Vyazovskiy et al., 2008).

An interesting example of the relationship between neural dynamics and synaptic strengths in a developing system is the case of the spontaneous episodic activity observed in chick spinal cord. In this case, activity-dependent depression has been identified as a possible mechanism for network bursting (Fedirchuk et al., 1999), and a computational model of a single excitatory recurrently connected neural population reproduces the observed dynamics (Tabak et al., 2000, 2001). This result has been since replicated using a network of leaky integrate-and-fire neurons (Lerchner and Rinzel, 2005). A recent study (Hanson et al., 2008) shows that these episodes of spontaneous activity influence motor axon pathfinding.

1.1.3 Structure and function of neuronal networks

Locomotor behaviour in the *Xenopus* tadpole

A large part of the work in this thesis focuses on the spinal cord network that generates swimming in developing *Xenopus* tadpoles. This is an attractive system, firstly because credible modelling is facilitated by the many anatomical and electrophysiological studies that are available, and secondly because a number of unanswered questions remain that are well suited to investigation with computational models.

Swimming in the *Xenopus* tadpole typically follows the following sequence (Roberts et al., 1997):

1. Swimming is initiated following a brief touch to the skin.
2. The animal swims at 10-20 Hz, with this frequency typically dropping slowly as swimming continues. During swimming, waves of bending pass from the head to the tail to drive the animal forward (and usually away from the source of stimulation).
3. Swimming stops abruptly following contact with a solid object or the surface meniscus.

In addition, the tadpole can produce a struggling pattern consisting of strong, slow (2-10Hz) bending movements with waves of bending spreading from tail to head. This may be elicited by repetitively stimulating the same skin sensory neurons that initiate swimming, for example by restraining the animal with forceps.

The following description of how the network produces behaviour is largely based on (Roberts et al., 1997).

Initiation of swimming. Rohon-Beard (RB) cells innervate the skin with nerve endings, and fire one or two impulses in response to touch. A single RB excites many sensory interneurons which amplify the excitation, and relay it to premotor interneurons and motoneurons on both sides of the body - a single spike

from a single RB cell can initiate swimming. Like RBs, the sensory interneurons fire only one or two spikes. In addition, they are phasically inhibited, and gate sensory input during swimming.

Functions of neurons active during swimming. It seems that only motoneurons, descending interneurons and commissural interneurons are necessary to generate the basic swimming pattern. All three show a very similar pattern of activity during fictive swimming, in which they fire a single spike on each cycle, are tonically excited, and receive mid-cycle inhibition. Commissural neurons are responsible for mid-cycle reciprocal inhibition of contralateral motoneurons and premotor interneurons. Descending interneurons produce a fast AMPA excitation of ipsilateral neurons as well as a slow NMDA excitation that sustains the next cycle of activity on the same side of the spinal cord. This may be regarded as a form of positive feedback within each half-center. Motoneurons excite more caudal ipsilateral motoneurons as well as exciting the segmentally organized swimming muscles.

Mechanisms of rhythm generation. Current evidence suggests that rhythm is sustained within each side of the spinal cord (half-center) by positive feedback excitation from premotor descending interneurons and motoneurons. Rhythmicity appears to involve three overlapping mechanisms:

1. Within a half-center, interaction between feedback excitation and intrinsic membrane properties "tunes" rhythmic firing to the appropriate frequency for swimming.

2. Also within a half-center, recurrent inhibition spaces firing through a hyperpolarization that slowly decays through excitatory input from more rostral neurons.

3. A powerful reciprocal inhibition between the two half-centers produces delayed rebound firing and organizes the alternation of the two halves.

Control of frequency during swimming. Roberts et al. (Roberts et al., 1997) suggest that many ionic, cellular, and synaptic functions may contribute to the slow drop in swimming frequency during a swim. What is known is that as swimming frequency falls, motoneurons continue to spike reliably on every cycle, but premotor neurons fire less and less, and may stop entirely. Experimental observation suggests that swimming frequency depends on the number of active premotor interneurons.

Longitudinal coordination during swimming. In fictive swimming, a small rostrocaudal delay (2-5 ms mm^{-1}) is observed in the motor output along the body, corresponding to the propagation of waves of movement from head to tail that can be observed when the animal is not restrained. Tunstall and Roberts (Tunstall and Roberts, 1991) proposed in 1991 that this delay might result from a head-to-tail gradient in the synaptic drive to the neurons generating motor output; such a relationship was confirmed by pharmacological manipulations designed to increase or decrease this gradient.

Stopping swimming. When the animal bumps into an obstruction, trigeminal pressure receptors are excited. These project into the hindbrain and excite reticulospinal hindbrain neurons which leads to inhibition in spinal motoneurons.

A few important open questions remain. The full pathway through which a stimulus initiates rhythmic activity in ipsilateral neurons has not been demonstrated. The physiological properties and degree of heterogeneity in premotor interneurons are not as well determined as in motoneurons. The role of ascending interneurons is not clear, though they are rhythmically active during swimming. Little is known about the connections that organize longitudinal coordination. Perhaps most intriguingly, it is not known how the swimming circuit produces the qualitatively different struggling behaviour.

Computational models of the swimming network

Basic rhythm generation. In 1990, Roberts and Tunstall (Roberts and Tun-

stall, 1990) described a computational model of four different neuronal populations representing descending and commissural interneurons in two halves of the spinal cord. Each cell was represented using a three compartment model with realistic properties. It was shown that this model was able to sustain a swimming rhythm after an initial excitation in the absence of continued sensory drive. An important feature of the model neurons (derived from experimental observation) was crucial to this ability: the neurons could not spike repeatedly under tonic excitation except as a consequence of post-inhibitory rebound. This prevents the positive feedback specified in the network architecture from driving the network into a pathological state of over-excitement.

In addition to varying cellular properties, the robustness of this network was investigated by varying synaptic parameters, initiating stimuli, and network connectivity. This showed the basic pattern-generating behaviour to be quite robust to changes in synaptic strengths. However, no dynamics analogous to the struggling pattern are observed in this network, and the network also does not capture any of the dynamics of the rostrocaudal axis.

Intersegmental coordination and rostrocaudal delays. It was mentioned earlier in this report that a rostrocaudal gradient of synaptic drive exists in the spinal cord (decreasing caudally), and that pharmacological manipulations of this gradient can exaggerate or reverse observed rostrocaudal delays in fictive swimming. In 1994, Roberts and Tunstall (Roberts and Tunstall, 1994) developed a computational model designed to investigate whether or not such a gradient might be sufficient to explain the observed behaviour in the animal.

This model consists of 12 connected segments, where each segment consists of 4 neurons and is similar to an instance of Roberts and Tunstall's 1990 model described above. Each segment is connected to its nearest neighbors through descending excitation and ascending crossed inhibition. The strengths of both within-segment and intersegmental connections decreased linearly in the rostrocaudal direction. On

the basis of this gradient, the model could be divided into 4 regions: the first 4 segments could oscillate in isolation from the rest, the middle 4 would only oscillate when they received descending excitation from the upper segments, and the caudal 4 showed no oscillator properties and were only active when driven to fire on each cycle.

This network demonstrated a rostrocaudal delay, and the cycle period decreased with increasing excitation. However, in the network rostrocaudal delay also scaled with cycle period, which does not happen in the animal. The paper proposed that such scaling could be eliminated by making intersegmental inhibition stronger than intrasegmental inhibition but there were no experimental data on these relative strengths at the time of publication. Struggling was not demonstrated in this network, but the paper proposes that the struggling pattern (in which the delay is caudorostral) may be explained by an increase in the excitatory drive to more caudal regions.

Tunstall et al. (Tunstall et al., 2002) use a similar model to the one just described but with unidirectional coupling to investigate the mechanisms by which one spinal oscillator can entrain another. This is analyzed computationally for both "intrinsic" oscillators, which can oscillate autonomously, and "potential" oscillators which require external drive. This work demonstrates that excitatory and inhibitory coupling allow entrainment in complimentary areas of parameter space in the simulated swimming network.

Development of the swimming network with rostrocaudal gradients. Dale (Dale, 2003) uses very simple developmental rules to obtain a 400-neuron network (100 excitatory/100 inhibitory on each side) which can reproduce some features of the tadpole spinal cord. The rules of connectivity are:

1. Neurons cannot synapse onto themselves.

2. Excitatory interneurons can make only ipsilateral AMPA and NMDA mediated

synapses.

3. Inhibitory interneurons can make only contralateral glycinergic synapses.

4. Each neuron has an intrinsic probability of synapse formation that is a monotonic function of the rostro-caudal position of the soma (P_{soma}).

5. Each neuron has one rostral and one caudal projecting axon of specified length (L_{axon}).

6. Synapses can be made only within the length of the axon *en passant* as the axon encounters other neurons within its length. A constant probability of synapse formation is associated with each axon (P_{axon}).

The activity observed in networks generated according to these rules demonstrates important features of *Xenopus* swimming (cycle period, burst duration, rostro-caudal delay), suggesting that segmental oscillator concepts are not necessary to produce these characteristics. Also very interesting is that the parameters of the network can be changed to mimic different stages of development, and there is some correspondence between the development of the real network and the simulated network:

1. Rhythmic activity is observed firstly only at the most rostral end of the spinal cord, and this activity spreads caudally as the network develops.

2. The cycle period of swimming decreases as the network develops.

3. The duration of swimming activity increases as the network develops.

4. Ventral root burst durations appear longer at younger stages and the pattern is clearly more variable and less coordinated.

The ability of the Dale network to reproduce all these features suggests that developmental approaches to network modelling with simple probabilistic rules will

be valuable in helping to understand the tadpole swimming network. We can suggest several interesting extensions to this work:

1. Use two-dimensional developmental rules to capture the dorso-ventral structure of the tadpole spinal cord - this appears to be crucial in specifying which types of neurons connect to each other.

2. Investigate the performance of the network when the level of excitability is varied and compare this with the effects of pharmacological manipulations in *Xenopus*.

3. Investigate the possibility that struggling patterns may be induced by high levels of tonic sensory drive.

In part II of the thesis (chapters 5-8) a simple mathematical model of axon growth in the spinal cord of tadpole is developed and fitted to experimentally measured characteristics of tadpole axons. The fitted model of axon growth allows us to generate a biologically realistic reconstruction of the anatomy of the full spinal cord. Using this anatomical structure we consider a neural network of spiking elements and study patterns of spatiotemporal activity; remarkably the model generates electrical activity corresponding to the swimming pattern of the tadpole.

1.2 Tour of the thesis

Here we would like to provide a bird's-eye view of the research presented in the thesis. For each chapter we describe the problem studied, results and contributions which have been achieved.

Chapter 2 is devoted to a study of neural activity in a simple computational neural network model of locally coupled binary elements with adjustable threshold. Our approach to the development of this model is based on the idea of homeostatic neural activity: we regulate the neuronal threshold on the basis of the level of incoming activity in such a way that the threshold is increased when spiking activity

is high, and vice versa. Our results demonstrate that this model can exhibit complex spatiotemporal patterns such as spiral waves and propagating waves. This kind of neural activity is of great interest due to similarities with known electrophysiological recordings.

Chapter 3 considers the question of what neural mechanisms can generate persistent variable activity in the brain. In order to examine the relationship between neural connectivity and stochasticity, we develop a model of locally coupled binary elements with noise. When the magnitude of the noise is set within a certain critical range, this model demonstrates long-lasting persistent high activity (UP state) and low activity (DOWN state) with rapid transitions between the two phases.

Chapter 4 contains a study of the relationship between adaptable characteristics of the network and neural dynamics. In the first part of this chapter, we consider the question of whether or not a system of local rules that allows each cell to adjust its threshold and synaptic connection strengths can produce a regime of homeostatic activity. The simulation results demonstrate that simple learning rules can produce a rapid reorganization of connection strengths which leads to a sudden phase transition. This demonstration of the possibility of phase transition effects in neural networks is very important for applications in neuroscience.

In the second part of this chapter, we expand the connection architecture to include a few long-range connections, making it similar to small-world connectivity. We found that in addition to UP and DOWN states and phase transitions, the system can demonstrate a remarkable phenomenon of a hysteresis-type loop between activity and connectivity. This loop exists in this system due to an increase in total synaptic weight during the low-activity phase, and a decrease in total synaptic weight during the high activity phase. We then study the mechanism of the interplay between neural activity and connectivity using a simple mathematical meta-model of this hysteresis phenomenon.

Chapter 5 presents a set of anatomical data from the spinal cord of *Xenopus*

tadpoles on the distribution of axons and dendrites of 6 cell types related to swimming behaviour. This experimental evidence provides the basis for the formulation of a new and simple mathematical model of axon growth. The goal of the development of this model was to keep it as simple as possible while retaining the ability to match the characteristics of experimentally measured axons. The important result of this modelling supports the hypothesis that detailed cellular recognition between spinal neuron types may not be necessary for the reliable formation of functional networks to generate early behaviour like swimming.

Chapter 6 is devoted to a mathematical study of the axon growth model. This model contains three difference equations with a stochastic component, and we consider the important question of whether the variance of the stochastic model increases without limit as the number of iterations is increased, or saturates at some value. An analytical expression is derived to describe how the variance of the current position and growth cone angle changes with the iteration number. Formulas provide conditions for the case when the increase of the variance is limited as well as an analytical expression for the saturation level. It is remarkable that optimal parameters corresponding to the best fitting of the model to experimental measurements always satisfy the condition of limited variance increase.

Chapter 7 describes the optimization procedure of fitting the model parameters to experimental measurements. This optimization is based on a cost function which includes both fitting of the statistical distribution of the dorso-ventral coordinates of the axon and tortuosity. We apply the optimization procedure to each cell type in both ascending and descending directions. This allows us to generate a biologically realistic model of the full spinal cord of the tadpole which includes approximately 1600 neurons. This is the most realistic model of the anatomical architecture of the *Xenopus* spinal cord created to date and shows great potential for use as a research tool.

Chapter 8 asks the crucial question of whether or not the reconstructed spinal

cord generated by the axon growth model is capable of generating a spatiotemporal pattern of neural activity corresponding to swimming. To answer this question, we create an electrophysiological model of the generated anatomy, using the Morris-Lecar model of action potential generation to represent the electrical activity of each cell in the network. We show that this model is able to generate activity having the same characteristics as the real neural network in the tadpole. This demonstrates that our anatomical model succeeds in capturing important features of the tadpole spinal cord.

Part I

Theoretical and Computational Models of Spatiotemporal Neuronal Activity and Self-Organization

Introduction to Part I

In this part of the thesis, several models are developed which demonstrate the emergence of global spatiotemporal patterns within networks that are predominantly locally coupled. In all cases, the basic element is a Hopfield-type model neuron, which is then subject to modifications including: threshold adjustment, noisy input, and synaptic plasticity.

In the first model presented, we can see how a simple homeostasis-directed threshold update rule leads to spiral waves in a model of Hopfield-type elements. This can be viewed as a demonstration of how large oscillations can develop in a network where local negative feedback operates on a slow timescale relative to the spread of activity which is governed by a process characterized by network-driven positive feedback.

The second model shows that an interaction between positive feedback and local noise can produce large oscillations in network activity, even when there is no negative feedback in the system.

In the third model, we see how a rapid network reorganization can occur as a result of patterned activity propagating across a network with synaptic plasticity. This can be interpreted as a pathologically stereotyped pattern developing as a result of stability-directed processes.

The last model in this part shows how the tendency towards positive feedback implicit in correlation based synaptic plasticity can potentially be regulated by a spontaneous change in the characteristic scale of network dynamics driven by a net increase in synaptic weights. This can be interpreted as a model of the functional

consequences of emergent spatiotemporal patterns.

Taken as a whole, these models offer some ideas as to how the emergent properties of networks with slightly modified Hopfield-type elements can be used to engineer specific spatiotemporal dynamics. They suggest ways in which the tendency of networks of coupled elements to demonstrate different dynamical regimes may be contained and exploited by the brain.

Chapter 2

Neural network with threshold adaptation: spiral waves

2.1 Introduction

Spiral waves are very common patterns in many biological systems. An example of a classical object in which spiral waves can be observed is the Belousov-Zhabotinsky chemical reaction. To model spatiotemporal dynamics, the reaction-diffusion approach can be used: a partial differential equation of diffusion is coupled with a non-linear equation of the B-Z reaction. The simplest mathematical model of this reaction consists of two nonlinear ordinary differential equations and demonstrates both oscillatory and chaotic behaviour (Strogatz, 2001). Such a model can demonstrate complex spatiotemporal dynamics including spiral waves.

A similar approach based on combining the diffusion equation with the FitzHugh-Nagumo nonlinear oscillator is widely used to model spatiotemporal dynamics in the heart (Starmer et al., 1993). The mathematical approach to the modelling of such a system is based on the concept of excitable media, consisting of locally interactive elements which can be excited by an incoming signal and generate an impulse (spike).

Evidence from experimental neuroscience has demonstrated the existence of spiral waves of neural activity or associated processes (e.g. calcium waves). For example, Huang et al. (Huang et al., 2004) observed spiral waves in rat neocortex visual-

ized by voltage-sensitive dye. The paper also describes a computational model which exhibits spiral waves with some features similar to their experimental findings.

Spontaneous waves of excitation, including spiral waves, have also been observed in the developing retina (Sernagor et al., 2003). These waves are controlled by neurotransmission mechanisms and various neurotransmitters may participate; for example glutamate was indicated as an important neurotransmitter for retinal waves in developing turtle retina (Sernagor and Grzywacz, 1999). A mechanism has been described through which neurotransmission controls waves in the developing rabbit retina (Zhou and Zhao, 2000).

Our approach to the modelling of spiral waves is based on the idea of a homeostatic level of neural activity: we regulate the neuronal threshold on the basis of the level of incoming activity in such a way that the threshold is increased when spiking activity is high, and vice versa. We believe that in developing neural tissue the homeostatic level of neural activity is regulated in a similar manner. Both neuronal parameters and coupling are subject to formation processes and may undergo drastic changes in short time periods (Sanes et al., 1988). Some regulatory mechanism which constrains the level of neural activity within some neurophysiologically acceptable range can provide a homeostatic level of neural activity. In our model we use the mechanism of threshold regulation (Henze and Buzsáki, 2001).

To realize this idea, we develop a simple computational model of locally coupled elements with adjustable threshold. The idea of adaptation of neuronal parameters to the level of input activity appears to be promising, for example this idea has been used to study different dynamical regimes of neural networks such as bumps, breathers and waves in a neural field model (Coombes and Owen, 2005).

2.2 Model description

We consider a system of coupled Hopfield type binary neurons (Hopfield, 1982) arranged on the 2D square grid and coupled with local connections to their eight

nearest neighbours. Each neuron is also connected to itself, and has a threshold which is adjusted in order to achieve a homeostatic level of activity.

The element which we use in our model is also equivalent to a binary piecewise linear McCulloch-Pitts neuron. Another analogy which can be made here relates to binary cellular automata which change state according to local rules, for example Conway's Game of Life (Gardner, 1970). This model bears some similarities to the Cellular Neural Network, the difference being that the latter uses real-valued state variables (Chua and Yang, 1988).

We use x_i to represent the activities of the neurons, and h_i to represent the thresholds of the neurons, $i = 1, 2, \ldots, M$. Here M is the total number of elements in the network. The states of all model neurons are updated synchronously. In order to calculate the state of a neuron i it is necessary to first compute its total input:

$$I_i(t) = \sum_{j \in N(i)} x_j(t) + x_i(t), \tag{2.1}$$

where N_i is the set of indices of all eight nearest neighbours of neuron i. Updating the state of a neuron is then a simple matter of comparing the current input level with the current threshold:

$$x_i(t+1) = \begin{cases} 1, & I_i(t) \geq h_i(t) \\ 0, & I_i(t) < h_i(t) \end{cases}. \tag{2.2}$$

Thresholds are updated according to the following difference equation:

$$h_i(t+1) = \begin{cases} h_i(t) + a, & I_i(t) \geq h_i(t) \\ h_i(t) - a, & I_i(t) < h_i(t) \end{cases}, \tag{2.3}$$

Here a represents the magnitude of the change in the threshold. In simulations we will consider cases $a = 1$ and $a = 2$ which result in different spatiotemporal

dynamics of neural network activity.

Because the possible input level is intrinsically limited to the range 0-9 (8 nearest neighbours and a self connection) where $a = 1$, the threshold will never drop below 0 (because when the threshold is 0 the cell will be active at the next time step regardless of input level and the threshold will then increase) or increase above 10 (because when the threshold is 10, even if all cells are active the total input is 9 and so the cell will be inactive at the next time step regardless of input level and the threshold will then decrease). For $a = 2$ the threshold will maintain either odd or even values depending on the initial value. Therefore it is possible for the threshold to take the value -1 as a step down from 1 or 11 as a step up from 9, if the initial value was odd.

An interesting property of this model is that every configuration has an equivalent inverse configuration. By this we mean that a transformation is possible from any configuration $(x_i(t), h_i(t))$ to its inverse $(\bar{x}_i(t), \bar{h}_i(t))$ where $\bar{x}_i(t) = 1$ if $x_i(t) = 0$ and vice versa, and $\bar{h}_i(t)$ is the mirror symmetry of $h_i(t)$ according to the value 5. For example if $h_i(t) = 4$ then $\bar{h}_i(t) = 6$.

2.3 Simulation results

2.3.1 Simulation software

In order to study this model, a simulation tool, *CellSimUI*, has been developed (available on request from the author) which allows simulation of the spatiotemporal dynamics of the system. This tool provides a user-friendly interface for convenient adjustment of model parameters, initial conditions, and visualization of simulation results.

Figure 2.1 shows a snapshot of the main window of the simulation software. There are three panels for graphical representation of simulation results and many controls for adjustment of model parameters, initial conditions and for controlling the process of simulation. In the example shown in figure 2.1 the lower left panel

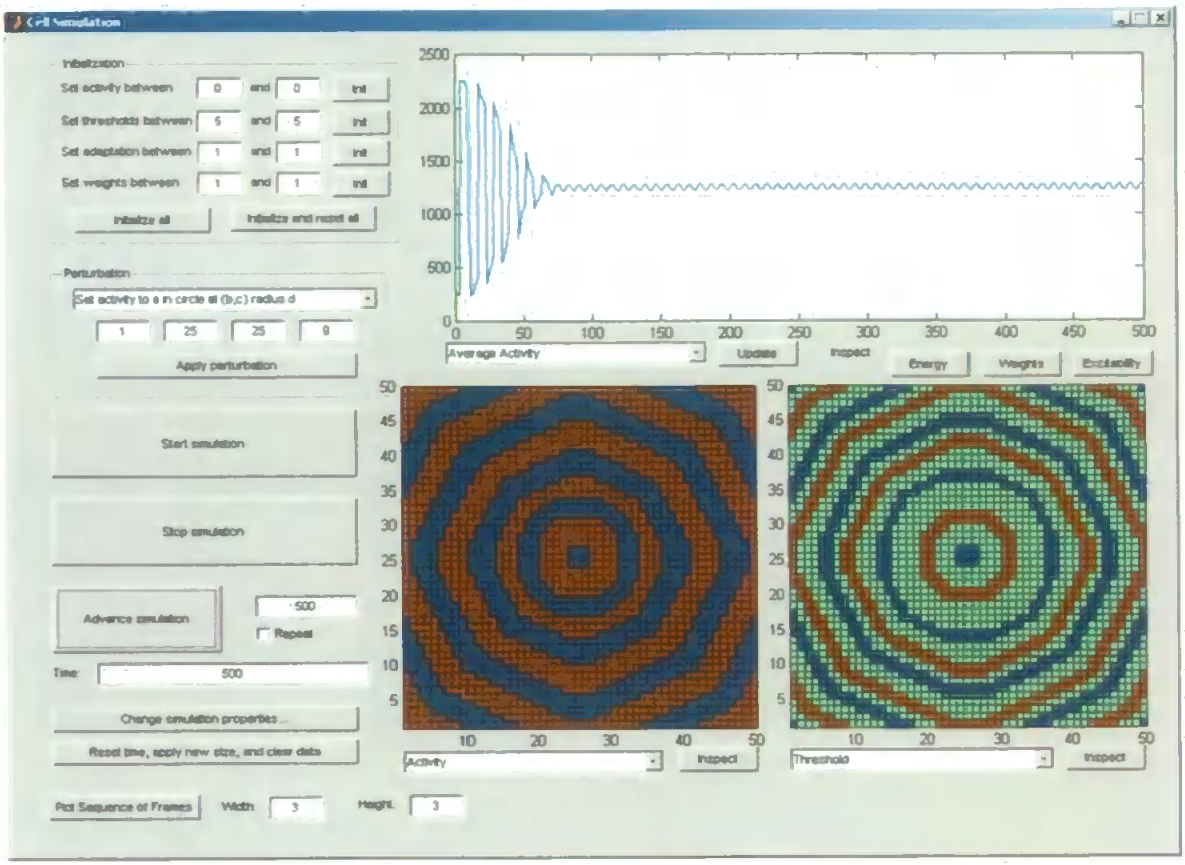

Figure 2.1: User interface for simulations.

shows the activity of the cells in the network, the lower right pane shows the thresholds of the cells in the network, and the upper pane shows the total activity vs time. From top to bottom, the left hand side of the window shows controls for setting initial conditions, applying perturbations, starting and stopping simulation animation, advancing the simulation by a fixed number of time steps, changing simulation parameters (called "simulation properties" in the GUI), resetting the network to the initial state and plotting sequences of frames.

For performance reasons, the main simulation code is developed in C++ and this is interfaced to the GUI using MATLAB's support for extensions.

For all simulations shown here, the size of the grid is 50×50 elements. The boundary conditions are periodic: the edges of the grid connect to each other, forming a torus.

2.3.2 Uniform initial conditions

The model is developed in such a way that all variables can take only discrete values. Generally speaking the dynamics of such a model converge to either steady state or periodic solutions. However, steady states are not possible in our model because the threshold is either increased or decreased at every time step.

In the case where $a = 1$, when all cells are given the same initial value of excitation and threshold, there is no breakage of symmetry and so their activities and thresholds will remain identical for all time. In this case, the dynamics is periodic with period 20 time steps. This is the length of time required for the threshold to be increased from 0 to 10 in increments of 1 unit and then decreased back to 0.

In the case where $a = 2$, the period of the solution depends on whether the initial value of the threshold is odd or even. In the case where the initial value is even, the period is 10, in the case where the initial value is odd, the period is 12.

2.3.3 Nonhomogeneous initial conditions for activity

We begin by considering the situation where $a = 1$ and all thresholds h are initially set to 5. The symmetry is broken by a circular perturbation of the initial conditions: all elements are initially in the 0 state, except for elements in a circle with radius $r = 8$ which for the purposes of easy visualization is centred at coordinates $(25, 25)$. From this initial configuration, we find that the network rapidly reaches a state in which all elements are completely synchronized and have the same value of h. This is due to the fact that the propagation of activity is fast relative to the threshold adaptation, producing a strong synchronizing effect.

We next consider the situation where $a = 2$ and all thresholds h are initially set to 5. The symmetry is again broken by a circular perturbation. For $r < 7$, the high degree of synchronization of the relatively large number of cells outside the stimulated region dominates the network dynamics, and the network again rapidly

reaches a configuration in which all the cells in the network have the same threshold value and transition between UP and DOWN states in synchrony. However, for $r = 7$, the stimulated region is large enough that a circular wave with period 8 develops within the first 100 time steps, with the same centre as the active region of the initial configuration. Figure 2.2 shows the circular wave for this case. As r is increased further, similar results are obtained, until $r = 24$. At $r = 25$, the activities of elements located on the edges of the stimulated region interact with each other, and this produces a large synchronized region resulting in the outcome that the network reaches a homogeneous fully synchronized state (FSS) within 200 time steps.

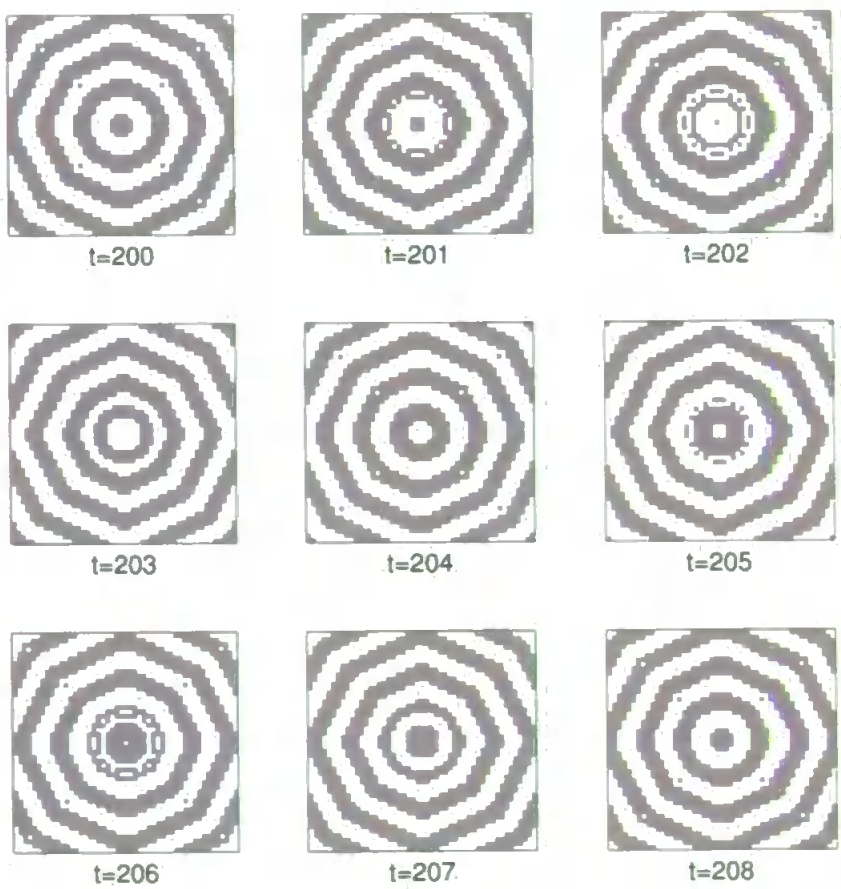

Figure 2.2: Circular wave configuration, $a = 2$, all thresholds $h = 5$ at $t = 0$, initial stimulus radius $r = 7$.

These results illustrate the general point that the dynamics of this model are substantially affected by the presence or absence of a large body of synchronized cells within the network.

We now consider the case where the symmetry of the initial configuration is broken by randomly and independently assigning the activity of each element. The probability of an element being active in the initial state is denoted by p. In this case $p = 0.5$. Activity is therefore uniformly distributed over the network due to the relatively large number of model elements. Initial thresholds are all equal to 5.

Multiple simulations of this system show that within a few hundred cycles, these initial configurations produce complex spatiotemporal dynamics with period equal to 12. All spatial configurations are different and resemble a spiral like cluster (SLC). Figure 2.3 shows an example of SLC behaviour when $a = 1$. If the simulation starts from an initial configuration with high activity level ($p = 0.7$) the system dynamics converges to the FSS state within a few hundred time steps. For the intermediate value of $p = 0.6$ (intermediate activity level of the initial configuration) the system dynamics is bistable: some initial configurations converge to the FSS state whereas others converge to the SLC state. Multiple simulations show that the frequency of FSS states is approximately 30%. It is interesting to note that the value $p = 0.65$ can be considered as an approximate boundary where the system bifurcates from bistability to the FSS state. Simulations show that for $p = 0.65$ the frequency of SLC states is approximately 5%. Figure 2.4 summarizes the results of multiple simulations. In fact we can see from this figure that the boundary between bistability and the FSS state is between $p = 0.65$ and $p = 0.7$. It is interesting to note that the spiral-like spatial configuration is quite different for different values of p. For example, for $p = 0.6$, a typical SLC is shown in figure 2.5. Another two examples for $p = 0.55$ and $p = 0.62$ are shown in figures 2.6 and 2.7. In figure 2.7, three spiral waves interact to produce a ring of activity that radiates outwards.

In the case of $a = 2$, the dynamics of the system are similar. Figure 2.8 shows

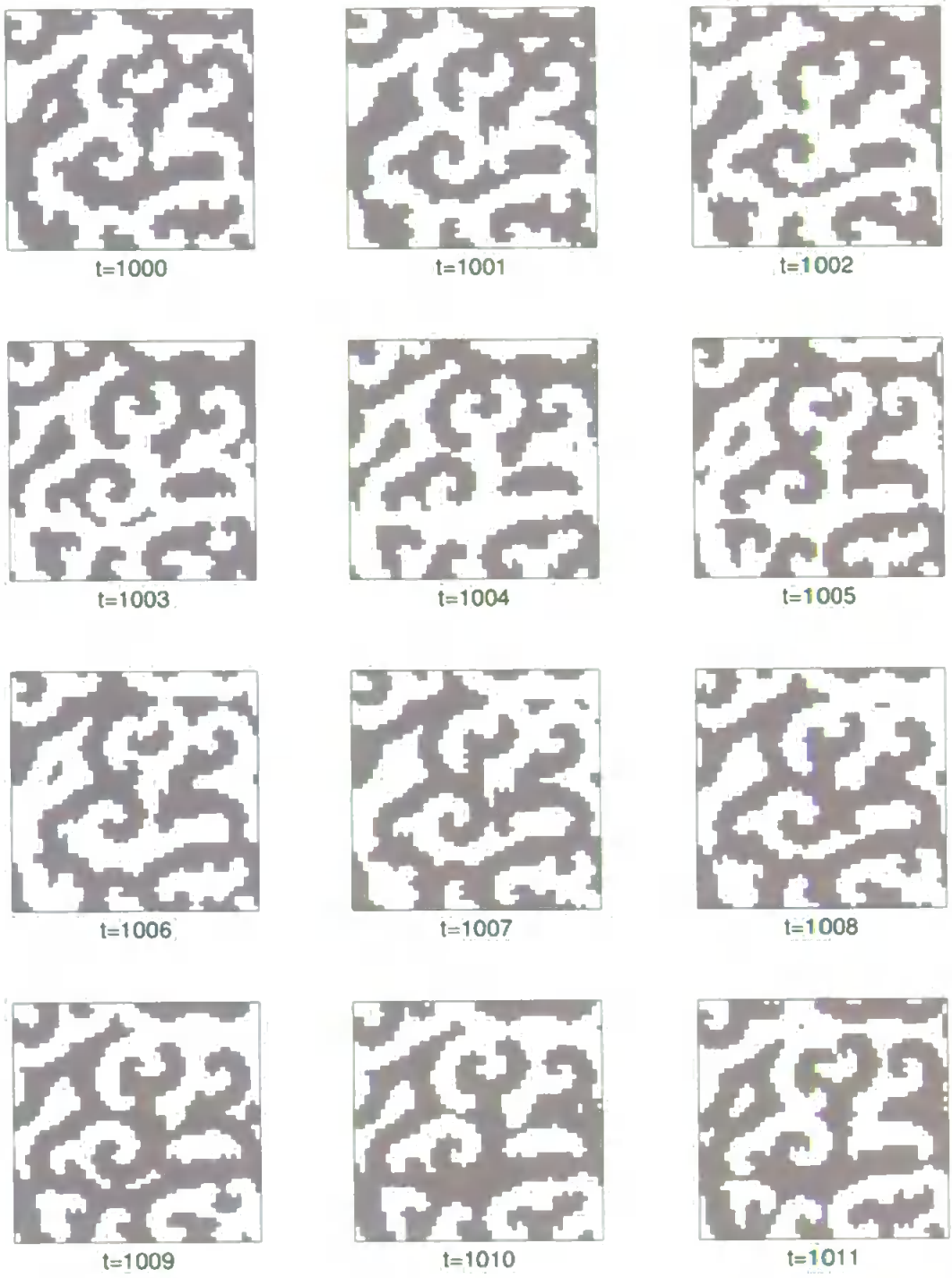

Figure 2.3: Sequence of frames from eventual periodic behaviour of the system where every cell has a 0.5 probability of being active in the initial configuration and $a = 1$. Period is 12.

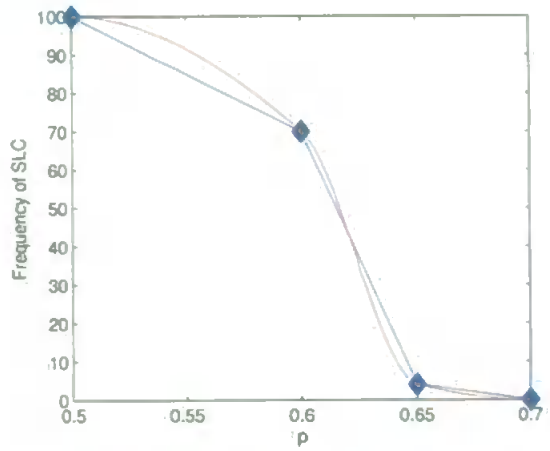

Figure 2.4: Frequency of SLC states vs probability of initial activity p. Boundary between bistability and the FSS state is between $p = 0.65$ and $p = 0.7$

a typical example of eventual dynamical behaviour, and an SLC configuration with period 8 can easily be seen. The shorter period of the $a = 2$ configuration in comparison with the $a = 1$ configuration is due to the faster adaptation of the threshold.

2.3.4 Heterogeneous initial conditions for threshold

So far, we have studied dynamics of the system under many different cases for initial conditions for the activity of the elements, but in these cases all thresholds were initially set to 5. If we break the symmetry of the initial conditions for thresholds as well, the dynamics of the system becomes even more complex. For example, in the case of $p = 0.7$ (see above) breaking the threshold symmetry in such a way that the initial values 5 and 6 have been independently and uniformly distributed among the network elements allows multistability: the FSS state coexists with several SLC states (SLC with period 12, 36, and 60 have been observed). An example of the SLC state with period 12 can be seen in figure 2.9.

We noted above that when $a = 1$ and asymmetry in the initial configuration is produced by making a circular region active, this asymmetry is rapidly lost and the network becomes completely synchronized. By introducing heterogeneity in the initial conditions for the threshold (by randomly assigning the initial value for the

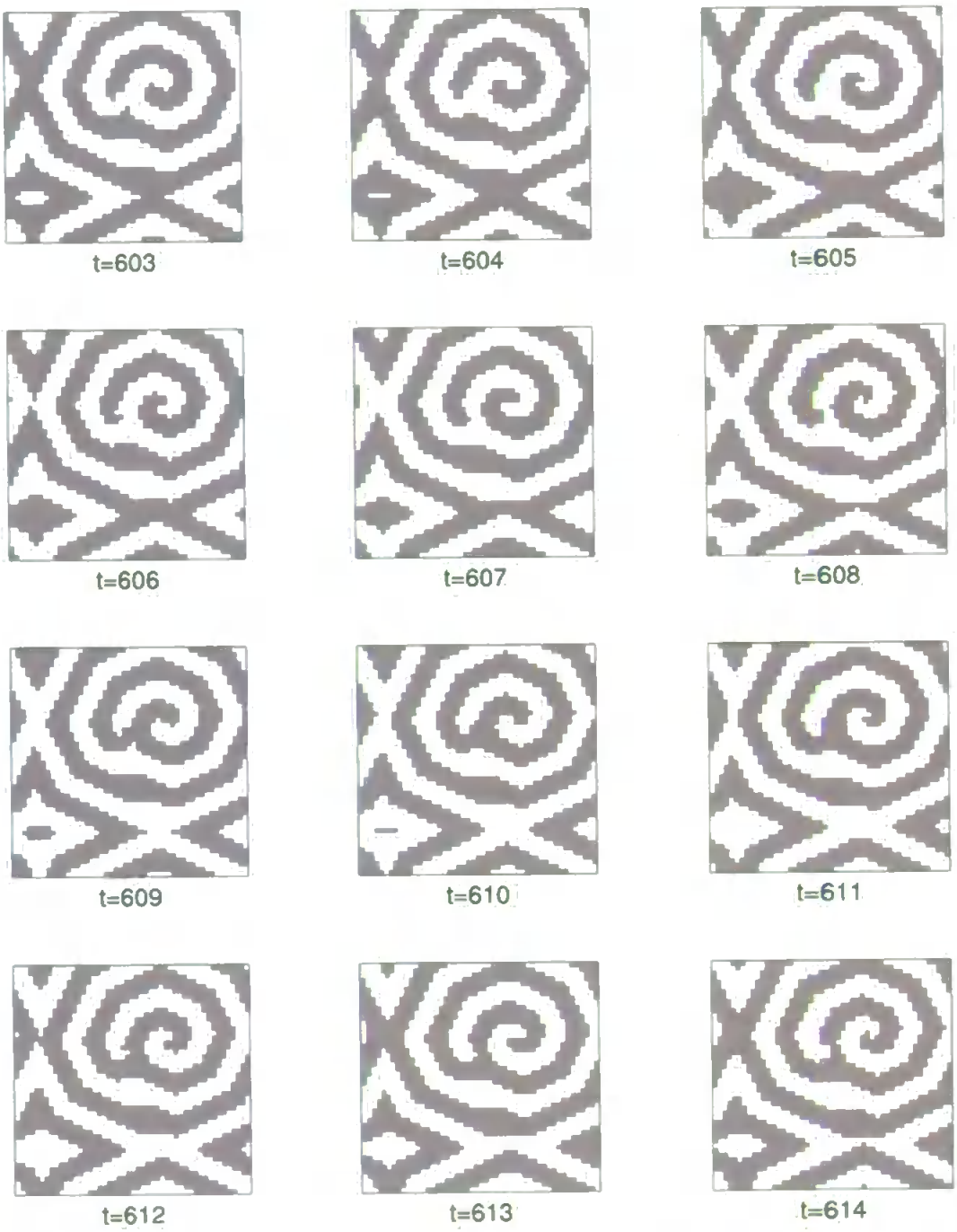

Figure 2.5: Sequence of frames from eventual periodic behaviour of system where every cell has a 0.6 probability of being active in the initial configuration and $a = 1$. Period is 12.

Figure 2.6: Frame from eventual periodic behaviour of system where every cell has a 0.55 probability of being active in the initial configuration and $a = 1$. Period is 12.

Figure 2.7: Frame from eventual periodic behaviour of system where every cell has a 0.62 probability of being active in the initial configuration and $a = 1$. Period is 12.

Figure 2.8: Sequence of frames from eventual periodic behaviour of system where every cell has a 0.5 probability of being active in the initial configuration and $a = 2$. The period is 8.

Figure 2.9: Frame from eventual periodic behaviour of system where every cell has a 0.7 probability of being active in the initial configuration, $a = 1$, thresholds are initialized by two values of 5 and 6 with equal probability. Period is 12.

Figure 2.10: Ring-like pattern generated in the $a = 1$ configuration by drawing initial thresholds randomly from the set {4,5,6} and specifying a initial active region of radius 9.

threshold of each cell to be drawn uniformly and independently from the set {4,5,6}), this synchronizing effect can be reduced and the $a = 1$ model can display an SLC with period 12 derived from a circular active region in the initial configuration of activity (figure 2.10).

Next we consider the case where $a = 2$. We again randomly assign the initial value for the threshold of each cell to be drawn uniformly and independently from the set {4,5,6}. A region of radius 9 grid units is set to be active in the initial state of the network, all other cells are inactive. As shown in figure 2.11, these initial conditions can generate a spiral pattern of period 8.

Again, this is the case of multistability and several SLC states with different periods may be observed. While the SLC with period 8 is the most common outcome from these initial conditions, other outcomes are possible, including approximately synchronous activity, and a propagating wave pattern (PWP) (fig. 2.12) of period 10. It is interesting to note that the initial spatial configuration of activity is symmetrical but due to the heterogeneity in the initial conditions for thresholds, the final configuration of activity is not symmetrical.

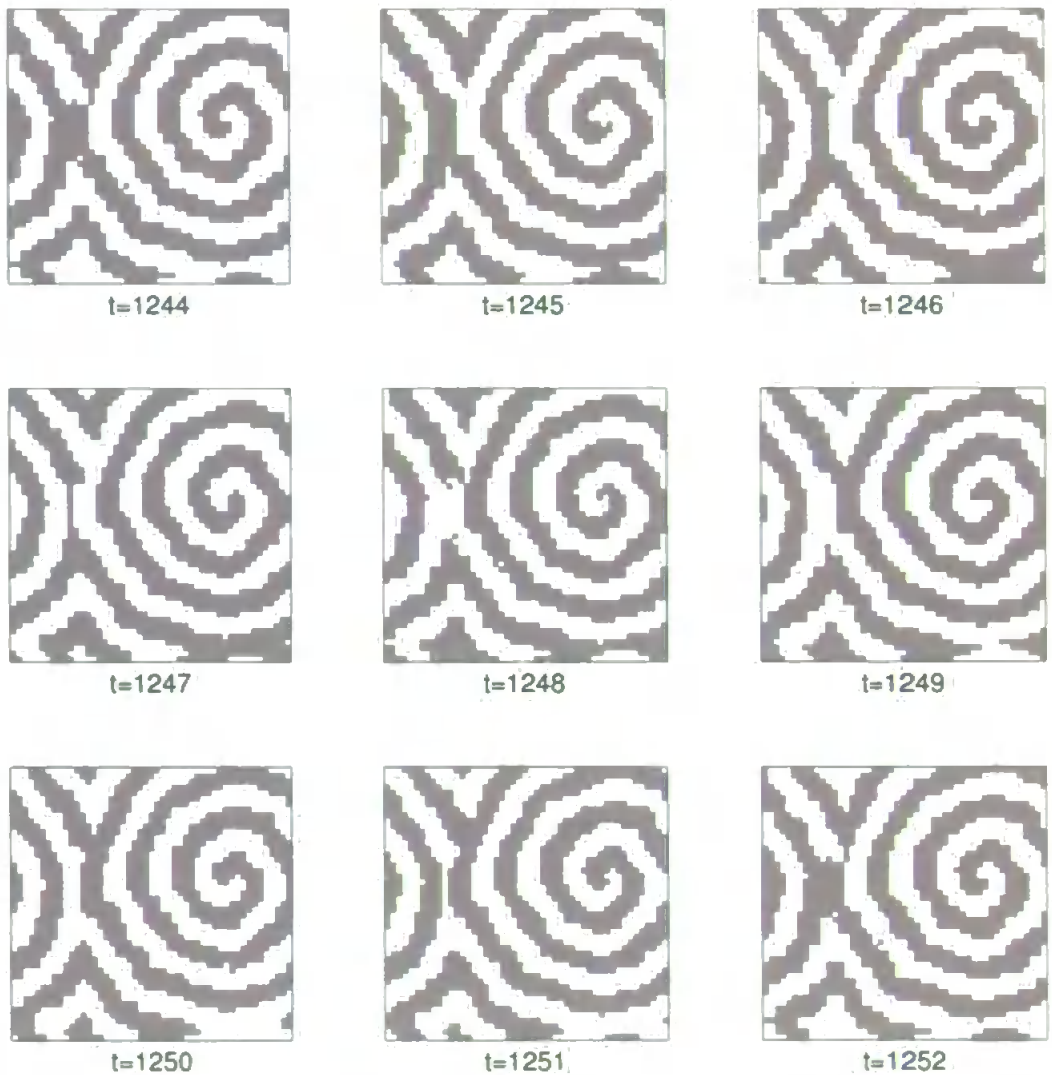

Figure 2.11: Period 8 spiral generated by drawing initial thresholds randomly from the set {4,5,6} and specifying an initial active region of radius 9. Here $a = 2$.

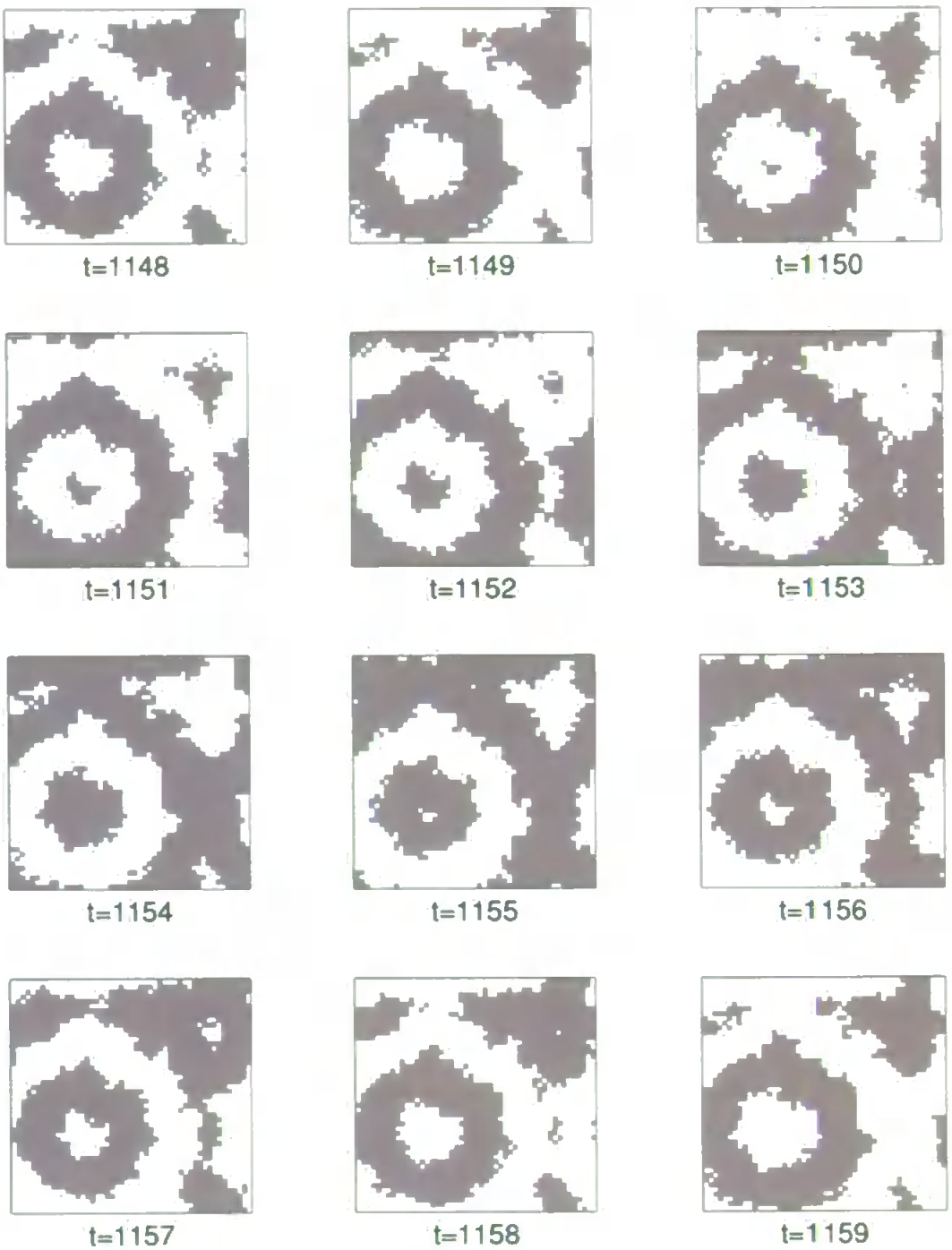

Figure 2.12: Propagating wave generated by drawing initial thresholds randomly from the set {4,5,6} and specifying an initial active region of radius 9. Here $a = 2$.

2.4 Discussion

We have demonstrated that a simple model consisting of locally coupled Hopfield-type neurons with adjustable threshold can exhibit interesting dynamical behaviours which demonstrate similarities with known electrophysiological recordings. The propagation of activity in the network can be considered as positive feedback - the more active neurons there are, the easier it is for inactive neurons to become active, and vice versa. If there were no threshold adaptation ($a = 0$), the network would quickly reach a steady state in which all neurons were active or all neurons were inactive. The threshold adaptation is a type of negative feedback which prevents the network from reaching a steady state configuration and the interaction between this slow process of threshold adaptation and the fast dynamics of the activity variable generates a variety of spiral wave-like spatiotemporal patterns.

Simulation results for $a = 1$ show that for different initiation protocols the resulting dynamics is of spiral wave type with typical period 12 time units. The number of possible spatiotemporal patterns is very large. Investigation of the effect of changing p revealed that the initial balance of activity vs inactivity in the initial state is important for the generation of spiral type dynamics.

For the case $a = 2$, a new type of propagating wave pattern (PWP) appears. It can be a symmetrical PWP (circular wave) similar to the wave shown in figure 2.2, or if we break symmetry by initial random distribution of thresholds, the PWP can be more complex (ring-type pattern) as seen in figure 2.12. In comparison with $a = 1$ the variation in the possible patterns is much higher and longer periods become more common.

We have not extensively investigated the case where $a = 3$, but preliminary simulations indicate that interesting behaviour is also possible in this case including complex dynamics with long period. For example, figure 2.13 shows total activity vs time. This plot shows significant variation (20%) of the total activity during the

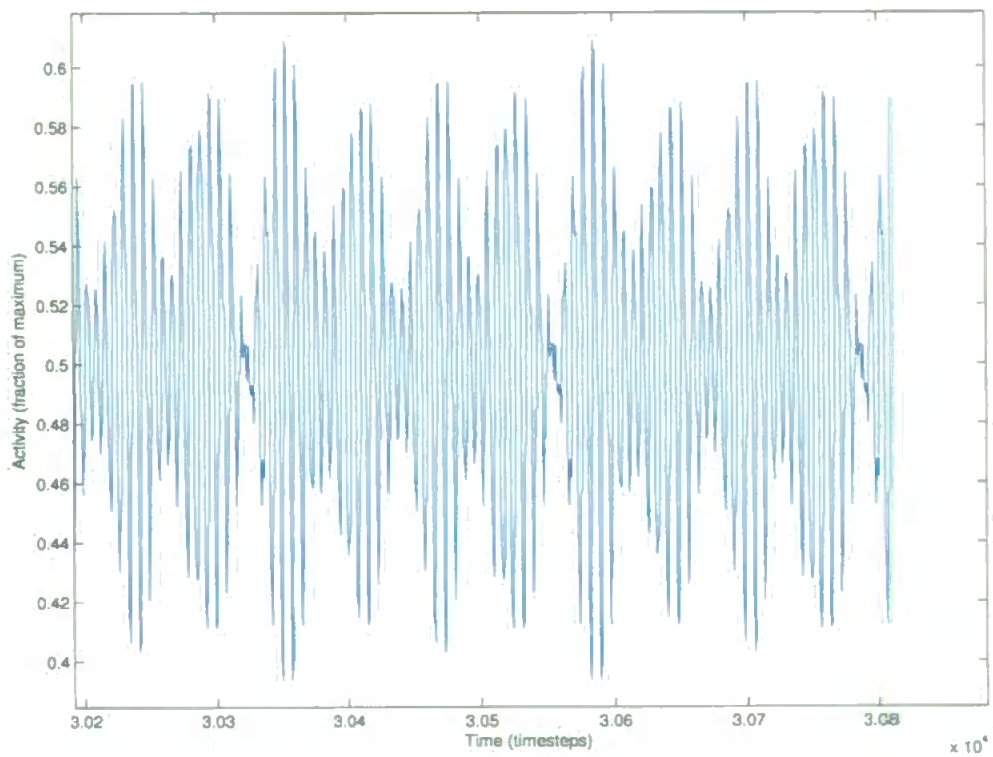

Figure 2.13: Total activity vs time for $a = 3$, initialized with $p = 0.5$ and initial thresholds $\{4,5,6\}$

Figure 2.14: Spiral wave produced with $a = 3$, initialized with $p = 0.5$ and initial thresholds {4,5,6}. The period of this spiral wave is 64.

period which is 232 time steps, and high frequency oscillations of the total activity are modulated by a lower frequency. Another example of dynamics in the $a = 3$ case is shown in figure 2.14. This figure demonstrates a very clear spiral wave; the exact period of the dynamics is 64, but this cycle includes 8 repetitions of a very similar pattern.

Chapter 3

Neural network with noise: persistent neural activity and metastable states

3.1 Introduction

In this section we introduce a system of locally coupled threshold elements with random noise on a square grid. This system was motivated by the discrete-time Hopfield model of associative memory (Hopfield, 1982). The rule for updating the state of each element contains two terms: a term taking into account the activities of the element's neighbours, and a noise term. The resulting dynamics appear due to the interaction of the deterministic term and the stochastic component. Thus, the dynamics of the model are richer than the pure deterministic dynamics of the Hopfield-type model and the pure stochastic behaviour of the Ising model (Amit, 1989). Of particular interest are the metastable (persistent) states and phase transitions which can be observed within a specific range of noise amplitudes. These observations are relevant to the general problem of clarifying the role of noise in system dynamics.

In the typical experimental paradigm under which persistent activity has been observed, activity appears as a response to the presentation of a specific short stimulus and lasts from a few seconds up to several minutes after stimulation is withdrawn. This type of neural activity is traditionally considered to be a process underlying

memory, specifically short-term memory formation (Brody et al., 2003). Another possible role of persistent activity is to provide a source of excitation to drive motor behaviour, for example, swimming in simple vertebrates (Roberts et al., 1997).

Recent experimental data show that persistent neural activity is observed in many brain systems. It has been shown (Egorov et al., 2002) that the neurons of the rat entorhinal cortex in the parahippocampal region demonstrate graded persistent activity (constant firing rate) lasting for several minutes in response to stimulation. The sustained activity level (firing frequency) can be either increased or decreased depending on the input. These findings indicate that the entorhinal cortex could play an important role in establishing associations between stimuli (Frank and Brown, 2003). It has also been found (Taube and Bassett, 2003), that many so-called head direction cells in the rat limbic system exhibit characteristics of persistent neural activity. It is likely that this type of neural activity reflects processes corresponding to the memorization of head direction. In vivo intracellular recordings from oculomotor neurons of the goldfish demonstrate persistent changes in firing rate following saccades (Aksay et al., 2000, 2001). This persistent activity can probably be associated with short-term memorization of eye position in the goldfish hindbrain. Local cortical neural circuits in the prefrontal cortex and visual cortex of the rat are capable of generating persistent activity for periods of seconds or longer as well as transitions between different states of persistent activity such as UP and DOWN states (McCormick et al., 2003). It is possible that this activity indicates processes of working memory based on recurrent network activity. Experimental recordings from prefrontal neurons of monkeys (Compte et al., 2003) reveal persistent activity during a delayed response task. This study shows that the persistent neural activity observed in prefrontal cortex is highly irregular and can best be characterised by statistical measures such as inter-spike interval distribution, autocorrelation function, mean, standard deviation, and other moments. This irregularity is more pronounced during the mnemonic delay period than in the

fixation period.

Computational models of persistent activity usually exploit one of the following approaches: (1) there are features of neuronal excitability or synaptic transmission which allow long characteristic times of some membrane and synaptic processes (Fransén et al., 2006); (2) persistent activity is a collective effect and dynamical phenomenon which appears as the result of specific interactions between neurons (Constantinidis and Wang, 2004). In this study we adopt the second approach and consider the problem of how to obtain persistent and long lasting activity in a population of interactive neurons with relatively short reaction times.

We study persistent activity in simple models of neural populations of excitatory neurons with random noise. This study was inspired by ideas from statistical physics which generalise the bistability approach by considering phase transitions and metastable states. It is well known that metastable states can be characterised by long lasting phases and such an approach appears to be promising for modelling persistent activity in the brain. A typical example of long lasting patterns is provided by the Ising model which is one of the simplest examples of a system in which metastable states and phase transitions can be seen.

In this chapter, we consider a model of a population of interactive neural elements on a square grid with local connections and noise, similar to the Ising model. The neural element considered here is a simple threshold device which integrates the activities of its neighbours and also includes a random variable which reflects both neural and synaptic noise. Thus, the dynamics of the model elements depends on the interplay of two factors: the total activity of neighbouring elements and the level of the noise. We show that this simple model can demonstrate an interesting dynamics: metastable and persistent states of UP and DOWN activity as well as phase transitions. We have found that there is a critical level of noise which maximizes the variance of neural activity; this is due to the appearance of frequent phase transitions between distinct metastable states in the vicinity of this noise level.

3.2 Model description

We consider a system of interacting elements coupled on the grid where the edges of the grid are connected to each other, forming a torus. Each element is connected with eight neighboring elements. Activity is described by $x_i \in \{0,1\}, i = 1,2,...,M$ where M is the number of elements. The firing threshold θ is fixed and is the same for all elements. All connections have weight 1.

Time is discrete and elements are updated synchronously. In order to compute the new activity of the element i at the moment $(t+1)$ it is necessary to first calculate the total input $I_i(t)$. In the equations below $N(i)$ refers to the set of indexes of eight nearest neighbours to the element i on the grid. As can be seen below, the element i also receives input from itself. The term ξ_i represents location and time independent Gaussian noise with zero mean and standard deviation σ.

$$I_i(t) = \sum_{j \in N(i)} x_j(t) + x_i(t) + \xi_i \tag{3.1}$$

$$x_i(t+1) = \begin{cases} 1, & I_i(t) \geq \theta \\ 0, & I_i(t) < \theta \end{cases} \tag{3.2}$$

If the number of active elements in the vicinity of node i is substantially less than or greater than the threshold, it is unlikely that the noise will affect the state of that node at the next time step. However if the level of input is close to the threshold, the effect of noise becomes crucial. For example, if the threshold value $\theta = 4.5$ and the standard deviation of the noise is $\sigma = 1$ then the borderline cases are $I_i(t) = 4$ or $I_i(t) = 5$ because they are closest to the threshold. In each case, we would like to find the probability that noise will not influence the deterministic dynamics in these cases: $P\{\xi_i < 0.5\} = 0.69$ (we calculate this taking into account the normal distribution of the random variable ξ). This probability increases rapidly as $I_i(t)$ takes values further away from θ; for the cases $I_i(t) = 3$ and $I_i(t) = 6$

the probability that the deterministic dynamics will not be influenced by noise is $P\{\xi_i < 1.5\} = 0.933$.

For all simulations, initial conditions are that the value of each x_i is randomized independently and uniformly to 0 or 1, unless stated otherwise. The dimensions of the grid are 50 elements on each side, and the number of elements $M = 2500$.

Inclusion of the above-mentioned self connection makes it possible to achieve symmetry between any given configuration and its inverse when the uniform threshold is set to 4.5. In this case we can consider two initial configurations where one is the inverse of the other (inactive elements in one area are active in the other and vice versa) and subject them to noise of the same value but opposite sign (e.g. by seeding our pseudo-random number generator with the same value in both cases and modifying Eq. 3.1 for either system to change the sign of the noise term), then subsequent states will also be the exact inverse. It also follows that any steady state in the system appears in a pair with its inverse.

3.3 Simulation results

We consider a series of simulations starting from many random initial configurations for a range of noise levels, with a particular interest in finding persistent and metastable states.

When $\sigma = 0$, the system rapidly (typically in around 18 time steps) converges to one of many possible steady states. When the initial conditions for activity are completely randomized, this steady state will contain distinct active and inactive regions (Fig. 3.1) with approximately 50% of elements active in the final configuration. This configuration is characterised by the presence of clusters of active and inactive nodes and we will refer to it as a cluster configuration.

It is helpful to consider the stability of the cluster in terms of the stability of the locality around each point. An active cell with four or more neighbours active will remain active. An inactive cell with four or more neighbours inactive will remain

Figure 3.1: Steady state resulting from a randomized initial configuration. White squares represent active elements.

inactive. These are the only possibilities for local stability and this constrains the set of possible stable system configurations; for example, an isolated 2×2 square of activity or inactivity cannot appear in a stable configuration because each element will only have three neighbours that share its state instead of the required four.

In the case where $\sigma > 0$ and small, the noise tends to destroy cluster configurations which are typical for the zero noise case. Starting from an arbitrary random configuration, the activity dynamics relatively rapidly (within a few hundred time steps when $\sigma = 1$) leads to one of three cases: (1) almost all elements are active (we will refer to this as the UP state), (2) almost all elements are inactive (DOWN state), or (3) approximately 50% of the elements are active, and a situation has developed where inactive and active regions exist side by side, neither surrounding the other. Fig. 3.2 illustrates these cases by plotting the mean activity of 20 random initial configurations which are simulated for 500 time steps. Fig. 3.3 shows the spatial pattern of activity for case (3), which we consider as an analogue of the metastable state in statistical physics.

When case (3) develops, the borders between the two regions shown in Fig. 3.3 are effectively neutral in the sense that they are equally likely to move in either direction. This means that they move according to a (very slow) random walk

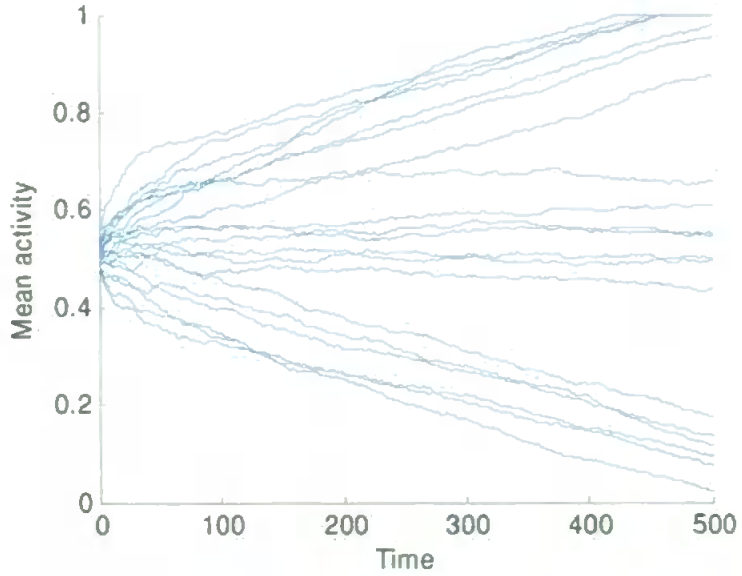

Figure 3.2: Mean activity trajectories from twenty randomized initial conditions where $\sigma = 1$. The three possible classes of outcome (UP state, DOWN state, metastable state) are clearly visible.

process, and so this configuration is long lived. Eventually the system will converge to a steady UP or DOWN state (with sparse spontaneous firing/quiescence) but this can take hundreds of thousands of cycles in some cases. This regime of long-lasting activity can be considered as a possible mechanism for persistent activity in the brain. Also, this regime can be used for modelling of short-term memory.

For large values of σ, the noise term in Eq. 3.1 dominates the deterministic term and the dynamical behaviour of the model can be characterised as the independent appearance of active/inactive states in nodes of the grid with equal probabilities. Thus, the spatial configuration of the network can be considered as homogeneous with symmetry in appearance of active and inactive states, therefore the mean of the total activity of the network is close to 50%. A typical spatial configuration is shown in Fig. 3.4.

The most interesting and sophisticated case corresponds to an intermediate value of σ. In this case there is a balance between the relative influences of the deterministic and stochastic terms in Eq. 3.1. As σ is increased past about 3.6, the influence of noise overwhelms the influence of the local neural activity. At this point the system

Figure 3.3: Long lasting intermediate activity state, in which the boundary between active and inactive regions moves according to a slow random walk process.

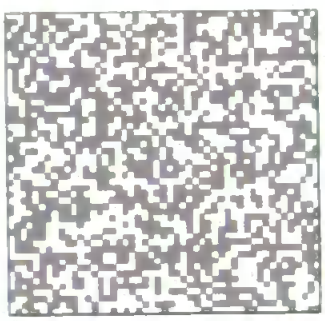

Figure 3.4: Spatial configuration when $\sigma = 20$, showing the lack of spatial organization in the system at high noise amplitudes.

is no longer able to maintain distinct UP and DOWN states and the mean activity of the system oscillates around 0.5 (half of the elements are active).

For intermediate values of σ ($\sigma \approx 3.3$), several phenomena can be seen: 1) the pattern irregularity (and therefore, variance of the total network activity) increases, 2) the transition time between UP and DOWN states is fast relative to the duration between successive transitions, and 3) there is an increase in the amount of spontaneous activity and spontaneous inactivity observed. As σ is increased above about 3.3, the high activity and low activity states very rapidly lose stability and a regime develops where the network switches between varying about a high level of activity, and varying about a low level of activity. This is the regime of phase transitions and each phase (UP or DOWN) can be characterised as a metastable state. Fig. 3.5 shows a typical time course of the mean activity and Fig. 3.6 shows typical spatial

configurations corresponding to the DOWN, intermediate, and UP phases.

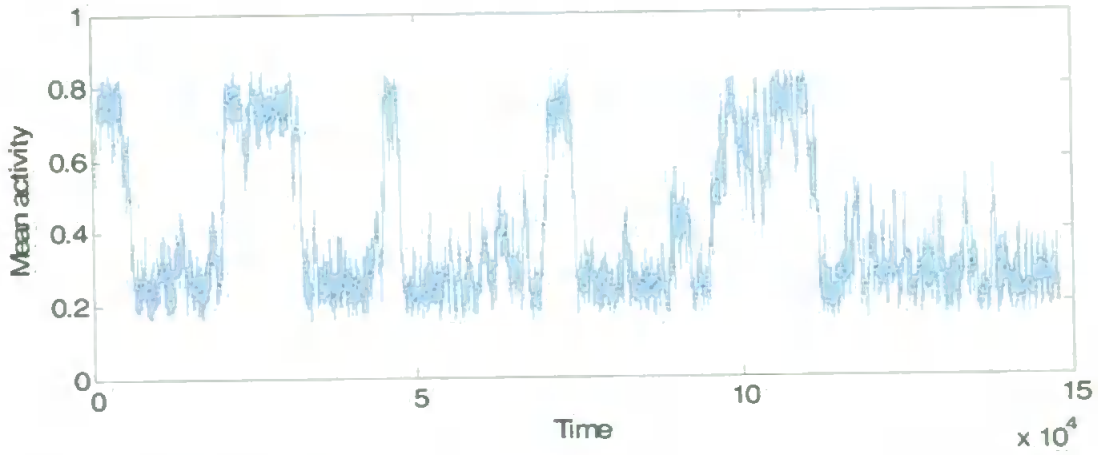

Figure 3.5: Plot of mean activity with $\sigma = 3.37$. The system alternates between metastable high and low activity states.

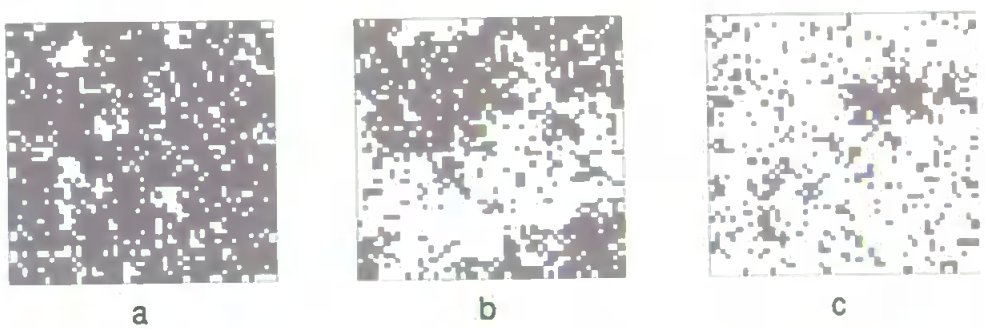

Figure 3.6: Low, intermediate, and high activity spatial configurations where $\sigma = 3.37$. The intermediate configuration is highly unstable and will quickly transition to a high or low activity state.

Fig. 3.7 shows a histogram of the instantaneous population activity in the regime of UP and DOWN alternation accumulated during a run of 10^6 time steps. We accumulate activity values (samples) for successive time steps and use them to calculate the histogram, which shows a bimodal form with a small bias towards DOWN phases due to limited run length.

Fig. 3.8 shows the variance of the instantaneous population activity vs σ. It shows that there is a critical value of noise which provides the biggest variance. This plot also reveals the region in parameter space in which the UP and DOWN/metastable regime exists, and therefore the variance is high. It indicates

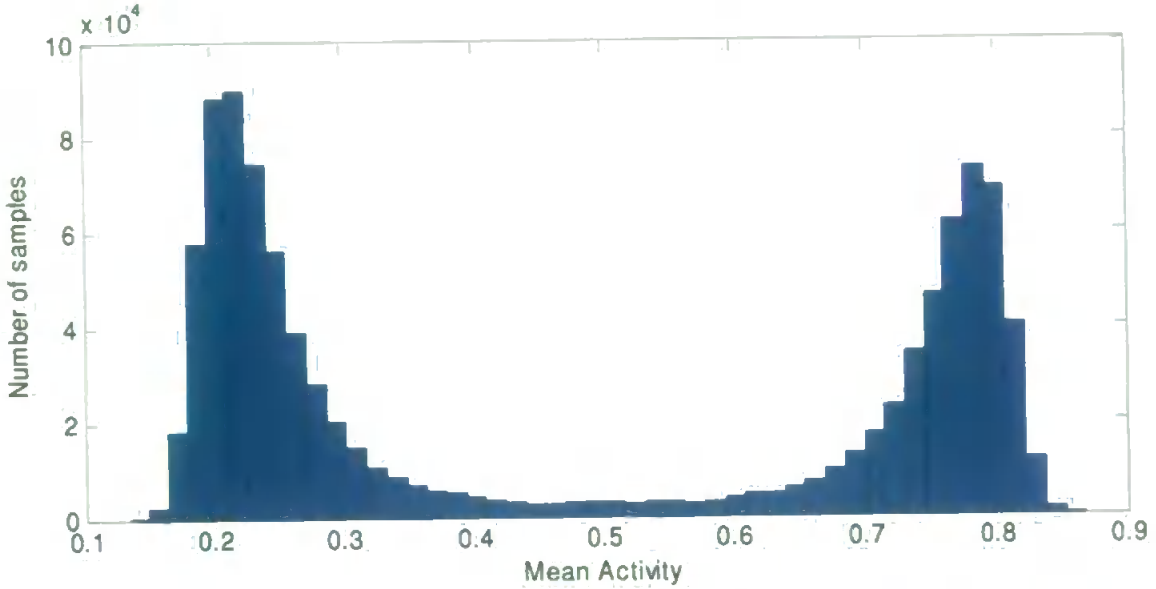

Figure 3.7: Distribution of instantaneous mean activity samples for $\sigma = 3.37$. Run length is 10^6 time steps.

that the critical level of noise for promoting metastability of the high and low activity states is approximately 3.4. This result is in line with the coherence resonance phenomenon which has been observed in excitable media and single neuron integrate and fire models (Pikovsky and Kurths, 1997; Lindner et al., 2002).

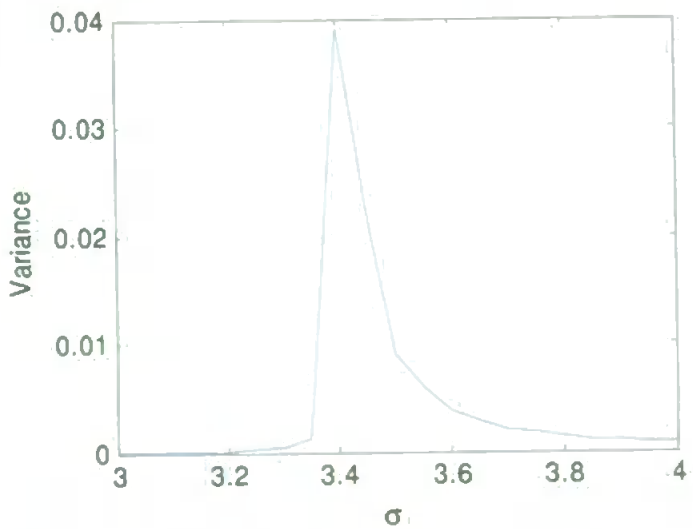

Figure 3.8: Variance of mean activity as a function of noise amplitude. Variance is maximized at approximately $\sigma = 3.4$.

3.4 Discussion

To understand the spatio-temporal activity in the metastable state, we study a simple discrete-time model of binary neurons locally coupled on the grid. This model is capable of producing rich dynamics including metastability when combined with noise. Moreover, we have noted that in this model metastability results from a balance between the strength of coupling between individual elements and the noise amplitude; if either dominates, the spatio-temporal activity of the network rapidly becomes stereotyped. Thus, critical values of noise amplitude generate interesting dynamical behaviour in this model. In this critical region the system is flexible and can easily be switched between metastable states both autonomously (UP and DOWN phase transitions) or by a control process.

We can suggest that such a balance between deterministic and stochastic components may be an important factor in the dynamics of coupled neural networks in the brain. We speculate that the working mode of the active brain is in the vicinity of the critical regime (Massimini et al., 2005) and modulation of this balance (for example, during sleep) may allow the network to act as an adaptive memory under certain conditions, and as a source of coherent variable activity under other conditions; such shifts in network dynamics may be implicated in both development (Tabak et al., 2001) and the maintenance of synaptic homeostasis (Tononi and Cirelli, 2003).

The simulation model considered here is very simple, nevertheless it already demonstrates many important characteristics of neural activity and persistent states. This model can exhibit long lasting states, transitions between UP and DOWN states, and a critical value of noise. Further support for the usefulness of this model comes from a similar model with local connections but with more realistic enhanced integrate-and-fire elements (Borisyuk, 2002) which demonstrates broadly equivalent behaviour.

A biologically inspired generalisation of this model has been developed which

includes both threshold adaptation and synaptic plasticity. To obtain the persistent regime in a neuronal system, thresholds and synaptic weights have to be properly adjusted. We can expect that under some constraints the system with threshold adaptation and synaptic plasticity can self-organize its dynamical behaviour in such a way that the parameter values will be automatically adjusted to generate persistent activity. Thus, the generalization of this model will be considered in the next chapter.

Chapter 4

Neural networks with synaptic plasticity: phase transitions

4.1 Introduction

The traditional approach to solving the problem of long lasting activity is based on bistability of the population spiking rate. This bistability can appear, for example, as the result of positive feedback in a population model (Brunel, 2003). Suppose that there are two stable states of neural activity such that in one of these, activity is low and in the other activity is high. These two stable states coexist and the population demonstrates a low or high spiking rate depending on the initial condition. If the initial condition belongs to the basin of attraction of the low state then the population will demonstrate a low activity level and vice versa. Let us suppose that the population is in the low activity state and a short external input is applied. This perturbation by external input can change the dynamical regime of the population and move it from the basin of attraction of the low state to the basin of attraction of the high state. Even a short input application can be sufficient to move the activity of the population through the critical boundary in the phase space of the system which separates these two basins of attraction. In principle the system can return back to the low level; for example, due to habituation, fatigue, or a limited amount of neuromodulators or other chemicals, the system parameters can slowly

change their values resulting in the neural activity returning to a low level. This is a hysteresis phenomenon which typically appears in systems with bistability and its explanation is based on the appearance of the cusp bifurcation which includes two fold bifurcations in the dynamical system that controls the spiking rate of the population.

Evidence suggests that neurons use cell-autonomous processes to regulate their internal level of activity (Turrigiano, 1999). It is also well known that synaptic strengths are adjusted according to some correlative learning rule (Abbott and Nelson, 2000).

This study considers a cellular automaton in which the homeostatic condition for each cell is that the cell changes state (from off to on or from on to off) on every cycle. If the cell is on for two or more cycles, it is considered to be overactive, and if the cell is off for two or more cycles is it considered to be underactive.

We examine the question of whether or not a system of local rules that allows each cell to adjust its threshold and synaptic inputs can produce a homeostatic condition in which all cells satisfy the condition specified above, or whether the effect of slower network dynamics will prevent this from taking place.

4.2 Model with nearest neighbour connections and synaptic plasticity

4.2.1 Model description

The system comprises a square grid of M discrete elements with local connections. Neurons are connected to their 8 immediate neighbours on the grid, and there are no self-connections. The edges of the network are connected to each other, creating a torus.

Each neuron is described by its current state $x_i(t)$ (1 or 0, analogous to activity or inactivity), and its threshold for firing, $\theta_i(t)$ which is adaptable depending on the neural activity. All elements of the network are updated synchronously according

to the following equations:

$$I_i(t) = \sum_{j \in N(i)} w_{ji}(t) x_j(t), \tag{4.1}$$

$$x_i(t+1) = \begin{cases} 1, & I_i(t) \geq \theta_i(t) \\ 0, & I_i(t) < \theta_i(t) \end{cases}, \tag{4.2}$$

$$\theta_i(t+1) = \theta_i(t) + [1 - |x_i(t) - x_i(t+1)|](2x_i(t) - 1)\Delta_\theta. \tag{4.3}$$

Where $N(i)$ is the set of indexes of the eight nearest neighbours of element i. $I_i(t)$ is the input to a neuron i and Δ_θ is the amount by which the threshold $\theta_i(t)$ changes in the event that $x_i(t)$ is the same as $x_i(t+1)$ ($\Delta_\theta = 1$). $w_{ji}(t)$ is the adjustable connection strength from element j to element i.

Technical remark: because the rule for updating the threshold includes both activity $x_i(t)$ and $x_i(t+1)$, it is necessary to store both these activities for this calculation. After $x_i(t+1)$ and $\theta_i(t+1)$ have been calculated for all $i = 1, \ldots, M$ it is possible to discard $x(t)$.

In chapter 3 we introduced a rule for threshold adjustment based on the idea of homeostatic activity, i.e. the threshold increases if activity is high and decreases if activity is low. In this model we use another rule which is based on the same idea but with one significant difference: the adaptation rule takes into account two sequential activity states of the element. Threshold adjustments are only made if the activities of the element are the same in two sequential time steps. The threshold will increase if an element was active in two sequential time steps and vice versa; the threshold will decrease if an element was inactive in two sequential time steps. Thus we can consider this rule as another variant of the idea of homeostatic activity.

The learning rule which governs the plasticity of synaptic connections is the following:

$$w_{ji}(t+1) = w_{ji}(t) + x_j(t+1)[x_i(t+1) - x_i(t)]\Delta_w. \tag{4.4}$$

Here Δ_w is the magnitude of the weight change. In addition, all weights w_{ji} are constrained to be in the range $[w_{min}, w_{max}]$.

Technical remark: because the rule for updating the connection weights includes both activity $x_i(t)$ and $x_i(t+1)$, it is necessary to store both these activities for this calculation. After $w_{ji}(t+1)$ have been calculated for all (j,i) it is possible to discard $x(t)$.

This rule can be stated as follows: when a presynaptic element is active at the time step before a postsynaptic element changes from the inactive state to the active state, the synaptic weight associated with that presynaptic element is increased. This is analogous to the main idea of STDP: inputs that influence postsynaptic firing are strengthened. However, when a presynaptic element is active at the time step before a postsynaptic element changes from the active state to the inactive state, the synaptic weight associated with that presynaptic element is decreased.

For results shown here $\Delta_w = 1, w_{min} = -1, w_{max} = 1$.

To study the dynamics of the network, we introduce the following useful index of homeostatic activity $C(t)$:

$$C(t) = \frac{1}{M} \cdot \sum_{i=1}^{M} 1 - |x_i(t) - x_i(t-1)| \tag{4.5}$$

This index shows the fraction of elements for which the threshold was adjusted at time t. In terms of network activity it can be regarded at the fraction of elements that did not change state between the previous and current time step. Thus it shows the fraction of elements that did not maintain a homeostatic level of activity across the two time steps. If index C is zero, it means that the whole network is in a state of homeostatic activity, i.e. each element is undergoing a period 2 oscillation. If the

index is high, this means that many network elements did not change their activity state between the last two time steps.

Note that because the threshold θ_i is only adjusted in the event that the neuron remains in the same state for two consecutive time steps, if the index is low this means that the thresholds of elements are kept constant and that many cells are working in the regime of period 2 oscillations. These oscillations reflect the fact that the input to the cell is also oscillating with period 2.

4.2.2 Simulation results

For all simulations in this section, initial conditions are that $w_{ji} = 1$ for all (i, j) related to local connections, the states of the elements x_i are randomly and independently assigned to be 0 or 1 with equal probability, and thresholds are drawn independently and uniformly from the set $\{0, 1, 2, \ldots, 9\}$.

Case 1: We start from a consideration of the case where there is no plasticity ($\Delta_w = 0$). Simulations show that the typical dynamics in this case are that within a few hundred time steps the system activity converges to a periodic solution with period 6. Figure 4.1 shows the value of the index C over the first 400 time steps. The index converges to a relatively high value of approximately 0.84. This means that the activity of the network is far from the mode of homeostatic activity which is characterized by $C = 0$.

Figure 4.2 shows an example configuration taken from one eventual periodic sequence of the network. In this figure, white cells are active, black cells are inactive. Bands of activity and inactivity can be seen which travel over the network. Through threshold adjustments, current activity promotes future inactivity and current inactivity promotes future activity, resulting in a periodic solution with period 6.

Case 2: Now we restore the value $\Delta_w = 1$. First we consider typical results from these simulations on the qualitative level. The typical result is that the index C shows irregular oscillations around $C = 0.5$ before suddenly dropping down to a

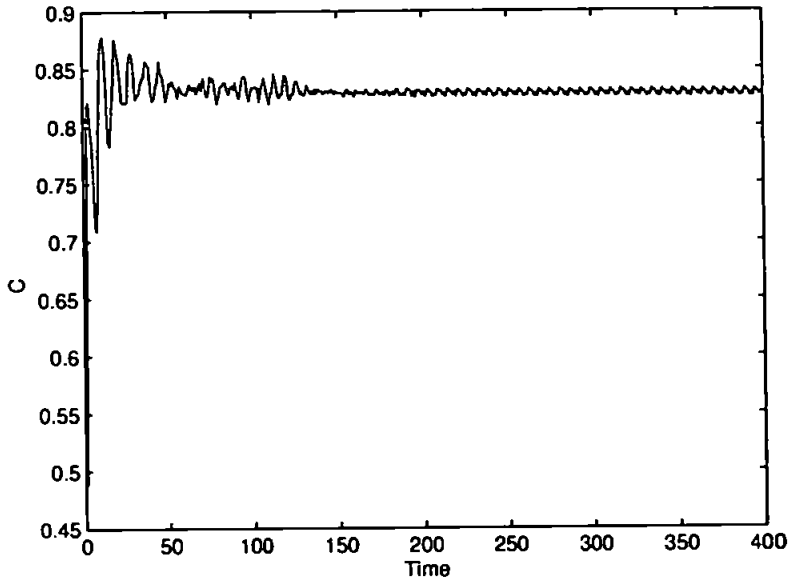

Figure 4.1: Convergence of index C which relates to homeostatic activity

small value $C \approx 0$. This is shown in figure 4.3.

Figure 4.3 shows the development of the index C in the system with synaptic plasticity over 100000 time steps. The addition of plastic synapses causes the system to take much longer to converge to periodic behaviour, but produces a significantly lower value of C than the non-plastic system even before the system converges.

Let us consider how the spatial configuration of network activity and connection strengths evolves as the system is transitioning from the phase where index C is high to the phase where C is low. Figure 4.4 shows 6 snapshots taken from the period of time relating to the phase transition. In these snapshots, for each element we show the change of activity between two sequential steps: black pixels indicate elements that have not changed state, white pixels indicate elements that have changed state. Before the phase transition the typical spatial configuration appears as randomly distributed black and white pixels. However in the bottom right-hand corner of snapshot (a), a cluster of white pixels can be seen. In this cluster, each element oscillates with period 2. Of course they are not in phase. It is likely that the probability of such a configuration is very low because the system stays in the phase

with high index C for a long time. This is similar to the process of crystallization where a small defect appears to give rise to the crystal. Snapshots (b)-(f) show how this initial spot of period 2 oscillation grows and involves the entire network. Thus the system transits to the phase of low C index with alternating activity.

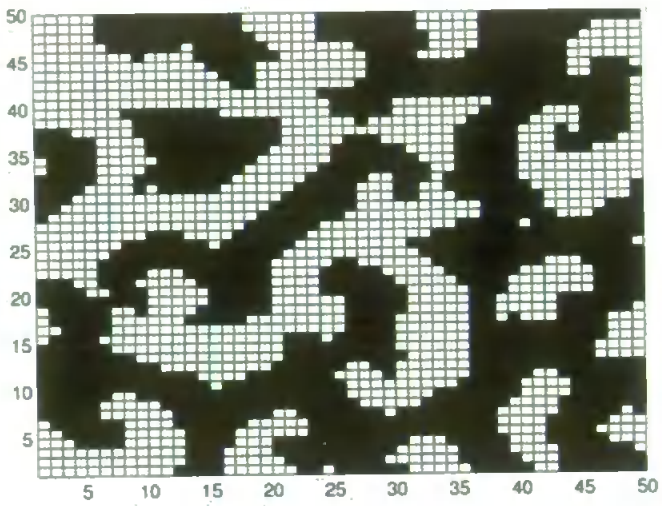

Figure 4.2: Activity of the neural network at t=400. White pixels represent active cells, black pixels represent inactive cells.

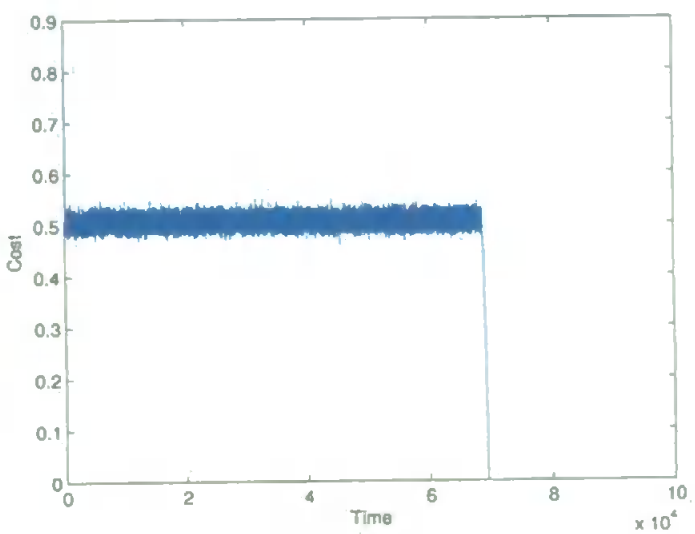

Figure 4.3: Evolution of index C which relates to homeostatic activity

To understand the evolution in the synaptic strengths, let us consider the very simple case of two cells, each connected to the other with fixed weights (no plas-

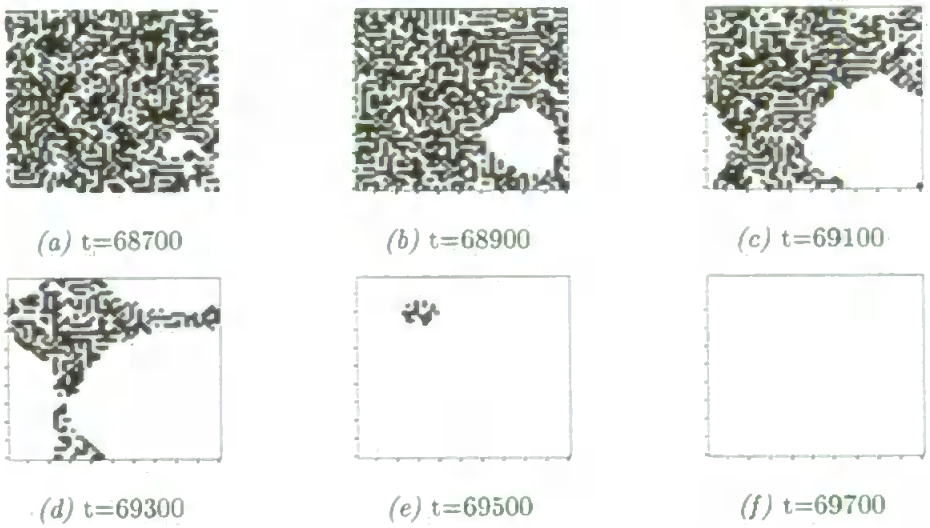

(a) t=68700 *(b)* t=68900 *(c)* t=69100

(d) t=69300 *(e)* t=69500 *(f)* t=69700

Figure 4.4: Development of global organization from local phenomenon

ticity). We will consider the case where each weight is either equal to -1 or 1. In fact we consider three configurations of connection strengths: mutually excitatory connections, mutually inhibitory connections, and excitatory-inhibitory connections.

Allowing initial thresholds in the set {-1, 0, 1, 2} and initial values of activity in the set {0,1} gives 64 possible states of the system for each configuration of connection strengths.

By simple calculations, we found that in the case of inhibitory connections, 10 out of the 64 possible initial states lead to a 2-cycle oscillation in which the two cells fire in phase, and all other initial states lead to one of three 6-cycles. In the case of excitatory connections, 8 out of the 64 initial states lead to a 2-cycle oscillation in which the cells fire in anti-phase, and all other initial states lead to one of three 6-cycles. In the case of excitatory-inhibitory connections, all configurations lead to one of two 4-cycles.

This simple consideration allows us to make the following prediction: if two coupled cells work in antiphase, it is likely that coupling is either mutually excitatory or mutually inhibitory. Furthermore, in order for any element to sustain a period 2 oscillation, it must fire in antiphase with at least one neighbour. Therefore, we can predict that there will be an increased incidence of reciprocally excitatory or

reciprocally inhibitory connections during the phase change.

This prediction is confirmed by simulation results. To demonstrate this, for each cell we calculate a measure of connection symmetry $R_i(t)$ using the following equation:

$$R_i(t) = \sum_{j \in N(i)} w_{ij}(t) w_{ji}(t) \tag{4.6}$$

Here all notations are the same as in equations 4.1-4.3.

Since weights are limited to the set {-1, 0, 1}, $R_i(t)$ will fall in the range $[-8, 8]$ where $R_i = 8$ means that all connections are symmetrical and nonzero. $R = -8$ means that all connections are asymmetrical and nonzero. Figure 4.5 shows a snapshot of measure R_i for the whole network, taken at the time of phase transition. The white spot in the top right-hand corner of the figure corresponds to elements with $R_i = 8$ and these elements demonstrate alternating activities.

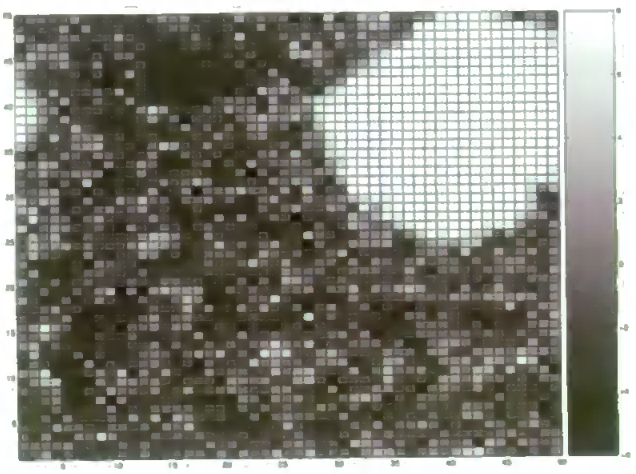

Figure 4.5: Symmetry of afferent/efferent connections in phase change region

4.2.3 Discussion

These results demonstrate that simple learning rules can produce a rapid reorganization of connection strengths which leads to a sudden phase transition. This phase

transition mechanism can be useful for modelling in neuroscience.

This is suggestive of a need for a learning rule to be balanced with additional mechanisms which would serve to limit the growth of a cluster of elements that has become locked into a stereotyped firing behaviour. One such mechanism may be the modulation of excitability as observed in cortex during sleep (Massimini et al., 2004). More experiments are needed to determine the effectiveness of this idea.

4.3 Model with small-world connections and synaptic plasticity

4.3.1 Introduction

In this section, we investigate the relationship between synaptic plasticity and network dynamics in a small-world type network. In chapter 4, we have already demonstrated that a simple model with local connections and noise can demonstrate metastable states and phase transitions. In this section we consider a similar model of simple elements with local connections and noise but we also introduce a few long-range connections to make the network architecture similar to small-world connectivity (Watts and Strogatz, 1998). Another important feature of this model is that synaptic connection strengths are modifiable and the learning rule is similar to the STDP rule (Abbott and Nelson, 2000). Model simulations show an interesting interplay between the total network activity and average connection strengths. The dynamics of these variables are arranged in a hysteresis-like loop. The states related to this loop can be interpreted in terms of neurophysiological UP and DOWN states. The system remains in each state for a long period with fast phase transitions. The mechanism of phase transition relates to the specific dynamics of connection strengths. The spatial organization of neural activity in the model with small-world architecture is complex, however when the system remains in the UP state or the DOWN state, the network dynamics demonstrate a regime of partial synchronization which is commonly seen in experimental studies (Borisyuk

and Kazanovich, 2006).

4.3.2 Model description

We consider a system of interacting binary Hopfield-type neurons. These are coupled on the grid where the edges of the grid are connected to each other, forming a torus. For our purposes, the distance between a node and any of its four nearest neighbours is defined to be one unit. The dimensions of the grid are 50×50 and the edges are connected to form a torus.

First of all, we define the architecture of connections of the model which includes both local and long-range connections. Local connections include seven randomly selected elements in the vicinity of the element. To prescribe a set of local neighbours we apply the following procedure: 1) We generate a pair of independent random variables (D, α) where $D = 1 + 2|\xi|$ with normally distributed $\xi \in \mathbf{N}(0, 1)$ and random variable α uniformly distributed in the interval $(0, 2\pi)$. 2) We identify the cartesian coordinates (x, y) where $x = D\cos(\alpha)$ and $y = D\sin(\alpha)$. 3) We find the node of the grid which is closest to the point with coordinates (x, y).

We repeat this procedure several times to find a set of seven different nodes which we use for local incoming connections to the considered element. We repeat this procedure for each element of the grid taking into account that in fact the grid is arranged to the torus and for elements near the boundary connections may cross the edges of the grid and reemerge on the other side according to the torus topology. In addition, each cell receives one long range input from a node of the grid which is calculated according to the same procedure with the exception that we use $D = 10 + 2|\xi|$ with normally distributed $\xi \in \mathbf{N}(0, 1)$.

The dynamics of activity of each element is described by $x_i(t) \in \{0, 1\}, i = 1, 2, ..., M$ where M is the number of elements.

Time is discrete and elements are updated synchronously. In order to compute the new activity of the element i at the moment $(t+1)$ it is necessary to first calculate

the total input $I_i(t)$. In the equations below $N(i)$ refers to the set of elements that provide input to element i. The term ξ_i represents a location and time independent normal variable with zero mean and standard deviation σ.

$$I_i(t) = \sum_{j \in N(i)} w_{ji}(t) x_j(t) + \xi_i \tag{4.7}$$

Here $w_{ji}(t)$ is the strength of the connection from j to i. The firing threshold θ is fixed and is the same for all elements. The update rule for activity of all elements is given in equation 4.8.

$$x_i(t+1) = \begin{cases} 1, & I_i(t) \geq \theta \\ 0, & I_i(t) < \theta \end{cases} \tag{4.8}$$

In the model implementation, synaptic weights w_{ij} are updated following the states of model elements, and it is convenient to use the concept of a half time step to make the sequence of updates clear. Thus, we use time step 1/2 and update elements at integer moments of time t, connection strengths are updated at times $t+1/2$, where $t = 1, \ldots$. The following formulas describe the initial update rule which is used to calculate intermediate values of synaptic strengths $\hat{w}_{ij}$ prior to thresholding being applied. In these formulas the presynaptic cell is denoted by i, and the postsynaptic cell is denoted by j.

$$\hat{w}_{ij}(t+1+1/2) = \begin{cases} w_{ij}(t+1/2) + \delta_{pot}, & x_i(t) = 1 \wedge (x_j(t) = 0 \wedge \boldsymbol{x_j(t+1) = 1}) \\ w_{ij}(t+1/2) - \delta_{depr}, & (x_i(t) = 0 \wedge \boldsymbol{x_i(t+1) = 1}) \wedge x_j(t) = 1 \\ w_{ij}(t+1/2) - \delta_{simul}, & (x_i(t) = 1 \wedge \boldsymbol{x_i(t+1) = 1}) \wedge x_j(t) = 1 \\ w_{ij}(t+1/2), & \text{otherwise} \end{cases} \tag{4.9}$$

Here $\wedge$ denotes logical AND. Parameter δ_{pot} represents the increase in the synaptic weight due to synaptic potentiation, δ_{depr} represents the decrease in the synaptic

weight due to synaptic depression, δ_{simul} represents a small decrease in the synaptic weight due to simultaneous pre- and postsynaptic activity. These three parameters are positive.

This learning rule is similar to the STDP rule for synaptic plasticity (Bi and Poo, 1998). In this learning rule we increase synaptic strengths if the presynaptic cell is active one time step before the postsynaptic cell is active (potentiation), and decrease synaptic strengths if the postsynaptic cell is active one time step before the presynaptic cell becomes active (depression). Also we slightly decrease the synaptic strength if both pre- and postsynaptic cells are simultaneously active. This relates to an asymmetrical variant of the STDP rule.

When updating the actual synaptic weight values $w_{ij}(t+1+1/2)$ we consider that synaptic strengths can be modified only within some limited range according to the following equations:

$$w_{ij}(t+1+1/2) = \begin{cases} \min(w_{max}, \hat{w}_{ij}(t+1+1/2)) & \hat{w}_{ij}(t+1+1/2) \geq w_{ij}(t+1/2) \\ \max(w_{min}, \hat{w}_{ij}(t+1+1/2)) & \hat{w}_{ij}(t+1+1/2) < w_{ij}(t+1/2) \end{cases} \tag{4.10}$$

Here, w_{min} and w_{max} represent the lower and upper limits for synaptic strengths.

4.3.3 Simulation results

Initial conditions are that all weights $w_{ij}(1/2) = 0.2$, and all element states $x_i(0) = 0$. Using these initial conditions we update states of elements at time $t = 1$ and connection weights at time $t = 3/2$ etc. We choose parameter values for the simulations as follows: $w_{min} = 0.2$, $w_{max} = 4.0$, $\sigma = 1.0$, $\delta_{pot} = 0.01$, $\delta_{decr} = 0.012$, $\delta_{simul} = 0.005$.

Figures 4.6-4.10 show spatial patterns, dynamics of firing rate and average connectivity. It can be seen that the network exhibits distinct low activity and high activity states which can persist for relatively long periods of time. We consider these states to be analogous to the UP and DOWN states described by McCormick (McCormick et al., 2003). Typical spatial patterns of activity in UP and DOWN

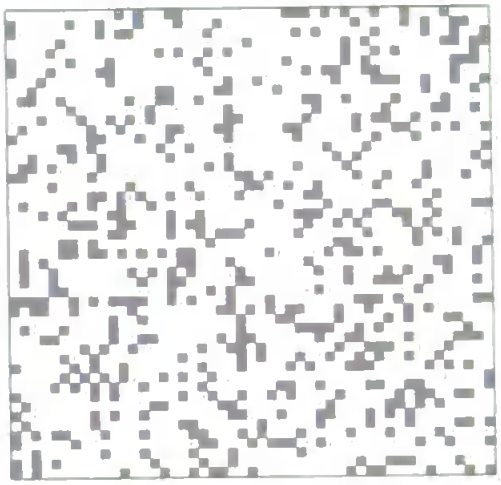

Figure 4.6: Spatial pattern of activity in UP state

states can be seen in figures 4.6 and 4.7.

Figure 4.8 shows dynamics of the firing rate of the network (fraction of active elements vs time). The system remains in UP and DOWN states for long periods (of varying length) and demonstrates very fast phase transitions between these states.

Figure 4.9 shows the dynamics of total synaptic weight vs time. This plot shows irregular behaviour of total synaptic weight which can be considered in parallel with the dynamics of the total activity of the network (figure 4.8).

If the total activity is low, the total connection weight gradually increases to reach a maximum value and suddenly drops down. This drop corresponds to a transition of the total activity from the UP state to the DOWN state. The slow increase of the total synaptic weight is due to the fact that presynaptic activity is correlated with postsynaptic firing and so conditions for synaptic potentiation occur more frequently than conditions for synaptic depression.

It can be seen that during the period where the total synaptic weight increases there is a point where the synaptic weight begins to grow very rapidly as the second derivative becomes positive. One of these points is marked with a circle in figure

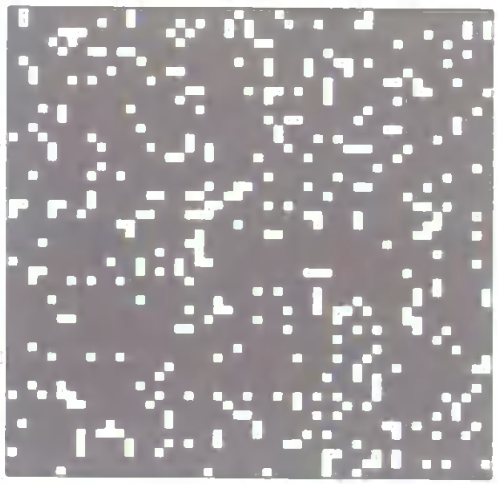

Figure 4.7: Spatial pattern of activity in DOWN state

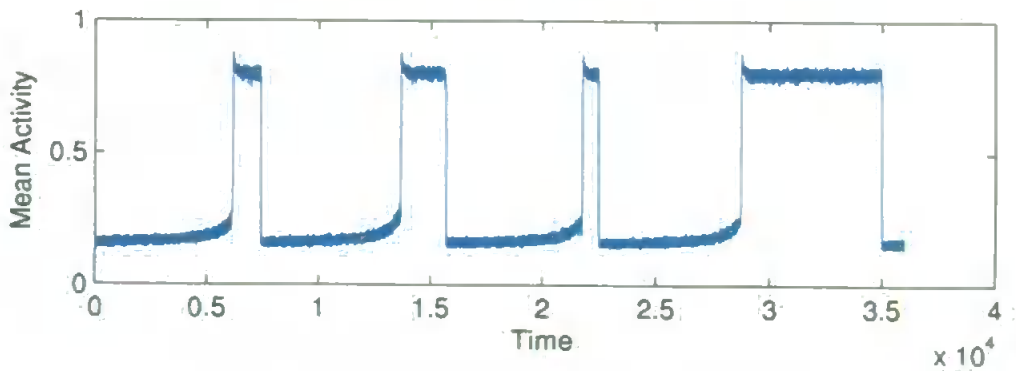

Figure 4.8: Total network activity versus time

4.9.

Figure 4.10 shows the total network activity vs the total synaptic weight. These two variables evolve according to a hysteresis-like loop. This loop can be described as follows: A) The total synaptic weight increases from a low level to a high level as total activity gradually increases while remaining at a relatively low level. B) The increasing synaptic weight eventually causes the total network activity to rapidly transition into a high activity state. C) In the high activity state, most cells fire all the time and so there is no longer a strong correlation between presynaptic firing at a particular time step and postsynaptic firing at the next time step. Under this

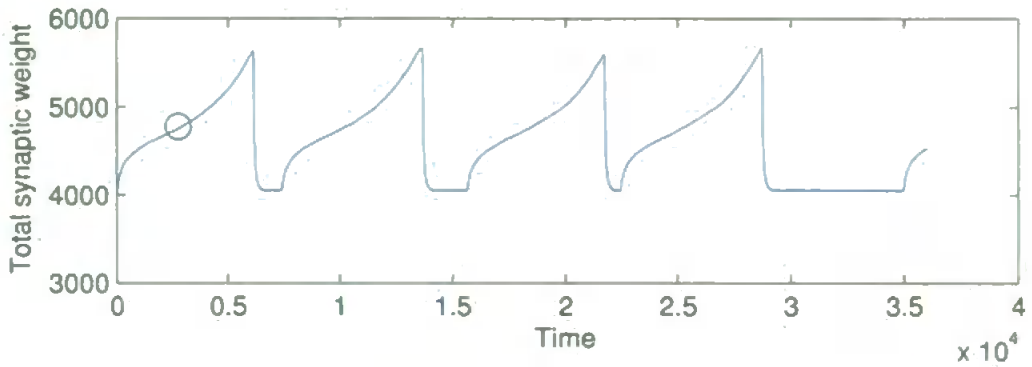

Figure 4.9: Total synaptic weight versus time

condition, the "simultaneous firing" rule dominates, synaptic weight changes are predominantly negative and so the total synaptic weight decreases. D) Eventually the total synaptic weight is low enough that the high activity state is no longer stable, and the network will eventually transit back to a low activity state. Due to the fact that each individual synaptic weight is constrained to not go below the value w_{min}, the UP state may persist for some time after the synaptic weights have temporarily stabilized at a low level, but the system will eventually transit back into a low activity state.

4.3.4 Population model

We now introduce a meta-model that describes the activity of the population of interactive neurons with plastic synaptic connections. The model includes two variables: the variable $x(t)$ describes average activity of the neural population and the variable $c(t)$ describes dynamics of average synaptic weight in this population. The dynamics of these two variables is governed by the following system of two differential equations:

$$\dot{x} = -x + cS(x) + I \tag{4.11}$$

$$\dot{c} = \epsilon(\alpha c - \gamma x + \rho) \tag{4.12}$$

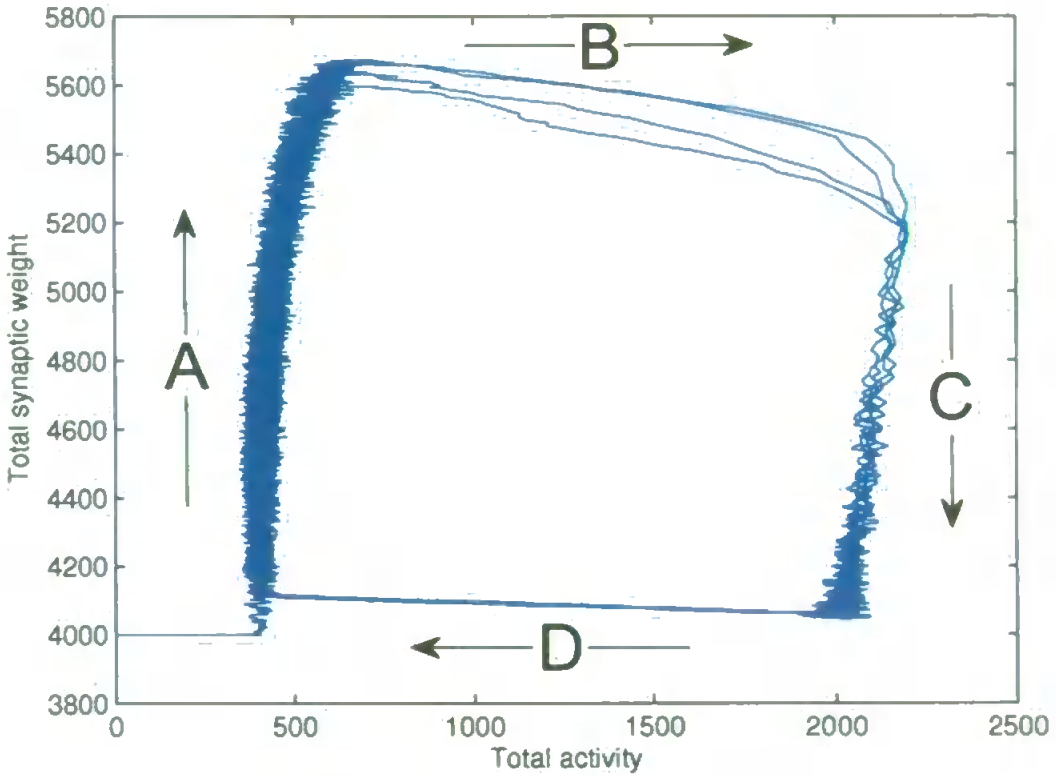

Figure 4.10: Weight versus activity.

Here $S(x)$ is a sigmoid function that constrains the overall level of activity and I is the input to the system.

$$S(x) = 0.4 + \frac{1}{1 + \exp(-\beta(x - \theta))} \tag{4.13}$$

Parameters are: $\alpha = 1$, $\epsilon = 0.001$, $\gamma = 5$, $\rho = 80$, $I = 0.5$, $\beta = 0.5$, $\theta = 20$.

Let us consider equation 4.11, supposing that variable c is fixed. Figure 4.11 shows the steady states of the equation of population activity for different connectivity conditions (values of c). This figure illustrates the classical hysteresis effect. When connectivity is strong ($c = 40$, green curve), the only fixed point is a high activity state (e), when connectivity is weak ($c = 0.1$, red line) the only fixed point is a low activity state (a), and for an intermediate level of connectivity ($c = 22$, blue line) there are three steady states - two are stable (b and d) and one steady state

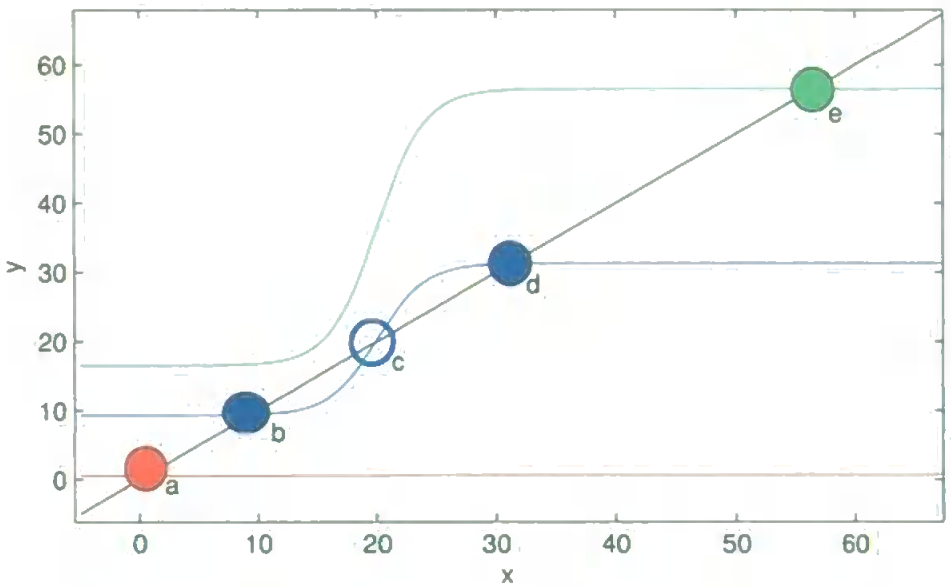

Figure 4.11: Hysteresis in the activity equation. The black line shows the equation $y = x$, and the other traces show the equation $y = cS(x) + I$. Steady states exist where these lines intersect. When $c = 22$ (blue line), there are two stable steady states representing high and low activity (filled blue circles marked by b and d), with an unstable steady state representing an intermediate level of activity (unfilled blue circle marked by c). When $c = 40$ (green), there is a single stable steady state at high activity (filled green circle marked by e), and when $c = 0.1$ (red), there is a single stable steady state at low activity (filled red circle marked by a).

is unstable (c). This unstable steady state corresponds to an intermediate level of activity of the neural population. By temporarily applying a strong connectivity condition, we can drive the system into a high activity state that will persist if connectivity is dropped back to the intermediate level, and vice versa, demonstrating the hysteresis loop.

In equations 4.11-4.12 the variable $x(t)$ is fast and the variable $c(t)$ is slow because ϵ is small. The simulation of the system shows typical relaxation oscillations which are shown on the phase plane in figure 4.12. The stable limit cycle which is shown in this figure is the only attractor of the system. The dynamics of the system variables is typical for fast-slow systems: figure 4.13 shows population activity vs time and figure 4.14 shows the average connectivity vs time

Comparison of figures 4.8-4.10 which represent the complex spatiotemporal be-

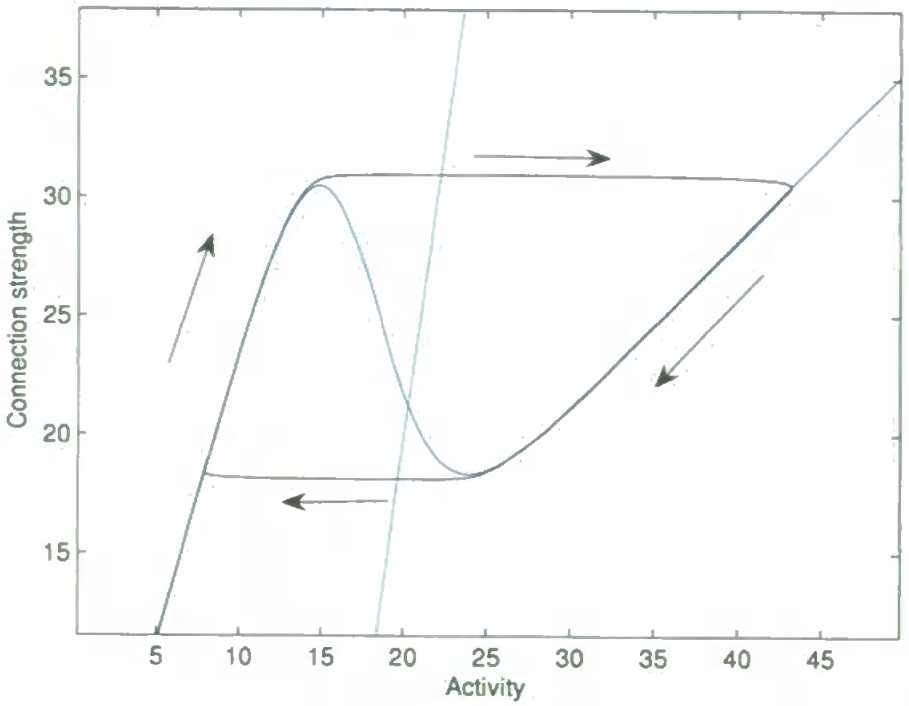

Figure 4.12: Activity of population model shown on phase plane. The isoclines for population activity and mean connection strength are shown in blue and green respectively. The system can be seen falling into the limit cycle from the initial conditions of low connectivity and low activity.

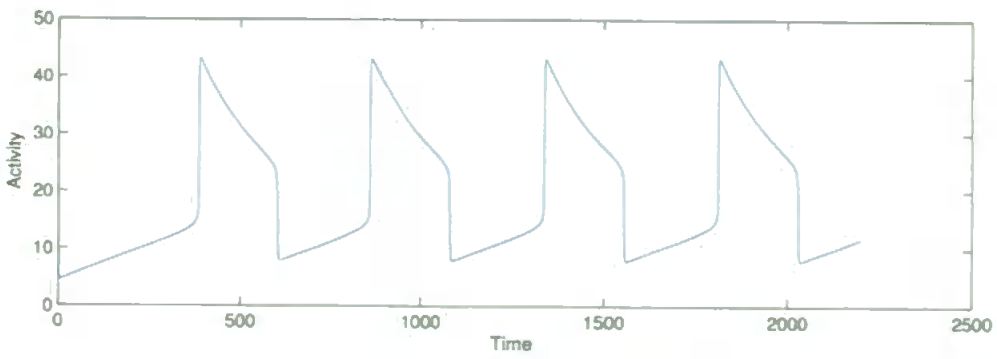

Figure 4.13: Population activity vs time.

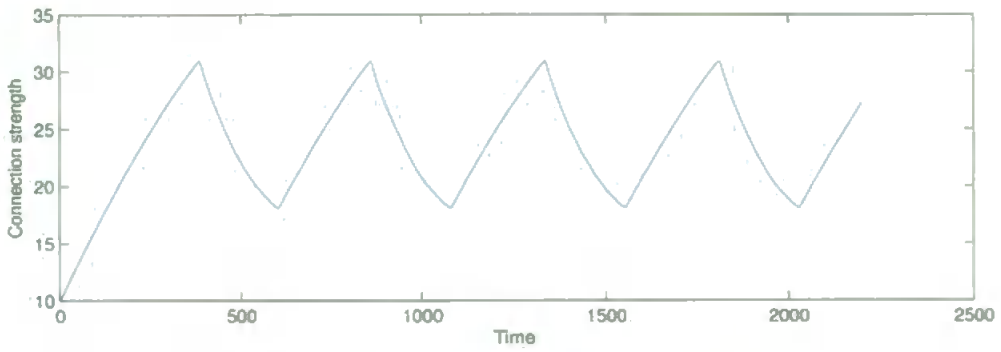

Figure 4.14: Population connectivity vs time.

haviour of the computational model with figures 4.12-4.13 which represent dynamics of the two-dimensional meta-model demonstrates that the main features of the computational model are nicely reflected in the population model. For example, the dynamical behaviour of average connectivity in the population model is very similar to the dynamics of average connectivity in the computational model.

4.3.5 Discussion

In this section we study dynamical behaviour of a computational model which includes simple elements with small-world connections, modifiable connection strengths and noise. Simulations show complex spatiotemporal patterns of network activity, however the interplay between total activity and total connectivity can be described by a simple hysteresis-like process. In fact, the complex spatiotemporal behaviour results from three factors: specific spatial clusters, flexibility of connection strengths according to the learning rule, and noise. Interaction of these factors results in irregular variations of spatial activity in the network, however the macro-characteristics of the system show simple behaviour. Total population activity and connectivity demonstrate irregular relaxation-type oscillations. To describe these macro-variable dynamics we consider a two-dimensional system of ordinary differential equations of fast-slow type and find that the dynamics of system variables are quite similar to the dynamics of the macro-characteristics of the system.

Our hypothesis is that the long range connections facilitate the UP state, allowing

it to persist long enough for effective synaptic downscaling to occur. Due to these long-range connections, long-lasting clusters of activity corresponding to UP and DOWN states will appear and in fact a choice of these connections (which are random in our model) defines spatial allocations of these specific clusters.

Part II

Computational Modelling of the Swimming Network of the Xenopus Tadpole Spinal Cord

Introduction to Part II

In this part of the dissertation, we present our research on modelling of the anatomy and electrophysiology of the tadpole spinal cord. This research has been developed in very close collaboration with Professor Alan Roberts (University of Bristol) and members of his laboratory. Modelling was closely based on experimental data which were provided by the Alan Roberts lab. These data include multiple measurements of axon, dendrite, and soma anatomy, electrophysiological properties of different kinds of neurons, and other important details relevant to modelling. Close collaboration with neurobiologists allows us to develop a biologically realistic model with statistical characteristics similar to the real tadpole.

We study a simple mathematical model of axon growth in the spinal cord of tadpole. Axon development is described by a system of three difference equations (the dorso-ventral and longitudinal coordinates of the growth cone and the growth angle) with stochastic components.

We find optimal parameter values by fitting the model to experimentally measured characteristics of the axon and using the quadratic cost function. The fitted model generates axons for different neuron types in both ascending and descending directions which are similar to the experimentally measured axons. Studying the model of axon growth we have found the analytical solution for dynamics of the variance of the dorso-ventral coordinate and the variance of the growth angle. Formulas provide conditions for the case when the increase of the variance is limited and the analytical expression for the saturation level. It is remarkable that optimal parameters always satisfy the condition of limited variance increase. Taking

into account experimental data on the distribution of neuronal cell bodies along the spinal cord and the dorso-ventral distribution of dendrites we generate a biologically realistic architecture of the whole tadpole spinal cord. Study of the electrophysiological properties of the model with Morris-Lecar neurons shows that the model can generate electrical activity corresponding to the experimentally observed activity during fictive swimming in the tadpole spinal cord within a broad range of parameter values.

Material of this chapter has been presented in two recent publications (Li et al., 2007; Borisyuk et al., 2008).

Chapter 5

Experimental data on tadpole anatomical development and model description

5.1 Introduction to anatomy of tadpole spinal cord

To function properly, nervous systems rely on highly specific synaptic connections between neurons. This specificity is achieved during development by many mechanisms, for example, correct neuronal specification and differentiation, axon path finding, cell recognition and synapse conditioning by neuronal activities. At the core of this, what are the rules that ensure that appropriate and specific synaptic connections are made as neuronal circuits develop? This is one of the most intensively studied areas of developmental neuroscience and has generated an extensive body of knowledge on the chemical cues that control the assembly of neuronal circuits in the central nervous system (CNS) (Dickson, 2002; Munno and Syed, 2003; Cline, 2003; Chilton, 2006; Schnorrer and Dickson, 2004).

The vertebrate spinal cord provides a simple example where chemical morphogens released from the dorsal roof plate and ventral floor plate form dorso-ventral molecular gradients. These initially control the fate of differentiating neurons to establish a dorso-ventral series of longitudinal columns of distinct neurons on each side (Figure 5.1c) (Helms and Johnson, 2003; Goulding and Pfaff, 2005). Once a cell has acquired a specific neuronal fate, the next step is to grow an axon from the

neuron soma. The factors controlling the directions of outgrowth are beginning to be revealed (de Anda et al., 2005). Remarkably, the same morphogen gradients that control cell fates can also influence axon growth. In all parts of the CNS such early patterns of growth by pioneer axons, controlled by chemical morphogens, lay down a basic scaffold of axon tracts that can be followed by later axons and in this way help to direct their growth (Wilson and Easter, 1991). Once the axons have grown to approximately the 'correct' area, they start to make connections (synapses) with the branched dendrites emerging from the cell bodies of other neurons.

The results of the experimental study and modelling provide answers to the following two questions about the formation of synaptic connections: how accurate and specific are the synaptic connections formed during early stages of development within the CNS? Once axons have reached a suitable area to make synapses, cellular recognition processes (Clandinin and Zipursky, 2002) and activity-dependent mechanisms (Stellwagen and Shatz, 2002; Cang et al., 2005; Hanson and Landmesser, 2006; Katz and Shatz, 1996) may be needed to ensure that appropriate synaptic connections are made. However, the second question is: can simple factors, such as the broad geographical distributions of axons and dendrites, themselves generate sufficient specificity in synaptic connections to ensure the development of functional neuronal circuits?

To investigate the specificity of early spinal cord formation, we use experimental evidence on connections between identified neuron types in a functioning neuronal network. Very few vertebrate networks are simple enough to allow this; an exception is the developing spinal cord of the newly hatched clawed toad (*Xenopus laevis*) tadpole. Like the developing zebrafish (McLean et al., 2007; Higashijima et al., 2004), this spinal cord contains less than 2,000 neurons divided into very few types (approximately ten) yet it allows simple reflexes and swimming. In Xenopus, whole-cell recordings from pairs of spinal neurons under visual control (recordings from Roberts lab) have allowed us to build a remarkably full picture of the morphology, proper-

ties, synaptic connections and functions of the neurons and networks controlling swimming behaviour (Li, ichi Higashijima, Parry, Roberts and Soffe, 2004; Li et al., 2001, 2003; Li, Soffe and Roberts, 2004*b*; Li et al., 2006, 2002). This detailed knowledge of the anatomy and function of different types of spinal neurons in developing Xenopus embryos provides a remarkable opportunity to use the whole-cell recording method to examine large numbers of synaptic connections between different types of identified spinal neuron to assess the specificity of the connections between them.

Examination of synaptic connections between spinal neurons shows that connections are widespread and non-specific. We therefore examine the anatomy to see whether some very simple factors, like the different dorso-ventral distributions of the axons and dendrites of different neuron types, are sufficient to predict the connectivity found physiologically. We then use modelling to ask whether simple rules can reproduce longitudinal axon growth paths, and whether network models of the spinal circuits can produce swimming activity when synaptic connections are determined by simple probabilistic rules. Overall, our results show that it is possible that the first, pioneer neuronal networks formed in the spinal cord could be generated without specific neuron-to-neuron recognition mechanisms playing a necessary role in determining synaptic connectivity.

5.2 Neuron types in the tadpole spinal cord

The experimental evidence has been collected from the two day old, hatchling Xenopus tadpole, which is 5 mm long (Figure 5.1A,B). The eyes are not yet functioning but the brain and spinal cord contain differentiated neurons. The spinal cord is a simple tube (approximately 0.1 mm diameter) with a central neural canal formed by ependymal cells and the ventral floor plate (Figure 5.1C). On each side lies a layer of nerve cells or neurons loosely organized into longitudinal columns. The neurons project processes into a superficial zone of longitudinal axons either directly or by first growing ventrally across the floor plate to the other side and then turning

or branching longitudinally. As in all vertebrates, newly formed neurons are positioned in a dorsal to ventral sequence: sensory neurons; sensory interneurons; other interneurons; motoneurons. Unlike adult vertebrates, the young tadpole spinal cord has remarkably few types of spinal neuron, possibly less than ten. We consider six types of spinal neuron involved in swimming (Figure 5.1D) where the synapses made onto other spinal neurons have been defined by electrical recordings from pairs of individual neurons (Roberts, 2000). All synapses are made directly from longitudinal axons as they pass small processes emerging from the neurons called dendrites that protrude towards the side of the spinal cord.

(1) Dorsal Rohon-Beard neurons (RB) are sensory, innervate the skin and respond to touch. Their central axons ascend and descend to excite other neurons.

(2) Motorneurons (mn) have short axons which are mostly ventrally located.

(3) Dorsolateral commissural interneurons (dlc) are sensory pathway interneurons excited by sensory RB neurons. They excite contralateral neurons and initiate swimming activity when the skin is stimulated (Li et al., 2003).

(4) Ascending interneurons (aIN) have a broad dorsal-ventral distribution. They inhibit neurons on the same side and it has been found that this inhibition can affect all types of neurons.

(5) Commissural interneurons (cIN) are a middle dorso-ventral group of neurons which produce inhibition of the opposite side of the spinal cord (Dale, 1985) to organize the alternation of activity between the two sides during swimming. The axons of cIN cells cross the ventral floor plate immediately after their initial outgrowth, and then rise dorsally on the other side where they branch to grow in the ascending and descending directions.

(6) Descending interneurons (dIN) excite other neurons (Li, Soffé and Roberts, 2004*a*; Li et al., 2006). They provide ipsilateral excitation during tadpole swimming (Dale, 1985; Li, Soffe and Roberts, 2004*a*).

All interneurons grow their axons in both ascending (from the tail to the head)

and descending (from the head to the tail) directions except excitatory dIN neurons which send their axons in the descending direction only. It is likely that these connections propagate activity from the head to the tail and form the metachronal wave of the swimming pattern.

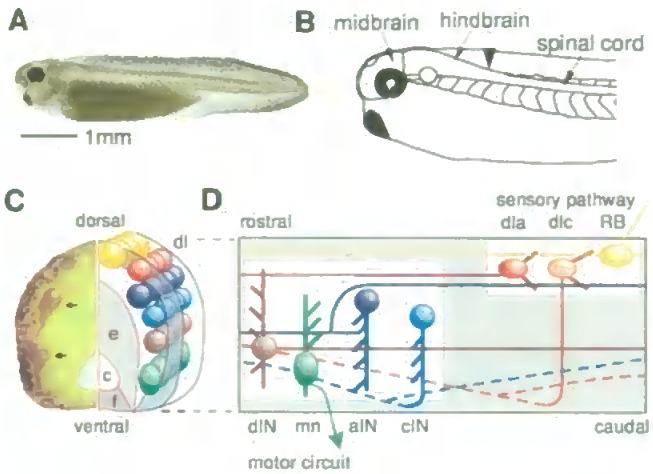

Figure 5.1: Hatchling Xenopus tadpole, nervous system and neurons. (A) Picture of tadpole at stage 37/38. (B) The main parts of the CNS with arrowhead at hindbrain/spinal cord border. (C) Transverse section of the spinal cord with the left side stained to show glycine immunoreactive cell bodies (arrows) and axons (in the marginal zone). Diagrammatic right side shows the main regions: neural canal (c) bounded by ventral floor plate (f) and ependymal cell layer (e), lateral marginal zone of axons (mauve), layer of differentiated neuron cell bodies arranged in longitudinal columns (coloured circles) lying inside the marginal zone except in dorso-lateral (dl) and dorsal positions. (D) Diagrammatic view of the spinal cord seen from the left side showing characteristic position and features of 7 different neuron types. Each has a cell body (solid ellipse), dendrites (thick lines) and axon(s) (thin lines). Commissural axons projecting on the opposite right side are dashed. More details in text

5.3 Anatomical evidence on the dorso-ventral distribution of axons and dendrites

One alternative to specific cell-cell recognition mechanisms is that axons can chemically recognise neuronal dendrites and simply make synapses with any that they contact (axon-soma synapses are very rare in Xenopus spinal cord). If this hypothesis is correct, the probability of contact will depend mainly on the dorsoventral distribution of axons and dendrites, since axons run along the spinal cord, rarely

branch, and make synapses directly onto dendrites that they pass. We have therefore examined these distributions for six spinal neuron types in the rostral spinal cord.

Neurons having somata in the region where the electrical recordings were made (1 to 3 mm from the midbrain; Figure 5.1B) were selected for anatomical analysis. The axons are all relatively straight with maximum tortuosity (actual length divided by straight line distance) of $T = 1.02$ (n = 6). Figure 5.2B uses the aINs to illustrate the dorso-ventral distributions of axons and dendrites.

The dorso-ventral range of dendrites was determined from the positions of the most ventral and dorsal dendrite for each neuron (Figure 5.2A,B). This range will limit the number of axons contacted. We ignore the possibility that dendrites might be unevenly distributed within this range. The dendrite dorso-ventral ranges were summed for each neuron type, except RB neurons, which do not have dendrites. For each 10% dorso-ventral position bin (spinal cord diameter is approximately 100 μm so bin width is approximately 10 μm) in the 10 μm thick marginal zone where dendrites and axons lie, we found the probability that an individual neuron of each type would have dendrites occupying that bin (Figure 5.3A). The dendrite distributions for neurons active during swimming (mns, aINs, cINs and dINs) were broad but all had a maximum just below the dorso-ventral midline (in the 30% or 40% bin) and fell away dorsally. In contrast, the dendrites of dlc sensory pathway interneurons had a maximum dorsally (in the 80% bin) and fell away ventrally.

The dorso-ventral position of axons was measured every 0.05 mm up to a maximum of 1 mm from the neuron soma (or branching point for branching axons). For each individual neuron, we pooled these measurements (discarding information about the distance from the soma and whether the axon was ascending or descending) and used them to calculate the probability of the axon occupying different dorso-ventral positions. These individual distributions were then averaged for all members of a type (Figure 5.3a). The dorso-ventral axon distributions of some neu-

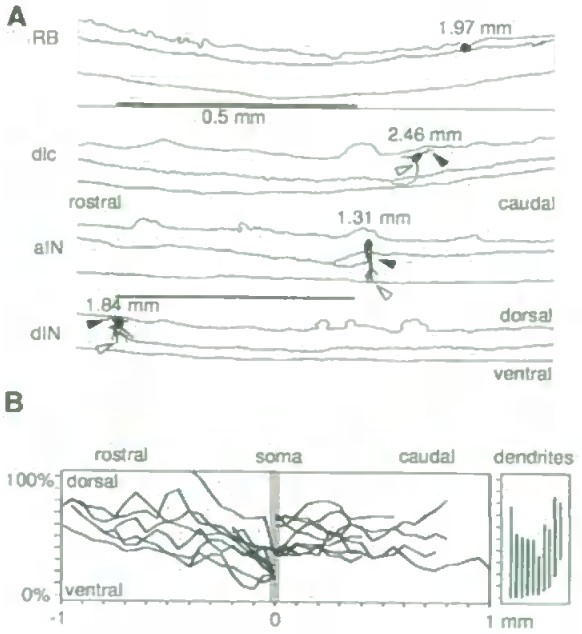

Figure 5.2: (A) Examples of neurobiotin filled neurons traced in lateral views of the spinal cord to show the dorso-ventral positions of the cell body, dendrites and part of the axons. Dendrites emerge from the black cell body with most ventral dendrite (open arrowhead) and most dorsal (black arrowhead) marked. Axons are on same side as cell body except for dlcs where they cross ventrally then branch. Rostral to left, dorsal up. (B) Examples of axon trajectories of individual aINs (measured at 0.05 mm steps from the cell body at 0mm) and dorso-ventral extent of their dendrites (vertical lines at right).

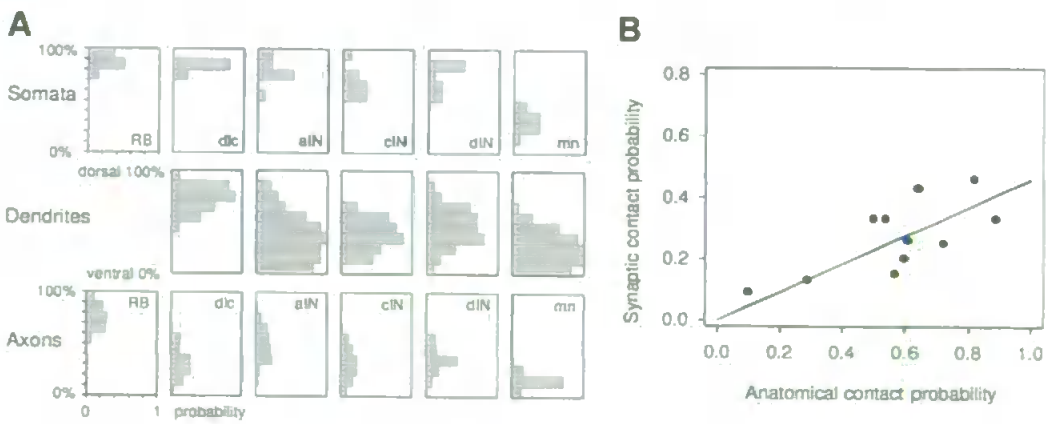

Figure 5.3: Axons, dendrites and synapses: A) Histograms summarise dorso-ventral distribution of cell bodies, dendrites and axons of different neuron types in 10% bins where 0% is ventral and 100% dorsal edge of spinal cord. Distributions are expressed as the probability that a neuron will have a cell body or dendrite in a particular dorso-ventral position. Axon distributions are expressed as the probability that a 50 μm segment of the axon from a type of neuron will lie in a particular dorso-ventral position. B) Plot of synapse probability from recordings vs contact probability from anatomy for cases shaded in Table 5.1.

rons are rather narrow. RB sensory neuron axons are dorsal (from 50% to 100%; maximum at 80%) while mns are ventral (from 10% to 30%; maximum at 20%). cINs, dINs and dlcs are all slightly biased towards ventral positions (from 10% to 60%) while inhibitory aINs have a broad axon distribution (10% to 90%; maximum at 40%).

Once the dorso-ventral distributions of axons and dendrites were established, 'contact' probabilities between axons and dendrites were calculated as follows for each pair of neuron types. The probabilities of individual axons or dendrites occupying a particular 10% dorso-ventral region were those plotted in Figure 5.3A. The probability that a particular pre-synaptic axon and post-synaptic dendrite would both occupy the same dorso-ventral region in the narrow marginal zone, and could therefore make contact, was simply the product of these probabilities. Overall contact probabilities between each type of neuron were then found by summing the separate probabilities for the ten dorso-ventral regions (Table 5.1). The contact probabilities range from 0.04 to 0.91 and relate intuitively to functions. They are higher for RB sensory neuron contacts onto sensory pathway dlcs (0.65) than onto other neurons like dINs (0.29); they are low for dlc contacts with each other (0.08) but higher onto the neurons activated after skin stimulation (0.54-0.89 for aINs, cINs, dINs and mns); they are quite high for contacts between neurons active during swimming (0.5-0.91 for aIN, cIN and dIN contacts to each other and to mns).

When contact probabilities determined from anatomy were compared to synapse probabilities determined directly by electrical recording (Table 5.1), the two were significantly correlated for pairs where the neurons were randomly chosen for recording (bold entries in Table 5.1; Pearson correlation coefficient 0.593; $p = 0.042$). This significant relationship based on data from both anatomy and physiology (Figure 5.3B) was then used to predict the synaptic contact probability for cases with only anatomical data (Table 5.1). We first omitted data for contacts from RB to dlc neurons where the extensive rostro-caudal dendrites of dlc neurons are likely to re-

sult in a relatively high synaptic contact probability. The slope obtained by linear regression for the remaining points suggests that the probability of a real synaptic contact is around 46% of that predicted by anatomy. In a later chapter, we will use this probability to generate a complete model of the spinal cord by growing axons of each neuron: when an axon passes the dendrite of some cell the probability of contact is 0.46.

We hypothesize on the basis of these results that during the formation of early synapses in the developing frog spinal cord, the different synapse probabilities found could depend simply on differences in the geographical distributions of axons and dendrites of different neuron types. These distributions could be sufficient to ensure, for example, that dorsal sensory RB axons synapsed mainly with dorsal sensory pathway interneurons rather than with more ventral neurons active during swimming (like motoneurons). This hypothesis is supported by modelling results which are presented in the next section.

axons	dlc	aIN	cIN	dIN	mn
RB ipsi					
Synapse	**0.63**	**0.13**	**0.09**	+(0.13)	+(0.02)
Contact	0.65	0.29	0.10	0.29	**0.04**
dlc contra					
Synapse	0+ (0.04)	**0.33**	**0.43**	**0.33**	**0.46**
Contact	0.08	0.89	0.64	0.54	**0.82**
aIN ipsi					
Synapse	(0.13)	**0.25**	**0.15**	**0.2**	**0.33**
Contact	0.28	0.72	0.57	0.60	**0.50**
cIN contra					
Synapse	0+ (0.04)	0++ (0.40)	**0.26**	++(0.24)	**0++** (0.37)
Contact	0.08	0.88	0.61	0.52	**0.80**
dIN ipsi					
Synapse	+(0.04)	*++ (0.42)	*++ (0.34)	*++ (0.29)	***++** (0.37)
Contact	0.08	0.91	0.73	0.64	**0.80**
mn ipsi					
Synapse	(0.00)	(0.41)	(0.18)	(0.10)	**(**0.45)
Contact	0.00	0.89	0.40	0.22	**0.98**

Table 5.1: Synapse probabilities in bold are those from recordings based on more random sampling. Where there are no data from recordings, estimates of synaptic contact probabilities (in parentheses) are 46% of the anatomically estimated contact probabilities. For each neuron type, ipsi refers to synapses made on the same side and contra refers to synapses made on the opposite side, + rare connections inferred from other experiments; ++, common connections but no quantitative data; *, connections frequent but preliminary recordings were used to select pairs of neurons that were connected, so connection probabilities are not meaningful.

5.4 Modelling axon growth and synaptic contact probabilities

The traditional approach to modelling axon growth is based on the idea that the growth cone follows different molecular gradients (Goodhill et al., 2004; Krottje and van Ooyen, 2007). Here we do not consider the details of growth cone navigation in steep and shallow chemical gradients; instead we build a simple computational model reflecting several key attraction and repulsion processes guiding axon development.

Since axons grow a considerable distance along the spinal cord (often 1 to 2mm in a 5mm long animal) and can wander dorsal or ventral as they grow, their pattern of growth will have a strong influence on their potential to contact dendrites of different neuron types (see figure 5.2A). We concluded above that synaptic contacts may depend simply on dorso-ventral axon and dendrite distribution patterns. We therefore investigated whether a simple model, without any cell-cell recognition, could generate patterns of axon growth that would reproduce the observed axon distributions and therefore the synaptic contact probabilities. For simplicity, we assumed that dendrites are static and passive.

Our computational model starts from the point when axons start to grow longitudinally (Figures 5.1D and 5.2A). This point will be determined by the position of the soma and the initial behaviour of the axon. In the case of RB neurons, the axons grow directly from the soma towards the head and tail. In most other spinal neurons the axon first grows ventrally and then turns to grow longitudinally either on the same side or after crossing ventrally to the other side. We use the experimental observations to give us starting positions and initial growth angles of axons as well as their final lengths. A repetitive process of advancing the axon 1 μm along its current growth angle and then modifying the growth angle is then applied until the predetermined rostrocaudal length of the axon is reached.

The current location and orientation of the tip of the axon (growth cone) are

represented by three variables: $x(t)$ rostrocaudal position, $y(t)$ dorsoventral position, and $\theta(t)$ growth angle. θ is defined as the deviation from longitudinal growth; positive values of $\theta(t)$ indicate a tendency to grow dorsally while negative values of $\theta(t)$ indicate a tendency to grow ventrally. In our first simple model just two parameters, α and γ are defined specifically for each neuron type. The equations are:

$$x(t+1) = x(t) + \Delta \cos(\theta(t)) \tag{5.1}$$

$$y(t+1) = y(t) + \Delta \sin(\theta(t)) \tag{5.2}$$

$$\theta(t+1) = (1-\gamma)\theta(t) + \xi, t = 0, 1, \ldots, m-1, \tag{5.3}$$

where t is the current iteration number in the process of axon growth; m is the full length of the axon; ξ is a random variable uniformly distributed in the interval $[-\alpha, \alpha]$; (α typically is about 2° to 5°). Δ is the 1 μm distance grown in each iteration step. The parameter γ ($0 < \gamma < 1$) represents the tendency of an axon to turn towards an angle of 0 degrees - in other words the tendency of the growth cone to orient towards longitudinal growth. We use aINs to illustrate our methods. Figure 5.4A shows aIN axons generated by the simple model for parameter values optimized using the procedure described below together with plots of the same number of real axons. It is clear that the simple model is able to generate the descending part of aIN axon growth (right part of the plot) but fails to fit the experimental data for ascending axons. This is because the descending aIN axons are mainly short with small turning angles while the ascending aIN axons are longer with larger turning angles. When all neuron types were considered we found that if model axons had appropriate tortuosities, then their D-V distributions were too broad and they often ran into the edges of the spinal cord.

The partial failure of the simple model suggested that, in life, some factors guide axons towards a longitudinal growth path and away from the edges of the cord. We

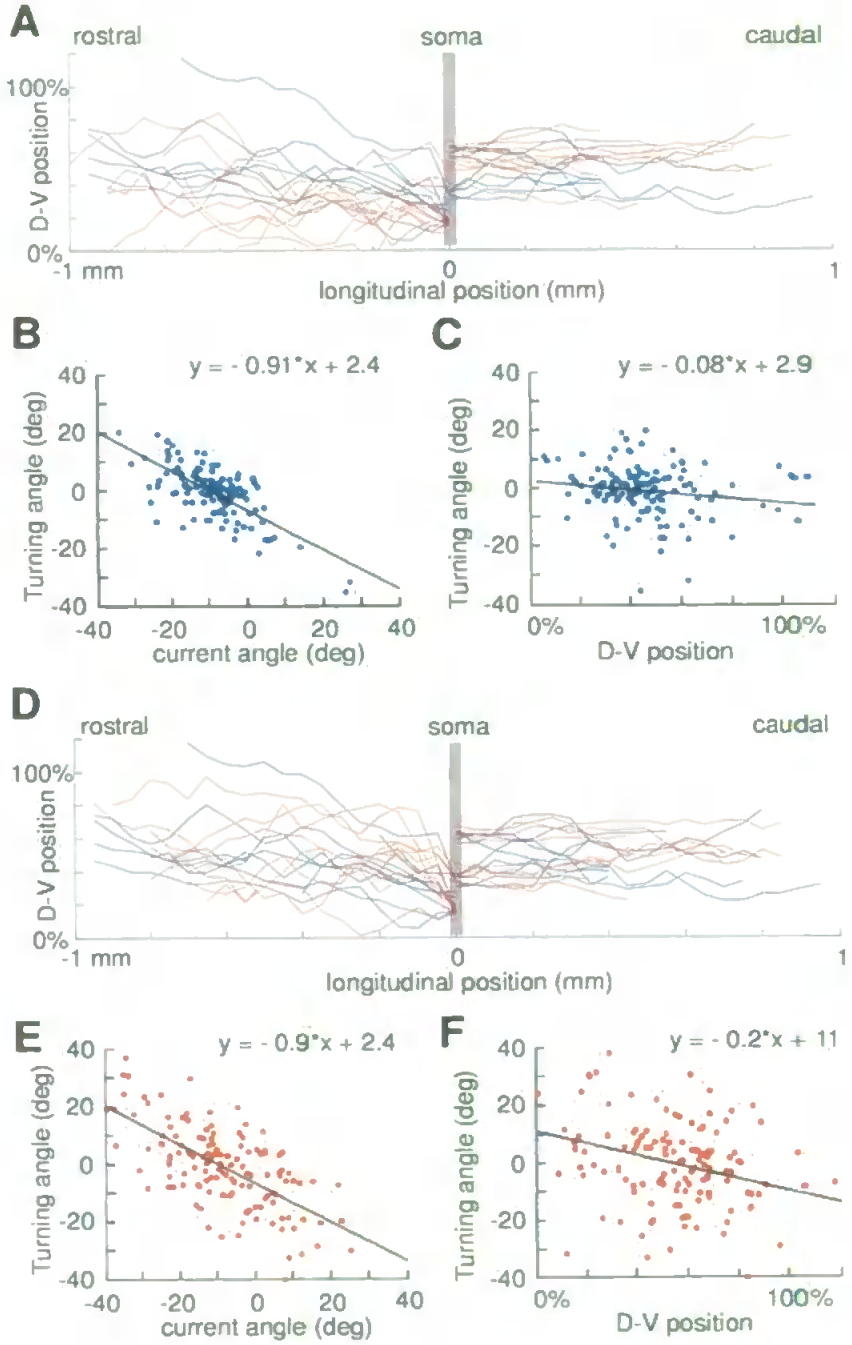

Figure 5.4: Modelling aIN axon growth and positional effects on axon turning angles. (A) aIN descending axons generated by a simple random growth model (red) fit the distribution to real descending axons (blue, to right) but model ascending axons do not match real ascending axons. (B and C) real aIN ascending axon turning angles depend on the current growth angle and D-V position. (D) in a model where growth angle depends on D-V position, generated aIN axons (red) match real axons (blue) closely. (E and F) show that turning angles of modelled axons significantly match real axons' dependence on current angle and D-V position

Axons	Slope of current angle vs turning angle	P-value	Slope of turning angle vs D-V position	P-value
RB				
Desc.	-1.15	0	-0.53	**0**
Asc.	-1.09	0	-0.57	**0**
dlc				
Desc.	-1	0	-0.16	**0.2**
Asc.	-0.87	0	-0.15	0.007
aIN				
Desc.	-0.95	0	-0.17	0.008
Asc.	-0.91	0	-0.08	**0.06**
cIN				
Desc.	-0.71	0	-0.31	0.003
Asc.	-0.89	0	-0.12	0.031
dIN				
Desc.	-1.15	0	-0.21	0.001
mn				
Desc.	-1.25	0	-0.29	**0.13**

Table 5.2: Dependence of axon turning angles on current growth angle and dorso-ventral position

therefore examined the turning angles of real axons (between points 0.05 mm apart) and found that they depended strongly on their current angle of growth and weakly on their D-V position. This is illustrated for aINs in figure 5.4 parts B and C where both scatter plots show negative correlations made clear by fitting the points by linear regression. For all measured neuron types the slope of the regression lines for axon turning angles were negatively dependent on current axon growth angle (-0.71 to -1.25) and dorso-ventral position (-0.08 to -0.53; see table 5.2). This remarkable finding means firstly that the more an axon deviates from longitudinal growth the more it will turn back. Secondly, the dependence of axon growth angle on dorso-ventral position means that for aIN axons the upper and lower boundaries of the cord are repulsive.

In life many possible factors could influence axons to direct them away from edges (eg physical barriers to growth cone extension, D-V gradients of repellent signals (Bourikas et al., 2005)) and guide them to a more longitudinal growth (eg

fasciculation with other longitudinal axons, longitudinal gradients of attractive or repellent signals (Lyuksyutova et al., 2003)). We aimed to encapsulate the essence of such diverse mechanisms by introducing a new feature into our model: $\bar{y}$ represents the dorsoventral position of an attractor to which axon trajectories are drawn with a strength of μ. Equations 5.1 and 5.2 are the same as above, but we replace equation 5.3 with:

$$\theta(t+1) = (1-\gamma)\theta(t) + \mu(y(t) - \bar{y}) + \xi, \qquad t = 0, 1, ..., n-1 \tag{5.4}$$

$$0 < \gamma < 1; 0 < \bar{y} < 1$$

This model contains four parameters (α,γ, μ and $\bar{y}$) and to specify their values we used the following optimisation procedure. For each neuron type we minimize the cost function to find the best parameters which provide the smallest possible value of the cost function. We repeat the same procedure to get optimal parameter values for each type of neuron separately for ascending and descending axons where both exist.

The revised model was able to generate axon growth patterns very similar to those in the spinal cord (for example aINs: Figure 5.4D). In many cases, the optimisation procedure was able to reach very small values of the cost function; for the few cases where it did not, the generated axons were still very similar to real ones. In addition, the modelled axon growth angles showed the same dependence on current angle and D-V position as the measured axons. Full details of the optimization procedure as well as optimal parameter values are presented in the next section. Just as in the real axons, scatter plots and linear regressions showed negative slopes (figure 5.4E and F and table 5.2).

The second revised model of axon growth establishes that axon growth paths and distributions can be generated by very simple rules based only on the initial position and growth angle of the axons. Since these modelled axon distributions closely

match those measured for real axons, it follows that their contact probabilities with dendrites will also be similar and we have confirmed this.

5.4.1 Model explanation

Experimental measurements have been made for different tadpoles with different spinal cord heights which are about 100 μm. To reflect that in the model, we consider axon growth in one side of the spinal cord represented as a rectangle with some height H randomly chosen in the range of admissible biological height values (about 100 μm) and length $W = 1000\mu m$. Thus we consider the rectangle $H \times W$ and growing axons are allocated inside this field. To start an axon simulation we need to choose the initial position of the axon and initial angle, after that the process of axon generation is governed by the model equations 5.1, 5.2, and 5.4.

Developing the model equations, we implicitly assume that chemical gradients experienced by the growth cone are exponential, which for a single gradient would produce a constant rate of turning independent of the location within the gradient (but not independent of the current growth angle). The dependence of axon growth angle on dorso-ventral position (note that dorso-ventral axis corresponds to vertical axis (height) of the rectangle and longitudinal location is considered to lie along the horizontal axis (length) of the rectangle) that we observe is assumed to be the consequence of interaction between at least two gradient-following processes: the noise in the axon growth angle and the tendency to grow towards some particular location. The noise component describes a random deviation of the current angle from the deterministic component (see equation 5.4). Thus the noise component is a random variable uniformly distributed in the interval $(-\alpha, \alpha)$ where parameter α defines the boundary for the angle deviation (Fig. 5.5). Thus, the noise is modelled by a uniformly distributed random variable with mean equal to zero and variance equal to $\alpha^2/3$.

The parameter γ represents the tendency of the axon to turn towards an angle of

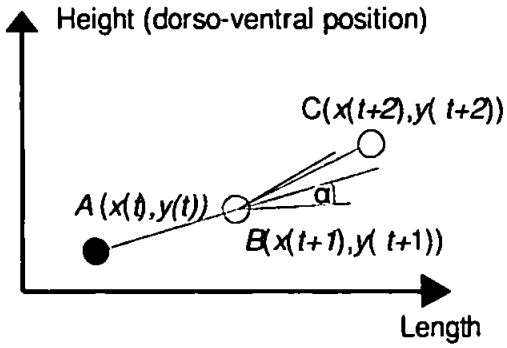

Figure 5.5: The deterministic direction of growth is shown by the black line connecting point A and the yellow dot. The angle α specifies the boundaries of the random deviation. The red line shows the chosen direction of growth for the next time step.

0 degrees - in other words, the tendency of the axon to orient towards longitudinal growth. If γ is zero (see equation 5.3) then the deterministic part of the growth angle is not changed at each time step and random deviation applies to this direction. When $0 < \gamma < 1$, the deterministic component of the growth angle will decay to zero. This part of the model can be justified by experimental findings which show that this orienting process towards zero angle is dependent on the current deviation from longitudinal growth - the steeper the current growth angle, the stronger the tendency to straighten towards horizontal growth. The effect of parameter γ can also be interpreted as the consequence of a longitudinal gradient-following process, which would be expected to produce the same dependence on growth cone angle.

The parameter $\bar{y}$ represents the dorsoventral position of an attractor to which axon trajectories are drawn with a strength which can be described by parameter μ (see equation 5.3). Thus, parameters μ and $\bar{y}$ characterise the interaction between two opposing gradient-following processes. The parameter $\bar{y}$ is the dorsoventral position at which these processes effectively cancel each other out. The parameter μ represents the strength of the net attraction towards $\bar{y}$. The effects of these parameters can be interpreted as a system with two repulsive gradients, one pushing from the ventral side to the dorsal side (we know that there is some drive here at least with the commissural neurons) and one pushing from the dorsal side to the

ventral direction. The relative sensitivity of the axon to these two gradients would determine the value of the parameter $\bar{y}$ and the absolute sensitivity of the growth cone to ligands would determine the value of the parameter μ.

In the next chapter we derive an analytical expression showing how the variance of the growth angle and position in this model depends on time.

Chapter 6

Mathematical analysis of axon growth model: time course of the variance

The model of axon growth is formed in terms of a system of three nonlinear difference equations, one of which has a stochastic term. The resulting process of axon growth is sculpted by a complicated interplay between the deterministic and stochastic components of this system of equations (5.4). On each iteration step we add a random variable with fixed variance. However, the variances of the three variables $(\theta,\ x,\ y)$ grow with the iteration number and may reach large values after some number of steps. Thus it is important to calculate how the variance of the growth angle and coordinates depends on the iteration number.

In particular, an important question is whether the variance is limited and saturates to some level when the iteration number tends to infinity or the variance increases without limitation. We have found the analytical solution to this problem which is presented below.

6.1 Simple model

We will start our analysis from the simple model (5.1-5.3) (with no explicit dependence on the dorso-ventral position). Let us restate this system:

$$\begin{cases} x(t+1) = x(t) + \Delta\cos(\theta(t)) \\ y(t+1) = y(t) + \Delta\sin(\theta(t)) \\ \theta(t+1) = (1-\gamma)\theta(t) + \xi, \end{cases} \tag{6.1}$$

where: $t = 0, 1, 2, ...;\ 0 < \gamma \leq 1$; ξ is the random variable uniformly distributed in $[-\alpha, \alpha]$. The equation for $\theta(t+1)$ does not include x and y and may be studied separately. Let us denote $\beta = (1-\gamma)$; use the notation n to represent time steps instead of t and rewrite the equation for θ_{n+1} in the following form:

$$\theta_{n+1} = \beta\theta_n + \xi_n;\ n = 0, 1, 2, ...;\ 0 < \beta < 1,$$

where $\xi_1, \ldots, \xi_n, \ldots$, are independent identically distributed random variables (with the same distribution as the random variable ξ). Starting from θ_0 we give the first few solutions of this equation:

$$\begin{aligned} \theta_1 &= \beta\theta_0 + \xi_1 \\ \theta_2 &= \beta^2\theta_0 + \beta\xi_1 + \xi_2 \\ \theta_3 &= \beta^3\theta_0 + \beta^2\xi_1 + \beta\xi_2 + \xi_3. \end{aligned}$$

This can be generalized as:

$$\theta_n = \beta^n\theta_0 + \beta^{n-1}\xi_1 + \beta^{n-2}\xi_2 + ... + \beta\xi_{n-1} + \xi_n.$$

In order to find the variance of θ_n from this equation, we consider the variance of both sides:

$$Var(\theta_n) = Var(\beta^n\theta_0 + \beta^{n-1}\xi_1 + \beta^{n-2}\xi_2 + ... + \beta\xi_{n-1} + \xi_n).$$

First we apply the property that the variance of a sum of two independent random variables A and B is the sum of the variances of these variables: $Var(A + B) = Var(A)+Var(B)$. We apply this property recursively until we arrive at the following expression:

$$Var(\theta_n) = Var(\beta^n\theta_0) + Var(\beta^{n-1}\xi_1) + Var(\beta^{n-2}\xi_2) + ... + Var(\beta\xi_{n-1}) + Var(\xi_n).$$

We can eliminate the first term, because $\beta^n\theta_0$ is a constant and so its variance is zero. In addition we apply the property that $Var(\alpha x) = \alpha^2 Var(x)$ to all the terms on the right hand side, and convert all $Var(\xi_n)$ to $Var(\xi)$ as the variance of all ξ_n is the same:

$$Var(\theta_n) = \beta^{2(n-1)}Var(\xi) + \beta^{2(n-2)}Var(\xi) + ... + \beta^2 Var(\xi) + Var(\xi).$$

Factorizing we get the following equation for variance:

$$Var(\theta_n) = Var(\xi)(\beta^{2(n-1)} + \beta^{2(n-2)} + ... + \beta^2 + 1).$$

To sum this geometric progression, we denote the common ratio as $b = \beta^2$:

$$Var(\theta_n) = Var(\xi)(1 + b + b^2 + ... + b^{n-2} + b^{n-1}).$$

Applying the formula for the sum of a geometric progression, we have the final result which describes how the variance of θ depends on n:

$$Var(\theta_n) = Var(\xi)\frac{1-b^n}{1-b}.$$

The random variable ξ is uniformly distributed in the interval $[-\alpha, \alpha]$. The mean of ξ is zero, so we can write:

$$Var(\xi) = \int_{-\alpha}^{\alpha} x^2 f(x)dx,$$

where $f(x)$ is the probability density function of ξ. As we are dealing with a uniform distribution, this is simply:

$$f(x) = \begin{cases} 1/2\alpha, & x \in [-\alpha, \alpha] \\ 0, & \text{otherwise} \end{cases}$$

Substitution of this expression into the equation for $Var(\xi)$ gives:

$$Var(\xi) = \frac{1}{3}\alpha^2,$$

and the full expression for the variance of θ_n is:

$$Var(\theta_n) = \frac{\alpha^2(1-\beta^{2n})}{3(1-\beta^2)}.$$

Substituting $(1-\gamma)$ for β we have the final result:

$$Var(\theta_n) = \frac{\alpha^2}{3}.\frac{1-(1-\gamma)^{2n}}{1-(1-\gamma)^2}$$

. This formula shows that the variance of θ_n saturates for large n in the case that $0 < \gamma \leq 1$. In case $n \to \infty$, $(1-\gamma)^{2n} \to 0$, therefore:

$$Var(\theta_\infty) = \frac{\alpha^2}{3(1-(1-\gamma)^2))} \tag{6.2}$$

Recall that $0 < \gamma < 1$. If $\gamma = 1$ then $Var(\theta_\infty)$ is minimized, and

$$Var(\theta_\infty) = \frac{1}{3}\alpha^2.$$

6.2 Full model

We will begin by restating the full axon growth model (Equation 5.4):

$$\begin{cases} x(t+1) = x(t) + \Delta\cos(\theta(t)) \\ y(t+1) = y(t) + \Delta\sin(\theta(t)) \\ \theta(t+1) = (1-\gamma)\theta(t) + \mu(\bar{y} - y(t)) + \xi \end{cases} \tag{6.3}$$

We only need to consider the last two equations because these equations contain only θ_t and y_t and not x_t. In addition $\Delta = 1$ so it can be omitted[1], we substitute β for $(1-\gamma)$ and we also use the small angle approximation $\sin(x) \simeq x$. We use n to represent discrete time instead of t and make the dependence of ξ on time explicit by rewriting ξ as ξ_n . Thus our model is reduced to the following system of two linear difference equations:

$$\begin{cases} \theta_{n+1} = \beta\theta_n + \mu(\bar{y} - y_n) + \xi_{n+1} \\ y_{n+1} = y_n + \theta_n. \end{cases} \tag{6.4}$$

[1]The same analysis can be carried out when $\Delta \neq 1$ by applying the following procedure: **1)** Divide equation for $y(t+1)$ by Δ to give $y(t+1)/\Delta = y(t)/\Delta + \sin(\theta(t))$ **2)** Apply substitution $Y(t) = y(t)/\Delta$ to equation for y to give $Y(t+1) = Y(t) + \sin(\theta(t))$ **3)** Apply same substitution to equation for θ to give $\theta(t+1) = (1-\gamma)\theta(t) + \mu(\bar{y} - \Delta Y(t)) + \xi$ **4)** Take Δ out of brackets in last term to give $\theta(t+1) = (1-\gamma)\theta(t) + \Delta\mu(\bar{y}/\Delta - Y(t)) + \xi$ **5)** Substitute $M = \Delta\mu$, $\bar{Y} = \bar{y}/\Delta$ to give $\theta(t+1) = (1-\gamma)\theta(t) + M(\bar{Y} - Y(t)) + \xi$. We now have a system of two equations of exactly the same form as equation 6.4 and can proceed in the same way.

Denoting the constant term in the first equation by $D = \mu\bar{y}$ we have the following system:

$$\begin{cases} \theta_{n+1} = \beta\theta_n - \mu y_n + D + \xi_{n+1}, \\ y_{n+1} = \theta_n + y_n. \end{cases} \tag{6.5}$$

We will convert this system of two first order difference equations into a single second-order difference equation. Let us sum the first equation of (6.5) with the second equation multiplied by μ:

$$\begin{cases} \theta_{n+1} = \beta\theta_n - \mu y_n + D + \xi_{n+1} \\ \theta_{n+1} + \mu y_{n+1} = (\beta + \mu)\theta_n + D + \xi_{n+1}. \end{cases}$$

We define a new variable $r_n = \theta_n + \mu y_n$. In the first equation we can add and subtract θ_n:

$$\theta_{n+1} = \beta\theta_n - (\theta_n + \mu y_n) + \theta_n + D + \xi_{n+1}.$$

Combining terms $\mu y_n + \theta_n$ we can substitute the new variable in to get a system of two equations for r_n and θ_n.

$$\begin{cases} \theta_{n+1} = (\beta + 1)\theta_n - r_n + D + \xi_{n+1} \\ r_{n+1} = (\beta + \mu)\theta_n + D + \xi_{n+1}. \end{cases}$$

From the second equation we have an expression for $r_n = (\beta + \mu)\theta_{n-1} + D + \xi_n$ and substitute it to the first equation:

$$\theta_{n+1} = (\beta + 1)\theta_n - [(\beta + \mu)\theta_{n-1} + D + \xi_n] + D + \xi_{n+1}.$$

Simplifying:

$$\theta_{n+1} = (\beta + 1)\theta_n - (\beta + \mu)\theta_{n-1} + (\xi_{n+1} - \xi_n).$$

More substitutions $p = \beta + 1; q = -(\beta + \mu)$ lead to the final form of a second order linear difference equation with a stochastic term:

$$\theta_{n+1} = p\theta_n + q\theta_{n-1} + \xi_{n+1} - \xi_n. \tag{6.6}$$

Our goal is to find the variance of θ_n as a function of n. Generally speaking this equation needs two arbitrary initial conditions. However, from a consideration of the initial conditions for system (6.5) we can find:

$$\begin{cases} y_1 = \theta_0 + y_0 \\ \theta_1 = \beta\theta_0 - \mu y_0 + D + \xi_1, \end{cases}$$

where θ_0 and y_0 are arbitrary constants. We can rewrite the second equation as: $\theta_1 = A_1 + \xi_1$ where A_1 includes all non-random terms. Thus the initial conditions for (6.6) are: θ_0 and $\theta_1 = A_1 + \xi_1$ where θ_0 and A_1 are arbitrary constants. Let us write several sequential solutions of (6.6):

$$\begin{aligned} \theta_0 &= A_0 \\ \theta_1 &= A_1 + \xi_1 \\ \theta_2 &= A_2 + (p-1)\xi_1 + \xi_2 \\ \theta_3 &= A_3 + (p^2 - p + q)\xi_1 + (p-1)\xi_2 + \xi_3 \\ \theta_4 &= A_4 + (p^3 - p^2 + 2pq - q)\xi_1 + (p^2 - p + q)\xi_2 + (p-1)\xi_3 + \xi_4, \end{aligned}$$

where A_0, A_1, ..., A_4 denote the sum of all non-random terms. From these equations we can see that any equation includes the same terms as the previous equation (with the index of ξ increased by 1), plus one new coefficient. Here we again denote the part of the equation without a random variable by A with corresponding indexes. Introducing coefficients B_k to give terms with ξ_k the form $B_{n-k}\xi_k$, we can write the

general form of the equation for θ_n:

$$\theta_n = A_n + B_{n-1}\xi_1 + B_{n-2}\xi_2 + ... + B_1\xi_{n-1} + B_0\xi_n. \tag{6.7}$$

Taking into account two sequential equations for $n = k$, $n = k + 1$:

$$\begin{aligned}\theta_k &= A_k + B_{k-1}\xi_1 + B_{k-2}\xi_2 + ... + B_1\xi_{k-1} + B_0\xi_k \\ \theta_{k+1} &= A_{k+1} + B_k\xi_1 + B_{k-1}\xi_2 + ... + B_1\xi_k + B_0\xi_{k+1}\end{aligned}$$

We can write an equation for θ_{k+2} using the equation (6.6):

$$\begin{aligned}\theta_{k+2} &= p\theta_{k+1} + q\theta_k + \xi_{k+2} - \xi_{k+1} = \\ &= (pA_{k+1} + qA_k) + (pB_k + qB_{k-1})\xi_1 + (pB_{k-1} + qB_{k-2})\xi_2 + \\ &+ ... + (pB_2 + qB_1)\xi_{k-1} + (pB_1 + qB_0)\xi_k + (pB_0 - 1)\xi_{k+1} + \xi_{k+2}\end{aligned}$$

Now we can write iterative equations for the coefficients B_k:

$$\begin{aligned}B_0 &= 1, \\ B_1 &= p - 1, \\ B_2 &= pB_1 + qB_0, \\ B_3 &= pB_2 + qB_1,\end{aligned}$$

and in the general case:

$$B_n = pB_{n-1} + qB_{n-2}. \tag{6.8}$$

Now we will solve the second order difference equation with the initial conditions $B_0 = 1, B_1 = p - 1$. Eq. 6.8 is a linear equation, so we look for solution $B_n = C\lambda^n$. Substituting:

$$C\lambda^n = pC\lambda^{n-1} + qC\lambda^{n-2}$$

Dividing by $C\lambda^{n-2}$ we obtain the characteristic equation:

$$\lambda^2 - p\lambda - q = 0.$$

The roots of the quadratic equation are:

$$\lambda_1 = \frac{p + \sqrt{p^2 + 4q}}{2}$$
$$\lambda_2 = \frac{p - \sqrt{p^2 + 4q}}{2}.$$

We now have the general solution of Eq. 6.8:

$$B_n = C_1\lambda_1^n + C_2\lambda_2^n, \tag{6.9}$$

where C_1 and C_2 are arbitrary constants. Next we use the initial conditions to determine C_1 and C_2:

$$n = 0 : B_0 = 1 \Rightarrow C_1 + C_2 = 1.$$

$$n = 1 : B_1 = p - 1 \Rightarrow C_1\lambda_1 + C_2\lambda_2 = p - 1.$$

$$\begin{cases} C_1 + C_2 = 1 \\ C_1\lambda_1 + C_2\lambda_2 = p - 1. \end{cases} \tag{6.10}$$

$$\begin{cases} C_2 = \dfrac{p - 1 - C_1\lambda_1}{\lambda_2} \\ C_1 + \dfrac{p - 1 - C_1\lambda_1}{\lambda_2} = 1. \end{cases} \tag{6.11}$$

From the second equation of 6.11 we find:

$$C_1\lambda_2 + p - 1 - C_1\lambda_1 = \lambda_2,$$

$$C_1 = \frac{\lambda_2 - p + 1}{\lambda_2 - \lambda_1}.$$

We can simplify this expression taking into account:

$$\lambda_1 - \lambda_2 = \sqrt{p^2 + 4q},\ \lambda_2 - p = -\lambda_1,$$

thus,

$$C_1 = \frac{\lambda_1 - 1}{\sqrt{p^2 + 4q}}$$

Similarly, we substitute C_1 to the first equation of (6.10):

$$C_2 + \frac{p - 1 - C_2\lambda_2}{\lambda_1} = 1,$$

$$C_2\lambda_1 + p - 1 - C_2\lambda_2 = \lambda_1,$$

$$C_2 = \frac{\lambda_1 - p + 1}{\lambda_1 - \lambda_2},$$

$$C_2 = -\frac{\lambda_2 - 1}{\sqrt{p^2 + 4q}}.$$

Substitution of C_1 and C_2 to equation 6.9 gives:

$$B_n = \lambda_1^n \frac{\lambda_1 - 1}{\sqrt{p^2 + 4q}} - \lambda_2^n \frac{\lambda_2 - 1}{\sqrt{p^2 + 4q}},$$

$$B_n = \frac{1}{\sqrt{p^2 + 4q}}[(\lambda_1 - 1)\lambda_1{}^n - (\lambda_2 - 1)\lambda_2{}^n]. \tag{6.12}$$

We can now return to 6.7 and consider the variance of both sides:

$$Var(\theta_n) = Var(\xi)[B_{n-1}{}^2 + B_{n-2}{}^2 + ... + B_1{}^2 + B_0{}^2] \tag{6.13}$$

We use the formula (6.12) to substitute for the coefficients B_n in (6.13):

$$\begin{aligned} Var(\theta_n) = \; & \frac{Var(\xi)}{(p^2+4q)}[(\lambda_1 - 1)^2(1 + {\lambda_1}^2 + ({\lambda_1}^2)^2 + ... + ({\lambda_1}^2)^{n-1}) \\ & +(\lambda_2 - 1)^2(1 + {\lambda_2}^2 + ({\lambda_2}^2)^2 + ... + ({\lambda_2}^2)^{n-1}) \\ & -2(\lambda_1 - 1)(\lambda_2 - 1)(1 + \lambda_1\lambda_2 + ... + (\lambda_1\lambda_2)^{n-1})]. \end{aligned}$$

Using the formula for summation of a geometric progression three times, substituting $Var(\xi) = \alpha^2/3$ and rearranging terms, we have the final formula for the variance of θ_n:

$$\begin{aligned} Var(\theta_n) = \; & \frac{\alpha^2}{3(p^2+4q)}[\frac{(\lambda_1-1)^2}{1-{\lambda_1}^2}(1 - ({\lambda_1}^2)^n) + \frac{(\lambda_2-1)^2}{1-{\lambda_2}^2}(1 - ({\lambda_2}^2)^n) - \\ & - \frac{2(\lambda_1-1)(\lambda_2-1)}{1-\lambda_1\lambda_2}(1 - (\lambda_1\lambda_2)^n)]. \end{aligned}$$

If $|\lambda_1| < 1$ and $|\lambda_2| < 1$ then the variance saturates for large n and we can simplify this expression for the case $n \to \infty$:

$$Var(\theta_\infty) = \frac{\alpha^2}{3(p^2+4q)}\left[\frac{(\lambda_1 - 1)^2}{1 - {\lambda_1}^2} + \frac{(\lambda_2 - 1)^2}{1 - {\lambda_2}^2} - \frac{2(\lambda_1 - 1)(\lambda_2 - 1)}{1 - \lambda_1\lambda_2}\right].$$

6.2.1 Variance of y

It is possible to derive an expression for the variance of y_n as a function of n using the same method we used for the variance of θ_n. Let us start from Eqn. 6.5 (restated here):

$$\begin{cases} \theta_{n+1} = \beta\theta_n - \mu y_n + D + \xi_{n+1}. \\ y_{n+1} = \theta_n + y_n. \end{cases} \tag{6.14}$$

Let us sum the first equation of 6.14 with the second equation multiplied by $(-\beta)$ to exclude θ_n from the right hand side.

$$\begin{cases} \theta_{n+1} - \beta y_{n+1} = -\beta y_n - \mu y_n + D + \xi_{n+1} \\ y_{n+1} = y_n + (\theta_n - \beta y_n) + \beta y_n \end{cases}$$

We define a new variable $u_n = \theta_n - \beta y_n$. Now the system 6.14 can be rewritten:

$$\begin{cases} u_{n+1} = -\beta y_n - \mu y_n + D + \xi_{n+1} \\ y_{n+1} = y_n + u_n + \beta y_n \end{cases} \tag{6.15}$$

From the first equation we have $u_n = -\beta y_{n-1} - \mu y_{n-1} + D + \xi_n$ and this can be substituted into the second equation of (6.15) to give a single second-order difference equation:

$$y_{n+1} = (\beta + 1)y_n - (\beta + \mu)y_{n-1} + D + \xi_n$$

We use the same substitutions as in the previous section: $p = \beta + 1; q = -(\beta + \mu)$ and this gives the following final form of the second order difference equation:

$$y_{n+1} = py_n + qy_{n-1} + D + \xi_n.$$

The initial conditions for this equation are y_0 and y_1, these can be considered as arbitrary constants, therefore both have zero variance. Also, we represent all terms containing no random variable by arbitrary constants A_n with corresponding indexes (A_2, A_3,...).

$$y_2 = A_2 + \xi_1$$
$$y_3 = A_3 + p\xi_1 + \xi_2$$
$$y_4 = A_4 + (p^2 + q)\xi_1 + p\xi_2 + \xi_3$$

Introducing coefficients B_k to give terms with ξ_k the form $B_{n-k}\xi_k$, we can write the general form of the equation:

$$y_{n+1} = A_{n+1} + B_{n-1}\xi_1 + B_{n-2}\xi_2 + ... + B_2\xi_{n-2} + B_1\xi_{n-1} + B_0\xi_n \tag{6.16}$$

A consideration of cases $n = k$, $n = k+1$, and $n = k+2$ similar to that used in the previous section yields a general expression for B_{k+1}:

$$B_{k+1} = pB_k + qB_{k-1}.$$

Solving this second order linear equation with initial conditions $B_0 = 1; B_1 = p$ gives the following formula for B_k:

$$B_k = \frac{1}{\sqrt{p^2+4q}}({\lambda_1}^{k+1} - {\lambda_2}^{k+1}).$$

Now we consider the variance of both sides of (6.16) and substitute the formula for B_k:

$$Var(y_{n+1}) = \frac{Var(\xi)}{p^2+4q^2}\left[({\lambda_1}^n - {\lambda_2}^n)^2 + ({\lambda_1}^{n-1} - {\lambda_2}^{n-1})^2 + \ldots + (\lambda_1 - \lambda_2)^2\right]$$

Rearranging this expression shows that it contains three geometric progressions with common ratios ${\lambda_1}^2$,${\lambda_2}^2$, and $\lambda_1\lambda_2$:

$$\begin{aligned} Var(y_{n+1}) = \tfrac{Var(\xi)}{p^2+4q}[\ & ((\lambda_1{}^2)^n + (\lambda_1{}^2)^{n-1} + \ldots + (\lambda_1)^2) + ((\lambda_2{}^2)^n + \ldots + (\lambda_2)^2) \\ & -2((\lambda_1\lambda_2)^n + \ldots + (\lambda_1\lambda_2))] \end{aligned}$$

Summing the geometric progressions and substituting $Var(\xi) = \alpha^2/3$ yields the following final expression for the variance of y_n:

$$Var(y_n) = \frac{\alpha^2}{3(p^2+4q)}\left[\lambda_1^2\frac{1-(\lambda_1{}^2)^n}{1-{\lambda_1}^2} + \lambda_2^2\frac{1-(\lambda_2{}^2)^n}{1-{\lambda_2}^2} - 2\lambda_1\lambda_2\frac{1-(\lambda_1\lambda_2)^n}{1-\lambda_1\lambda_2}\right]. \quad (6.17)$$

If $|\lambda_1| < 1$ and $|\lambda_2| < 1$ then the variance saturates for large n and the formula for the case $n \to \infty$ is:

$$Var(y_\infty) = \frac{\alpha^2}{3(p^2+4q)}\left[\frac{{\lambda_1}^2}{1-{\lambda_1}^2} + \frac{{\lambda_2}^2}{1-{\lambda_2}^2} - \frac{2\lambda_1\lambda_2}{1-\lambda_1\lambda_2}\right]. \quad (6.18)$$

Figures 6.1-6.2 show both analytical and computational variances versus iteration number. These figures show the variances for aIN cells with axons growing in descending direction. Optimal parameter values (the first row in Table 6.1) have been calculated according to the model fitting procedure (model fitting and parameter optimisation are described in the next section, in which these parameter values will be repeated). The analytical solution for the variance of the dorso-ventral coordinate y_n is shown by a smooth red line on Fig. 6.1 calculated according to formula (6.17). This variance saturates on the level 127.5 (dotted line) and this saturation level has been calculated by using the formula 6.18. It is interesting to note that using optimal parameters for calculation of the roots of the characteristic equation (Eqn. 6.2) gives $|\lambda_1| < 1$ and $|\lambda_2| < 1$ for all cell types in all directions. For example for aIN axons in descending direction $\lambda_1 = 0.999$ and $\lambda_2 = 0.882$.

Computational variance has been calculated according to the following procedure. First, optimal parameter values of the model have been found by nonlinear least squares fit of the model to experimental measurements of axons. Second, using optimal parameter values we generate 200 axons starting from different initial values of the random number generator. Each axon is generated in the interval $x \in [0, m], m = 2, 3, 4, \ldots, 3000$. Thus, for each repetition of this procedure we generate an axon and sample its D-V coordinate at the last point y_m^k ($k = 1, \ldots, 200$). So we accumulate the sample $[y_m^1, y_m^2, \ldots, y_m^{200}]$ and calculate a standard statistical estimate of the variance. It is clear from Fig. 6.1 that the estimate of the variance varies in a wide range. Similar computations have been done for the variances of axon growth angle θ and both analytical and computational variances are shown in Fig. 6.2. The variance of axon growth angle saturates much faster than the variance of the D-V coordinate of the axon.

Table 6.1 also shows the roots λ_1 and λ_2 of the characteristic equation (Eqn. 6.2), which have been used in the formulas for calculation of the dynamics of the variances. All roots are positive and less than one. Only in the case of RB cells (both

ascending and descending) the roots are complex conjugates with modulus less than one. These facts mean that for all cell types in both directions, the variance of the D-V coordinate is limited and asymptotically approaches the saturation level. The variance for growth angle also saturates with increase of iteration number.

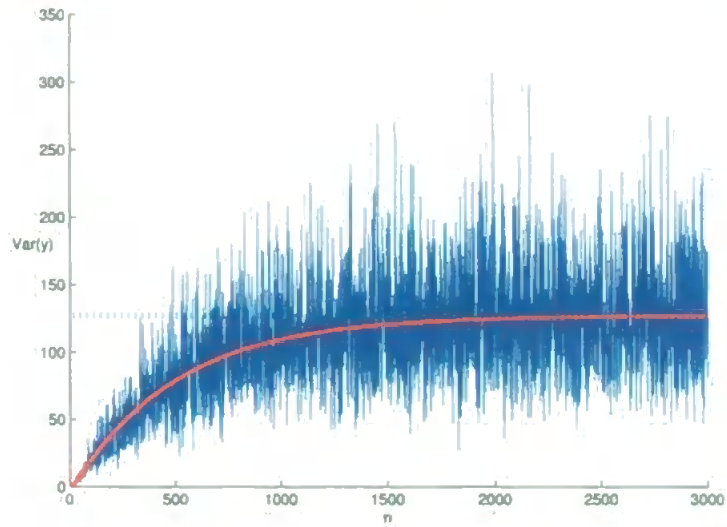

Figure 6.1: Analytical and computational variances of axon D-V coordinate vs. the iteration number.

In the next chapter, we show how the parameters of the model can be optimized to match the anatomical data from the tadpole and generate a reconstruction of the tadpole spinal cord anatomy.

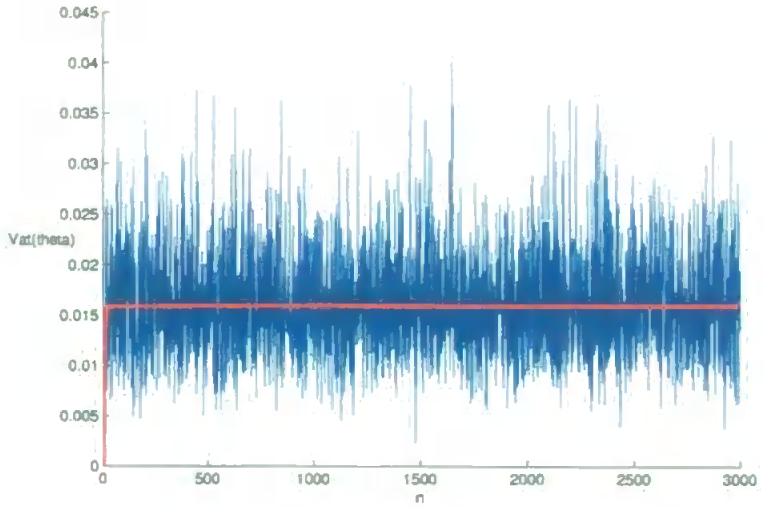

Figure 6.2: Analytical and computational variances of axon growth angle vs. the iteration number.

	α	γ	μ	$\bar{y}$
aIN des	0.1037	0.1192	0.01182	0.5512
aIN as	0.2373	0.08814	0.02674	0.6978
cIN des	0.05376	0.06153	0.01392	0.7359
cIN as	0.05905	0.08263	0.01092	0.7111
dIN des	0.1219	0.09565	0.02109	0.3806
RB des	0.1165	0.04534	0.05581	0.6982
RB as	0.1224	0.04323	0.05000	0.7917
dlc des	0.1419	0.09199	0.04113	0.4116
dlc as	0.1136	0.1145	0.01791	0.6500
MN	0.1048	0.4173	0.02819	0.1764

	λ_1	λ_2	Modulus
aIN des	0.999	0.8818	
aIN as	0.9969	0.915	
cIN des	0.9976	0.9408	
cIN as	0.9987	0.9187	
dIN des	0.9977	0.9066	
RB des	0.9773 + 0.0067i	0.9773 - 0.0067i	0.9774
RB as	0.9784 + 0.0057i	0.9784 - 0.0057i	0.9784
dlc des	0.9953	0.9127	
dlc as	0.9984	0.8871	
mn	0.9993	0.5834	

Table 6.1: Parameters for model axon generation and corresponding roots of the characteristic equation

Chapter 7

Optimization of model parameters and reconstruction of tadpole spinal cord

7.1 Fitting the model to experimental measurements and optimal parameter values

Our goal is to simulate an axon growth process which can generate axons that are similar to biological axons which have been measured experimentally. This similarity is measured using a cost function with two components: 1) similarity of distributions of axon projections in the dorso-ventral dimension and 2) similarity of tortuosities. Thus, the optimization procedure searches for a set of values of the four model parameters which minimize the cost function. The optimization procedure is formulated in detail below.

The available experimental data provide measurements of spinal cord axons for each neuron type in both descending and ascending directions when both are present. Considering the example of aIN ascending axons, we will demonstrate how the optimization procedure works. Available experimental data provide measurements of 10 axons from different tadpoles. The longitudinal dimension in the model was always 1000 μm however axons can be shorter or longer than this full length. Experimental measurements of dorso-ventral axon position (in micrometers) were made every

50 μm. An example of a measured axon is shown in Fig. 7.1. The horizontal red line (y=94.7 μm) shows the dorso-ventral height boundary of the spinal cord and the vertical red line shows the longitudinal boundary of considered spinal cord measurements.

The next step is the projection of axon measurements in the dorso-ventral direction and the calculation of the distribution of these projections. Because the dorso-ventral height of the rectangles varies for different axons extracted from tadpoles with different spinal cord lengths, we normalise axon coordinates before projecting them. Thus, we normalise both axes by dividing both vertical and horizontal axon coordinates by the dorso-ventral height of the spinal cord (in this example the height H=94.7). Division of both coordinates allows us to keep the angle structure unchanged. Of course, after this transformation a step along the horizontal axis will be different from 50 μm however the image representation will be the same.

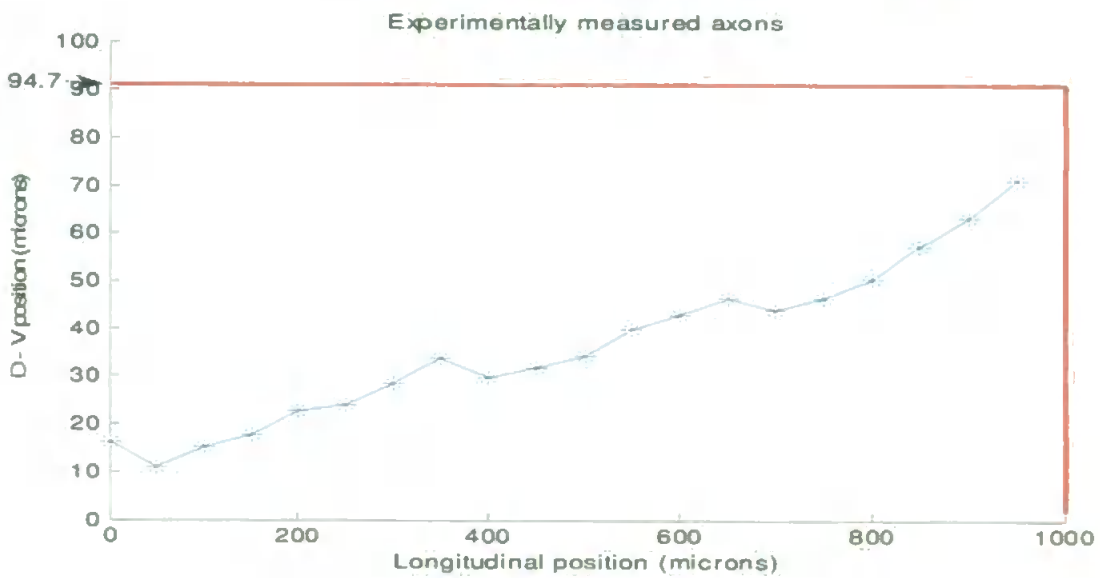

Figure 7.1: An example of axon measurements

After normalization we project all aIN ascending axon data to the vertical axis and repeat this procedure for each axon. The total number of axon measurements is n_e ($n_e = 167$) and these data represent the dorso-ventral distribution of axon

measurements in the interval 0-100. We divide this interval into 10 bins, count the number of measurements in each bin, and normalize it by the total number n_e to get the probability of finding an axon measurement in the bin. The resulting distribution is shown in Fig. 7.2.

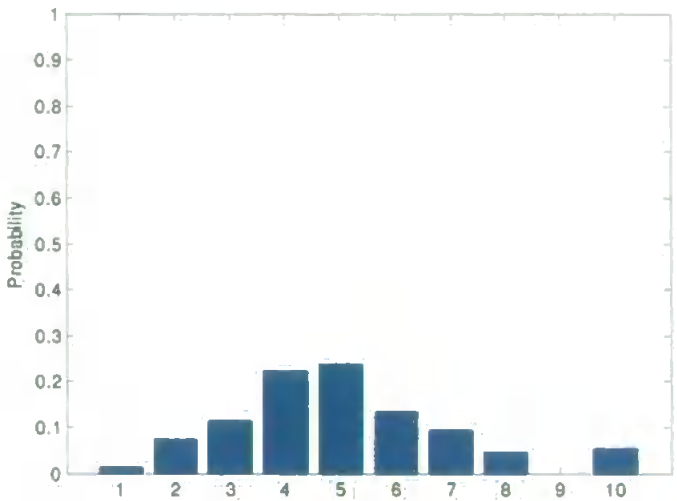

Figure 7.2: An example of the distribution of measured D-V coordinates for aIN ascending axons

Moreover, we would also like the cost function to take into account the extent to which the path of the axon is circuitous rather than direct. Results from multiple model simulations suggest that tortuosity (total path length divided by straight line distance between start and end points) is an appropriate measure for this purpose. Thus, we calculate the tortuosity of each axon using the following formula:

$$T = \frac{\sum_{i=1}^{k} \sqrt{(x_i - x_{i-1})^2 + (y_i - y_{i-1})^2}}{\sqrt{(x_k - x_0)^2 + (y_k - y_0)^2}} \tag{7.1}$$

where $(x_i, y_i), i = 0, 1, \ldots, k$ are measured coordinates of the axon, and k is the number of measurements for the axon. After that we calculate the average tortuosity of experimental axons $\bar{T}^e$.

We can now describe the process of axon generation. Supposing that the values of the four model parameters are known, we can start the process of axon generation

described by equations 5.1, 5.2, and 5.4. For this we need to choose initial values for the variables of the dynamical system, i.e. coordinates of the starting point of the axon (x_0, y_0) and the initial growth angle θ_0. We also need to fix the length of the generated axon.

All generated axons have the same initial horizontal position $x_0 = 0$. To determine the initial value of the vertical coordinate we first calculate the sample distribution (in 10 equally sized bins covering the interval 0-100) of normalised initial vertical coordinates of all experimentally measured axons and generate a random number ran according to this distribution, thus, $y_0 = ran$. To determine the initial angle, we consider the bin of distribution where ran is and study the initial angles $\eta_1, ..., \eta_q$ of those axons for which the vertical coordinate of the starting point falls into this bin. We generate uniformly distributed random angle η in the interval $(min(\eta_1, ..., \eta_q)$ and the initial growth angle $\theta_0 = \eta$. Similarly, for the axon length we build the distribution of experimental axon lengths and generate a random number according to this distribution. We use the same procedure to generate the dorso-ventral height of the spinal cord: we build the distribution of experimentally measured dorso-ventral heights and generate the random number ran_height according to this distribution; thus, we have chosen the rectangle $ran\_height \times 1000$ where all model generated axons will be allocated, i.e. we use the same rectangle to generate several axons and allocate them to the same rectangle.

After fixing all initial values and axon lengths we run the system of difference equations 5.1, 5.2, and 5.4 and generate an axon. For axon generation we use step $\Delta = 1\mu m$. To obtain generated axon data similar to the experimental measurements we sample model axon coordinates every 50 μm and use these sampled data for the following procedures: projection of axons, building D-V distribution, calculation of tortuosity, etc. Fig. 7.3 shows an example of a generated model axon for the optimal parameter values fitted to aIN ascending experimental measurements. The green line shows a generated axon with 1 μm step, markers show measurements at

50 μm steps along the horizontal axis, the same sampling as in experiments.

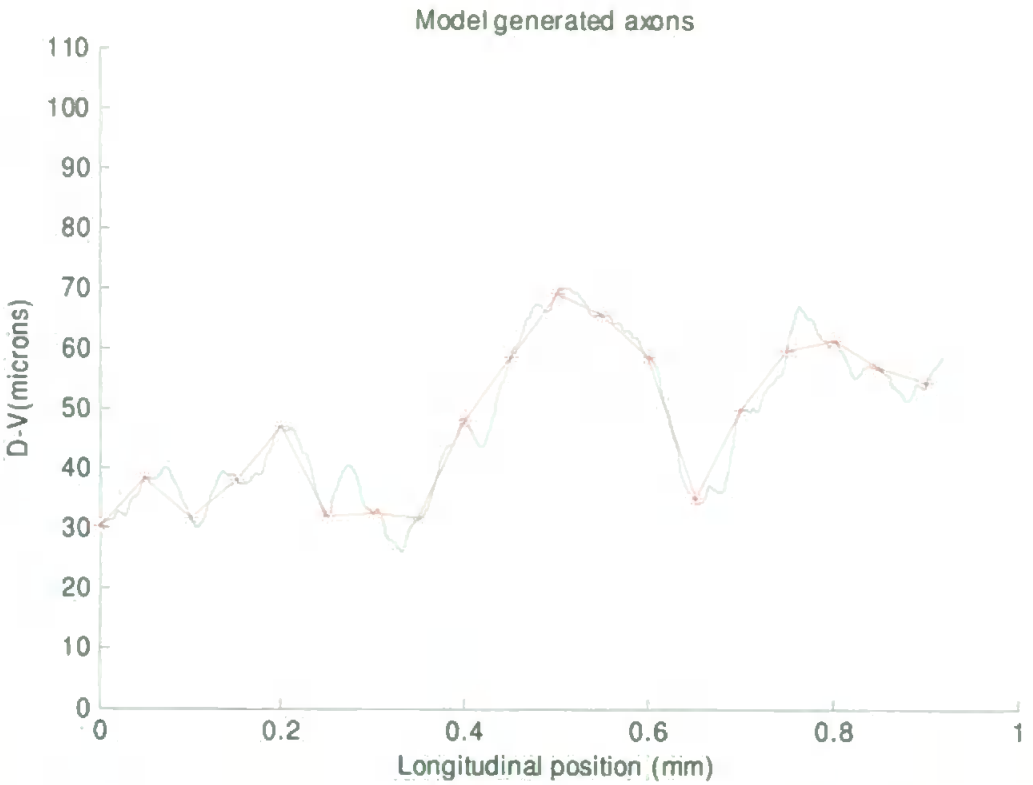

Figure 7.3: Example of generated axon for optimal parameter values of aIN ascending neuron type. Green line shows generated axon and red line shows approximation with 50 μm sampling along the horizontal axis.

It is important to note that the procedure for choosing initial values and axon lengths involves the generation of random numbers. This means that repetition of the same procedure will result in the generation of a different axon with different initial values and a different length. Thus, we repeat this procedure r times ($r = 70$), generate r axons allocated inside of the same rectangle, and calculate the dorso-ventral distribution (10 bins covering the interval 0-100) of all vertical coordinates of all generated axons. We denote this distribution by $(y_1^m, ..., y_{10}^m)$, and the total number of coordinates used for calculation of the distribution is n_m (index m here means relates to 'model'). Also, we calculate the tortuosity for each model axon and find the average tortuosity of generated axons $\bar{T}^m$.

Now we can define the cost function which includes both the similarity of the

spatial distributions and the similarity of axon tortuosities. To measure similarities of distributions we use the sum of squared differences between experimental and modelled distributions. To interpret the values of this sum, we use a normalization which is traditionally used in statistics for comparing distributions and representations of random variables with chi-square distribution. Thus the first term of the cost function is:

$$f_{chi} = \sum_{i=1}^{10} \frac{(y_i^e - y_i^m)^2}{y_i^e n_e + y_i^m n_m} \tag{7.2}$$

It is known in statistics that the 5% critical value with 9 degrees of freedom for the one-tailed χ^2-test is 16.9. Thus, this value can serve as guidance for understanding the scale of cost function values and judging the quality of the optimization process.

The second term of the cost function is the squared difference between the average experimental tortuosity and the average model tortuosity. The two terms of the cost function have very different scales and to balance them we consider a weight coefficient w which makes these terms consistent and with values in the same interval. Thus, the final expression for the cost function is:

$$f_{cost} = f_{chi} + w(\bar{T}^e - \bar{T}^m)^2, \text{where } w = 10^5 \tag{7.3}$$

It is worth noting that the cost function includes a stochastic component, therefore, repeated calculation for the same parameter values will always result in different values of the cost function. Thus, gradient based methods are not appropriate for optimization because they usually require the cost function to be smooth which it is not in our case. We use the Nelder-Mead simplex method (Lagarias et al., 1998) which can deal with non-smooth cost functions and even with cost functions including a stochastic component.

7.2 Results of optimization and testing the optimization quality

It is important to note that the result of the optimization procedure is a random variable. This means that if we have found a set of optimal parameter values and use them to calculate the cost function several times, we will get different cost function values, because the random number generator will start from different initial values resulting in generation of different axons. Thus, we would like to test the result of optimization studying the distribution of the cost function values generated for the set of optimal parameter values.

The optimization procedure was run for each cell type and separately for their descending and ascending axons. The best values of model parameters and quality of optimization are summarised in Table 7.1. To quantitatively characterise the quality of optimization we define the measure Q in the following way. One trial of the testing procedure includes the generation of 300 axons for the optimal parameter values and calculation of the cost function. We repeat this procedure 100 times, generate 100 values of the cost function, and build a histogram which we call the testing histogram (examples are given below). We denote by Q a value of the cost function such that the interval $(0, Q)$ corresponds to 90% of the area of the histogram. We consider the optimisation procedure to be: *very good* quality if Q is less than 4; *good quality* if $4 < Q < 8.5$; and *poor quality* if $Q > 8.5$. The last two columns of Table 7.1 show the quantitative and qualitative characteristics of the optimization procedure for each cell type.

Following the optimization process, we tested the sensitivity of the optimal parameter values to small variations. We consider 3 levels of variation: 5%, 10% and 20% (accordingly, the fractions of variation are $Fr = 0.05$, $Fr = 0.1$; $Fr = 0.2$) and for each level, (e.g. 5%), we consider three cases for each of the four parameters: 1) the parameter value decreases (e.g. by 5%) ($ind = -1$); 2) the parameter value is

	alpha	gamma	mu	ybar	quality	Q
aIN des	0.1037	0.1192	0.01182	0.5512	good	8
aIN as	0.2373	0.08814	0.02674	0.6977	good	8
cIN des	0.05376	0.06153	0.01392	0.7359	good	6
cIN as	0.05905	0.08263	0.01092	0.7111	good	4.5
dIN des	0.1219	0.09565	0.02109	0.3806	poor	21
RB des	0.1165	0.04534	0.05581	0.6982	poor	18
RB as	0.1224	0.04323	0.05000	0.7917	good	6
dlc des	0.1419	0.09199	0.04113	0.4116	good	6
dlc as	0.1136	0.1145	0.01791	0.6500	poor	17
MN	0.1048	0.4173	0.02819	0.1764	very good	1.5

Table 7.1: Parameters for model axon generation and quality of optimization

not disturbed ($ind = 0$); 3) the parameter value increases (e.g. by 5%) ($ind = +1$). We calculate variations of the optimal parameters and use them to calculate the performance of the model for different degrees of parameter variation in terms of the quantitative measure Q. The results of sensitivity testing are presented in the Appendix. These results show that for 75% of considered cases of different variations at the level of 5%, the value of Q remains below 8.5 which is our criterion for good quality results. Variation of parameters at the 10% level shows that 42% of cases produce good quality results. Thus the quality of optimization is sufficient and is not overly sensitive to variation of optimal parameters.

An example of generated and measured axons for the case of RB cells in ascending direction is shown in Fig. 7.4. Average tortuosities for generated and measured axons are: model tortuosity $\bar{T}^m = 1.01$ and experimental tortuosity $\bar{T}^e = 1.009$.

Fig. 7.5 shows distributions of dorsoventral coordinates of experimental and generated axons. Both figures demonstrate a very good correspondence between generated and measured axon distributions. Similar figures have been produced for all other cell types in ascending and descending directions; these are provided in the Appendix.

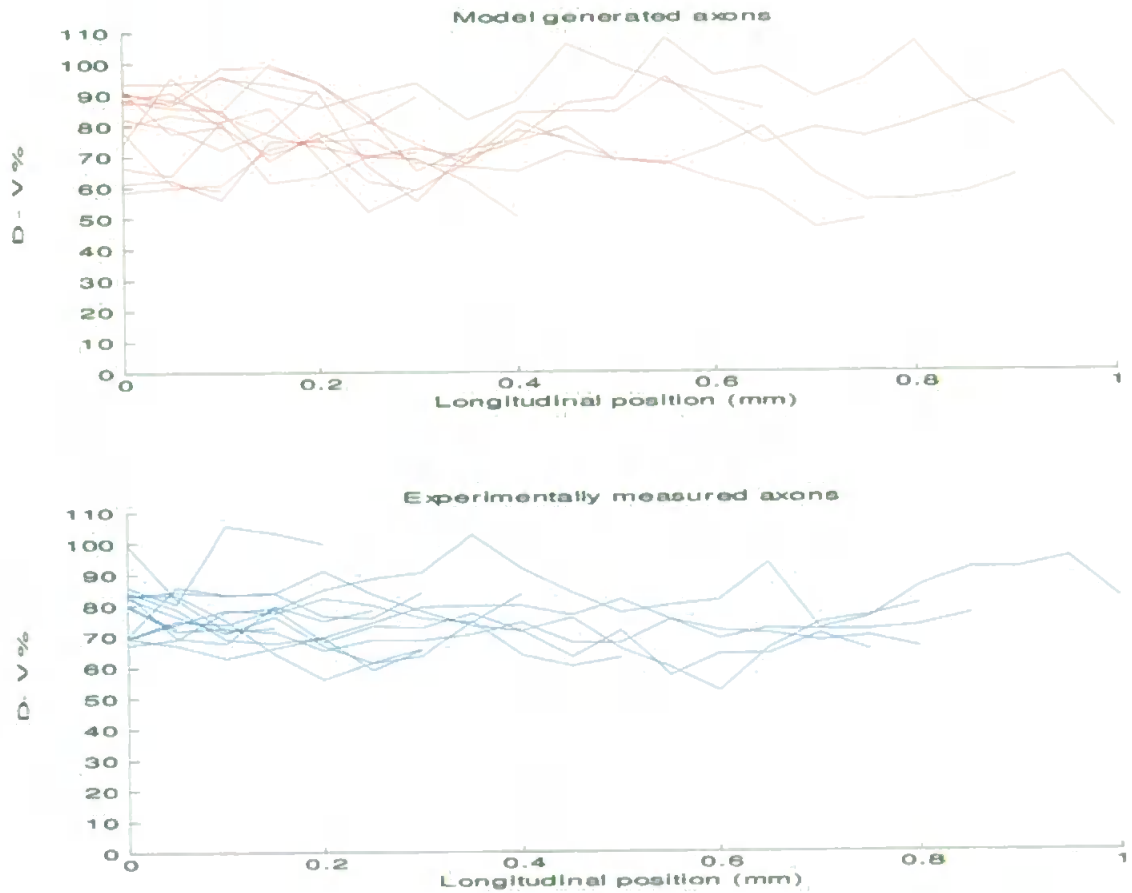

Figure 7.4: An example of axons generated by model (upper panel in red) and experimentally measured axons (lower panel in blue). Model tortuosity: 1.01. Experimental tortuosity: 1.009

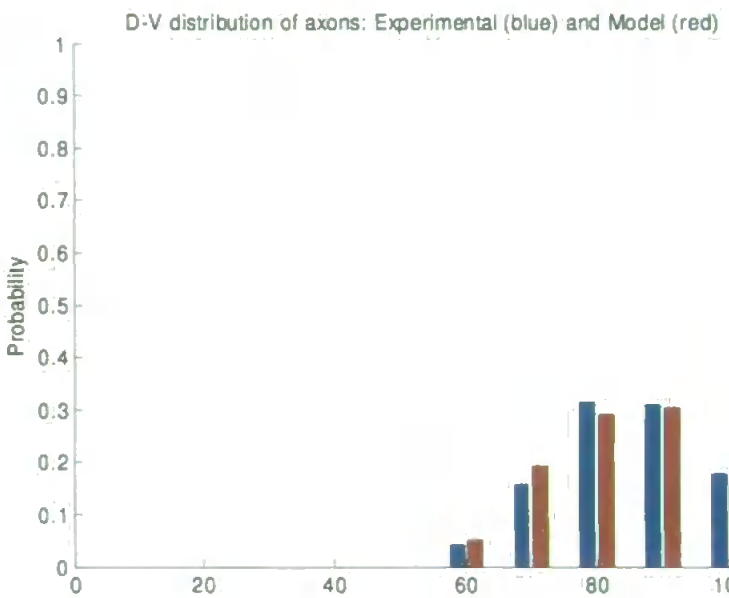

Figure 7.5: Comparing the dorso-ventral distributions of model axons (blue) and experimental axons (red).

7.3 Spinal cord network reconstruction

Having developed a model of axon growth that produces axons that approximate those observed in the tadpole, we can now use this model to generate a reconstruction of the tadpole spinal cord. This model allows us to make some general predictions about how connectivity varies with longitudinal distance and will be used in the next chapter as the basis for an electrophysiological model of the network.

We consider a 2000 μm section of spinal cord. This section contains 6 cell types, the density of which is equivalent to 7 cells of each type per 100 μm section of spinal cord. This is a very approximate figure provided by Prof. Roberts. This section corresponds to one side (e.g. left side) of the spinal cord. In fact, in our simulations we only need to consider one side in order to study the statistical properties of axons, dendrites and synaptic contact distributions. This is due to the fact that the statistical characteristics of one side are very similar to the statistical characteristics of the other side. In the biological spinal cord, interneurons of the cIN and dlc types cross the ventral floor plate and make synaptic connections with neurons of the opposite side. In our model, we do not consider the opposite side but instead we use the branching point for these cell types and grow axons starting from these branching points. Branching points have the same rostrocaudal distribution as the somas of corresponding cell types. In fact we do not consider cIN and dlc cells as special cases here; the procedure of modelling axon growth is the same as for other cell types. Using this procedure we can generate distributions of cell positions, dendrites, and axons for all cell types and by doing so we can obtain synaptic couplings between all cell types. These distributions will be used in the next chapter for electrophysiological modelling. Also in the next chapter we extend this model to generate both sides of the spinal cord.

The total number of neurons in the model of one side of the spinal cord is 840, which includes neurons of 6 types: 140 neurons labelled by 1, 140 labelled by 2 and so

on until label 6. These neurons are allocated uniformly with space $\delta = 2000/840\mu$m, in the order 1,2,3,4,5,6 and there are 140 repetitions of this sequence. Then the distribution is randomized by randomly picking a cell and swapping it with its immediate neighbour to the right, repeating this process many times. As a result of applying this permutation process, all the cell types become uniformly distributed over the length of the spinal cord. This process captures the known anatomical property that cells of the same type tend not to appear very close to each other, but avoids the artificial situation of a perfectly regularly laid out spinal cord.

The available experimental data provide only the dorsal (d_i) and ventral (v_i) extents of the dendritic field for each cell i. Thus in our model we represent the dendrite by a vertical bar with coordinates in the interval (v_i, d_i). We consider a two dimensional probability distribution of the two dimensional random variable (v_i, d_i) where the dorsal extent is v_i and the ventral extent is d_i. This random variable is distributed in a triangle with two sides of 100 μm. We suppose that our experimental data gives us the ability to approximate this two dimensional random variable by a 10 × 10 table, where each entry contains the probability of a $(ventral - bin, dorsal - bin)$ pair as found in the anatomical data set. In this table, cells under the diagonal contain approximate probabilities, but cells above the diagonal are zero, because the dorsal extent cannot be lower than the ventral extent. Having determined which 10% bins the dorsal and ventral extent will fall into, the actual dorsal and ventral extents are uniformly distributed within these bins.

For visualization purposes we represent the dendrite by a bar with width 1 μm in the longitudinal direction and the dorsoventral extent of this bar is randomly generated on the basis of the two dimensional distribution for this particular cell type. This two dimensional table was produced for each cell type, and the dorsal and ventral extents are generated at random according to the corresponding table.

At this point, all 840 cells are allocated in their proper longitudinal and dorsoven-

tral positions, meaning that the distribution corresponds to the experimental distribution and the longitudinal positions are uniformly distributed for all cells.

We now apply the following procedure for each cell:

1. Generate a random initial angle and position using the procedure detailed in section 7.1.

2. Generate a length for the axon taken from the experimental distribution of axon lengths.

3. Grow the axon to the determined length using the algorithm detailed in section 7.1. When the path of the axon intersects with the bar representing the dendritic field of a cell, generate a random variable x uniformly distributed between 0 and 1 and if $x < P_{syn}$ then generate a synapse. If a synapse was made then any subsequent intersection between the axon and this particular dendritic field will be ignored. So it is not possible that one presynaptic neuron will make two or more synapses onto the same postsynaptic cell. Professor Roberts's data from electrophysiological studies indicate that $P_{syn} \approx 0.46$ as mentioned before.

7.3.1 Full reconstruction of the spinal cord

Using the procedures described above, we generate a biologically realistic model of the full spinal cord of the tadpole. Of course we use corresponding optimal parameter values to generate axons of each particular cell type and this provides us with a set of axons which have similar statistical characteristics to the real axons. The same is correct for the distribution of dorsoventral positions of dendrites: the generated dendrites have the same statistical characteristics as those that were experimentally measured.

Figure 7.6 shows a fragment of the reconstructed anatomy of the whole tadpole spinal cord. Each cell type is represented by a separate colour: RB cells are shown

in red, dlcs are green, aINs are blue, cINs are magenta, dINs are brown, and mns are black. These colours are used to represent axons (curves), dendrites (long vertical bars), initial branching points of axons (squares), and synapses (circles which have the same colour as the presynaptic cell). In some cases the initial branch point will appear inside the dendritic bar of the cell to which it relates and in other cases it will be located outside of the bar but in all cases the longitudinal position will be the same. RB neurons are represented only by their axons because they have no dendrites - they are sensory neurons that respond to skin stimulation.

Figure 7.7 shows a zoomed view of a 30 μm by 30 μm section of spinal cord taken from the middle section of the dorsoventral axis. Many synaptic connections can be seen.

From this reconstruction, a complete description of the connectivity of the spinal cord can be produced which can be used as the basis for electrophysiological modelling.

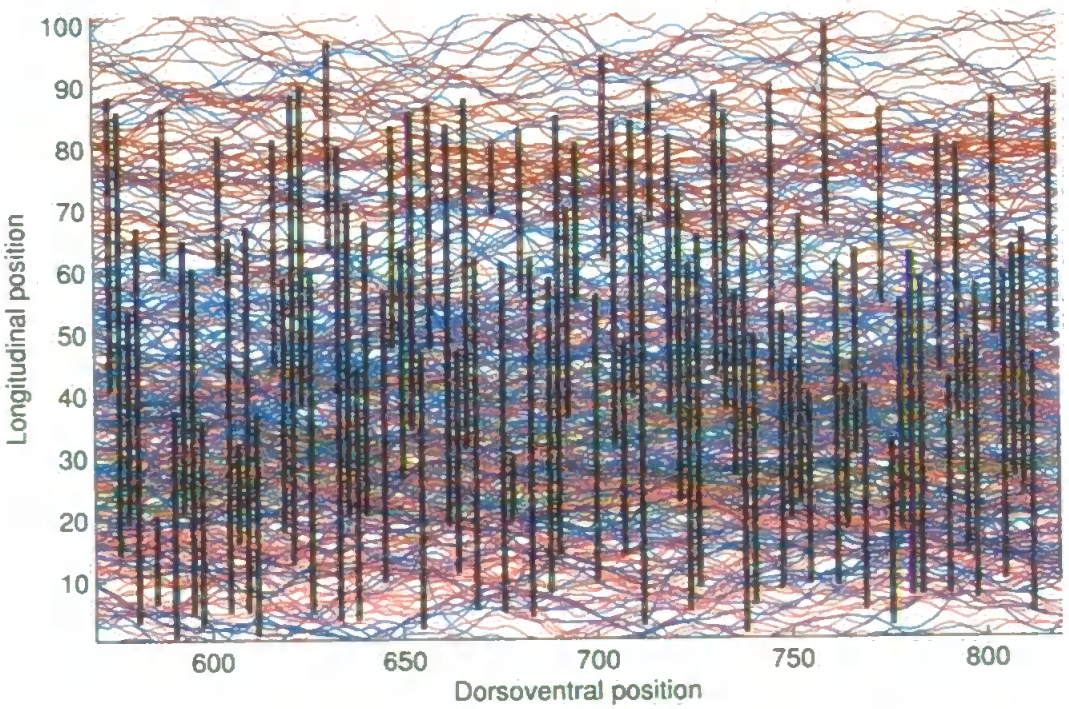

Figure 7.6: 200 μm section of spinal cord reconstruction. RB cells are shown in red, dlcs are green, aINs are blue, cINs are magenta, dINs are brown, and mns are black.

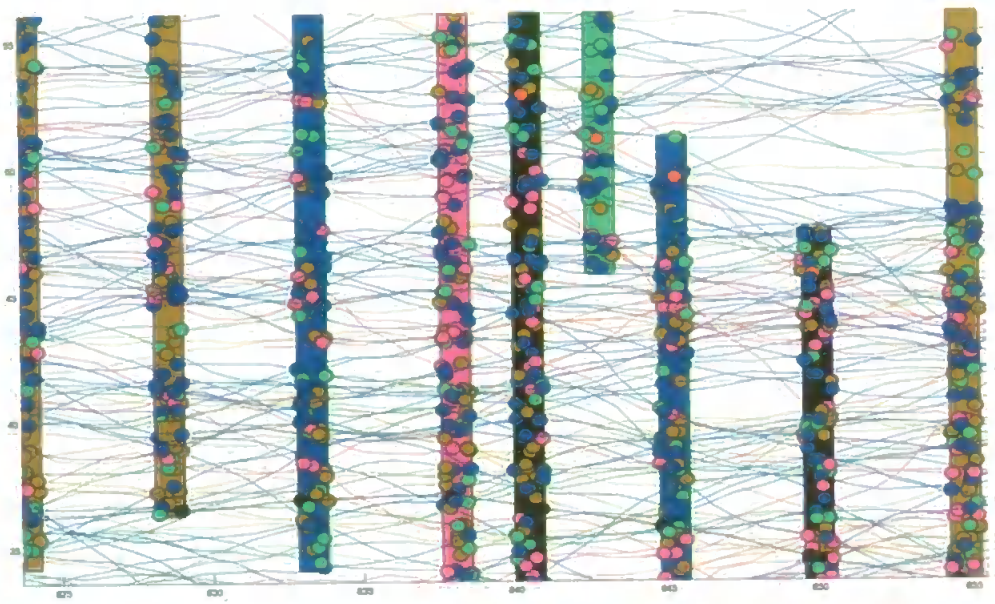

Figure 7.7: 30 μm section of spinal cord reconstruction. RB cells are shown in red, dlcs are green, aINs are blue, cINs are magenta, dINs are brown, and mns are black.

7.3.2 Variation of connectivity with distance

Using the data from the reconstructed spinal cord we can generate a receptive field like graph for each cell type, showing how its inputs from other cell types vary with distance (which we measure in μm). These are shown in figures 7.8-7.12.

To generate these figures we apply the following procedure which we repeat for all pairs of cell types. As an example we can consider the case of synaptic connections from RB cells to dlc cells (red line on figure 7.8. The procedure is as follows: 1) Select one dlc cell and consider all incoming connections from RB cells for this particular cell. 2) Count the number of connections related to some particular distance. Negative distance indicates a connection from a more rostral cell (closer to the head), positive indicates a connection from a more caudal cell (closer to the end of the tail). 3) Accumulate these counts for all dlc cells. Having done this we repeat the procedure for all other possible connections to dlc cells.

The most remarkable feature of these receptive field-like distributions is that connections incoming to a particular cell are mostly local. The typical radius of

local connections is about 200 μm. An interesting exception is the case of aIN to dlc cells where it can be seen that connections are relatively rare when the aIN cell is very close to the dlc cell and become more frequent as the distance increases, before reaching a maximum at about 200 μm away (in either direction) and then declining. This is due to the fact that the aIN axons need to grow dorsally for some distance from the branch point before they are able to contact the relatively dorsal dendrites of dlc cells. The fact that dlc dendrites are dorsally located is also why they receive much more synaptic input from RB cells (which have very dorsal axons) than other cell types.

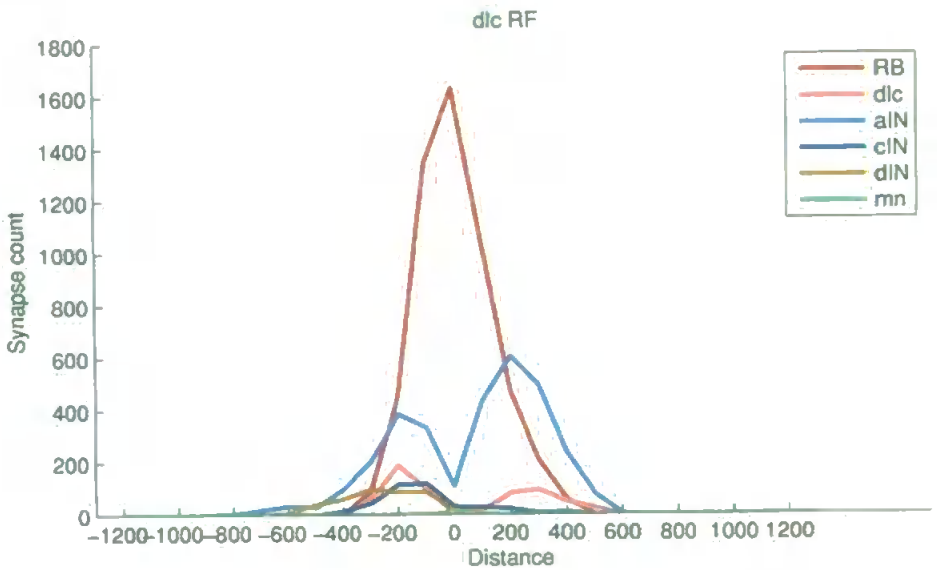

Figure 7.8: Variation of inputs to dlc cells with distance (μm)

7.3.3 Discussion

To the best of our knowledge, for the first time a complete biologically realistic neural circuit of the tadpole spinal cord has been generated. This model has great potential for further investigation. For example, probabilities of synaptic contacts between cells of different types can be calculated from the generated architecture and compared with experimentally measured probabilities of synaptic contacts between the same cells. Indeed, this comparison reveals that the probabilities of synaptic

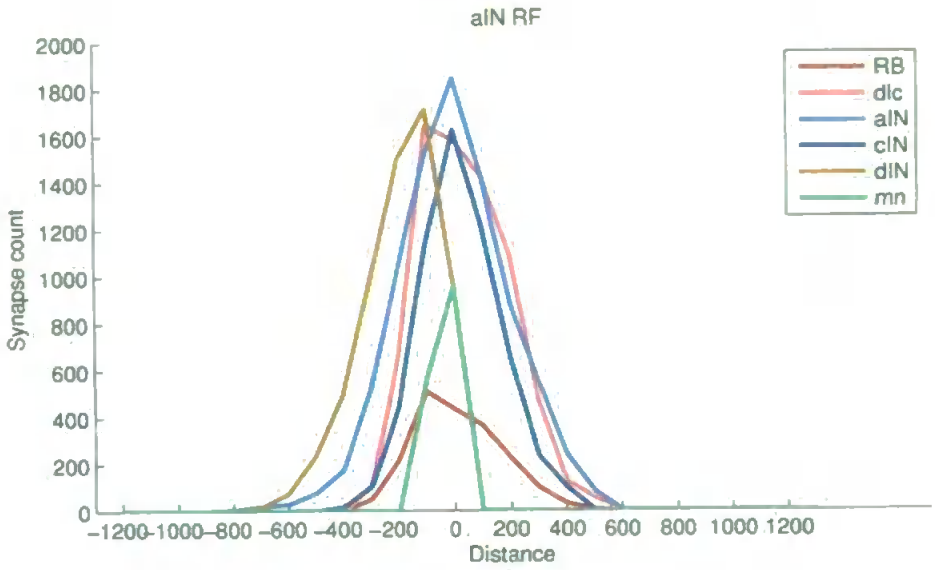

Figure 7.9: Variation of inputs to aIN cells with distance (μm)

contacts for the generated architecture correspond well to experimental measurements.

Combined with an advanced visualization system, the anatomical model could be used to demonstrate many interesting properties of spinal architecture. For example, for each neuron we can find and visualize all incoming connections. Identification of incoming connections is crucial for the development of a model of electrical activity and the study of the functionality of this neural architecture.

The spinal cord reconstruction provides information about longitudinal and dorsoventral positions of each neuron, allocation of its dendritic field, coordinates of its axon, and all afferent and efferent synaptic connections. This, the complete anatomical description of neural architecture of the spinal cord is achieved. Due to stochasticity in the model of axon growth, the neural architecture is not unique and starting from different initial states of the random number generator we can generate a number of anatomical circuits of the spinal cord. All these architectures will be similar in the sense that they have the same statistical characteristics as experimental measurements.

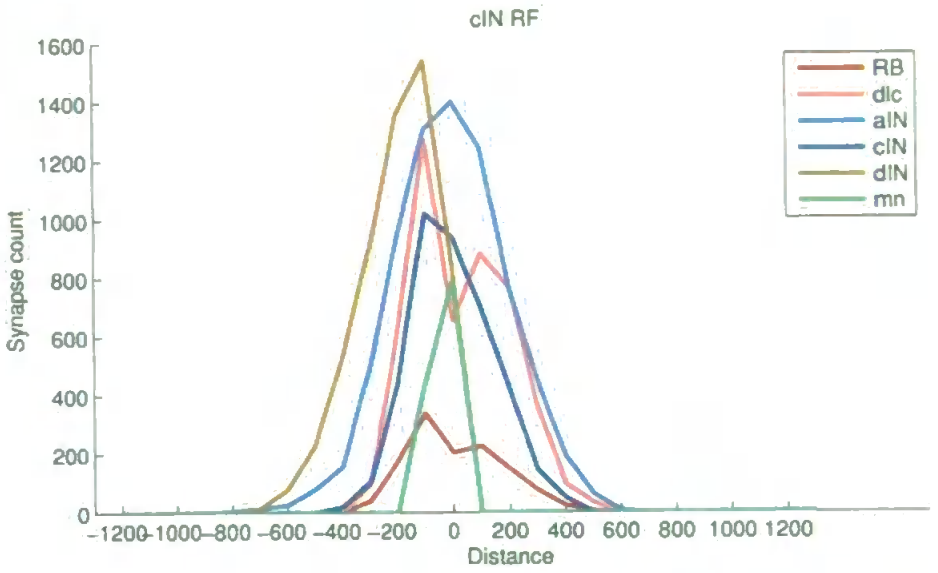

Figure 7.10: Variation of inputs to cIN cells with distance (μm)

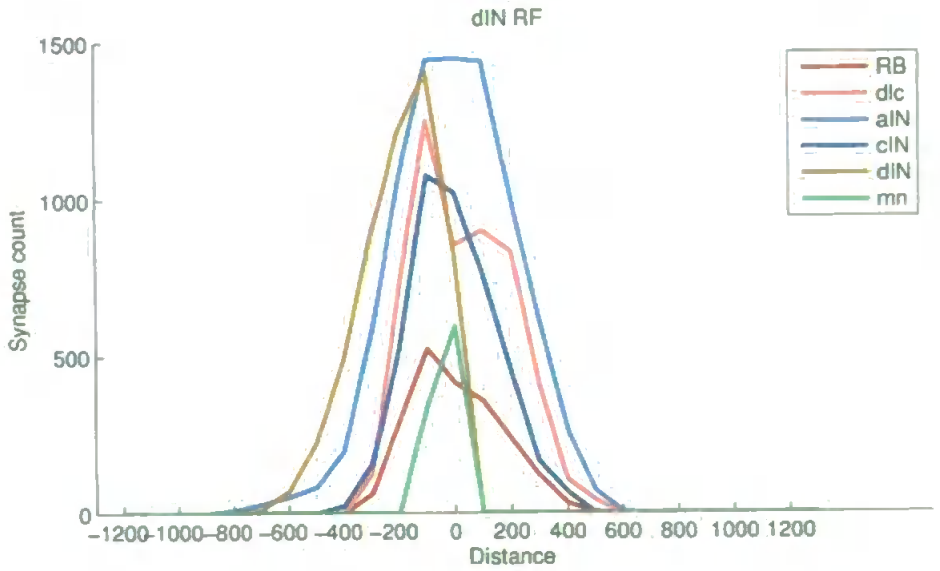

Figure 7.11: Variation of inputs to dIN cells with distance (μm)

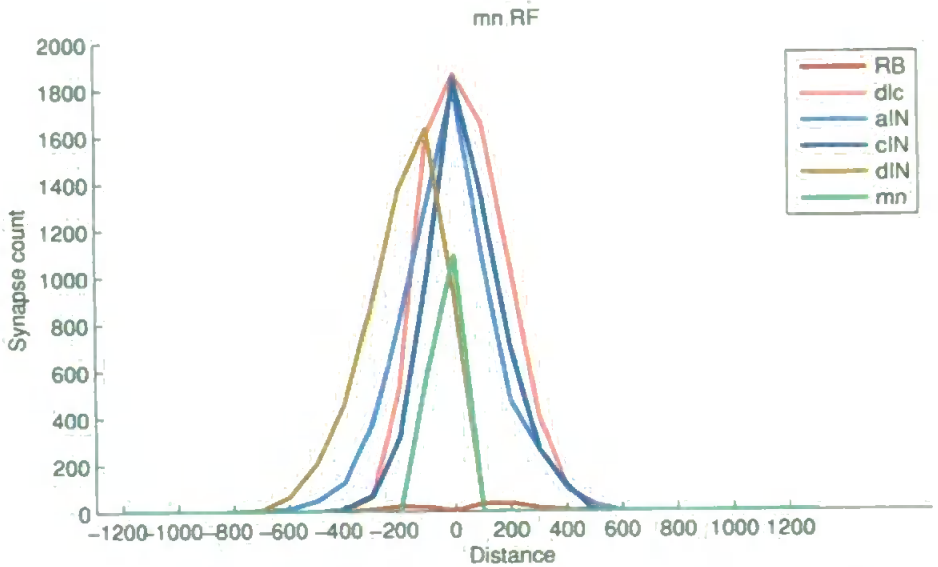

Figure 7.12: Variation of inputs to mn cells with distance (μm)

Chapter 8

Electrophysiological modelling of tadpole swimming

8.1 Introduction

In the previous chapter we showed how a complete model of the neural architecture of the tadpole spinal cord can be generated using simple developmental rules. Now we will go on to demonstrate that this architecture can generate a pattern of activity corresponding to the swimming pattern observed in the tadpole. We construct an electrophysiological model of action potential generation for each neuron and connect these model elements together according to the generated neural architecture. Our aim is only to demonstrate that the generated architecture can potentially reproduce the swimming pattern, and we do not attempt to model more sophisticated behaviours such as the initiation of swimming or transitions between swimming and struggling behaviours. For this purpose, it is sufficient to use a simple neural network model of the spinal cord, in which identical models of spiking elements are used for all neuron types and the anatomy of the left and right sides of the body is symmetrical.

The full electrophysiological model of the tadpole spinal cord includes 1680 neurons. In order to allow these simulations to take place in a reasonable time we ignore the details of known tadpole electrophysiology and use a simplified model

of the spiking element. Instead of the classical four-dimensional Hodgkin-Huxley model of spike generation we use the two-dimensional Morris-Lecar model. The parameters of this model have been chosen so that the elements exhibit the regime of postinhibitory rebound; along with recurrent excitation, this phenomenon has been demonstrated to be the basis of the pattern of activity observed in tadpole swimming (Roberts and Tunstall, 1990; Sautois et al., 2007). We therefore examine the possibility that coupling together model elements with this property will allow swimming-like activity to develop.

We begin from a consideration of two coupled Morris-Lecar neurons in the regime of postinhibitory rebound. This study provides the parameter range where the regime of postinhibitory rebound is stable. These parameters are then used in the full neural network to generate the pattern of swimming activity.

8.2 Model of two coupled Morris-Lecar neurons with postinhibitory rebound

We would like to base our swimming model on a neural model that captures important experimentally observed features of the dynamics of spike generation. However, the standard Hodgkin-Huxley model contains four differential equations of the first order and we would prefer to reduce the number of dimensions in order to make relatively simple phase-plane analysis of the system possible and reduce the amount of computation that must take place when simulations of the full model of the spinal cord are run.

In this section, we describe the Morris-Lecar model neuron and its derivation from the Hodgkin-Huxley model (as described in Gerstner and Kistler (2002)). We go on to show how this model can exhibit the phenomenon of postinhibitory rebound when its parameters are set to appropriate values. Finally we show how two cells of this type coupled together with inhibitory synapses can produce stable alternating firing. This result will form the basis of our full swimming model in the next section.

Let us state the Hodgkin-Huxley equations. Firstly we state that the membrane charging current Cdu/dt is equal to the applied current $I(t)$ minus the sum of different ionic currents $I_k(t)$ (Kirchoff's law):

$$C\frac{du}{dt} = -\sum_{k=1}^{4} I_k(t) + I(t). \tag{8.1}$$

Here $u(t)$ is the membrane voltage at time t, I_1 is the sodium ionic current, I_2 is the potassium ionic current, I_3 is the leakage current and I_4 is the synaptic current.

The next equation shows how the ionic currents depend on the reversal potentials E_{Na}, E_K, and E_L and their respective gating variables $m(t)$, $n(t)$, and $h(t)$ govern the dynamics of the ionic currents.

$$\sum_k I_k = g_{Na}m^3h(u - E_{Na}) + g_kn^4(u - E_K) + g_L(u - E_L) + I_{syn}. \tag{8.2}$$

The gating variables evolve according to the following differential equations:

$$\begin{aligned} \dot{m} &= \alpha_m(u)(1 - m) - \beta_m(u)m \\ \dot{n} &= \alpha_n(u)(1 - n) - \beta_n(u)n \\ \dot{h} &= \alpha_h(u)(1 - h) - \beta_h(u)h. \end{aligned} \tag{8.3}$$

Where $\alpha_m(u)$, $\alpha_n(u)$, $\alpha_h(u)$, $\beta_m(u)$, $\beta_n(u)$, and $\beta_h(u)$ are functions which control the dynamics of the gating variables. Hodgkin and Huxley determined the functions α and β from data recorded from the giant axon of the squid (Hodgkin and Huxley, 1952). These functions are given below:

$$\begin{aligned} \alpha_n(u) &= (0.1 - 0.01u)/[\exp(1 - 0.1u) - 1] \\ \alpha_m(u) &= (2.5 - 0.1u)/[\exp(2.5 - 0.1u) - 1] \\ \alpha_h(u) &= 0.07\ \exp(-u/20) \end{aligned} \tag{8.4}$$

$$\begin{aligned} \beta_n(u) &= 0.125\exp(-u/80) \\ \beta_m(u) &= 4\exp(-u/18) \\ \beta_h(u) &= 1/[\exp(3-0.1u)+1] \end{aligned} \tag{8.5}$$

The parameter values are as follows: $E_{Na} = 115, E_K = -12, E_L = 10.6, g_{Na} = 120, g_K = 36, g_L = 0.3$.

We have a system of four variables: u, m, n, and h. In order to better understand the dynamics of this system, we can write the equations for $\dot{n}$, $\dot{m}$, and $\dot{h}$ in terms of time constants $\tau_n(u)$, $\tau_m(u)$, $\tau_h(u)$. All these equations have the same form, which we give using $m(t)$ as an example:

$$\dot{m} = -\frac{1}{\tau_m(u)}[m - m_0(u)]. \tag{8.6}$$

Here:

$$\tau_m(u) = [\alpha_m(u) + \beta_m(u)]^{-1} \tag{8.7}$$

$$m_0(u) = \alpha_m(u) \cdot \tau_m(u) \tag{8.8}$$

The following plot shows how the constants τ depend on u.

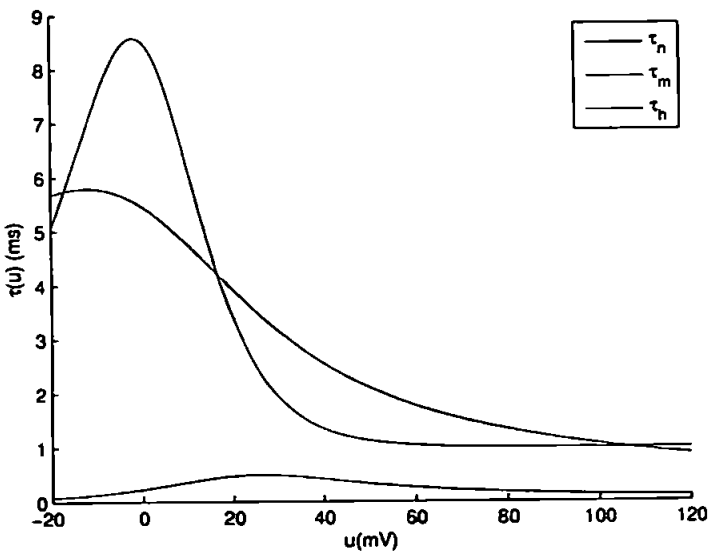

Figure 8.1: Dependency of gating variable time constants on u

It is apparent from Fig. 8.1 that the function which describes the time course for m is much smaller than the respective functions for n and h. Therefore the dynamics of $m(t)$ is much faster. We might therefore consider $m(t)$ to almost instantaneously approach the steady-state value of m_0. The next plot shows the difference between m and m_0 during action potential generation:

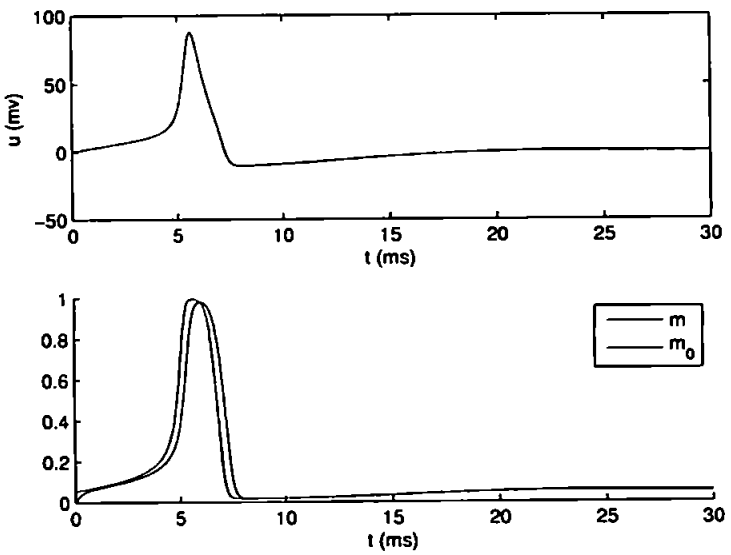

Figure 8.2: The gating variable of the sodium channel $m(t)$ closely follows m_0 with a small time lag

As we can see, $m(t)$ closely follows m_0 relative to the time scale of action potential generation. This supports our contention that we can reasonably assume $m(t)$ to be instantaneous. In addition, notice that the time courses for $n(t)$ and $h(t)$ are reasonably close to each other, and this motivates the idea of combining these two factors into a single slow variable. These two ideas form the basis for the reduction of the Hodgkin-Huxley equations to a two-dimensional system.

8.2.1 The Morris-Lecar equations

The Morris-Lecar equations (Morris and Lecar, 1981) describe dynamics of voltage $V(t)$ and the activation variable $w(t)$. The equation for voltage is similar to the Hodgkin-Huxley model and incorporates a delayed-rectifier potassium current similar to the Hodgkin-Huxley model and a fast non-inactivating Ca^{2+} current which

is similar to the sodium current in the H-H model. The activation of the calcium current is so fast that in the model it is instantaneous. The Morris-Lecar model equations are:

$$C\frac{\mathrm{d}V}{\mathrm{d}t} = -(\bar{g}_{Ca}m_\infty(V)(V - V_{Ca}) + \bar{g}_K w(V - V_K) + \bar{g}_L(V - V_L)) + I_{app} + I_{syn}, \quad (8.9)$$

$$\frac{\mathrm{d}w}{\mathrm{d}t} = \phi[w_\infty(V) - w]/\tau_w(V). \quad (8.10)$$

where:

$$m_\infty(V) = .5(1 + \tanh((V - E_1)/E_2)) \quad (8.11)$$

$$w_\infty(V) = .5(1 + \tanh((V - E_3)/E_4)) \quad (8.12)$$

$$\tau_w(V) = 1/\cosh((V - E_3)/(2E_4)) \quad (8.13)$$

Parameters: $E_1 = -1.2$, $E_2 = 18$, $E_3 = 2$, $E_4 = 30$, $\phi = .04$, $C = 20$, $\bar{g}_{Ca} = 4$, $V_{Ca} = 120$, $\bar{g}_K = 8$, $V_K = -84$, $\bar{g}_L = 2$, $V_L = -60$. Function I_{app} describes applied external current and function I_{syn} describes synaptic input from other neurons.

Figure 8.3 shows the nullclines of this system with $I_{app} = 70$, $I_{syn} = 0$. The green curve shows the nullcline of the voltage variable ($\dot{V}(t) = 0$). The blue curve shows the nullcline of the activation variable ($\dot{w}(t) = 0$). There is only one fixed point where these nullclines meet, and this fixed point is stable. Figure 8.4 shows the effect of a small perturbation of V from this fixed point: perturbation decays with time and the trajectory (red curve) immediately returns back to the vicinity of the stable steady state. The effect of a larger perturbation of V from this fixed point is shown in figure 8.5: a larger perturbation results in more complex behaviour where the trajectory (red curve) makes a long excursion before returning to the vicinity of the fixed point. This shows how the Morris-Lecar equations are able to model action potential generation.

When the current I_{app} is increased, an Andronov-Hopf bifurcation occurs, the

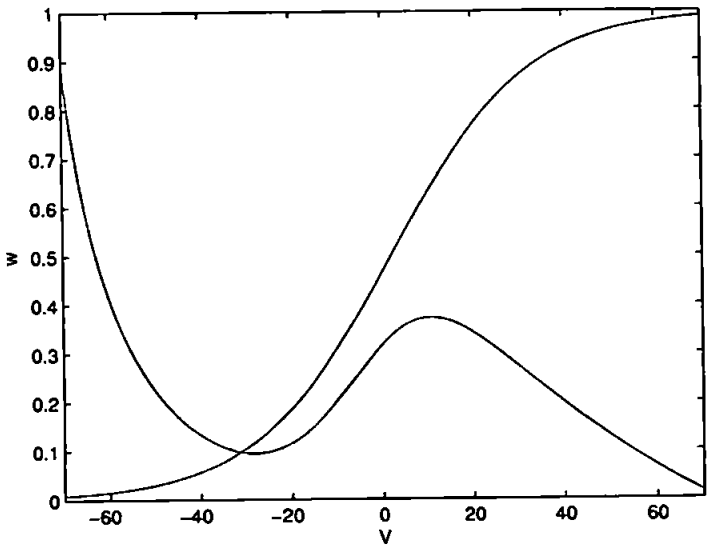

Figure 8.3: Nullclines of Morris-Lecar equations with $I_{app} = 70$, $I_{syn} = 0$. Green curve shows nullcline of voltage, blue curve shows nullcline of activation variable.

fixed point loses stability and a stable limit cycle is established, this produces regular, repetitive firing in the model neuron. The limit cycle is small for values of I_{app} close to the bifurcation. Figure 8.7 shows the limit cycle for $I_{app} = 120$.

8.2.2 Postinhibitory rebound in the Morris-Lecar model

The basic mechanism of postinhibitory rebound in the Morris-Lecar model (Wang and Rinzel, 1992; Borisyuk and Rinzel, 2005) is illustrated in figure 8.8. The model neuron is subjected to a tonic current of 80 μA/cm^2. With this input, the model has a stable fixed point located at the intersection of the two solid lines. Now we subject the neuron to an additional input current of -80 μA/cm^2 for a few milliseconds, so the total input is 0. The isocline for w is unchanged, but the isocline for V moves down, and the model transitions to the new stable fixed point. Now the inhibitory current is switched off and the net input is once again 80 μA/cm^2. In order to get back to the fixed point, the system must make a long excursion using the right branch of the V isocline, generating an action potential.

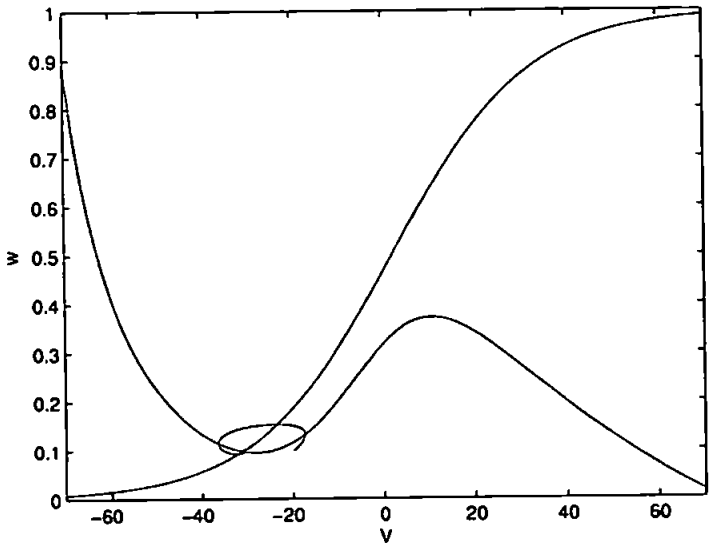

Figure 8.4: Effect of a small perturbation of V from fixed point. Green curve shows nullcline of voltage, blue curve shows nullcline of activation variable, red curve shows trajectory.

8.2.3 Two coupled inhibitory cells with postinhibitory rebound

We showed above how an inhibitory pulse can cause postinhibitory rebound in a Morris-Lecar cell. We will now consider that this inhibitory pulse could occur due to a synaptic input from another cell. In this case, two identical or similar cells that inhibit each other should be able to maintain a sustained alternating firing pattern.

In order to describe the synaptic connection from one neuron to another, we consider the variable $s(t)$ which describes the dynamics of synaptic coupling. The following equation (Ermentrout, 2003) describes the time course of this variable:

$$\frac{\mathrm{d}s}{\mathrm{d}t} = \alpha k(V)(1-s) - \beta s. \tag{8.14}$$

Where V is the potential of the presynaptic cell, $k(V)$ is a sigmoid function: $k(V) = 1/[1+exp(-(V-V_T)/V_S)]$ (figure 8.9). Parameter values: $\alpha = 1$, $\beta = 0.25$, $V_T = 20$, $V_S = 2$.

Figure 8.10 shows V vs time and s vs time in the regime of repetitive firing of

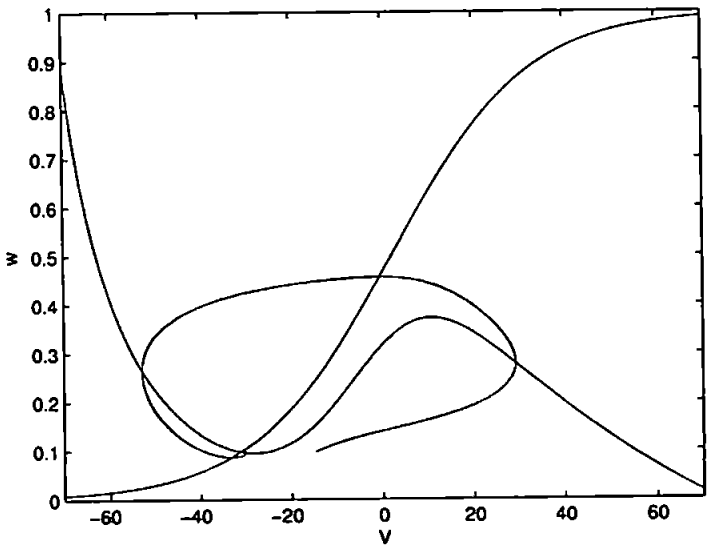

Figure 8.5: Effect of a larger perturbation of V from fixed point. Green curve shows nullcline of voltage, blue curve shows nullcline of activation variable, red curve shows trajectory

the presynaptic cell. From this figure we can see that $s(t)$ is significantly different from zero only during a short period of time where the potential of the presynaptic cell is sufficiently large.

We use the synaptic current I_{syn} in equation 8.9 to describe synaptic connectivity. The formula for this current in the case of inhibitory connections is:

$$I_{syn} = g_{inh}s(t)(V(t) - V_{inh}), \tag{8.15}$$

where reversal potential $V_{inh} = -46$ and synaptic conductance $g_{inh} = 10$.

We now change parameter V_L to take the value -50 as opposed to its previous value of -60. This increases the value of V at the fixed point, and so postinhibitory rebound can be achieved more easily (Borisyuk and Rinzel, 2005).

The equations for the dynamics of two coupled cells are:

$$C\frac{dV_1}{dt} = -(\bar{g}_{Ca}m_\infty(V_1)(V_1-\bar{V}_{Ca})+\bar{g}_K w_1(V_1-\bar{V}_K)+\bar{g}_L(V_1-\bar{V}_L)+I_{syn1}+I_{app}), \tag{8.16}$$

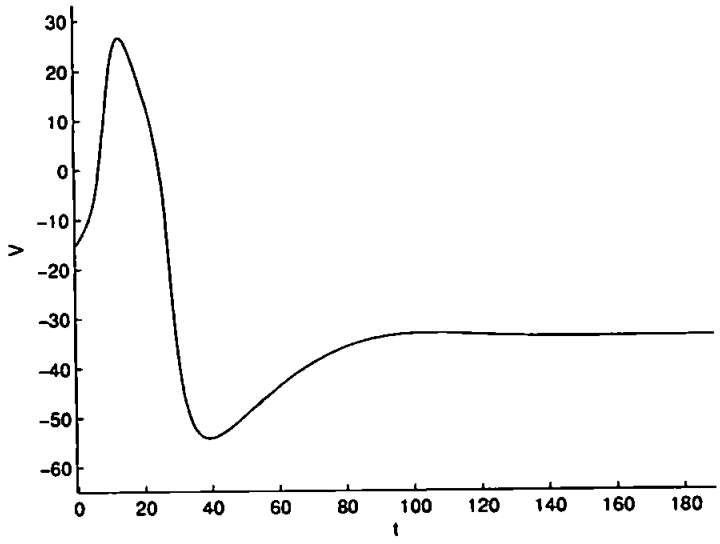

Figure 8.6: Action potential generation in the Morris-Lecar model.

$$\frac{dw_1}{dt} = \phi[w_\infty(V_1) - w_1]/\tau_w(V_1), \tag{8.17}$$

$$\frac{ds_1}{dt} = \alpha k(V_1)(1 - s_1) - \beta s_1, \tag{8.18}$$

$$C\frac{dV_2}{dt} = -(\bar{g}_{Ca} m_\infty(V_2)(V_2 - \bar{V}_{Ca}) + \bar{g}_K w_2(V_2 - \bar{V}_K) + \bar{g}_L(V_2 - \bar{V}_L) + I_{syn2} + I_{app}), \tag{8.19}$$

$$\frac{dw_2}{dt} = \phi[w_\infty(V_2) - w_2]/\tau_w(V_2), \tag{8.20}$$

$$\frac{ds_2}{dt} = \alpha k(V_2)(1 - s_2) - \beta s_2, \tag{8.21}$$

$$I_{syn1} = g_{inh} s_2 (V_1 - V_{inh}),$$

$$I_{syn2} = g_{inh} s_1 (V_2 - V_{inh}),$$

where variables $V_1(t)$, $w_1(t)$, $s_1(t)$, $V_2(t)$, $w_2(t)$, $s_2(t)$ describe activity and synaptic connections for the first and the second cells. The meanings of parameters have been described above.

The activity in this system is shown in figure 8.11. We can see that the postinhibitory rebound produces alternating firing between the two cells. The initial conditions are chosen so that one of the two cells produces an action potential at the

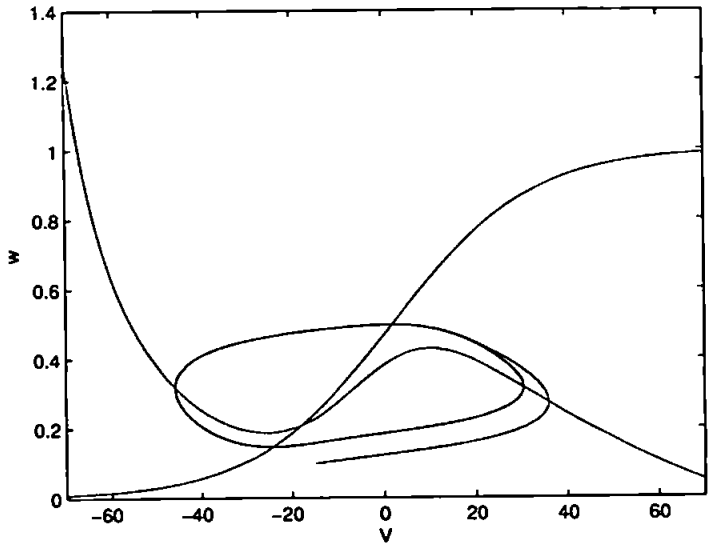

Figure 8.7: Repetitive firing in the Morris-Lecar model.

start of the simulation.

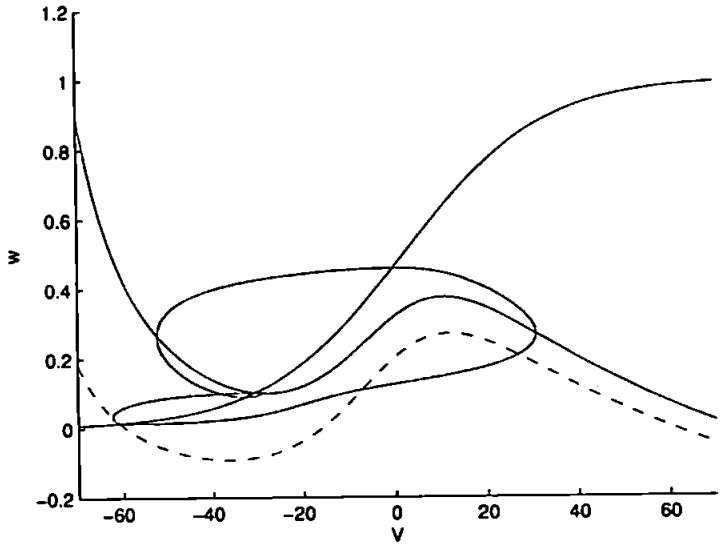

Figure 8.8: Postinhibitory rebound in Morris-Lecar model.

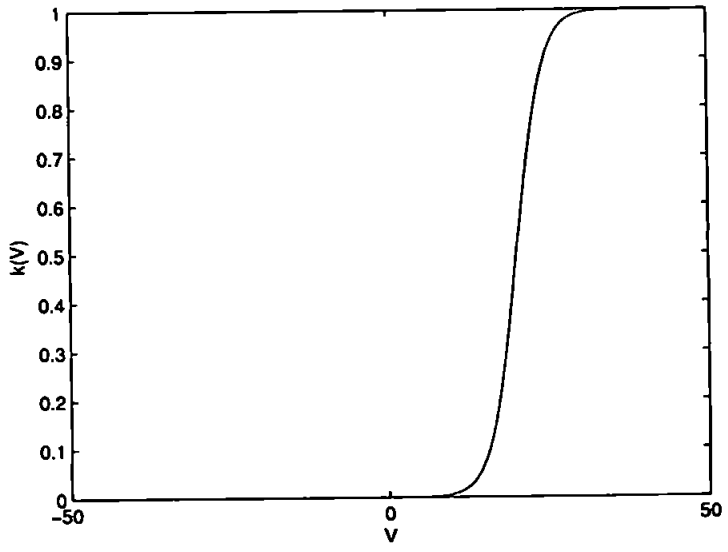

Figure 8.9: Relationship between voltage V and threshold function $k(V)$.

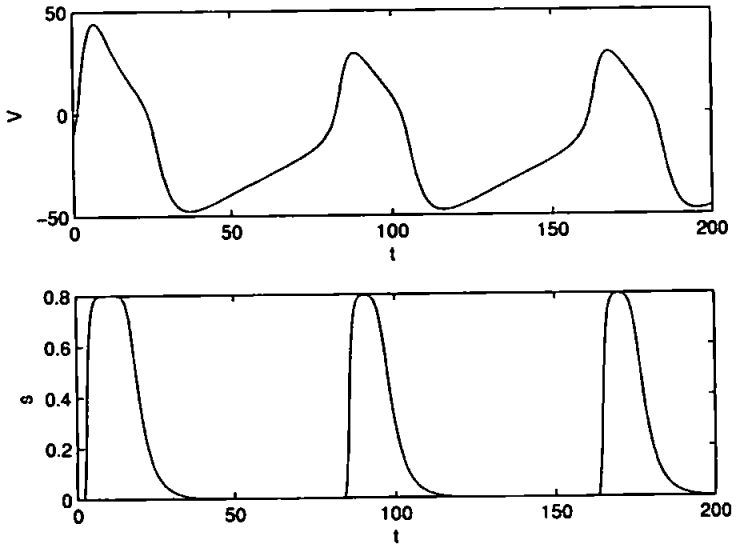

Figure 8.10: Relationship between presynaptic voltage V and synaptic connection function s.

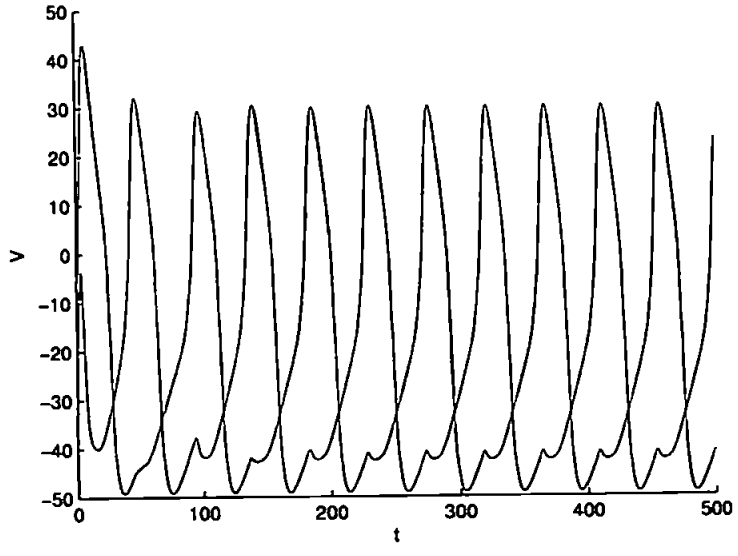

Figure 8.11: Voltage vs time for two M-L cells coupled with inhibitory synapses.

8.3 Full electrophysiological model of tadpole spinal cord

8.3.1 Model description

The full neural network model of the spinal cord includes neurons of 6 different types relevant to swimming as described in the previous chapter. These neurons are arranged in two sub-networks relating to the left and right sides of the body. The electrophysiological properties of each neuron are described by the two-dimensional Morris-Lecar equations. To study the neural activity related to the swimming pattern we only need to consider cIN and dIN cells because all other cell types are either related to sensory input (RBs), initiation of swimming (dlcs), motor output (mns), or struggling (aINs). While aIN cells do fire in the swimming pattern, evidence suggests that they are more important for the generation of the struggling behavior (Green and Soffe, 1998). This subnetwork of cIN and dIN cells generates the pattern of neural activity related to swimming: antiphase oscillations between the left and right sides of the spinal cord and a metachronal wave of activity along the body from head to tail.

We use the Morris-Lecar equations to model the spike generation process for each element of the neural network. The equations for the dynamics of the voltage $V_i(t)$ and the activation variable $w_i(t)$ are the same as equations 8.16 and 8.17, but the synaptic current now includes both excitatory and inhibitory synaptic couplings (equation 8.22). The equations are:

$$C\frac{\mathrm{d}V_i}{\mathrm{d}t} = (-\bar{g}_{Ca}m_\infty(V_1)(V_1-\bar{V}_{Ca})+\bar{g}_K w_1(V_1-\bar{V}_K)+\bar{g}_L(V_1-\bar{V}_L)+I_{syn}+I_{app}), \quad (8.22)$$

$$\frac{\mathrm{d}w_i}{\mathrm{d}t} = \phi[w_\infty(V) - w_i]/\tau_w(V). \quad (8.23)$$

The meanings of the variables and parameters have been explained in the previous section and all parameter values relating to model elements (but not to connections) are the same as in this previous case, with the exception that now $I_{app} = 74$ for all

cells. To simplify the model we suppose that all neurons are identical and have the same parameter values.

We first use the spinal cord reconstruction procedure to generate the left side of the spinal cord. An exact copy of this is then created to represent the anatomy of the right side of the spinal cord. To bridge together the two sides of the spinal cord we use the following procedure for each cIN and dlc cell: for some neuron with index i we remove the existing ipsilateral connection to neuron j, and generate a contralateral connection to the complement of neuron j on the opposite side of the body. Because connections from all cell types except cIN and dlc are ipsilateral and symmetrical no modifications are necessary in this case.

The term I_{syn} in equation 8.22 describes synaptic currents resulting from all incoming connections to some particular neuron. In the subnet of cIN and dIN neurons we consider excitatory connections from dIN cells and inhibitory connections from cIN cells. The total synaptic input to a cell i is described by the following formula:

$$I_{syn} = g_{inh_i}(V - V_{inh}) + g_{exct_i}(V - V_{exct}). \tag{8.24}$$

$$g_{inh_i} = \bar{g}_{inh} \sum_{j \in IS(i)} s_j(t) \tag{8.25}$$

$$g_{exct_i} = \bar{g}_{exct} \sum_{j \in ES(i)} s_j(t) \tag{8.26}$$

Where $ES(i)$ is the set of all cell indexes of excitatory cells that make synapses onto cell i, $IS(i)$ is the set of indexes of inhibitory cells that make synapses onto cell i, and the reversal potentials for excitatory and inhibitory synapses are $V_{exct} = 0$ and $V_{inh} = -46$ respectively. These sets are derived from the anatomical reconstruction.

Maximal synaptic conductances for inhibitory and excitatory connections are $\bar{g}_{inh} = 0.5$ and $\bar{g}_{exct} = 0.2$ respectively. The variable $s_j(t)$ describes the dynamics of synaptic connections from cell j to other cells. The equation which governs the

dynamics of $s(j)$ is the following:

$$\frac{ds_j}{dt} = \alpha k(V_j)(1 - s_j) - \beta s_j. \tag{8.27}$$

Where V_j is the potential of the presynaptic cell j, parameter $\alpha = 1$ is the same for all synapses, for all inhibitory synapses parameter $\beta = 0.25$ and for all excitatory synapses parameter $\beta = 0.5$. The sigmoid function $k(V)$ defines the dependence on voltage and is defined as $k(V) = 1/(1 + exp(-(V - V_T)/V_S))$, $V_T = 20$,$V_S = 2$.

This is a standard model for synaptic coupling as used in the previous section.

8.4 Simulation results

To simulate the model, we use the ODE solver $rk4$, which is the fourth-order Runge-Kutta solver included as part of the Numerical Recipes package (Press et al., 2002), using a constant time step of 1ms. We have checked the appropriateness of this time step by comparing simulation results with simulations that were carried out with 0.1ms and 0.01ms time steps; no significant differences were observed in a 600ms time interval.

Initial conditions for all cells i are as follows: $w_i(0) = 0.125$, $s_i(0) = 0$, and $V_i(0) = -26 + \xi$, $i = 1, \ldots, 1680$ where ξ is a uniformly distributed random number in the interval $(0, 1)$; this is added to break the symmetry.

For the first 50ms of the simulation, the most rostral 100 cells in the left side of the spinal cord are excited by an increase of applied current; they receive an input $I_{app} = 100$ μA/cm^2. All other cells receive the same input of 74 μA/cm^2 for the entire duration of the simulation. The cIN cells within this excited population fire and provide an inhibitory input to cells of all types on the right side of the spinal cord. The cIN cells on the left side then generate spikes due to postinhibitory rebound. In this case the population of stimulated cells includes all cell types, however we have also confirmed that it is sufficient to excite only cIN cells in a

similar manner.

It is known (Sautois et al., 2007) that dIN cells can also fire spikes on postinhibitory rebound and it has been proposed that this property may have an active role in rhythm generation: neurons depolarized by synaptic excitation can fire on rebound after reciprocal inhibition from neurons on the opposite side of the spinal cord (Roberts and Tunstall, 1990). In the case of our simulations we use a tonic current to simulate the effect of slow excitatory synaptic input that would normally be needed to move neurons in this network into the regime of postinhibitory rebound, however the dIN cells still have a role which is to quickly propagate the initial wave down the spinal cord; this is enabled by their relatively long axons. If synaptic input from dINs is removed from our simulations, several cycles are required before the wave reaches the caudal part of the network.

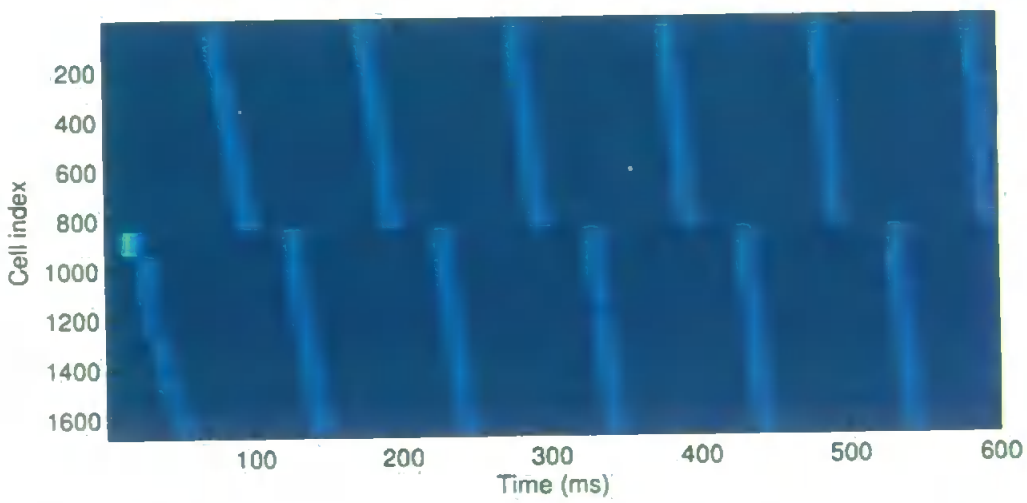

Figure 8.12: Raster plot of voltage in 1680 neurons comprising a model of 1.9mm of tadpole spinal cord. Cell indices 1-840 are assigned to the right side of the spinal cord, cell indices 841-1680 represent the left side. In both cases the index represents the rostrocaudal position of the cell.

Results from this model clearly demonstrate that the model is able to produce a swimming pattern, as shown in figure 8.12. This figure shows a raster plot type visualization of spiking activity of the full model of the spinal cord. Cell indices 1-840 comprise the right side (upper half of plot), cell indices 841-1680 comprise the left

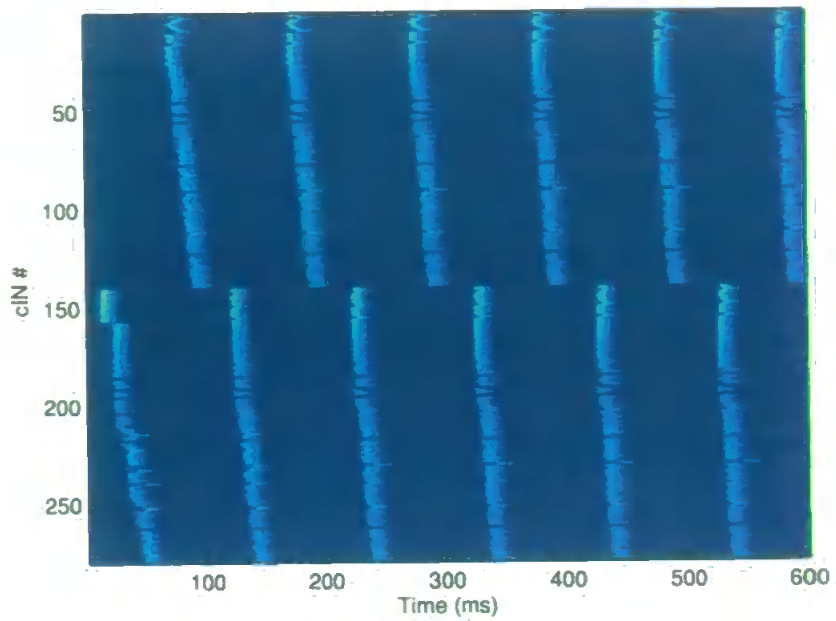

Figure 8.13: Raster plot of voltage in cIN neurons only.

side (lower half of plot). Within one side, the cell index corresponds to rostrocaudal position. Cell types are pseudorandomly distributed within these populations as described in the previous chapter. Brighter parts of the image correspond to higher voltage. Thus the spiking activity on one side of the spinal cord appears as a slightly skewed line of bright pixels with the skew indicating the rostrocaudal delay from head to tail. A bright spot is visible at the beginning of the lower half of the plot, this shows the 50ms of excitatory input applied on the left side of the spinal cord in order to initiate swimming.

The two main features of the swimming pattern, alternation between the two sides and a rostrocaudal metachronal wave are clearly visible. There is no overlap in activity between the left and right sides, and this is consistent with observations of tadpole spinal cord (Kahn and Roberts, 1982). Moreover, the period is approximately 100ms and the delay between the head and tail is roughly 20ms; these figures are consistent with experimental observations (Kahn and Roberts, 1982).

Because this figure shows all cell types together it is not possible to distinguish

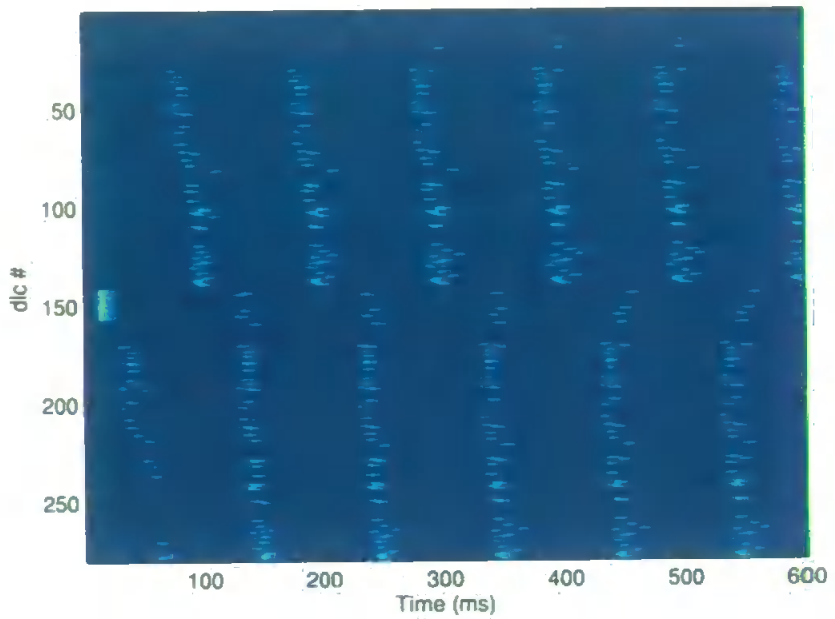

Figure 8.14: Raster plot of voltage in dlc neurons only.

the different dynamics of different cell types. Figures 8.13 to 8.17 show activity of each cell type separately (excepting the skin sensory RB cells which do not receive synaptic input). Each of these plots shows the spiking activity of 280 cells of a particular type. For example, figure 8.13 shows the spiking activity of the cIN neurons. Along the vertical axis, we show the numbers of cIN cells (from 1-140 for the right side and 141-280 for the left side). This numbering of cIN cells reflects the order of the cells according to rostrocaudal position - lower numbers are more rostral. As the level of brightness corresponds to activity, dark horizontal lines on the plot represent inactive cIN cells.

Figure 8.14 shows the pattern of activity in only the dlc cells. It can be seen that many dlc cells do not fire at all, and some of them have an irregular pattern of activity. This is due to the fact that dlc cells typically receive only very weak input from cIN and dIN cells (as seen in the previous chapter) which is often not sufficient for the generation of a spike. This is consistent with the fact that dlc cells are more important for the initiation of swimming than for the maintenance of the swimming

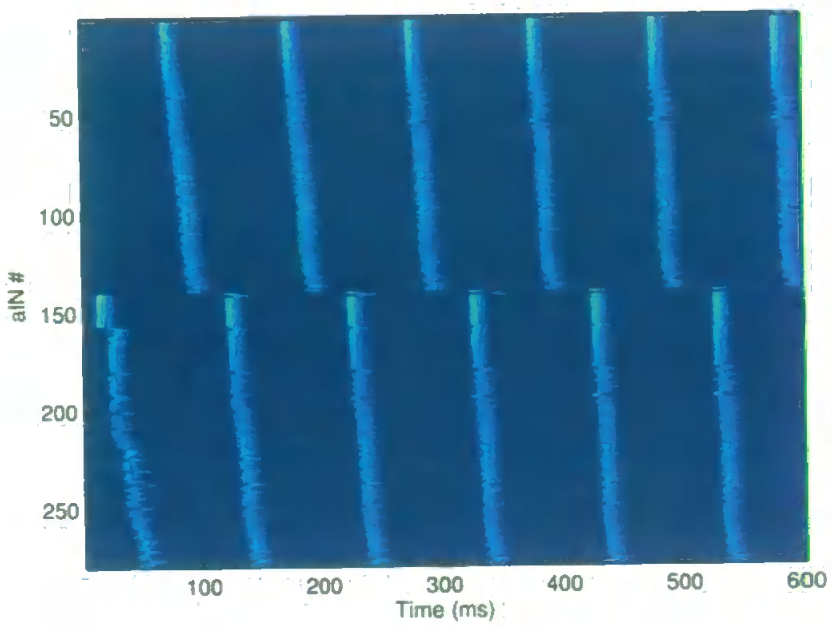

Figure 8.15: Raster plot of voltage in aIN neurons only.

pattern itself.

In contrast the activity in aIN cells following the initial propagation of activity from head to tail is much more reliable and regular. The activities of cIN, dIN, and mn cells are similar, with the mn cells being particularly consistent.

The raster-like plots do not make the distinction between subthreshold dynamics of membrane potential and spiking activity clear and so we also show example plots of voltage against time for four different cases (figs 8.18 - 8.21).

Figure 8.18 shows the spiking activity of a cIN cell located in the middle of the rostrocaudal axis, together with the activity of its complement on the contralateral side. The left-right alternation of this activity can be clearly seen. Figure 8.19 shows the same situation for two complementary dIN cells in approximately the same position.

Figure 8.20 shows the spiking activity in the most rostral and most caudal cIN cells in the right half of the spinal cord. The same case for dIN cells is shown in figure 8.21. In both these cases the rostrocaudal delay is clearly visible.

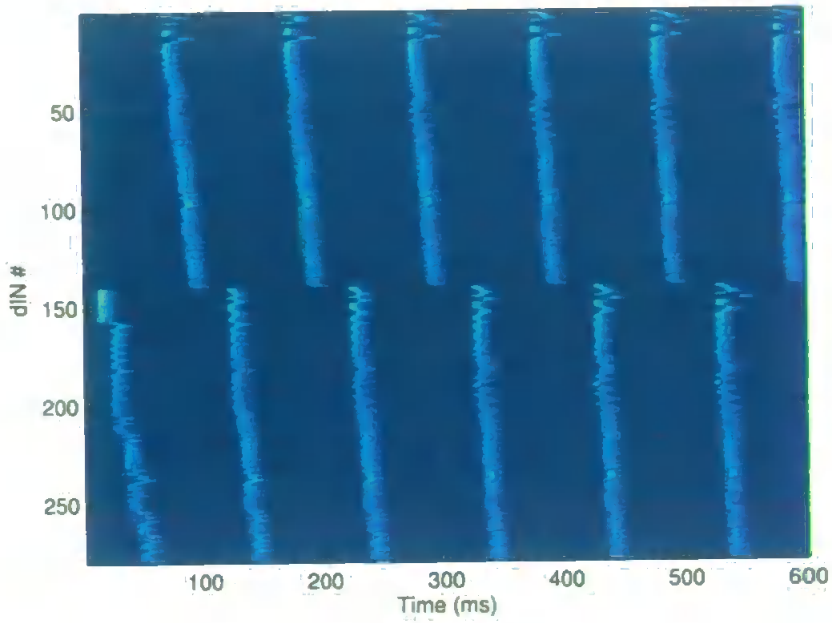

Figure 8.16: Raster plot of voltage in dIN neurons only.

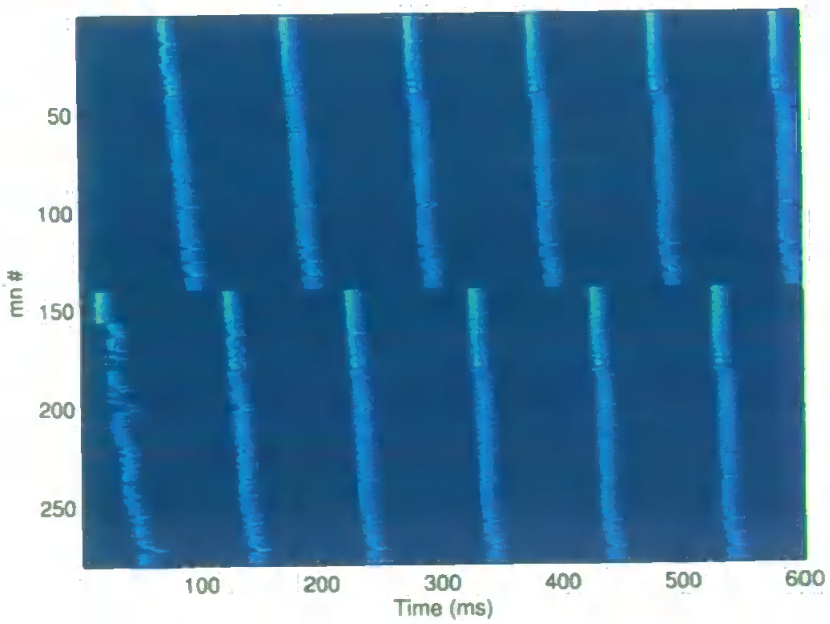

Figure 8.17: Raster plot of voltage in mn neurons only.

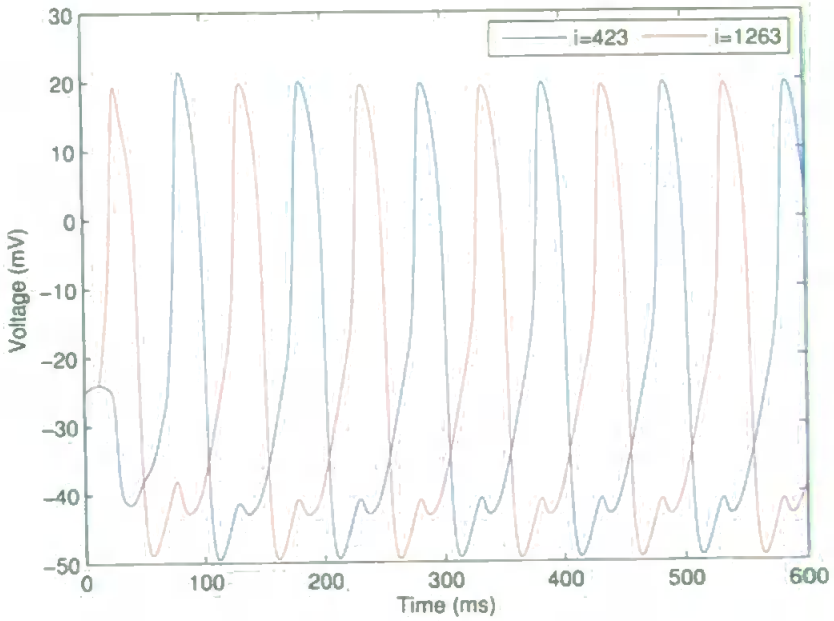

Figure 8.18: Voltage in a cIN cell and its matching cell on the other side of the spinal cord. These cells are located in the middle of the rostrocaudal axis.

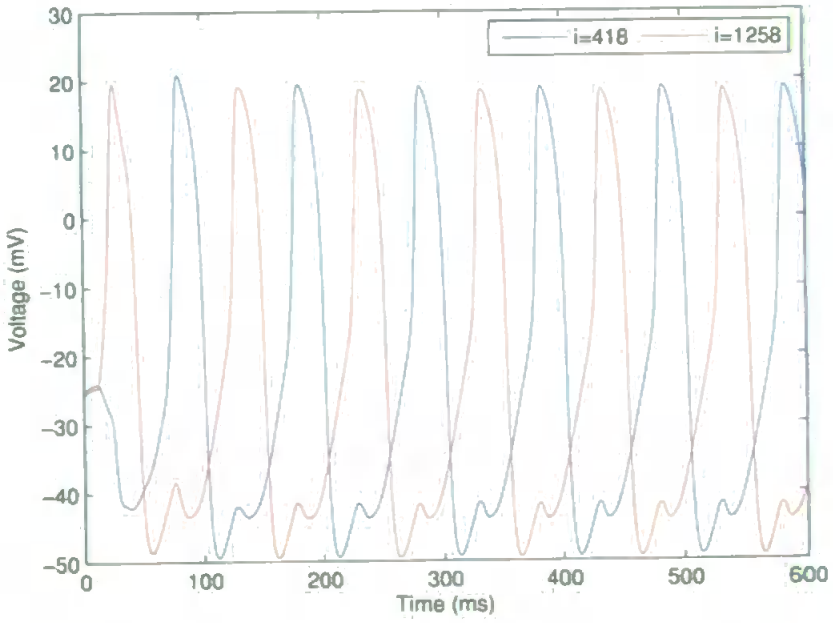

Figure 8.19: Voltage in a dIN cell and its matching cell on the other side of the spinal cord. These cells are located in the middle of the rostrocaudal axis.

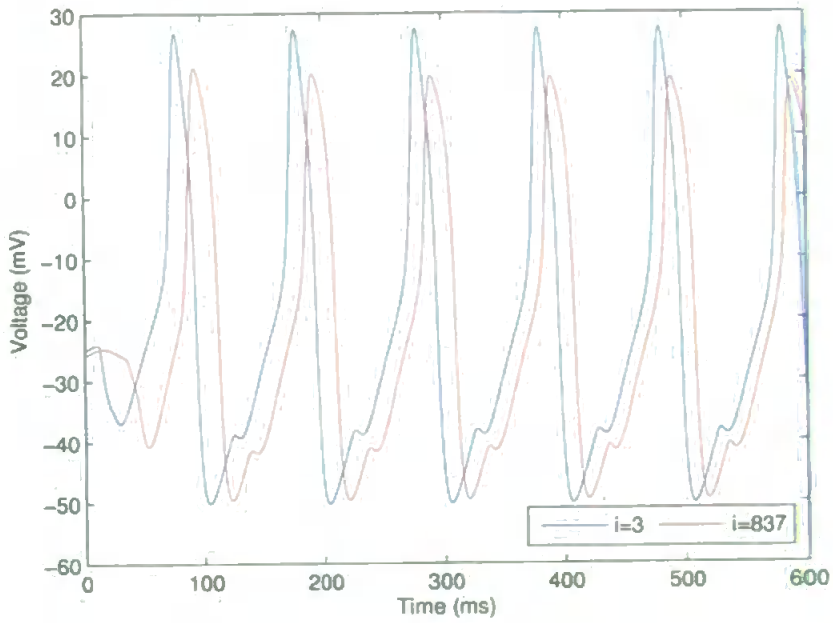

Figure 8.20: Voltage in a rostral cIN cell (blue) and a caudal cIN cell (red). The caudal cell lags the rostral cell.

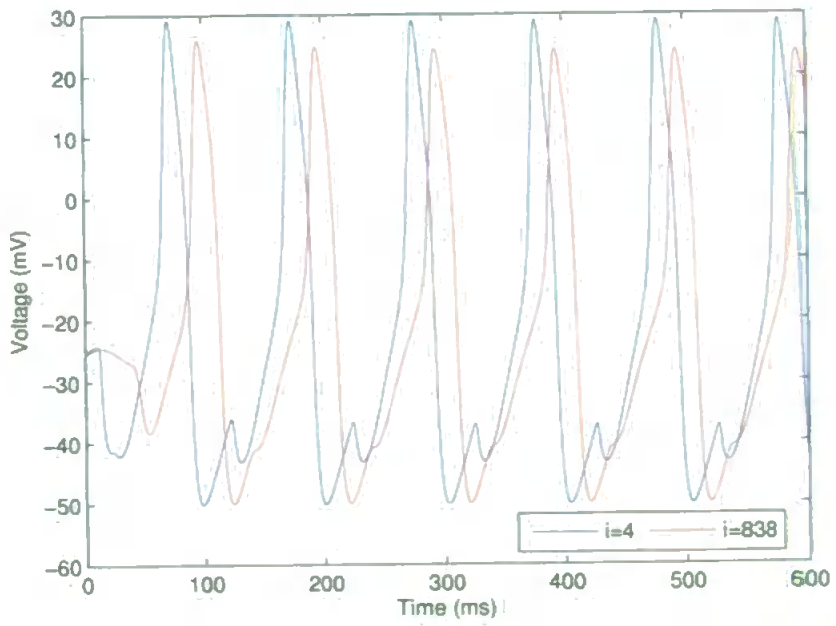

Figure 8.21: Voltage in a rostral dIN cell (blue) and a caudal dIN cell (red). The caudal cell lags the rostral cell.

8.5 Discussion

We have demonstrated that simple developmental rules suggested by anatomical data taken from the tadpole spinal cord can generate a neural network capable of generating a pattern of activity corresponding to the tadpole swimming pattern. The most important features of the pattern, left-right alternation and a metachronal wave travelling from head to tail are present, and the frequency of the pattern and rostrocaudal delay take values within the normal range of experimental observations.

The most obvious improvement to the model would be to make synapses from all six cell types functional. While dINs and cINs are sufficient for the maintenance of the swimming pattern, adding functional aINs would make it possible to investigate the struggling pattern, and adding RB and dlc cells would make it possible to investigate the initiation of swimming through skin stimulation. More detailed neural models tailored to the specific characteristics of each of the cell types (as discussed in (Sautois et al., 2007)) would almost certainly be needed to achieve useful results from such a model.

A smaller project would be to implement a rostrocaudal gradient in the probability of synapse formation as suggested in several papers (Tunstall and Roberts, 1991; Roberts and Tunstall, 1994; Tunstall and Roberts, 1994) and implemented in the model by Dale (Dale, 2003), and examine the effect of this gradient on the stability of the swimming pattern.

Chapter 9

Concluding remarks

9.1 Homeostatic neural activity

In the first part of the dissertation we mostly consider simple computational models of neural networks with local connections. These neural networks have the ability to adapt the parameters of neurons and/or connections according to specific rules. It is important to note that all these rules are formulated in such a way that they facilitate homeostatic total activity of the neural network. For example, a local rule for threshold adaptation is developed in such a way that the threshold becomes lower if local activity is low (to facilitate an increase in local activity), and higher if local activity is high. We consider this to be an important rule for regulation of the total activity which allows it to be contained within a specific range. It is well known in neuroscience that an excessively high activity level can result in epileptic seizure. Therefore, the learning rules which we consider in the first part of the dissertation are designed to prevent such pathological dynamical regimes of activity.

In a network of locally connected binary neurons with this form of threshold adaptation and local connections, we found that complex spatiotemporal patterns were exhibited by the network, including spiral and propagating waves. Although spiral waves are common in models of interactive FitzHugh-Nagumo elements (e.g. heart tissue model (Starmer et al., 1993)), it is difficult to get spiral waves in tra-

ditional computational neuroscience models such as the Wilson-Cowan or Amari models, and additional features have to be added to the model (Huang et al., 2004). Our finding shows that threshold adaptation is a suitable mechanism for the generation of spiral waves even in very simple neural networks.

In fact, in part one we consider two different rules for the regulation of homeostatic neural activity. The first rule is the threshold adaptation described above. The second is homeostatic synaptic plasticity, discussed in the next section. We combine these rules in a model of locally coupled elements. Simulation results demonstrate that simple learning rules can produce a rapid reorganization of connection strengths which leads to a sudden phase transition. It is remarkable that this phenomenon appears in a pure deterministic system without noise (the role of noise is considered below).

The most interesting dynamical behaviour has been found in a network with small-world type connections. This neural network consists of binary elements with adjustable synaptic connections (local connections on the torus with a few random long-range connections). The activity of this network alternates between UP and DOWN states, and these transitions are due to a hysteresis-type loop between activity and connectivity. We study this phenomenon on two levels of consideration: on the micro-level where we simulate a network of 2500 neurons with 20000 adjustable synaptic connections, and on the macro-level where we describe this phenomenon using only two variables - the average activity of the neural population and the average connection strength. There is a close correspondence between the results in both cases.

9.2 Homeostatic synaptic plasticity

The idea of homeostatic synaptic plasticity is the subject of intensive investigation. For example, in many papers from the Turrigiano laboratory, evidence is presented that scaling of synaptic strengths allows neural excitability to be regulated (Turri-

giano et al., 1998; Turrigiano, 1999).

In the models described in the thesis we consider an alternative perspective on homeostatic synaptic plasticity based on spike-timing dependent plasticity (STDP). In this formulation, synaptic homeostasis arises from the interaction between the learning rule as it operates at individual synapses and the dynamics of the network. This allows an interesting regime to appear where the total synaptic strength increases in low activity states and decreases in high activity states despite the fact that there is no explicit negative feedback in the model.

A hypothesis originally proposed by Tononi and Cirelli (2003), and recently supported by experimental evidence from Vyazovskiy et al. (2008) states that the specific dynamics of slow-wave sleep may lead to a generalized synaptic downscaling in the cortex. It is further proposed that the amount of slow-wave sleep may be driven by the total synaptic weight. This would represent an elegant system where spontaneous changes in neural dynamics during sleep driven by neural excitability would have a functional role in regulating this excitability.

Models like the one developed in the second part of chapter 4 allow the plausibility of such a mechanism to be assessed computationally.

9.3 Role of noise and stochastic processes in neural systems

Despite extensive experimental and theoretical research, the role of noise in neural systems is not yet well understood. For example, in vitro experiments show that stimuli with fluctuations resembling synaptic activity produced spike trains with timing reproducible to less than 1 millisecond (Mainen and Sejnowski, 1995). This suggests that there is a low intrinsic noise level in the process of spike generation. However, in-vivo experiments indicate that the spike train that is produced in neurons of the extrastriate visual cortex following stimulus presentation is highly stochastic (Shadlen and Newsome, 1994). Development of neural structures also demonstrates large variability in the resulting neural anatomy. For example, Li

et al. (2007) shows that synapse formation may not require chemically driven axons to recognize specific correct dendrites and detailed cellular recognition between spinal neuron types may not be necessary for the reliable formation of functional networks. How can a brain maintain stable behaviours when its underlying electrical and chemical structures are constantly changing?

We partly address this question in chapter 3 of the dissertation, considering a simple network model of binary elements with local connections and noise. We demonstrate that this neural network with a high level of stochasticity can demonstrate metastable states and phase transitions. Remarkably there is a critical level of noise which provides the greatest value of the variance of neural activity in the network, which corresponds to metastability. The dynamics of the neural activity has the interesting feature of being organized (in the sense that the neurons in the network display a high degree of synchronization) and yet highly stochastic (the times of phase changes are random). This interesting finding closely corresponds to some other similar results in physics and computational neuroscience, for example the coherence resonance phenomenon reported by Pikovsky and Kurths (1997).

In the second part of chapter 4 we study a neural network with noise and STDP type small-world connections. We discovered that interplay between stochasticity and deterministic behaviour (which is mostly governed by the dynamical variability of synaptic connection strengths) results in a very interesting dynamical phenomenon which can be described by a hysteresis-type behaviour between activity and connectivity. When the average synaptic connection strength is low, the influence of noise is relatively high. At intermediate levels of synaptic strength, the activity of the network becomes more ordered as the dynamics becomes dominated by highly potentiated synapses and this leads to a rapid increase in synaptic strengths due to positive feedback implicit in the STDP learning rule. When synaptic strengths are high, almost all the cells in the network are active simultaneously, the dynamics are almost completely deterministic, and this leads to a net decrease in synaptic

weights as in our model presynaptic firing must occur before postsynaptic firing if potentiation is to take place; simultaneous firing leads to a small synaptic depression.

As we have already discussed above, sleep is widely recognized to be important for consolidation of memory traces, and adjustment of synaptic strengths. There is also evidence that sleep is important in maintaining the capacity of the network to produce variable activity which is important for learning. For example, a recent paper (Derégnaucourt et al., 2005) shows that in the developmental learning of birdsong in zebra finches, the biggest improvements occur in the period of a few hours following sleep. These experiments show that neural song-replay may occur during sleep resulting in the adjustment of synaptic weights, creating the opportunity to reshape previously learned motor skills. It is likely that a similar phenomenon of synaptic strength adjustment has also been observed in experiments with hippocampal place cells in rats (Foster and Wilson, 2006). Experimental data show that sequential replay occurs in the rat hippocampus during awake periods immediately after spatial experience. This replay has a unique form in which episodes of spatial experience are replayed in a temporally reversed order which closely relates to reinforcement learning rules for adjustment of synaptic strengths.

9.4 Development of neural structures and their function

As discussed above, there are many sources of noise and stochasticity in neural systems. For example, in earlier phases of development of neurons, stochasticity plays an important role and in fact controls many intracellular and extracellular developmental processes (Kaern et al., 2005). The presence of stochasticity increases the complexity of neural systems and makes their functional behaviour more diverse, complex and controllable. In the second part of the dissertation, we model the development of the neural architecture of the spinal cord of the young frog tadpole. Although the development of the tadpole spinal cord includes a variety of stochastic processes governing the assembly of the neural architecture, this neural system

demonstrates extremely robust functional behaviour. In fact, the interplay between deterministic rules pre-wired in genetic instructions and stochastic processes of the growth of individual cells results in the neural circuit of the spinal cord controlling swimming.

Although there is a significant body of biological knowledge regarding the chemical cues and gradients that control the development of neuronal circuits (Dickson, 2002; Cline, 2003; Chilton, 2006; Schnorrer and Dickson, 2004; Wen and Zheng, 2006) many details of the biological mechanisms of axon growth are still unknown. The traditional approach to modelling axon growth is based on the idea that the growth cone follows different molecular gradients (Goodhill et al., 2004; Xu et al., 2005; Krottje and van Ooyen, 2007). For example, the mathematical model presented in a recent paper (O'Toole et al., 2008) takes into account forces at the growth cone, the viscoelastic properties of the axon, and the adhesions between the axon and surrounding substrate. These three factors define whether the axon elongates by tip growth or simply by stretching. In the second part of the dissertation we do not consider the details of growth cone navigation in steep and shallow chemical gradients. Instead, we build a simple mathematical model reflecting several key attraction and repulsion processes guiding axon development. Thus, our approach is to develop a mathematical model of axon growth which is as simple as possible and includes only a small number of parameters. The model allows fitting to all available experimental measurements of axons of tadpole spinal cord: all cell types in both ascending and descending directions.

The biochemical factors controlling the direction of axon growth are beginning to be revealed (de Anda et al., 2005; Shirasaki and Murakami, 2001; Lyuksyutova et al., 2003; Moon and Gomez, 2005; Charron et al., 2003; Gomez and Zheng, 2006) and we have included in the model several basic biological rules controlling both the dorso-ventral and longitudinal positions of the growing axon. For example, some axons start to grow ventrally and cross to the opposite side. After crossing,

these commissural axons are transformed and they then turn to grow longitudinally (Imondi and Kaprielian, 2001), either towards the head or the tail, or they branch to grow in both directions. Early patterns of growth by pioneer axons provide a basic scaffold of axon tracts that can be followed by later axons and in this way help to direct their growth (Wilson and Easter, 1991). Once the axons have grown to more or less the "right" area, they start to make synapses with the branched dendrites emerging from the cell bodies of other neurons.

Our study of axon growth is based on a new hypothesis: there are no specific targets in this system and the axon grows according to some general gradient following rules which guide it to a particular Dorso-Ventral (D-V) region of the spinal cord (Li et al., 2007). The growing axon runs along the spinal cord (without branching) and makes synapses directly onto dendrites that it passes with some probability. More precisely: if the growing axon meets a dendrite of some other neuron allocated in the same D-V part of the spinal cord, then there will be some probability that a synaptic contact will be made.

We have formulated and studied a simple mathematical model which is described by a nonlinear system of three difference equations and includes a stochastic process. Fitting the model to the statistical features of experimental axon measurements allows us to find optimal parameter values for each neuron type in the spinal architecture. Using these optimal parameters, we have generated a biologically realistic model of the tadpole spinal cord and demonstrated that this architecture can generate electrical activity corresponding to swimming.

To make the anatomical model more realistic, a future version could be developed without the current constraint that the reconstructed spinal cord is anatomically symmetrical. In addition, it would be very interesting to investigate the effect of modelling longitudinal gradients in synapse formation probability (Roberts and Tunstall, 1994; Tunstall and Roberts, 1994) on the longitudinal coordination of the swimming pattern. The current electrophysiological model of tadpole swimming

could be enhanced by using more detailed conductance-based modelling that would reproduce the known characteristics of the different neuron types more accurately.

It is hoped that in the future, a larger and more detailed data set will be collected that fully characterizes the typical anatomical morphology of individual cells, their axons and dendrites, as well as providing information about their longitudinal distributions. This would also cover cell types that are missing from the current data set: dIa, dINr and ecIN. The availability of such data would make it feasible to develop an anatomical model complete and accurate enough to enable the initiation of swimming and the selection between swimming and struggling behaviours to be modelled, along with more characteristics of the basic swimming pattern such as the gradual decrease of frequency within a swim and the different characteristics of the activity of rostrocaudal sections taken from different longitudinal positions.

Appendix A

Results of optimization and testing the optimization quality

A.1 Sensitivity to parameter variation

Following the optimization process, we tested the sensitivity of the optimal parameter values to small variations. We consider 3 levels of variation: 5%, 10% and 20% (accordingly, the fractions of variation are $Fr = 0.05$, $Fr = 0.1$; $Fr = 0.2$) and for each level, (e.g. 5%), we consider three cases for each of the four parameters: 1) the parameter value decreases (e.g. by 5%) ($ind = -1$); 2) the parameter value is not disturbed ($ind = 0$); 3) the parameter value increases (e.g. by 5%) ($ind = +1$). The following formulas show how we calculate new parameters for testing based on the optimal parameter values:

$$par_k = par_k + ind_k \times Fr \times par_k, k = 1, 2, 3, 4$$

$$ind_k \in -1, 0, +1; Fr \in 0.05, 0.1, 0.2$$

$$par_1 = \alpha; par_2 = \gamma; par_3 = \mu; par_4 = \bar{y}$$

Here ind_k can take any value from the designated set and Fr can also take any of three possible values indicating different degrees of variation. Table A.1 shows

the performance of the model for different degrees of parameter variation in terms of the measure Q (described above), for the case of cIN ascending axons. The first column of the table shows the sequential number of the test case (1-81), the following 4 columns show the values of *ind* for each parameter. For example, the first row shows that the values of all four parameters have been decreased, the second row shows the test case when the values of α, γ, μ have been decreased but the value of $\bar{y}$ has not been changed, etc. The last three columns show the quality of optimization for different levels of variation.

This table indicates that for 75% of these cases at the 5% variation level, the value of Q remains below 8.5, which is our criterion for good quality results. At the 10% variation level, 42% of cases produce good quality results, and even at the 20% variation level, 20% of cases give good quality results. In the case of the cIN ascending axons considered here, the poorest results occur when $\bar{y}$ is reduced (made more ventral), especially when μ is decreased at the same time, as in these cases the axons do not reach a sufficiently dorsal position to adequately match the experimental data set.

#	J_alp	J_gam	J_mu	J_ybar	Q(5%)	Q(10%)	Q(20%)
1	-1	-1	-1	-1	8.76	22.05	91.55
2	-1	-1	-1	0	4.31	4.07	4.22
3	-1	-1	-1	1	5.77	9.55	21.39
4	-1	-1	0	-1	5.59	10.02	39.90
5	-1	-1	0	0	4.08	5.73	11.32
6	-1	-1	0	1	7.34	15.99	44.83
7	-1	-1	1	-1	4.65	5.25	16.77
8	-1	-1	1	0	5.47	9.82	25.12
9	-1	-1	1	1	10.00	24.63	70.43
10	-1	0	-1	-1	13.49	53.28	288.08
11	-1	0	-1	0	5.83	9.38	32.76
12	-1	0	-1	1	4.44	4.83	5.91
13	-1	0	0	-1	10.02	27.67	198.88
14	-1	0	0	0	4.51	4.63	5.63
15	-1	0	0	1	5.61	8.70	19.88
16	-1	0	1	-1	6.48	15.23	129.85
17	-1	0	1	0	4.07	5.02	8.45
18	-1	0	1	1	7.28	14.55	38.73
19	-1	1	-1	-1	23.36	121.69	577.93
20	-1	1	-1	0	10.12	26.09	155.43
21	-1	1	-1	1	4.69	5.91	11.38
22	-1	1	0	-1	18.13	78.40	354.82
23	-1	1	0	0	5.91	12.17	46.41
24	-1	1	0	1	4.32	4.54	6.71
25	-1	1	1	-1	11.36	37.27	249.86
26	-1	1	1	0	4.81	5.04	10.61
27	-1	1	1	1	5.01	8.40	19.29
28	0	-1	-1	-1	7.26	16.27	50.14
29	0	-1	-1	0	4.38	4.64	5.65
30	0	-1	-1	1	5.84	10.10	22.15
31	0	-1	0	-1	4.98	8.09	17.15
32	0	-1	0	0	4.46	6.25	12.36
33	0	-1	0	1	7.52	16.93	44.34
34	0	-1	1	-1	4.34	3.86	6.11
35	0	-1	1	0	5.62	9.90	25.84
36	0	-1	1	1	9.89	24.07	68.00
37	0	0	-1	-1	12.48	35.72	205.52
38	0	0	-1	0	5.75	8.08	19.18
39	0	0	-1	1	4.58	5.65	7.76
40	0	0	0	-1	9.62	21.85	103.94
41	0	0	0	0	4.20	4.32	4.18

Table A.1: Sensitivity to parameter variation: part I

#	J_alp	J_gam	J_mu	J_ybar	Q(5%)	Q(10%)	Q(20%)
42	0	0	0	1	5.50	9.26	20.19
43	0	0	1	-1	5.91	10.70	59.80
44	0	0	1	0	4.16	4.84	8.40
45	0	0	1	1	7.09	14.68	38.82
46	0	1	-1	-1	20.80	80.36	380.80
47	0	1	-1	0	9.76	18.97	103.05
48	0	1	-1	1	4.65	5.27	8.91
49	0	1	0	-1	12.68	43.65	274.92
50	0	1	0	0	6.10	8.44	24.03
51	0	1	0	1	4.32	5.12	7.74
52	0	1	1	-1	9.19	29.89	184.43
53	0	1	1	0	4.35	4.46	4.94
54	0	1	1	1	5.21	8.84	19.37
55	1	-1	-1	-1	7.36	13.29	30.91
56	1	-1	-1	0	4.46	5.74	8.57
57	1	-1	-1	1	6.07	11.30	23.76
58	1	-1	0	-1	5.37	6.55	12.55
59	1	-1	0	0	5.02	6.99	13.67
60	1	-1	0	1	8.13	16.88	43.92
61	1	-1	1	-1	4.34	4.03	5.01
62	1	-1	1	0	6.11	10.57	26.03
63	1	-1	1	1	10.36	24.55	67.62
64	1	0	-1	-1	11.24	32.00	111.02
65	1	0	-1	0	5.54	7.94	15.76
66	1	0	-1	1	4.96	6.35	9.56
67	1	0	0	-1	7.66	16.04	56.80
68	1	0	0	0	4.15	4.78	5.52
69	1	0	0	1	5.68	9.63	22.18
70	1	0	1	-1	5.38	8.91	26.40
71	1	0	1	0	4.43	5.48	9.67
72	1	0	1	1	7.31	15.35	37.81
73	1	1	-1	-1	16.99	59.76	291.09
74	1	1	-1	0	8.30	17.50	58.05
75	1	1	-1	1	4.78	5.98	9.35
76	1	1	0	-1	12.30	35.43	180.90
77	1	1	0	0	5.49	7.48	14.64
78	1	1	0	1	4.69	5.56	8.48
79	1	1	1	-1	8.56	19.83	112.91
80	1	1	1	0	4.26	4.48	4.64
81	1	1	1	1	5.57	9.28	20.45

Table A.2: Sensitivity to parameter variation: part II

A.2 Optimization results for each neuron type and examples of generated model axons compared with measured axons

For each neuron type we have included two figures. The left side of the upper figure shows the test histograms, which are calculated from 100 trials where each trial includes the generation of 300 axons, and the caption of this figure indicates the quality of the optimization. In this histogram, the horizontal axis shows the cost function value for each bin and the vertical axis shows the percentage for the bin. The right side of the upper figure shows the distributions of dorsoventral coordinates of model axons (in blue) compared to experimental axons (in red). The lower figure shows the model axons (upper panel) and the experimental axons (lower panel); the caption gives both experimental and model axon tortuosities.

A.2.1 Test results: aIN descending

For an explanation of these figures, please see page 171.

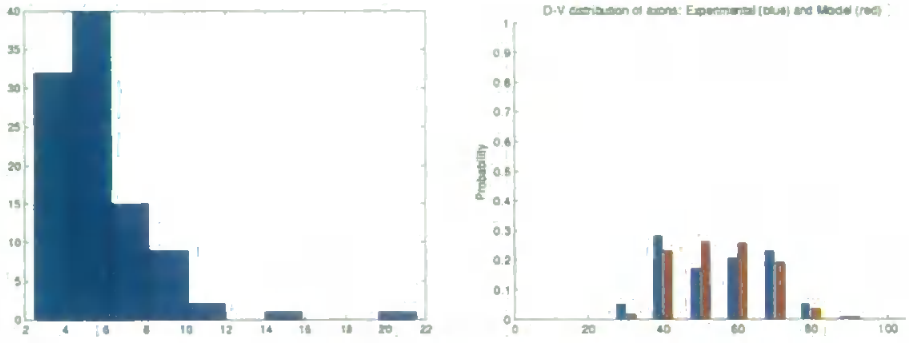

Figure A.1: Test of optimization quality: GOOD.

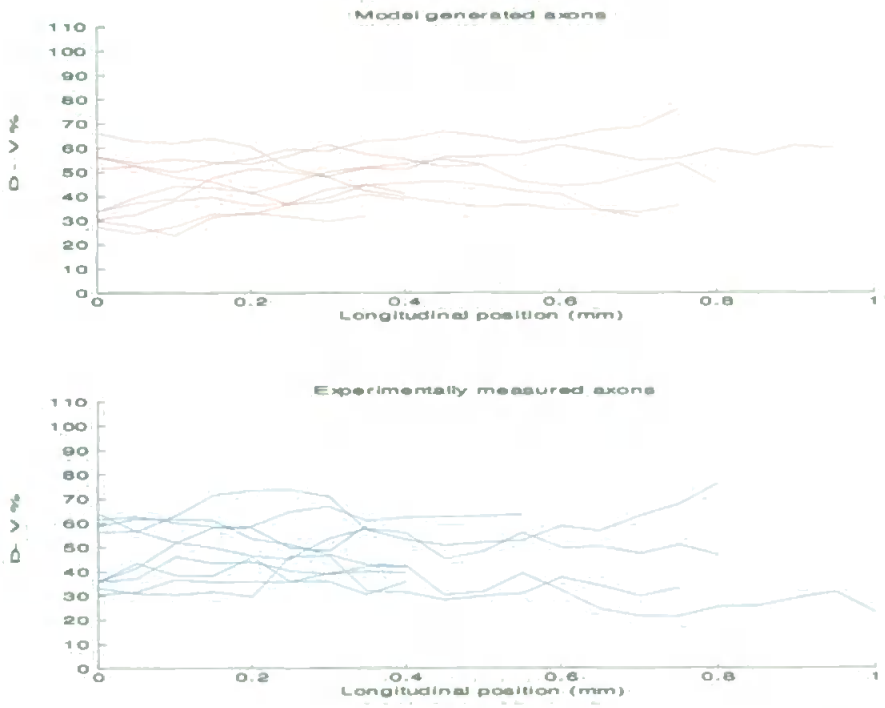

Figure A.2: Model tortuosity: 1.002. Experimental tortuosity: 1.005

A.2.2 Test results: aIN ascending

For an explanation of these figures, please see page 171.

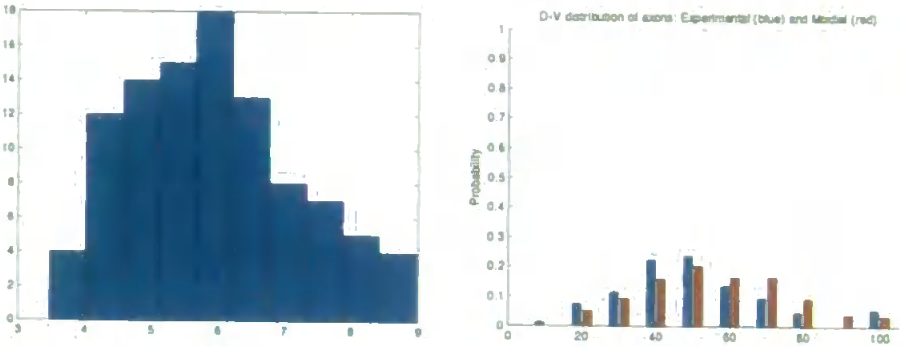

Figure A.3: Test of optimization quality: GOOD.

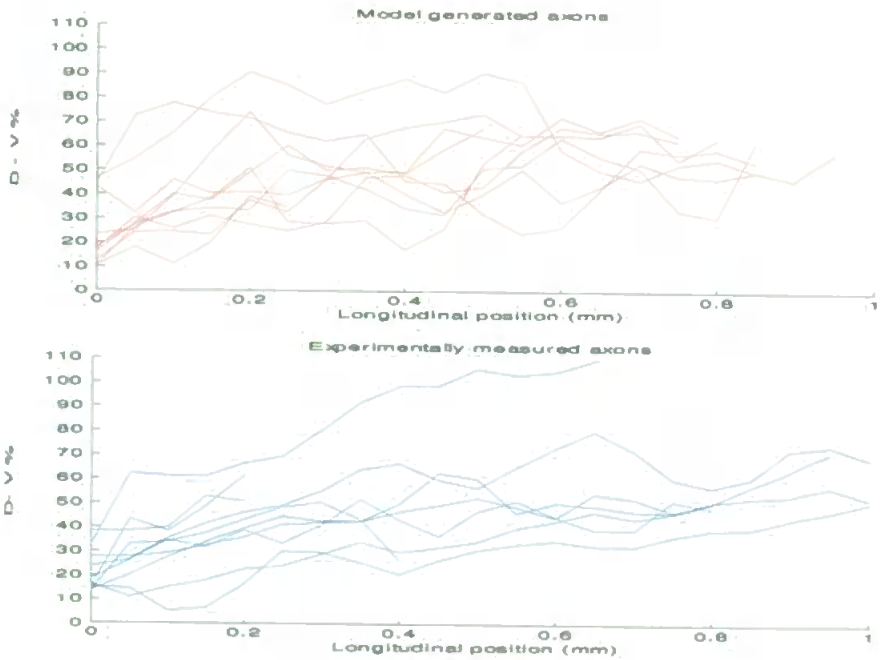

Figure A.4: Model tortuosity: 1.02. Experimental tortuosity: 1.009

A.2.3 Test results: cIN descending

For an explanation of these figures, please see page 171.

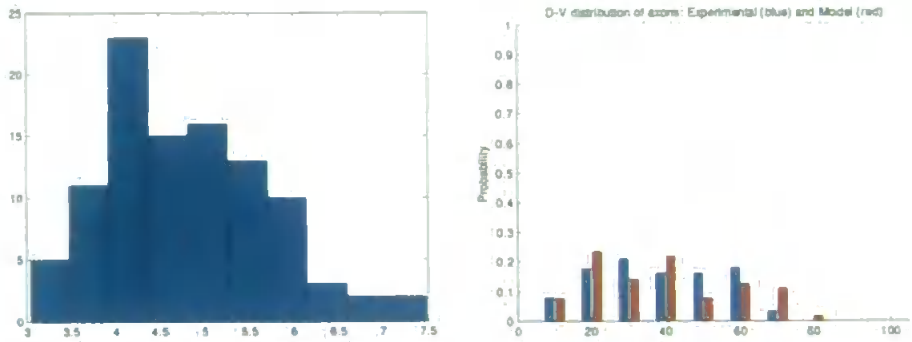

Figure A.5: Test of optimization quality: GOOD.

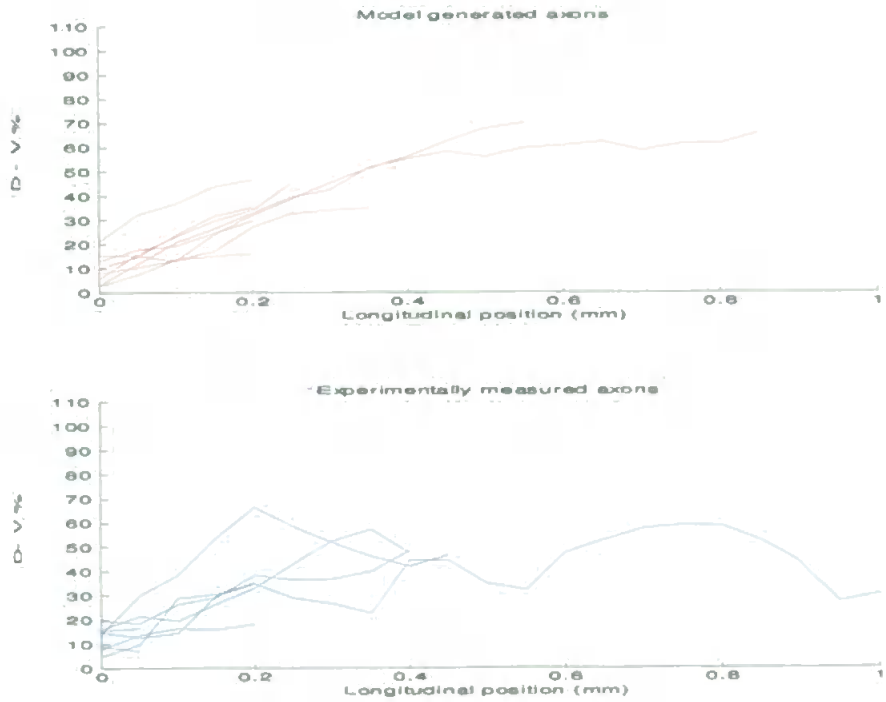

Figure A.6: Model tortuosity: 1.001. Experimental tortuosity: 1.006

A.2.4 Test results: cIN ascending

For an explanation of these figures, please see page 171.

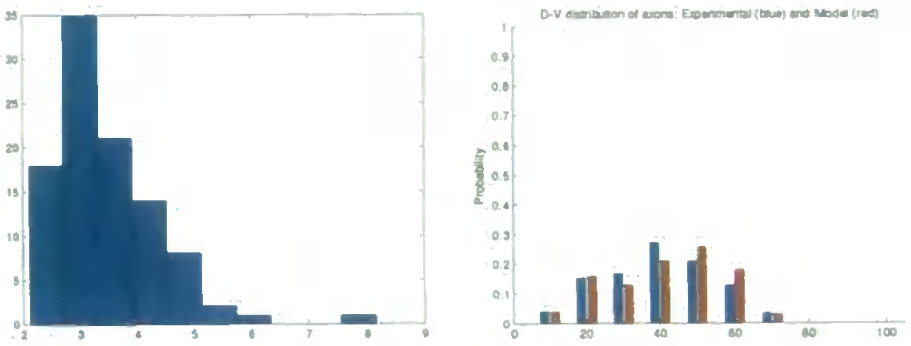

Figure A.7: Test of optimization quality: GOOD.

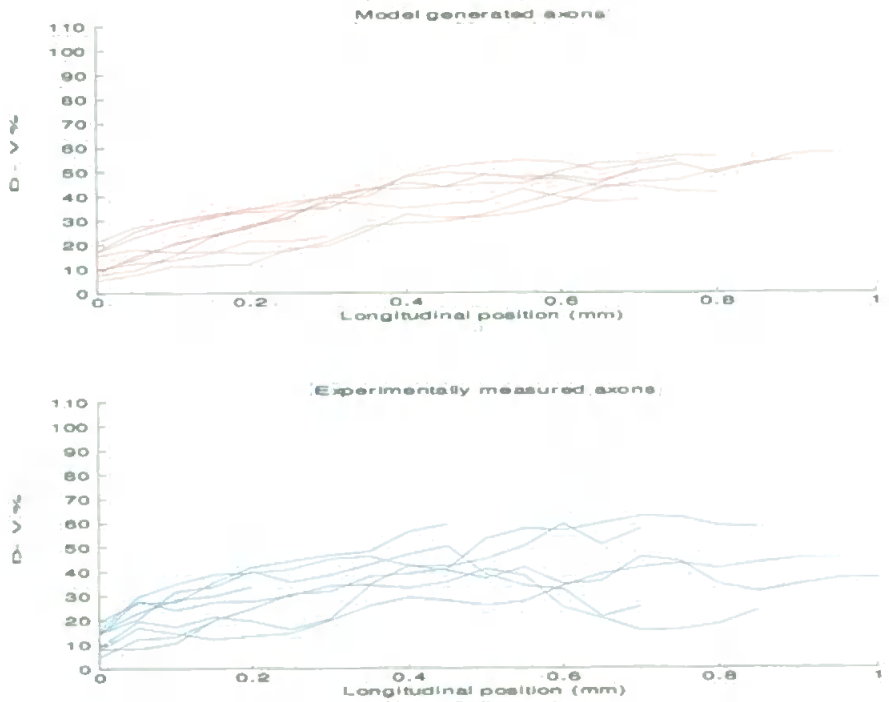

Figure A.8: Model tortuosity: 1.001. Experimental tortuosity: 1.004

A.2.5 Test results: dIN descending

For an explanation of these figures, please see page 171.

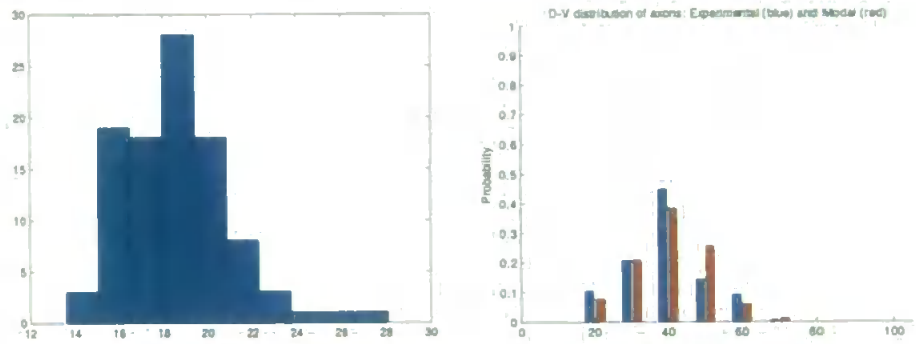

Figure A.9: Test of optimization quality: POOR.

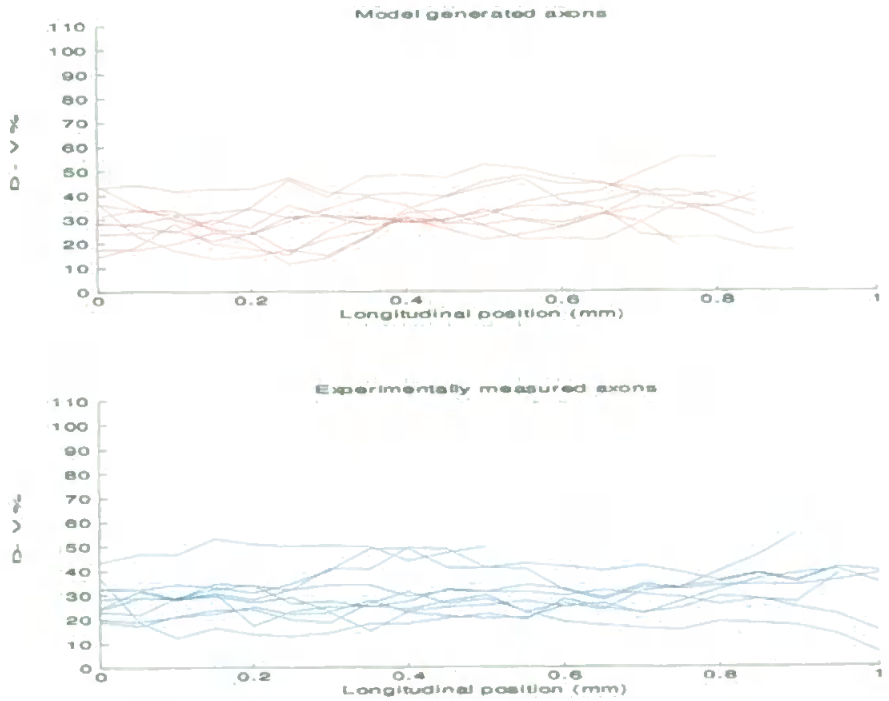

Figure A.10: Model tortuosity: 1.004. Experimental tortuosity: 1.003

A.2.6 Test results: RB descending

For an explanation of these figures, please see page 171.

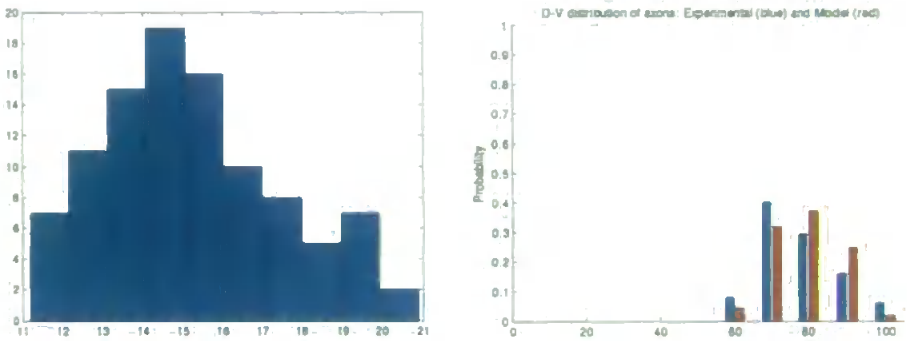

Figure A.11: Test of optimization quality: POOR.

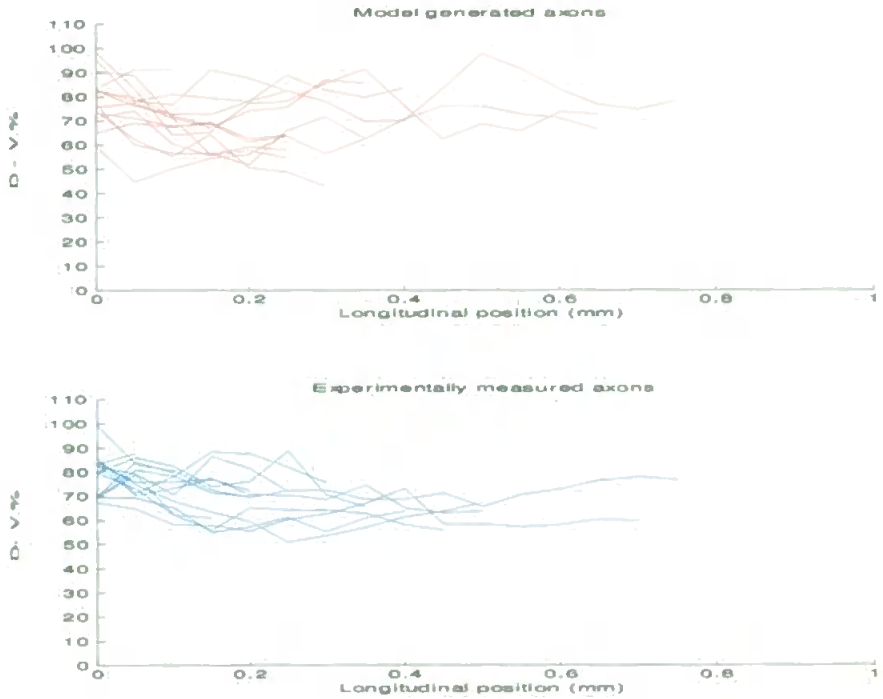

Figure A.12: Model tortuosity: 1.009. Experimental tortuosity: 1.009

A.2.7 Test results: RB ascending

For an explanation of these figures, please see page 171.

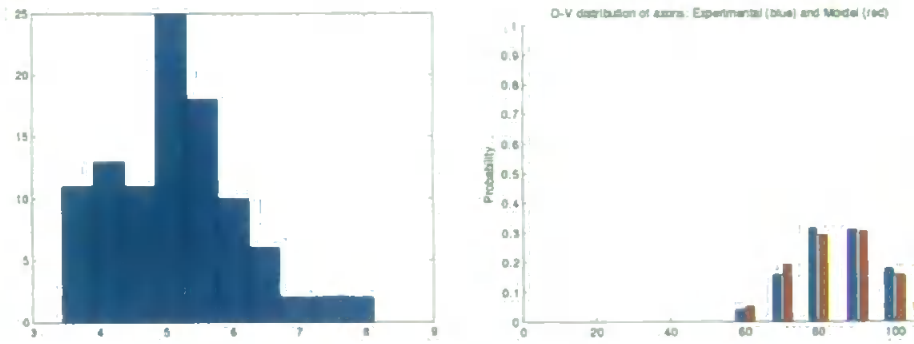

Figure A.13: Test of optimization quality: GOOD.

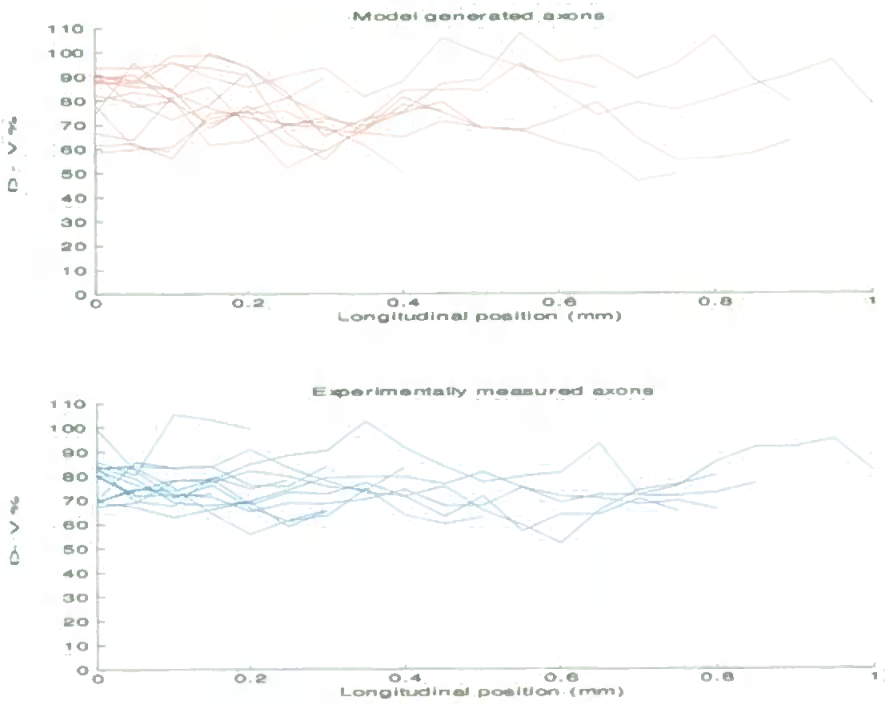

Figure A.14: Model tortuosity: 1.01. Experimental tortuosity: 1.009

A.2.8 Test results: dlc descending

For an explanation of these figures, please see page 171.

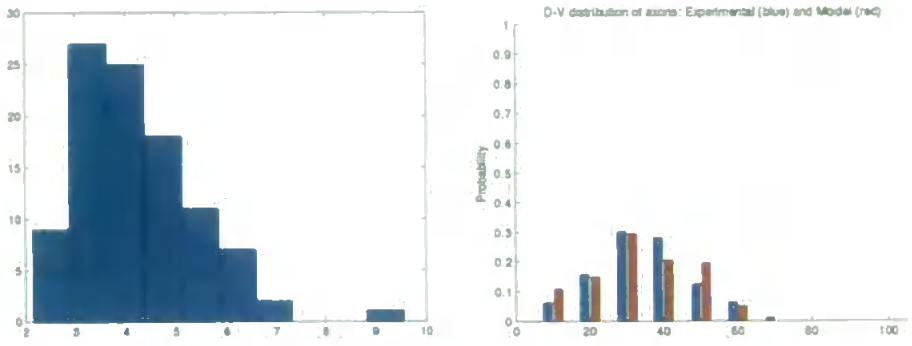

Figure A.15: Test of optimization quality: GOOD.

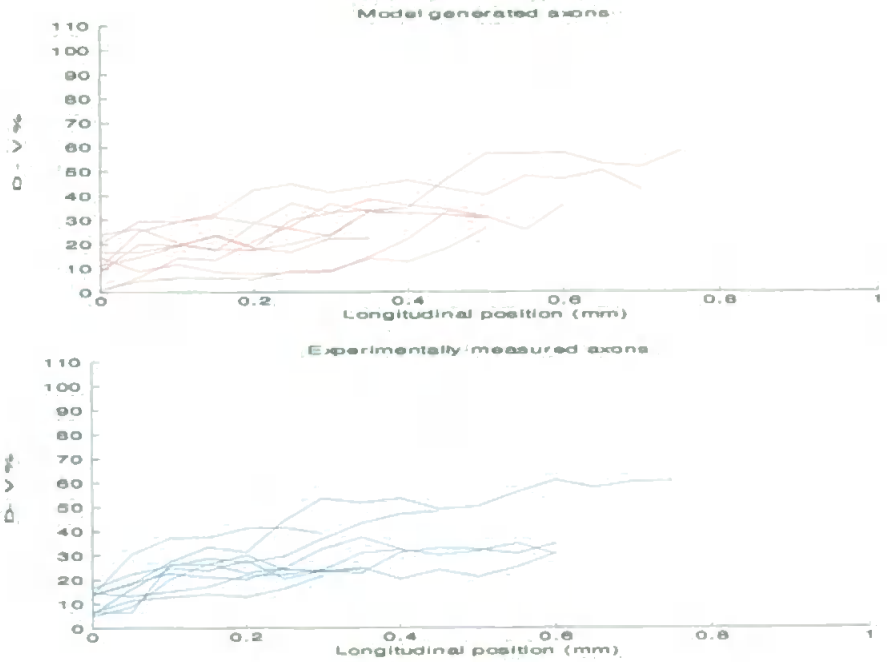

Figure A.16: Model tortuosity: 1.002. Experimental tortuosity: 1.005

A.2.9 Test results: dlc ascending

For an explanation of these figures, please see page 171.

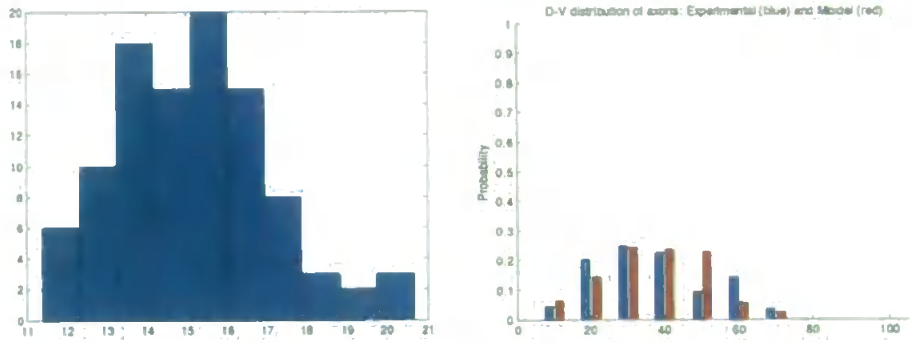

Figure A.17: Test of optimization quality: POOR.

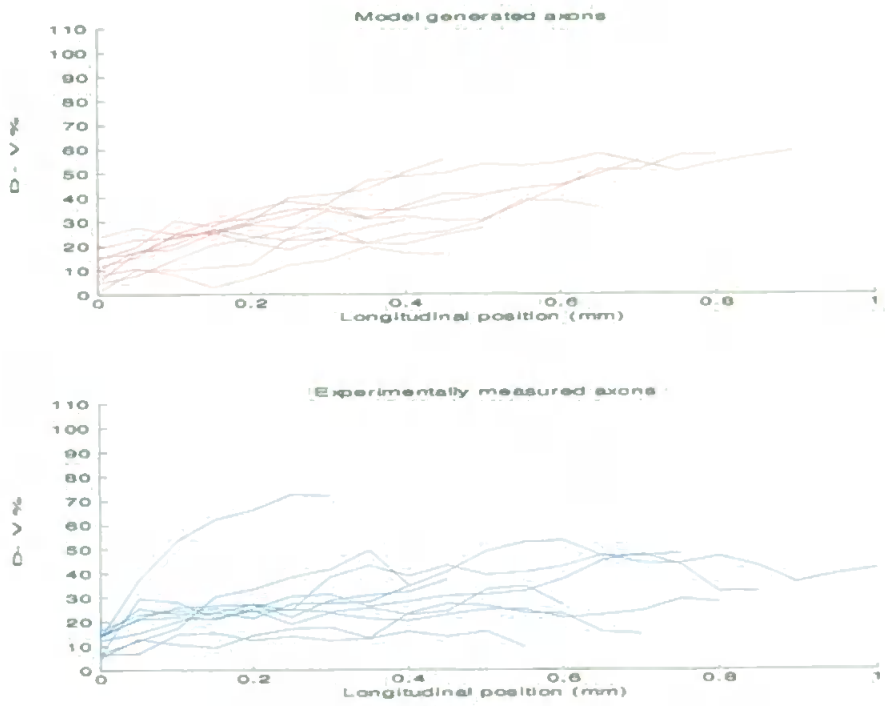

Figure A.18: Model tortuosity: 1.003. Experimental tortuosity: 1.006

A.2.10 Test results: mn descending

For an explanation of these figures, please see page 171.

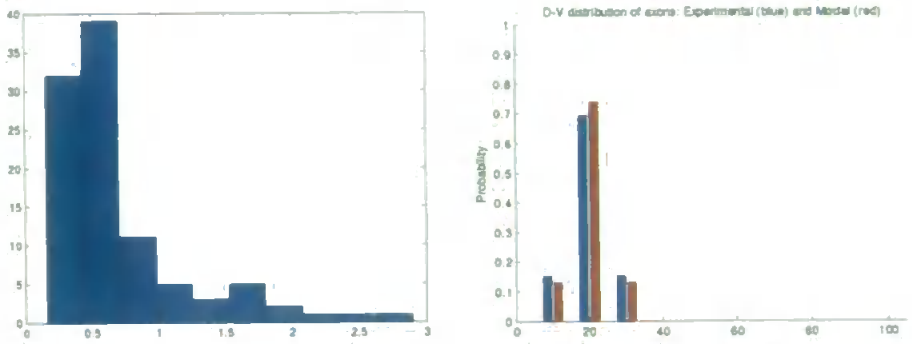

Figure A.19: Test of optimization quality: VERY GOOD.

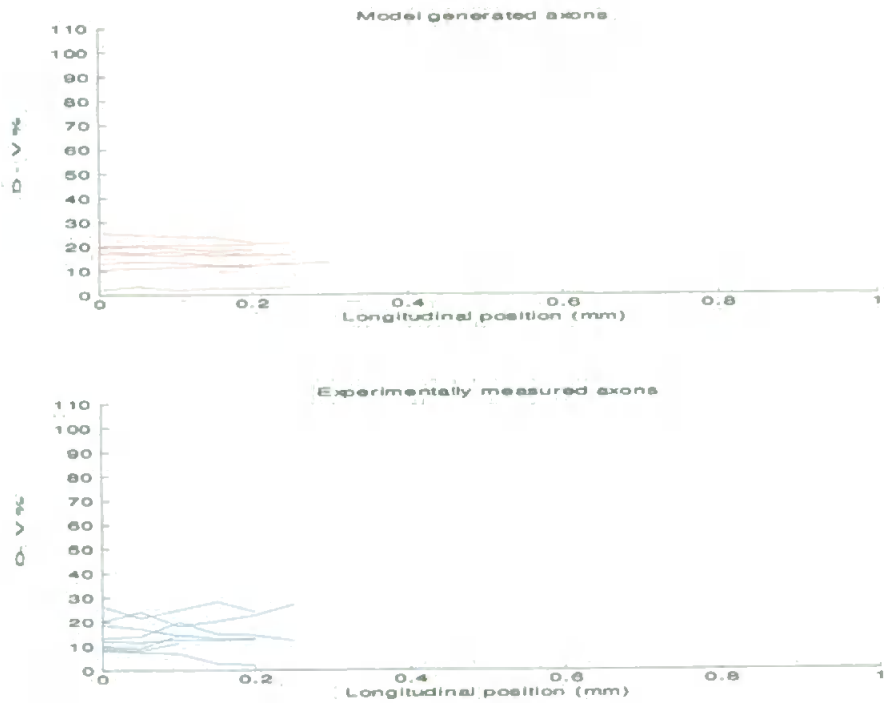

Figure A.20: Model tortuosity: 1.0001. Experimental tortuosity: 1.001

List of references

Abbott, L. and Nelson, S. (2000), 'Synaptic plasticity: taming the beast.', *Nat Neurosci* **3 Suppl**, 1178–83.
URL: *http://dx.doi.org/10.1038/81453*

Aksay, E., Baker, R., Seung, H. S. and Tank, D. W. (2000), 'Anatomy and discharge properties of pre-motor neurons in the goldfish medulla that have eye-position signals during fixations.', *J Neurophysiol* **84**(2), 1035–1049.

Aksay, E., Gamkrelidze, G., Seung, H. S., Baker, R. and Tank, D. W. (2001), 'In vivo intracellular recording and perturbation of persistent activity in a neural integrator.', *Nat Neurosci* **4**(2), 184–93.
URL: *http://dx.doi.org/10.1038/84023*

Amit, D. (1989), *Modeling brain function the world of attractor neural networks*, Cambridge University Press, Cambridge England.
URL: *http://www.loc.gov/catdir/description/cam023/89015741.html;http://www.loc.gov*

Bayer, S. and Altman, J. (2001), *Development of the human spinal cord : an interpretation based on experimental studies in animals*, Oxford University Press.

Ben Ari, Y. (2002), 'Excitatory actions of GABA during development: the nature of the nurture', *Nat.Rev.Neurosci.* **3**(9), 728–739.
URL: *PM:12209121*

Bi, G. Q. and Poo, M. M. (1998), 'Synaptic modifications in cultured hippocampal neurons: dependence on spike timing, synaptic strength, and postsynaptic cell type.', *J Neurosci* **18**(24), 10464–10472.

Borisyuk, A. and Rinzel, J. (2005), Understanding neuronal dynamics by geometrical dissection of neural models, *in* C. Chow, B. Gutkin, D. Hansel, C. Meunier and J. Dalibard, eds, 'Methods and Models in Neurophysics', Elsevier, pp. 19–72.

Borisyuk, R. (2002), 'Oscillatory activity in the neural networks of spiking elements', *Biosystems* **67**(1-3), 3–16.
URL: *PM:12459279*

Borisyuk, R., Cooke, T. and Roberts, A. (2008), 'Stochasticity and functionality of neural systems: Mathematical modelling of axon growth in the spinal cord of tadpole.', *Biosystems* **93**(1-2), 101–114.
URL: *http://dx.doi.org/10.1016/j.biosystems.2008.03.012*

Borisyuk, R. and Kazanovich, Y. (2006), 'Oscillations and waves in the models of interactive neural populations.', *Biosystems* **86**(1-3), 53–62.
URL: *http://dx.doi.org/10.1016/j.biosystems.2006.02.017*

Borodinsky, L., Root, C., Cronin, J., Sann, S., Gu, X. and Spitzer, N. (2004), 'Activity-dependent homeostatic specification of transmitter expression in embryonic neurons', *Nature* **429**(6991), 523–530.
URL: *PM:15175743*

Bourikas, D., Pekarik, V., Baeriswyl, T., Grunditz, A., Sadhu, R., Nardó, M. and Stoeckli, E. T. (2005), 'Sonic hedgehog guides commissural axons along the longitudinal axis of the spinal cord.', *Nat Neurosci* **8**(3), 297–304.
URL: *http://dx.doi.org/10.1038/nn1396*

Brody, C. D., Romo, R. and Kepecs, A. (2003), 'Basic mechanisms for graded persistent activity: discrete attractors, continuous attractors, and dynamic representations.', *Curr Opin Neurobiol* **13**(2), 204–211.

Brunel, N. (2003), 'Dynamics and plasticity of stimulus-selective persistent activity in cortical network models.', *Cereb Cortex* **13**(11), 1151–1161.

Cang, J., Rentería, R. C., Kaneko, M., Liu, X., Copenhagen, D. R. and Stryker, M. P. (2005), 'Development of precise maps in visual cortex requires patterned spontaneous activity in the retina.', *Neuron* **48**(5), 797–809.
URL: *http://dx.doi.org/10.1016/j.neuron.2005.09.015*

Charron, F., Stein, E., Jeong, J., McMahon, A. P. and Tessier-Lavigne, M. (2003), 'The morphogen sonic hedgehog is an axonal chemoattractant that collaborates with netrin-1 in midline axon guidance.', *Cell* **113**(1), 11–23.

Chilton, J. K. (2006), 'Molecular mechanisms of axon guidance.', *Dev Biol* **292**(1), 13–24.
URL: *http://dx.doi.org/10.1016/j.ydbio.2005.12.048*

Chua, L. and Yang, L. (1988), 'Cellular neural networks: theory', *Circuits and Systems, IEEE Transactions on* **35**(10), 1257–1272.

Clandinin, T. R. and Zipursky, S. L. (2002), 'Making connections in the fly visual system.', *Neuron* **35**(5), 827–841.

Cline, H. (2003), 'Sperry and Hebb: oil and vinegar?', *Trends Neurosci* **26**(12), 655–661.

Compte, A., Constantinidis, C., Tegner, J., Raghavachari, S., Chafee, M. V., Goldman-Rakic, P. S. and Wang, X.-J. (2003), 'Temporally irregular mnemonic persistent activity in prefrontal neurons of monkeys during a delayed response task.', *J Neurophysiol* **90**(5), 3441–3454.
URL: *http://dx.doi.org/10.1152/jn.00949.2002*

Constantinidis, C. and Wang, X.-J. (2004), 'A neural circuit basis for spatial working memory.', *Neuroscientist* **10**(6), 553–565.
URL: *http://dx.doi.org/10.1177/1073858404268742*

Coombes, S. and Owen, M. R. (2005), 'Bumps, breathers, and waves in a neural network with spike frequency adaptation.', *Phys Rev Lett* **94**(14), 148102.

Dale, N. (1985), 'Reciprocal inhibitory interneurones in the xenopus embryo spinal cord.', *J Physiol* **363**, 61–70.

Dale, N. (2003), 'Coordinated motor activity in simulated spinal networks emerges from simple biologically plausible rules of connectivity', *J.Comput.Neurosci.* **14**(1), 55–70.
URL: *PM:12435924*

de Anda, F. C., Pollarolo, G., Silva, J. S. D., Camoletto, P. G., Feiguin, F. and Dotti, C. G. (2005), 'Centrosome localization determines neuronal polarity.', *Nature* **436**(7051), 704–708.
URL: *http://dx.doi.org/10.1038/nature03811*

Derégnaucourt, S., Mitra, P., Fehér, O., Pytte, C. and Tchernichovski, O. (2005), 'How sleep affects the developmental learning of bird song.', *Nature* **433**(7027), 710–6.
URL: *http://dx.doi.org/10.1038/nature03275*

Dickson, B. J. (2002), 'Molecular mechanisms of axon guidance.', *Science* **298**(5600), 1959–1964.
URL: *http://dx.doi.org/10.1126/science.1072165*

Dickson, B. J. and Gilestro, G. F. (2006), 'Regulation of commissural axon pathfinding by slit and its robo receptors.', *Annu Rev Cell Dev Biol* **22**, 651–675.
URL: *http://dx.doi.org/10.1146/annurev.cellbio.21.090704.151234*

Egorov, A. V., Hamam, B. N., Fransén, E., Hasselmo, M. E. and Alonso, A. A. (2002), 'Graded persistent activity in entorhinal cortex neurons.', *Nature* **420**(6912), 173–178.
URL: *http://dx.doi.org/10.1038/nature01171*

Ermentrout, B. (2003), 'Dynamical consequences of fast-rising, slow-decaying synapses in neuronal networks.', *Neural Comput* **15**(11), 2483–2522.
URL: *http://dx.doi.org/10.1162/089976603322385054*

Fedirchuk, B., Wenner, P., Whelan, P., Ho, S., Tabak, J. and O'Donovan, M. (1999), 'Spontaneous network activity transiently depresses synaptic transmission in the embryonic chick spinal cord', *J.Neurosci.* **19**(6), 2102–2112.
URL: *PM:10066263*

Ferri, R., Huber, R., Aricò, D., Drago, V., Rundo, F., Ghilardi, M. F., Massimini, M. and Tononi, G. (2008), 'The slow-wave components of the cyclic alternating pattern (cap) have a role in sleep-related learning processes.', *Neurosci Lett* **432**(3), 228–231.
URL: *http://dx.doi.org/10.1016/j.neulet.2007.12.025*

Foster, D. J. and Wilson, M. A. (2006), 'Reverse replay of behavioural sequences in hippocampal place cells during the awake state.', *Nature* **440**(7084), 680–683.
URL: *http://dx.doi.org/10.1038/nature04587*

Frank, L. M. and Brown, E. N. (2003), 'Persistent activity and memory in the entorhinal cortex', *Trends in Neurosciences* **26**(8), 400–401.
URL: *http://www.sciencedirect.com/science/article/B6T0V-48WJH7C-2/2/49446310696bb18c4462aa246fba6c57*

Fransén, E., Tahvildari, B., Egorov, A. V., Hasselmo, M. E. and Alonso, A. A. (2006), 'Mechanism of graded persistent cellular activity of entorhinal cortex layer v neurons.', *Neuron* **49**(5), 735–746.
URL: *http://dx.doi.org/10.1016/j.neuron.2006.01.036*

Gardner, M. (1970), 'Mathematical games: The fantastic combinations of John Conway's new solitaire game 'Life", *Scientific American* **223**(4), 120–123. The original description of Conway's game of LIFE.

Gerstner, W. and Kistler, W. M. (2002), *Spiking neuron models single neurons, populations, plasticity*, Cambridge University Press, Cambridge, U.K.
URL: *http://www.loc.gov/catdir/samples/cam031/2002067657.html;http://www.loc.gov/*

Gomez, T. M. and Zheng, J. Q. (2006), 'The molecular basis for calcium-dependent axon pathfinding.', *Nat Rev Neurosci* **7**(2), 115–125.
URL: *http://dx.doi.org/10.1038/nrn1844*

Goodhill, G. J., Gu, M. and Urbach, J. S. (2004), 'Predicting axonal response to molecular gradients with a computational model of filopodial dynamics.', *Neural Comput* **16**(11), 2221–43.
URL: *http://dx.doi.org/10.1162/0899766041941934*

Goulding, M. and Pfaff, S. L. (2005), 'Development of circuits that generate simple rhythmic behaviors in vertebrates.', *Curr Opin Neurobiol* **15**(1), 14–20.
URL: *http://dx.doi.org/10.1016/j.conb.2005.01.017*

Green, C. S. and Soffe, S. R. (1998), 'Roles of ascending inhibition during two rhythmic motor patterns in xenopus tadpoles.', *J Neurophysiol* **79**(5), 2316–2328.

Hanson, M. G. and Landmesser, L. T. (2006), 'Increasing the frequency of spontaneous rhythmic activity disrupts pool-specific axon fasciculation and pathfinding of embryonic spinal motoneurons.', *J Neurosci* **26**(49), 12769–12780.
URL: *http://dx.doi.org/10.1523/JNEUROSCI.4170-06.2006*

Hanson, M. G., Milner, L. D. and Landmesser, L. T. (2008), 'Spontaneous rhythmic activity in early chick spinal cord influences distinct motor axon pathfinding decisions.', *Brain Res Rev* **57**(1), 77–85.
URL: *http://dx.doi.org/10.1016/j.brainresrev.2007.06.021*

Helms, A. W. and Johnson, J. E. (2003), 'Specification of dorsal spinal cord interneurons.', *Curr Opin Neurobiol* **13**(1), 42–49.

Hemond, P., Epstein, D., Boley, A., Migliore, M., Ascoli, G. A. and Jaffe, D. B. (2008), 'Distinct classes of pyramidal cells exhibit mutually exclusive firing patterns in hippocampal area ca3b.', *Hippocampus* **18**(4), 411–424.
URL: *http://dx.doi.org/10.1002/hipo.20404*

Henze, D. A. and Buzsáki, G. (2001), 'Action potential threshold of hippocampal pyramidal cells in vivo is increased by recent spiking activity.', *Neuroscience* **105**(1), 121–30.

Higashijima, S.-I., Schaefer, M. and Fetcho, J. R. (2004), 'Neurotransmitter properties of spinal interneurons in embryonic and larval zebrafish.', *J Comp Neurol* **480**(1), 19–37.
URL: *http://dx.doi.org/10.1002/cne.20279*

Hill, A. V. (1936), 'Excitation and accommodation in nerve', *Proceedings of the Royal Society of London. Series B, Biological Sciences* **119**(814), 305–355.

Hodgkin, A. and Huxley, A. (1952), 'A quantitative description of membrane current and its application to conduction and excitation in nerve', *J.Physiol* **117**(4), 500–544.
URL: *PM:12991237*

Hopfield, J. J. (1982), 'Neural networks and physical systems with emergent collective computational abilities.', *Proc Natl Acad Sci U S A* **79**(8), 2554–2558.

Huang, X., Troy, W. C., Yang, Q., Ma, H., Laing, C. R., Schiff, S. J. and Wu, J.-Y. (2004), 'Spiral waves in disinhibited mammalian neocortex.', *J Neurosci* **24**(44), 9897–9902.
URL: *http://dx.doi.org/10.1523/JNEUROSCI.2705-04.2004*

Huber, R., Ghilardi, M., Massimini, M. and Tononi, G. (2004), 'Local sleep and learning', *Nature* **430**(6995), 78–81.
URL: *PM:15184907*

Imondi, R. and Kaprielian, Z. (2001), 'Commissural axon pathfinding on the contralateral side of the floor plate: a role for b-class ephrins in specifying the dorsoventral position of longitudinally projecting commissural axons.', *Development* **128**(23), 4859–4871.

Jessell, T. M. (2000), 'Neuronal specification in the spinal cord: inductive signals and transcriptional codes.', *Nat Rev Genet* **1**(1), 20–29.
URL: *http://dx.doi.org/10.1038/35049541*

Jontes, J. D., Buchanan, J. and Smith, S. J. (2000), 'Growth cone and dendrite dynamics in zebrafish embryos: early events in synaptogenesis imaged in vivo.', *Nat Neurosci* **3**(3), 231–237.
URL: *http://dx.doi.org/10.1038/72936*

Kaern, M., Elston, T. C., Blake, W. J. and Collins, J. J. (2005), 'Stochasticity in gene expression: from theories to phenotypes.', *Nat Rev Genet* **6**(6), 451–464.
URL: *http://dx.doi.org/10.1038/nrg1615*

Kahn, J. A. and Roberts, A. (1982), 'The central nervous origin of the swimming motor pattern in embryos of xenopus laevis.', *J Exp Biol* **99**, 185–196.

Kandler, K. and Katz, L. (1995), 'Neuronal coupling and uncoupling in the developing nervous system', *Curr.Opin.Neurobiol.* **5**(1), 98–105.
URL: *PM:7773012*

Katz, L. and Shatz, C. (1996), 'Synaptic activity and the construction of cortical circuits', *Science* **274**(5290), 1133–1138.
URL: *PM:8895456*

Kempter, R., Gerstner, W. and van Hemmen, J. (2001), 'Intrinsic stabilization of output rates by spike-based Hebbian learning', *Neural Comput.* **13**(12), 2709–2741.
URL: *PM:11705408*

Kennedy, T. E., Wang, H., Marshall, W. and Tessier-Lavigne, M. (2006), 'Axon guidance by diffusible chemoattractants: a gradient of netrin protein in the developing spinal cord.', *J Neurosci* **26**(34), 8866–8874.
URL: *http://dx.doi.org/10.1523/JNEUROSCI.5191-05.2006*

Kirov, S., Goddard, C. and Harris, K. (2004), 'Age-dependence in the homeostatic upregulation of hippocampal dendritic spine number during blocked synaptic transmission', *Neuropharmacology* **47**(5), 640–648.
URL: *PM:15458835*

Krottje, J. K. and van Ooyen, A. (2007), 'A mathematical framework for modeling axon guidance.', *Bull Math Biol* **69**(1), 3–31.
URL: *http://dx.doi.org/10.1007/s11538-006-9142-4*

Lagarias, J. C., Reeds, J. A., Wright, M. H. and Wright, P. E. (1998), 'Convergence properties of the Nelder-Mead simplex algorithm in low dimensions', *SIAM Journal on Optimization* **9**, 112–147.
URL: *citeseer.ist.psu.edu/lagarias96convergence.html*

Lauri, S., Lamsa, K., Pavlov, I., Riekki, R., Johnson, B., Molnar, E., Rauvala, H. and Taira, T. (2003), 'Activity blockade increases the number of functional

synapses in the hippocampus of newborn rats', *Mol.Cell Neurosci.* **22**(1), 107–117.
URL: *PM:12595243*

Lerchner, A. and Rinzel, J. (2005), 'Synaptic model for spontaneous activity in developing networks', *Neurocomputing* **65-66**, 777–782.
URL: *http://dx.doi.org/10.1016/j.neucom.2004.10.074*

Li, W.-C., Cooke, T., Sautois, B., Soffe, S. R., Borisyuk, R. and Roberts, A. (2007), 'Axon and dendrite geography predict the specificity of synaptic connections in a functioning spinal cord network.', *Neural Develop* **2**, 17.
URL: *http://dx.doi.org/10.1186/1749-8104-2-17*

Li, W.-C., ichi Higashijima, S., Parry, D. M., Roberts, A. and Soffe, S. R. (2004), 'Primitive roles for inhibitory interneurons in developing frog spinal cord.', *J Neurosci* **24**(25), 5840–5848.
URL: *http://dx.doi.org/10.1523/JNEUROSCI.1633-04.2004*

Li, W. C., Perrins, R., Soffe, S. R., Yoshida, M., Walford, A. and Roberts, A. (2001), 'Defining classes of spinal interneuron and their axonal projections in hatchling xenopus laevis tadpoles.', *J Comp Neurol* **441**(3), 248–265.

Li, W.-C., Soffe, S. R. and Roberts, A. (2002), 'Spinal inhibitory neurons that modulate cutaneous sensory pathways during locomotion in a simple vertebrate.', *J Neurosci* **22**(24), 10924–10934.

Li, W.-C., Soffe, S. R. and Roberts, A. (2003), 'The spinal interneurons and properties of glutamatergic synapses in a primitive vertebrate cutaneous flexion reflex.', *J Neurosci* **23**(27), 9068–9077.

Li, W.-C., Soffe, S. R. and Roberts, A. (2004*a*), 'Dorsal spinal interneurons forming a primitive, cutaneous sensory pathway.', *J Neurophysiol* **92**(2), 895–904.
URL: *http://dx.doi.org/10.1152/jn.00024.2004*

Li, W.-C., Soffe, S. R. and Roberts, A. (2004*b*), 'Glutamate and acetylcholine corelease at developing synapses.', *Proc Natl Acad Sci U S A* **101**(43), 15488–15493.
URL: *http://dx.doi.org/10.1073/pnas.0404864101*

Li, W.-C., Soffe, S. R., Wolf, E. and Roberts, A. (2006), 'Persistent responses to brief stimuli: feedback excitation among brainstem neurons.', *J Neurosci* **26**(15), 4026–4035.
URL: *http://dx.doi.org/10.1523/JNEUROSCI.4727-05.2006*

Lindner, B., Schimansky-Geier, L. and Longtin, A. (2002), 'Maximizing spike train coherence or incoherence in the leaky integrate-and-fire model', *Phys Rev E Stat Nonlin Soft Matter Phys* **66**(3 Pt 1), 031916.

Lyuksyutova, A. I., Lu, C.-C., Milanesio, N., King, L. A., Guo, N., Wang, Y., Nathans, J., Tessier-Lavigne, M. and Zou, Y. (2003), 'Anterior-posterior guidance of commissural axons by Wnt-Frizzled signaling.', *Science* **302**(5652), 1984–1988.
URL: *http://dx.doi.org/10.1126/science.1089610*

Madison, D. V. and Nicoll, R. A. (1984), 'Control of the repetitive discharge of rat ca 1 pyramidal neurones in vitro.', *J Physiol* **354**, 319–331.

Mainen, Z. F. and Sejnowski, T. J. (1995), 'Reliability of spike timing in neocortical neurons.', *Science* **268**(5216), 1503–1506.

Maletic-Savatic, M., Malinow, R. and Svoboda, K. (1999), 'Rapid dendritic morphogenesis in CA1 hippocampal dendrites induced by synaptic activity', *Science* **283**(5409), 1923–1927.
URL: *PM:10082466*

Massimini, M., Ferrarelli, F., Huber, R., Esser, S. K., Singh, H. and Tononi, G. (2005), 'Breakdown of cortical effective connectivity during sleep.', *Science* **309**(5744), 2228–2232.
URL: *http://dx.doi.org/10.1126/science.1117256*

Massimini, M., Huber, R., Ferrarelli, F., Hill, S. and Tononi, G. (2004), 'The sleep slow oscillation as a traveling wave', *J.Neurosci.* **24**(31), 6862–6870.
URL: *PM:15295020*

McCormick, D., Shu, Y., Hasenstaub, A., Sanchez-Vives, M., Badoual, M. and Bal, T. (2003), 'Persistent cortical activity: mechanisms of generation and effects on neuronal excitability', *Cereb.Cortex* **13**(11), 1219–1231.
URL: *PM:14576213*

McLean, D. L., Fan, J., ichi Higashijima, S., Hale, M. E. and Fetcho, J. R. (2007), 'A topographic map of recruitment in spinal cord.', *Nature* **446**(7131), 71–75.
URL: *http://dx.doi.org/10.1038/nature05588*

Moon, M.-S. and Gomez, T. M. (2005), 'Adjacent pioneer commissural interneuron growth cones switch from contact avoidance to axon fasciculation after midline crossing.', *Dev Biol* **288**(2), 474–486.
URL: *http://dx.doi.org/10.1016/j.ydbio.2005.09.049*

Morris, C. and Lecar, H. (1981), 'Voltage oscillations in the barnacle giant muscle fiber.', *Biophys J* **35**(1), 193–213.

Muller, M., Gahwiler, B., Rietschin, L. and Thompson, S. (1993), 'Reversible loss of dendritic spines and altered excitability after chronic epilepsy in hippocampal slice cultures', *Proc.Natl.Acad.Sci.U.S.A* **90**(1), 257–261.
URL: *PM:8093558*

Munno, D. W. and Syed, N. I. (2003), 'Synaptogenesis in the CNS: an odyssey from wiring together to firing together.', *J Physiol* **552**(Pt 1), 1–11.
URL: *http://dx.doi.org/10.1113/jphysiol.2003.045062*

O'Toole, M., Lamoureux, P. and Miller, K. E. (2008), 'A physical model of axonal elongation: force, viscosity, and adhesions govern the mode of outgrowth.', *Biophys J* **94**(7), 2610–2620.
URL: *http://dx.doi.org/10.1529/biophysj.107.117424*

Pikovsky, A. S. and Kurths, J. (1997), 'Coherence resonance in a noise-driven excitable system', *Phys. Rev. Lett.* **78**(5), 775–778.

Press, W. H., Teukolsky, S. A., Vetterling, W. T. and Flannery, B. P. (2002), *Numerical Recipes in C++: The Art of Scientific Computing*, Cambridge University Press.
URL: *http://www.amazon.ca/exec/obidos/redirect?tag=citeulike09-20&path=ASIN/0521750334*

Price, D. and Willshaw, D. (2000), *Mechanisms of Cortical Development*, Oxford University Press.

Roberts, A. (2000), 'Early functional organization of spinal neurons in developing lower vertebrates', *Brain Res.Bull.* **53**(5), 585–593.
URL: *PM:11165794*

Roberts, A., Soffe, S. and Perrins, R. (1997), *Neurons, Networks, and Motor Behavior*, The MIT Press, chapter 7, pp. 83–89.

Roberts, A. and Tunstall, M. (1990), 'Mutual re-excitation with post-inhibitory rebound: A simulation study on the mechanisms for locomotor rhythm generation in the spinal cord of xenopus embryos', *Eur.J.Neurosci.* **2**(1), 11–23.
URL: *PM:12106099*

Roberts, A. and Tunstall, M. (1994), 'Longitudinal gradients in the spinal cord of xenopus embryos and their possible role in coordination of swimming', *Eur.J.Morphol.* **32**(2-4), 176–184.
URL: *PM:7803164*

Rohrbough, J. and Spitzer, N. (1999), 'Ca(2+)-permeable ampa receptors and spontaneous presynaptic transmitter release at developing excitatory spinal synapses', *J.Neurosci.* **19**(19), 8528–8541.
URL: *PM:10493753*

Sanes, J. N., Suner, S., Lando, J. F. and Donoghue, J. P. (1988), 'Rapid reorganization of adult rat motor cortex somatic representation patterns after motor nerve injury.', *Proc Natl Acad Sci U S A* **85**(6), 2003–2007.

Sautois, B., Soffe, S., Li, W.-C. and Roberts, A. (2007), 'Role of type-specific neuron properties in a spinal cord motor network.', *J Comput Neurosci* **23(1)**, 59–77.
URL: *http://dx.doi.org/10.1007/s10827-006-0019-1*

Schnorrer, F. and Dickson, B. J. (2004), 'Axon guidance: morphogens show the way.', *Curr Biol* **14**(1), R19–R21.

Sernagor, E. and Grzywacz, N. M. (1999), 'Spontaneous activity in developing turtle retinal ganglion cells: pharmacological studies.', *J Neurosci* **19(10)**, 3874–3887.

Sernagor, E., Young, C. and Eglen, S. J. (2003), 'Developmental modulation of retinal wave dynamics: shedding light on the GABA saga.', *J Neurosci* **23**(20), 7621–7629.

Shadlen, M. N. and Newsome, W. T. (1994), 'Noise, neural codes and cortical organization.', *Curr Opin Neurobiol* **4**(4), 569–579.

Shirasaki, R. and Murakami, F. (2001), 'Crossing the floor plate triggers sharp turning of commissural axons.', *Dev Biol* **236**(1), 99–108.
URL: *http://dx.doi.org/10.1006/dbio.2001.0321*

Song, S., Miller, K. and Abbott, L. (2000), 'Competitive Hebbian learning through spike-timing-dependent synaptic plasticity', *Nat.Neurosci.* **3**(9), 919–926.
URL: *PM:10966623*

Spitzer, N., Root, C. and Borodinsky, L. (2004), 'Orchestrating neuronal differentiation: patterns of Ca2+ spikes specify transmitter choice', *Trends Neurosci.*

27(7), 415–421.
URL: *PM:15219741*

Starmer, C. F., Biktashev, V. N., Romashko, D. N., Stepanov, M. R., Makarova, O. N. and Krinsky, V. I. (1993), 'Vulnerability in an excitable medium: analytical and numerical studies of initiating unidirectional propagation.', *Biophys J* **65**(5), 1775–1787.

Stellwagen, D. and Shatz, C. J. (2002), 'An instructive role for retinal waves in the development of retinogeniculate connectivity.', *Neuron* **33**(3), 357–367.

Strogatz, S. H. (2001), *Nonlinear Dynamics and Chaos: With Applications to Physics, Biology, Chemistry and Engineering*, Perseus Books Group.
URL: *http://www.amazon.ca/exec/obidos/redirect?tag=citeulike04-20&path=ASIN/0738204536*

Tabak, J., Rinzel, J. and O'Donovan, M. (2001), 'The role of activity-dependent network depression in the expression and self-regulation of spontaneous activity in the developing spinal cord', *J.Neurosci.* **21**(22), 8966–8978.
URL: *PM:11698607*

Tabak, J., Senn, W., O'Donovan, M. and Rinzel, J. (2000), 'Modeling of spontaneous activity in developing spinal cord using activity-dependent depression in an excitatory network', *J.Neurosci.* **20**(8), 3041–3056.
URL: *PM:10751456*

Taube, J. S. and Bassett, J. P. (2003), 'Persistent neural activity in head direction cells.', *Cereb Cortex* **13**(11), 1162–1172.

Tononi, G. and Cirelli, C. (2003), 'Sleep and synaptic homeostasis: a hypothesis', *Brain Res.Bull.* **62**(2), 143–150.
URL: *PM:14638388*

Torborg, C., Hansen, K. and Feller, M. (2005), 'High frequency, synchronized bursting drives eye-specific segregation of retinogeniculate projections', *Nat.Neurosci.* **8**(1), 72–78.
URL: *PM:15608630*

Tunstall, M. and Roberts, A. (1991), 'Longitudinal coordination of motor output during swimming in xenopus embryos', *Proc.R.Soc.Lond B Biol.Sci.* **244**(1309), 27–32.
URL: *PM:1677193*

Tunstall, M. and Roberts, A. (1994), 'A longitudinal gradient of synaptic drive in the spinal cord of xenopus embryos and its role in co-ordination of swimming', *J.Physiol* **474**(3), 393–405.
URL: *PM:8014901*

Tunstall, M., Roberts, A. and Soffe, S. (2002), 'Modelling inter-segmental coordination of neuronal oscillators: synaptic mechanisms for uni-directional coupling during swimming in xenopus tadpoles', *J.Comput.Neurosci.* **13(2)**, 143–158.
URL: *PM:12215727*

Turrigiano, G. (1999), 'Homeostatic plasticity in neuronal networks: the more things change, the more they stay the same', *Trends Neurosci.* **22**(5), 221–227.
URL: *PM:10322495*

Turrigiano, G., Leslie, K., Desai, N., Rutherford, L. and Nelson, S. (1998), 'Activity-dependent scaling of quantal amplitude in neocortical neurons', *Nature* **391**(6670), 892–896.
URL: *PM:9495341*

Turrigiano, G. and Nelson, S. (2000), 'Hebb and homeostasis in neuronal plasticity', *Curr.Opin.Neurobiol.* **10**(3), 358–364.
URL: *PM:10851171*

Turrigiano, G. and Nelson, S. (2004), 'Homeostatic plasticity in the developing nervous system', *Nat.Rev.Neurosci.* **5**(2), 97–107.
URL: *PM:14735113*

Vajda, I., van Pelt, J., Wolters, P., Chiappalone, M., Martinoia, S., van Someren, E. J. W. and van Ooyen, A. (2008), 'Low-frequency stimulation induces stable transitions in stereotypical activity in cortical networks.', *Biophys J* **94(12)**.
URL: *http://dx.doi.org/10.1529/biophysj.107.112730*

van Rossum, M., Bi, G. and Turrigiano, G. (2000), 'Stable Hebbian learning from spike timing-dependent plasticity', *J.Neurosci.* **20**(23), 8812–8821.
URL: *PM:11102489*

Vyazovskiy, V. V., Cirelli, C., Pfister-Genskow, M., Faraguna, U. and Tononi, G. (2008), 'Molecular and electrophysiological evidence for net synaptic potentiation in wake and depression in sleep.', *Nat Neurosci* **11**(2), 200–208.
URL: *http://dx.doi.org/10.1038/nn2035*

Wang, X.-J. and Rinzel, J. (1992), 'Alternating and synchronous rhythms in reciprocally inhibitory model neurons', *Neural Comput.* **4**(1), 84–97.

Watts, D. J. and Strogatz, S. H. (1998), 'Collective dynamics of 'small-world' networks.', *Nature* **393**(6684), 440–442.
URL: *http://dx.doi.org/10.1038/30918*

Wen, Z. and Zheng, J. Q. (2006), 'Directional guidance of nerve growth cones.', *Curr Opin Neurobiol* **16**(1), 52–58.
URL: *http://dx.doi.org/10.1016/j.conb.2005.12.005*

Wilson, S. W. and Easter, S. S. (1991), 'A pioneering growth cone in the embryonic zebrafish brain.', *Proc Natl Acad Sci U S A* **88**(6), 2293–2296.

Wolpert, L. (2002), *Principles of development*, Vol. 2nd ed, Oxford University Press, Oxford.
URL: *http://www.loc.gov/catdir/enhancements/fy0613/2002265416-d.html;http://www.loc.gov/catdir/enhancements/fy0613/2002265416-t.html*

Xu, J., Rosoff, W. J., Urbach, J. S. and Goodhill, G. J. (2005), 'Adaptation is not required to explain the long-term response of axons to molecular gradients.', *Development* **132**(20), 4545–4552.
URL: *http://dx.doi.org/10.1242/dev.02029*

Yeung, L., Shouval, H., Blais, B. and Cooper, L. (2004), 'Synaptic homeostasis and input selectivity follow from a calcium-dependent plasticity model', *Proc.Natl.Acad.Sci.U.S.A* **101**(41), 14943–14948.
URL: *PM:15466713*

Zhou, Z. J. and Zhao, D. (2000), 'Coordinated transitions in neurotransmitter systems for the initiation and propagation of spontaneous retinal waves.', *J Neurosci* **20**(17), 6570–6577.

Zhuang, B. and Sockanathan, S. (2006), 'Dorsal-ventral patterning: a view from the top.', *Curr Opin Neurobiol* **16**(1), 20–24.
URL: *http://dx.doi.org/10.1016/j.conb.2005.11.001*

Bound copies of published papers

Journal of Integrative Neuroscience, Vol. 5, No. 3 (2006) 483–488

Imperial College Press
www.icpress.co.uk

Book Review

S. Coombes and P. Bressloff, eds., (2005) Bursting: The Genesis of Rhythm in the Nervous System

Roman Borisyuk and Tom Cooke
Centre for Theoretical and Computational Neuroscience,
University of Plymouth, A223 Portland square, Plymouth, PL4 8AA

This book consists of 14 chapters written by different authors, all of which are concerned with the mathematical modeling of bursting neural activity. Bursting neural activity comprises a repetitive sequence of two events: burst generation in which a neuron produces several spikes (usually from 3 to 20 spikes) with relatively short inter-spike intervals (1–5 ms) and a relatively long quiescent interval. The book is amazingly focused; in all the chapters, the authors use very similar approaches to the development and analysis of models of bursting activity. Typically, two mathematical theories are combined: the bifurcation theory and the theory of singular perturbations.

The bifurcation theory is a tool which allows us to characterize the ways in which a dynamical system can undergo a qualitative change in behavior under variation of conditions, parameters, perturbations, etc. For example, the system is in a steady state and parameter variation causes a transition to another dynamical regime, e.g., the regime of regular oscillations. The bifurcation theory provides two possible scenarios for such transitions: (1) Hopf (or Andronov–Hopf) bifurcation where the steady state becomes unstable at the point of bifurcation (or critical parameter value) and the oscillations that appear have small amplitude and a pre-defined frequency of oscillation; (2) Saddle-Node on Invariant Curve (SNIC) bifurcation where the stable steady state disappears by merging with the unstable one and the resulting oscillations have a pre-defined amplitude and a small frequency of oscillation. These two mathematical mechanisms of oscillation appearance are *universal* and they can be applied to the modeling of a broad spectrum of dynamical systems in different scientific disciplines — a beautiful example of the generality of mathematics. Also, bifurcation theory provides critical parameter values or critical boundaries in parameter space separating different dynamical behaviors. Where no bifurcation occurs between one set of parameters and another, we can be sure that the dynamics will be qualitatively the same.

The theory of singular perturbations (as described by Tikhonov in 1953) considers dynamical systems with two different time scales: some variables are fast and others are slow. In this case, a small perturbation of the system can result in a large deviation from the unperturbed trajectory, producing a response with a spike-like shape. The main idea used in the analysis of the fast-slow system is to consider the limiting case when the slow system is stopped completely, i.e., the slow variables are in a steady state. In this case, instead of the full dynamical system, we can consider a reduced dynamical system with only the fast variables. Analysis of the dynamical behavior of the fast system with fixed values of the slow variables is a simpler problem due to the smaller dimensionality of the reduced system. However, the slow variables are also present in the fast system as parameters and some values of these parameters may be critical values for some bifurcations of the fast system.

The combination of the fast-slow system approach with the bifurcation theory provides a powerful tool for modeling bursting activity. Let us consider a simple example. Suppose that the model of bursting activity includes two fast variables, (e.g., voltage and the gating variable for the calcium current) and one slow variable (e.g., the gating variable for the potassium current) and the fast system is bistable, i.e., for some parameter values, the stable steady state coexists with a stable limit cycle. In this case, the bursting regime can be described in the following way: the quiescent interval relates to a steady state in which activity of the fast system is at a low level, and the burst corresponds to high amplitude oscillations. The slow variable (parameter) periodically switches the system between these dynamical regimes in a hysteretic manner.

Another idea used in the modeling of bursting activity comes from the consideration of a model with a two-dimensional fast system and a two-dimensional slow system. Let us suppose that the fast system has some bifurcations in the range of changes of the slow variables and the slow system demonstrates regular oscillations. In this case, the full system will demonstrate bursting activity with a specific shape (e.g., elliptic burster) which depends on the bifurcation of the fast system; bistability in the fast system is not needed to achieve bursting in this model.

The above examples illustrate some typical mechanisms that can be used to describe the generation of bursting activity. Different chapters of the book consider different systems of slow-fast variables and different types of bifurcation which cause the appearance and disappearance of oscillations; nevertheless, the approach to modeling is universal for all book chapters.

The book is divided into two parts: the first is devoted to bursting on the single cell level (six papers) and the second concerns the generation of bursting in neural networks (8 papers).

The first chapter of the book by J. Hindmarsh and P. Cornelius describes the development of the classical Hindmarsh–Rose equations in the 1980s and demonstrates that the introduction of a calcium T-current to a simplified version of the Hodgkin–Huxley equations, makes it possible to generate a bursting behavior driven

by subthreshold oscillations which is not possible in the classical Hindmarsh–Rose equation.

Chapter 2 by R. Bertram and A. Sherman is an interesting pedagogical introduction to the modeling of bursting activity of insulin-secreting pancreatic beta-cells. The authors start from historical remarks on different models of spiking activity based on the idea of relaxation oscillations (fast-slow equations) such as the van der Pol-von der Mark and FitzHugh–Nagumo models of the cardiac pacemaker, the Morris–Lecar model for barnacle muscle fibre, and a modified Morris–Lecar model for beta-cell activity. They formulate the Chay–Keizer model (1982) and follow the progression from the Chay–Keizer model to modern models of beta cell activity investigating the role of different factors in burst generation such as calcium-related negative feedback, calcium-dependent and voltage-independent potassium channels, and the interplay between membrane processes and calcium storage in the endoplasmic reticulum.

In Chap. 3, Roper *et al.* present a study of autoregulation of the bursting of AVP (Arginine Vasopressin) neurons of the rat hypothalamus. These neurons secrete AVP into the blood to regulate both blood osmolality and pressure. The authors analyze the electrical properties of AVP cells and develop a Hodgkin–Huxley type model which includes five currents. An elegant reduction to a fast-slow system similar to the Morris–Lecar model makes it possible to model the bursting regime and clarify the role of calcium in regulating a fine balance between after burst depolarization and hyperpolarization.

Chapter 4 concerns bifurcation in the fast dynamics of neurons and its implications for bursting. J. Guckenheimer *et al.*, J. Tien and A. Willms present a detailed two-parametric bifurcation analysis of a two-dimensional Hodgkin–Huxley reduction containing fast sodium and leak currents only. The authors consider this system to be a typical example of a fast system such as appears in many models of bursting activity. The two-dimensional bifurcation diagram shows a broad variety of interesting bifurcations including a homoclinic bifurcation when the stable and unstable separatrices of the saddle point coincide; a Bogdanov–Takens bifurcation point; a narrow region of canard limit cycles, etc. The authors use this bifurcation diagram as a basis for a systematic consideration of several models of bursting activity in different cell types: the R15 neuron of Aplysia; a thalamocortical relay neuron; a leech heart interneuron; and a neuron in the pre-Botzinger complex participating in breathing rhythm generation.

In Chap. 5, A. Bose and V. Booth study the bursting regime in a Pinsky–Rinzel model of a pyramidal neuron in the CA3 region of the hippocampus. The model consists of dendritic and somatic compartments, and each of them includes active ionic conductances. The authors consider both the Pinsky–Rinzel model and its simplified version (similar to the Morris–Lecar model). The authors discuss several interesting questions relating to burst generation, e.g., the role of backpropagating spiking activity from the somatic compartment to the dendritic compartment. A fine balance of the strength and timing characteristics of the interaction between

the two compartments can result in the appearance of an interesting regime of bursting activity named somatic-dendritic ping-pong.

Further study of the role of active dendrites is undertaken by C. Laing and B. Doiron in Chap. 6 where they analyze a model of bursting activity observed in sensory processing neurons of a weakly electric fish. The authors discuss a novel type of bursting activity known as ghostbursting. A characteristic feature of ghost-bursting activity is that the frequency of spikes within the burst increases from zero to some finite value (i.e., interspike intervals inside the burst become shorter and shorter). It is natural to model this experimentally observable phenomenon by the use of the abovementioned Saddle-Node on Invariant Curve (SNIC) bifurcation of the fast system. When the system passes close to the region of phase space where this bifurcation occurs, the passage is very slow. It is as if the trajectory is "sensing the ghost" of the bifurcation, hence the name of this bursting phenomenon. A particularly interesting feature of this model is that there is no bistability in the fast system which is unusual for bursters with only one slow variable.

The second part of the book is devoted to the modeling of bursting activity in neural networks. It begins from Chap. 7 in which C. Canavier considers the stability of the phase locking regime in small circuits of two interacting neurons or three neurons on the ring by the Phase Resetting Curve (PRC) approach. An interesting hybrid system of one real biological and one model bursting neuron is considered and the PRC method is applied to study 1:1 locking under variation of experimental conditions.

In Chap. 8, Golubitsky *et al.* also investigate a system of two identical bursting neurons. The authors' mathematical approach is based on consideration of a system with symmetry which appears due to the identity of interactive two-dimensional fast-slow systems of differential equations. Using bifurcation analysis of a general fast system with symmetry, the authors find a collection of interesting burster shapes which can be realized in such systems.

Chapter 9 by G. de Vries is devoted to a study of models of bursting activity based on one- and two-dimensional maps. The author reviews purposely constructed maps that can generate a series of points in discrete time resembling bursting activity in a conventional model. For example, in the case of the one-dimensional map, the function is non-continuous and contains a non-linear parabolic term which generates irregular oscillations with increasing amplitude (the burst) and a linear part (almost flat with a small increase), which corresponds to quiescent activity. In the case of the two-dimensional map, the idea of fast and slow variables is used for the construction of appropriate maps. The fast map is bistable and the stable fixed point (quiescent state) coexists with a stable periodic or chaotic orbit (burst). Changes in a slow variable allow bursting activity to be generated through a hysteresis loop. The author analyzes (both numerically and analytically) the influence of different symmetric couplings between two identical maps on the resulting dynamics and unsurprisingly finds both in-phase and anti-phase locking, as well as out of phase oscillations. The map-based approach to burster modeling considered in this chapter is simple

and elegant; however, a significant disadvantage is that models are formulated in an abstract mathematical form without taking into account biophysical aspects of spike generation such as voltage, conductance, etc.

Chapter 10 by G. de Vries and A. Sherman also studies the effect of coupling between two identical neuronal models. The neuron model is of Hodgkin–Huxley type with square wave burster dynamics and coupling is the so-called diffusion type where the difference between voltages defines the influence of one cell to another. This type of coupling is standard for modeling electrical connections between neurons. The authors found that when bursters are coupled, the period of oscillations can increase. In the case that uncoupled neurons do not burst but are close to the bursting mode, coupling can induce bursting and the authors name this phenomenon "emergent bursting". The authors present an interesting discussion of the possibility of emergent bursting in oscillators with other types of intrinsic behavior and synaptic connectivity.

In Chap. 11, J. Tabak and J. Rinzel study a population rate model of spontaneous activity in the developing spinal cord. The model considered describes the average rate of a population of excitatory neurons and the evolution of synaptic efficacy by both fast and slow variables, representing depression of effective connectivity. The authors apply the fast-slow "dissection" technique to analyze the dynamical behavior of this three-dimensional model. They find bistability in the slow equation and by combining oscillations in the two-dimensional fast system with the dynamics of the slow variable, the bursting regime is generated. This model explains the intermittency of episodes of spontaneous activity in the spinal cord with longer quiescent intervals. The described mechanism of burst generation is typical for square wave bursting and is similar to many other models considered in the book (see, for example, Chaps. 2, 8, 10, 12, 13): a slow variable periodically switches the fast system from a low activity steady state to a high activity oscillatory regime. Also, the authors consider important parallels and similarities in the generation of bursting activity between coarse grain population models and conductance-based models. Finding such similarities makes it possible to bring results from the population level to the level of spiking neurons. It is worth noting that this model reproduces another interesting phenomenon experimentally observable in the chick spinal cord: the blockade of some connections results in the cessation of spontaneous activity with consequent recovery. The model demonstrates longer inter-episode intervals after recovery, in a manner that matches the experimental data.

Chapter 12 by R. Butera *et al.* provides a detailed and deep review of the bursting activity of neurons that generate breathing rhythms in the pre-Botzinger complex of the brainstem. The authors consider both spike generation models and neural network models of bursting cells, and address important questions regarding the biophysical mechanism of bursting, regulators of bursting frequency, synchronization in a coupled population of bursting cells, etc. It is shown that coupling between square-wave bursters can result in a new type of bursting, so-called top hat bursting

where spiking ceases via a fold bifurcation of limit cycles. The authors simulate a heterogeneous population of coupled neurons with randomly distributed parameter values; some neurons are silent, some are bursting, and some are tonically spiking. Remarkably, the introduction of excitatory coupling of sufficient strength results in a regime in which all neurons participating in synchronous bursting oscillations.

In Chap. 13, J. Best and D. Terman nicely demonstrate how the powerful tool of geometric singular perturbation methods can be applied to prove mathematical theorems concerning the properties of bursting activity. In particular, it is proven that in a model with a two-dimensional fast system and a one-dimensional slow system under general conditions, the unique and stable solution corresponding to the square-wave burster can exist in a small interval of parameter values. Another interesting result relates to a study of propagating activity patterns in a mutually inhibitory chain of neuronal oscillators. Singular perturbation makes it possible to find parameter values corresponding to the propagation of smooth and lurching waves, as well as analytical estimates for the speed of wave propagation. A neural network of excitatory and inhibitory cells in the basal ganglia models the shift from irregular firing to synchronous bursting, during the development of Parkinson's disease. Geometrical methods are used to find parameter regions corresponding to different regimes as well as to analyze the clustering of neural activity.

Lastly, Chap. 14 by B. Ermentrout *et al.* is a short and elegant report on new studies of wave propagation models describing spike propagation in cortical slices with reduced inhibition. This relates to the extremely important question of understanding the role of spatio-temporal patterns of neural activity, particularly, wave propagation, in the information processing within the brain. The neuron model considered demonstrates elliptic bursting, and analysis of this system makes it possible to find parameter regions in which the oscillatory waves break up, as well as provide insight into the underlying mechanism of wave propagation.

In summary, the book is a good description of the state-of-the-art within the area of computational and mathematical modeling of bursting phenomena, containing contributions from many of the leading researchers in this field; experts in computational neuroscience are certain to find it interesting and useful. Many chapters are written in a review style with remarks on the history of the study of mechanisms of bursting generation; thus, it can also be recommended to graduate students. For beginners, we can recommend first reading the introductory book "Dynamical Systems in Neuroscience: The Geometry of Excitability and Bursting" (MIT Press, 2006) by E. Izhikevich, which will allow them to familiarize themselves with the subject and prepare for reading the reviewed book.

Available online at www.sciencedirect.com
ScienceDirect
BioSystems 89 (2007) 30–37
BioSystems
www.elsevier.com/locate/biosystems

Metastable states, phase transitions, and persistent neural activity

Roman Borisyuk *, Tom Cooke [1]

Centre for Theoretical and Computational Neuroscience, University of Plymouth, Plymouth PL4 8AA, UK

Received 15 December 2005; accepted 28 May 2006

Abstract

A new mathematical model to describe the spiking rate of a neural population is derived, which considers both the mean and the variance of the activity. Bifurcation analysis identifies a critical interval of parameter values in which the standard bistability regime coexists with an additional third attractor corresponding to the metastable state of bounded mean activity and high variance. To understand the structure of spatio-temporal activity in the metastable state, we study a simple discrete-time model of binary elements with random noise locally coupled on the grid, which produces rich dynamics including metastability. A critical value of the noise amplitude is identified; in the vicinity of this value the system is flexible and can easily generate transitions between UP and DOWN metastable states, either autonomously or in response to a control process. These metastable states and phase transitions provide a proper basis for the modelling of persistent neural activity reported in many experimental studies.

Keywords: Bistability; Self-organization of neural activity; Role of noise

1. Introduction

In the typical experimental paradigm under which persistent activity has been observed, activity appears in response to the presentation of a specific short stimulus and lasts from a few seconds up to several minutes after stimulation is withdrawn. This type of neural activity is traditionally considered to be a process underlying memory, specifically short-term memory formation (Brody et al., 2003). Another possible role of persistent activity is to provide a source of excitation to drive a motor behaviour, for example, swimming in simple vertebrates (Roberts et al., 1997, also recent unpublished results).

Recent experimental data show that persistent neural activity is observed in many brain systems. It has been shown (Egorov et al., 2002) that the neurons of the rat entorhinal cortex in the parahippocampal region demonstrate graded persistent activity (constant firing rate) lasting for several minutes in response to stimulation. The sustained activity level (firing frequency) can be either increased or decreased depending on the input. These findings indicate that the entorhinal cortex could play an important role in establishing associations between stimuli (Frank and Brown, 2003). It has also been found (Taube and Bassett, 2003), that many so-called head direction cells in the rat limbic system exhibit characteristics of persistent neural activity. It is likely that this type of neural activity reflects processes corresponding to the memorization of head direction. In vivo intracellular recordings from oculomotor neurons of the goldfish demonstrate persistent changes in firing rate following

* Corresponding author. Tel: +44 1752 232619; fax: +44 1752 233349.
E-mail addresses: rborisyuk@plymouth.ac.uk (R. Borisyuk), tcooke@plymouth.ac.uk (T. Cooke).
URL: http://www.tech.plym.ac.uk/soc/staff/roman/home2.htm (R. Borisyuk).
[1] Tel.: +44 1752 232714; fax: +44 1752 233349.

0303-2647/$ – see front matter
doi:10.1016/j.biosystems.2006.05.008

saccades (Aksay et al., 2000, 2001). This persistent activity can probably be associated with short-term memorization of eye position in the goldfish hindbrain. Local cortical neural circuits in the prefrontal cortex and visual cortex of the rat are capable of generating persistent activity for periods of seconds or longer as well as transitions between different states of persistent activity such as UP and DOWN states (McCormick et al., 2003). It is possible that this activity indicates processes of working memory based on recurrent network activity. Experimental recordings from prefrontal neurons of monkeys (Compte et al., 2003) reveal persistent activity during a delayed response task. This study shows that the persistent neural activity observed in prefrontal cortex is highly irregular and can best be characterised by statistical measures such as inter-spike interval distribution, autocorrelation function, mean, standard deviation, and other moments. This irregularity is more pronounced during the mnemonic delay period than in the fixation period.

Computational models of persistent activity usually exploit one of the following approaches: (1) there are features of neuronal excitability or synaptic transmission which allow long characteristic times of some membrane and synaptic processes; (2) persistent activity is a collective effect and dynamical phenomenon which appears as the result of specific interactions between neurons. In this paper we adopt the second approach and consider the problem of how to obtain persistent and long lasting activity in a population of interactive neurons with relatively short reaction times.

The traditional approach to solving the problem of long lasting activity is based on bistability of the population spiking rate. This bistability can appear, for example, as the result of positive feedback in a population model (Brunel, 2003). Suppose that there are two stable states of neural activity such that in one of these activity is low and in the other activity is high. These two stable states coexist and the population demonstrates a low or high spiking rate depending on the initial condition. If the initial condition belongs to the basin of attraction of the low state then the population will demonstrate a low activity level and vice versa. Let us suppose that the population is in the low activity state and a short external input is applied. This perturbation by external input can change the dynamical regime of the population and move it from the basin of attraction of the low state to the basin of attraction of the high state. Even a short input application can be sufficient to move the activity of the population through the critical boundary in the phase space of the system which separates these two basins of attraction. In principle the system can return back to the low level; for example, due to habituation, fatigue, or a limited amount of neuromodulators or other chemicals, the system parameters can slowly change their values resulting in the neural activity returning to a low level. This is a hysteresis phenomenon which typically appears in systems with bistability and its explanation is based on the appearance of two fold bifurcations in the dynamical system that controls the spiking rate of the population.

In this paper we study persistent activity in simple models of neural populations of excitatory neurons with random noise. This study was inspired by ideas from statistical physics which generalise the bistability approach by considering phase transitions and metastable states. It is well known that metastable states can be characterised by long lasting phases and such an approach appears to be promising for modelling persistent activity in the brain. A typical example of long lasting patterns is provided by the Ising model which is one of the simplest examples of a system in which metastable states and phase transitions can be seen. We will start by studying persistent activity at the macro-level using a mathematical stochastic model of neural activity which describes the dynamics of the probability density function of spiking neurons (Kryukov et al., 1990). From this model we derive a generalisation of the standard model of population activity rate. This generalised model includes two equations for the dynamics of the mean and variance of the spiking rate. A new feature of this generalised model is that there are three basins of attraction in this system. Two of them correspond to stable low and high activity levels and the third can be considered as an analogue of the metastable state in the Ising model. In this new attractor state, the level of mean activity is bounded while the variance increases without limit. This increase in variance means that the population of neurons demonstrates irregular spiking activity. Note that experimental data indicates that spiking is highly irregular during the persistent activity state (Compte et al., 2003).

In the second part of the paper, we study persistent activity and metastable states in a more detailed model which represents the micro-level. We consider a model of a population of interactive neural elements on a square grid with local connections, similar to the Ising model. The neural element considered here is a simple threshold device which integrates the activities of its neighbours and also includes a random variable which reflects neural and synaptic noise. Thus, the dynamics of the model elements depend on the interplay of two factors: the total activity of neighbouring elements and the level of the noise. We have found that there is a critical level of noise which maximizes the variance of neural activity; this is due to the appearance of frequent phase transitions

between distinct metastable states in the vicinity of this noise level.

2. Population rate model of metastability

2.1. Model description

We consider a neural network of M spiking neurons with homogeneous (e.g. local) connections and mean connection strength a. Suppose that multiple spike trains generated by the neural network are represented by the M-dimensional random point process which is defined by the backward recurrent times: $s=\{s_i(t)\}$, $i=1, 2, \ldots, M$. Here, $s_i(t)$ is the duration of the time interval between the last spike generated by the ith neuron and the current time t. Average neural network activity at time t is described by the random variable $\xi(t)=(1/M)\sum_{j=1}^{M}\exp(-\alpha s_j(t))$ with probability density function $\mu(t)$, mean $E(t)=\mathbf{E}\{\xi(t)\}$ and variance $V(t)=\mathbf{E}\{E(t)-(\mathbf{E}\{\xi(t)\})^2\}$, where $\mathbf{E}\{\cdot\}$ denotes expectation, and α is the characteristic decay of spike influence to other neurons. The random variable $\xi(t)$ reflects the dynamics of the membrane potential of a typical representative element of the network activity. It has been shown (Kryukov et al., 1990) that the probability density function satisfies the Kolmogorov equation:

$$\frac{\partial \mu_t}{\partial t}=\frac{\partial}{\partial \xi}[(a\xi - S(a\xi))\mu_t]+\frac{1}{M}\frac{\partial^2}{\partial \xi^2}[D(a\xi)\mu_t].$$

From the Kolmogorov equation the system of kinetic equations can be derived by a standard transformation, and we consider here an approximation based on equations for the first two moments: the mean $E(t)$ and the variance $V(t)$:

$$\begin{cases}\dfrac{dE}{dt}=-E+S(aE)+\dfrac{S''(aE)}{2}a^2V\\[2ex]\dfrac{dV}{dt}=-2V(1-aS'(aE))\end{cases}, \qquad (1)$$

where a sigmoid function $S(x)=1/(1+\exp(-b(x-\theta)))-1/(1+\exp(b\theta))$; S' and S'' are the first and second derivatives of sigmoid function, respectively; parameter a is a characteristic of coupling strength; parameter values for simulations are: $b=3$, $\theta=2$.

2.2. Metastability and other dynamical regimes

A typical phase portrait of the system (1) is shown in Fig. 1 for the connection strength $a=4$. Here for $V=0$ there are three equilibria: two of these at $E=0$ (low activity) and $E=1$ (high activity) are stable, and the third at

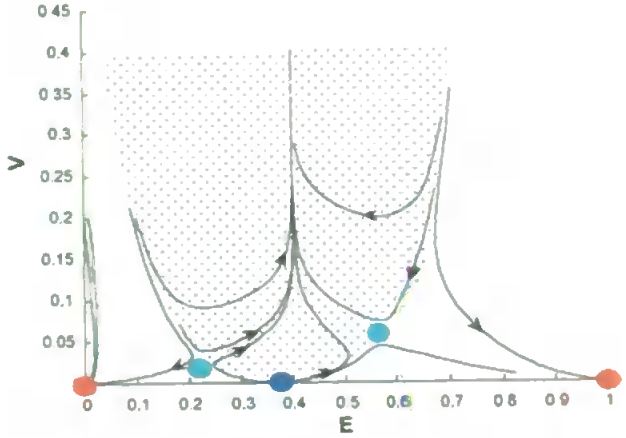

Fig. 1. Phase portrait of system (1). The basin of attraction of the metastable state is indicated by shading. This region is bounded by incoming separatrices of two saddle equilibria.

$E=0.4$ is unstable. Also, there are two saddle equilibria with $V>0$.

The traditional simplified approach to the modelling of bistability is based on the consideration of the average activity of the neural population without taking into account the variance and other moments characterizing probabilistic properties of neural activity in a stochastic model. In this case of zero higher order moments, two stable equilibria on the horizontal axis ($V=0$) are the only attractors in the system, and this gives bistability. The model (1) is more sophisticated and takes into account both the mean and the variance of neural activity. In this case we have an additional attractor which is shown in Fig. 1. This attractor is formed by the two outgoing separatrices of the saddles which approach each other increasing the value of variance and engaging many other trajectories in the region of metastability. The basin of attraction of this metastable state is indicated by shading in Fig. 1. Interestingly, this new regime of metastability is characterised by the following property: the mean is bounded, and the variance grows to infinity. This reflects the experimental finding that neural activity in persistent states is very irregular. However, unlimited growth of the variance is an undesirable feature of the model; in reality variance will always be bounded. This feature appears due to the fact that the activity distribution is approximated by two moments. Of course, in the case that a more realistic approximation with a larger number of moments is used, we can expect that the variance will grow up to some limit (Feller, 1967). It is important to note that the basin of attraction of this new regime covers a large part of the phase plane.

Let us consider the evolution of the phase portrait under variation of the connection strength $a>0$. For

small values of this parameter there is only one stable equilibrium $E=0, V=0$, which corresponds to a low level of background neural activity. If the value of this parameter increases, the system goes through two sequential fold bifurcations ($a_1^{cr} = 1.35, a_2^{cr} = 3$) and for $a>3$ the phase portrait is topologically equivalent to the phase portrait shown in Fig. 1 for $a=4$.

Let us fix initial values of variables of the system (1) as $E=0.4$, $V=0.05$ which correspond to the intermediate level of the mean and small variance. Let us keep these initial values fixed and study the final destination of the trajectory starting from this initial point of the phase plane under variation of the connection strength parameter. The result is:

- For all values $a<3.35$ the trajectory tends to a low activity level with zero variance.
- For all values $3.35<a<7.45$ the trajectory tends to the metastable state with limited mean and high variance.
- For all values $a>7.45$ the trajectory tends to a high activity level with zero variance.

Fig. 2 illustrates three attractors in the system: two stable steady states and the metastable state. This figure shows three trajectories starting from the same initial point for different values of the connection strength parameter, resulting in three different final destinations. For small or large connection strengths the destination is a low or high level of background activity with zero variance, however for intermediate connection strengths the destination is a metastable state with limited mean of neural activity and unlimited growth of variance.

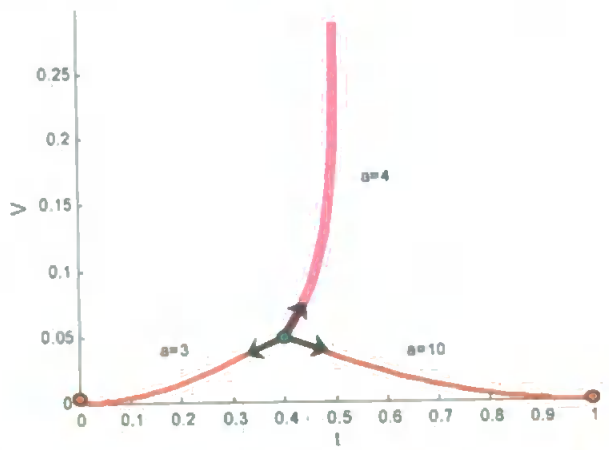

Fig. 2. Initial conditions are fixed: $E=0.4$, $V=0.05$. Figure shows three different destinations of trajectories corresponding to different coupling strengths a: weak coupling (e.g. $a=3$) results in low activity; strong coupling (e.g. $a=10$) results in high activity; an intermediate coupling (e.g. $a=4$) results in the metastable state.

3. Metastability and persistent activity in Ising type model with noise and homogeneous local coupling

3.1. Model motivation

In this section we introduce a system of locally coupled threshold elements with random noise and local connections in a square grid topology. This system was motivated by the discrete-time Hopfield model of associative memory (Hopfield, 1982). The rule for updating the state of each element contains two terms: a term taking into account the activities of the element's neighbours, and a noise term. The resulting dynamics appear due to the interaction of the deterministic term and the stochastic component. Thus, the dynamics of the model are richer than the pure deterministic dynamics of the Hopfield model and the pure stochastic behaviour of the Ising model. Of particular interest are the metastable and phase transition regimes which can be observed within a specific range of noise amplitudes. These observations are relevant to the general problem of characterizing the role of noise in system dynamics.

3.2. Model description

We consider a system of interacting elements coupled on the grid where the edges of the grid are connected to each other, forming a torus. Each element is connected with eight neighbouring elements. Activity is described by $x_i=\{0,1\}$, $i=1, 2, \ldots, M$, where M is the number of elements. The firing threshold θ is fixed and is the same for all elements. All connections have weight 1.

Time is discrete and elements are updated synchronously. In order to compute the new activity of the element i at the moment $(t+1)$, it is necessary to first calculate the total input $I_i(t)$. In the equations below $N(i)$ refers to the set of eight nearest neighbours to the element i on the grid. As can be seen below, the element i also receives input from itself. The term ξ_i represents location and time independent Gaussian noise with zero mean and standard deviation σ.

$$\begin{cases} I_i(t) = \sum_{j \in N(i)} x_j(t) + x_i(t) + \xi_i \\ x_i(t+1) = \begin{cases} 1, & \text{if } I_i(t) \geq \theta \\ 0, & \text{if } I_i(t) < \theta \end{cases} \end{cases} \quad (2)$$

If the number of active elements in the vicinity of node i is substantially less than or greater than threshold, it is unlikely that the noise will affect the state of that node at the next time step. For example, if the noise standard

deviation is $\sigma = 1$ then the probability of an element having $I_i(t) = 4$ or 5 (these are the borderline cases) changing state due to noise is 0.31 and this decreases rapidly as $I_i(t)$ takes values further away from 4.5; for $I_i(t) = 3$ or 6 the probability of a noise-driven switch is 0.067.

For all simulations, initial conditions are that the value of each x_i is randomized independently and uniformly to 0 or 1, unless stated otherwise. The dimensions of the grid are 50 elements on each side, and the number of elements $M = 2500$.

Inclusion of the above-mentioned self connection makes it possible to achieve symmetry between any given configuration and its inverse when the uniform threshold is set to 4.5. In this case we can consider two initial configurations where one is the inverse of the other (inactive elements in one area are active in the other and vice versa) and subject them to noise of the same value but opposite sign (e.g. by seeding our pseudo–random number generator with the same value in both cases and modifying Eq. (2) for either system to change the sign of the noise term), then subsequent states will also be the exact inverse. It also follows that any steady state in the system appears in a pair with its inverse.

3.3. Simulation results

We consider a series of simulations starting from many random initial configurations for a range of noise levels, with a particular interest in finding persistent and metastable states.

When $\sigma = 0$, the system rapidly (typically in around 18 time steps) converges to one of many possible steady states. When the initial conditions for activity are completely randomized, this steady state will contain distinct active and inactive regions (Fig. 3) with approximately 50% of elements active in the final configuration. This configuration is characterised by the presence of clusters of active and inactive nodes and we will refer to it as a cluster configuration.

It is helpful to consider the stability of the cluster in terms of the stability of the locality around each point. An active cell with four or more neighbours active will remain active. An inactive cell with four or more neighbours inactive will remain inactive. These are the only possibilities for local stability and this constrains the set of possible stable system configurations; for example, an isolated 2×2 square of activity or inactivity cannot appear in a stable configuration because each element will only have only three neighbours that share its state instead of the required four.

In the case where $\sigma > 0$ and small, the noise tends to destroy cluster configurations which are typical for the zero noise case. Starting from an arbitrary random configuration, the activity dynamics relatively rapidly (within a few hundred time steps when $\sigma = 1$) leads to one of three cases: (1) almost all elements are active (we will refer to this as the UP state), (2) almost all elements are inactive (DOWN state), or (3) approximately 50% of the elements are active, and a situation has developed where inactive and active regions exist side by side, neither surrounding the other. Fig. 4 illustrates these cases by plotting the mean activity of 20 random initial configurations which are simulated for 500 time steps. Fig. 5 shows the spatial pattern of activity for case (3), which we consider as an analogue of the metastable state in statistical physics.

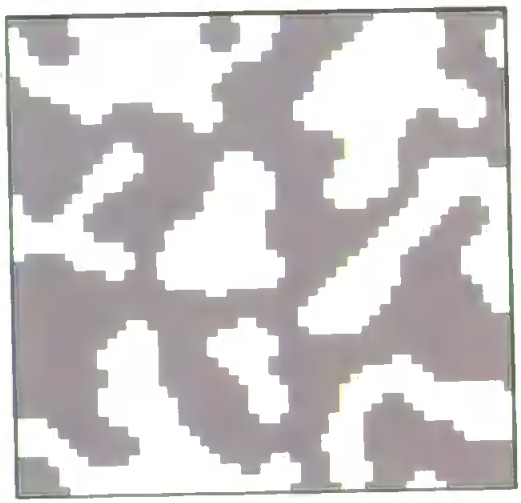

Fig. 3. Steady state resulting from a randomized initial configuration. White squares represent active elements.

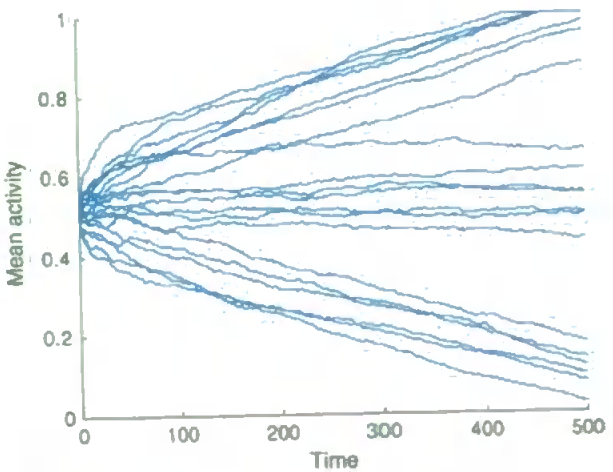

Fig. 4. Mean activity trajectories from twenty randomized initial conditions where $\sigma = 1$. The three possible classes of outcome (UP state, DOWN state, metastable state) are clearly visible.

Fig. 5. Long lasting intermediate activity state, in which the boundary between active and inactive regions moves according to a slow random walk process.

When case (3) develops, the borders between the two regions shown in Fig. 5 are effectively neutral in the sense that they are equally likely to move in either direction. This means that they move according to a (very slow) random walk process, and so this configuration is long lived. Eventually the system will converge to a steady UP or DOWN state (with sparse spontaneous firing/quiescence) but this can take hundreds of thousands of cycles in some cases. In this regime, the system has the interesting and biologically useful property of acting like a kind of memory.

For large values of σ, the noise term in Eq. (2) dominates the deterministic term and the dynamical behaviour of the model can be characterised as the independent appearance of active/inactive states in nodes of the grid with equal probabilities. Thus, the mean activity is close to 50% and a typical spatial configuration is shown in Fig. 6.

The most interesting and sophisticated case corresponds to intermediate values of σ. In this case there is a balance between the relative influences of the deterministic and stochastic terms in Eq. (2). As sigma is increased past about 3.6 the influence of noise overwhelms the influence of the local neural connectivity. At this point the system is no longer able to maintain distinct UP and DOWN states and the mean activity of the system oscillates around 0.5 (half of the elements are active). For intermediate values of σ (σ is about 3.3), several phenomena can be seen: the pattern irregularity (and therefore, variance of the total network activity) increases, the mean time to reach a steady state decreases, and there is an increase in the amount of spontaneous activity and spontaneous inactivity observed. As sigma

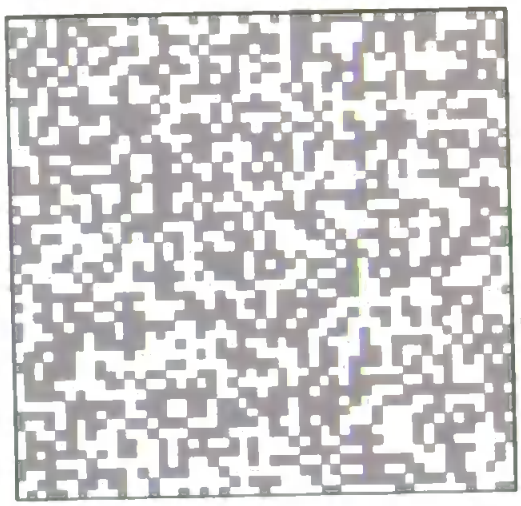

Fig. 6. Spatial configuration when $\sigma = 20$, showing the lack of spatial organization in the system at high noise amplitudes.

is increased above about 3.3, the high activity and low activity states very rapidly lose stability and a regime develops where the network switches between varying about a high level of activity, and varying about a low level of activity. This is the regime of phase transitions and each phase (UP and DOWN) can be characterised as a metastable state. Fig. 7 shows a typical time course of the mean activity and Fig. 8 shows typical spatial configurations corresponding to the DOWN, intermediate, and UP phases.

Fig. 9 shows a histogram of samples of the mean of population activity in the regime of UP and DOWN alternation accumulated during a run of 10^6 time steps. The histogram shows a bimodal form with a small bias towards DOWN phases due to limited run length.

We can use a plot of variance against sigma to reveal the region in parameter space in which the UP and DOWN/metastable regime exists (Fig. 10). This indicates that the critical level of noise for promoting metastability of the high and low activity states is approximately 3.4. This result is in line with the coherence resonance phenomenon which has been observed in

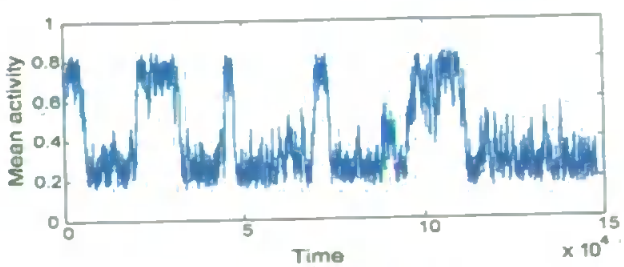

Fig. 7. Plot of mean activity with $\sigma = 3.37$. The system alternates between metastable high and low activity states.

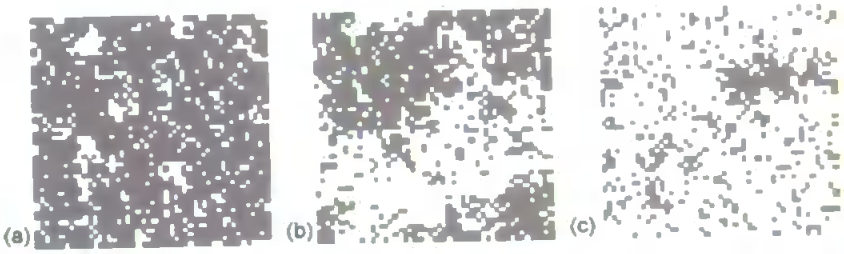

Fig. 8. Low, intermediate, and high activity spatial configurations where $\sigma = 3.37$. The intermediate configuration is highly unstable and will quickly transition to a high or low activity state.

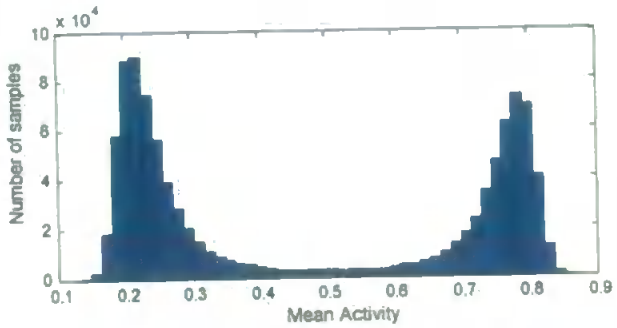

Fig. 9. Distribution of instantaneous mean activity samples for $\sigma = 3.37$. Run length is 10^6 time steps.

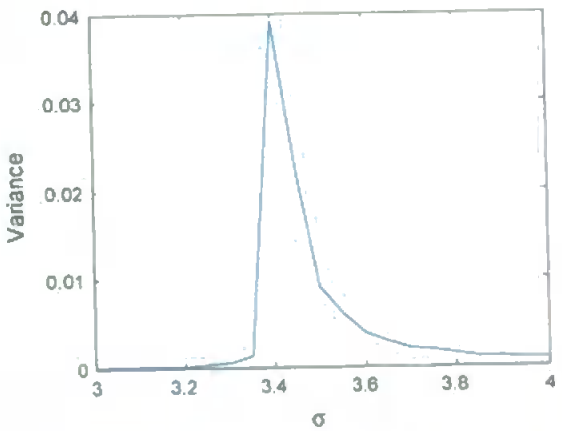

Fig. 10. Variance of mean activity as a function of noise amplitude. Variance is maximized at approximately $\sigma = 3.4$.

excitable media and single neuron integrate and fire models (Pikovsky and Kurths, 1997; Lindner et al., 2002).

4. Discussion

A new mathematical model to describe the activity rate of a neural population is derived. The derivation is based on a probabilistic model of multiple interactive point processes mimicking the interaction of neural spike generators. The model considers both the mean and the variance of the activity rate. The bifurcation analysis according to coupling strength variation shows that there is a critical interval of parameter values in which the standard bistability regime coexists with a third attractor which corresponds to the metastable state which is characterised by a bounded value of the mean and unlimited growth of the variance of the activity rate.

We speculate that the metastable state is an appropriate mathematical description of persistent activity in neural networks. Indeed, many properties of the metastable state are similar to features of experimentally recorded persistent activity. Also, a metastable activity state can be autonomously switched to another state without the involvement of any external influence. Thus, a system of interactive populations in a metastable state can be considered as an example of self-organized system behaviour. This self-organization process can be controlled by external influences which can mimic a learning process in a neural system. Suppose that a neural network consists of many interactive populations which are described by similar dynamical systems with metastable states, specifically each small population has three steady states: low and high stable states and a metastable state. Such a network can demonstrate rich dynamics related to different types of information processing. For example, perturbations from the internal part of the network or from an input signal can result in system transition from one metastable state to another. These transitions can be easily performed by the network due to high variability of neural activity in the metastable state (high variance).

To understand the structure of spatio-temporal activity in the metastable state, we study a simple discrete-time model of binary neurons locally coupled on the grid. This model is capable of producing rich dynamics including metastability when combined with noise. Moreover, we have noted that in this model metastability results from a balance between the strength of coupling between individual elements and the noise amplitude; if either dominates, the spatio-temporal activity of the network rapidly becomes stereotyped. Thus, critical values of noise amplitude generate interesting dynamical

behaviour in the model. In this critical region the system is flexible and can be easily switched between metastable states both autonomously (UP and DOWN phase transitions) or by a control process.

We can suggest that such a balance between deterministic and stochastic components may be an important factor in the dynamics of coupled neural networks in the brain. We speculate that the working mode of the active brain is in the vicinity of the critical regime (Massimini et al., 2005) and modulation of this balance (for example, during sleep) may allow the network to act as an adaptive memory under certain conditions, and as a source of coherent variable activity under other conditions; such shifts in network dynamics may be implicated in both development (Tabak et al., 2001) and the maintenance of synaptic homeostasis (Tononi and Cirelli, 2003).

The simulation model considered here is very simple; nevertheless it already demonstrates many important characteristics of neural activity and persistent states. This model can show some long lasting states, transitions between UP and DOWN states, and a critical value of noise. Further support for the usefulness of this simple model comes from our development of a similar model with local connections along the grid edges but with more realistic enhanced integrate-and-fire elements (Borisyuk, 2002), which demonstrates broadly equivalent behaviour.

A biologically inspired generalisation of this model has been developed which includes both threshold adaptation and synaptic plasticity. To obtain the persistent regime in a neuronal system thresholds and synaptic weights have to be properly adjusted. We can expect that under some constraints the system with threshold adaptation and synaptic plasticity can self-organize its dynamical behaviour in such a way that the parameter values will be automatically adjusted to generate persistent activity. In addition, the results of studying simplified models, both theoretically and computationally, have been used to simulate a more realistic neural network of enhanced integrate and fire neurons and demonstrate the existence of persistent activity in this model. Our preliminary simulations have yielded some promising results in this direction which are under preparation for publication.

Acknowledgement

RB was supported by EPSRC grant EP/D036364/1.

References

Aksay, E., Baker, R., Seung, H.S., Tank, D.W., 2000. Anatomy and discharge properties of pre-motor neurons in the goldfish medulla that have eye-position signals during fixation. J. Neurophysiol. 84, 1035–1049.

Aksay, E., Gamkrelidze, G., Seung, H.S., Baker, R., Tank, D.W., 2001. In vivo intracellular recording and perturbation of persistent activity in a neural integrator. Nat. Neurosci. 4, 184–193.

Borisyuk, R., 2002. Oscillatory activity in the neural networks of spiking elements. Biosystems 67 (1–3), 3–16.

Brody, C.D., Romo, R., Kepecs, A., 2003. Basic mechanisms for graded persistent activity: discrete attractors, continuous attractors, and dynamics representations. Curr. Opin. Neurobiol. 13, 204–211.

Brunel, N., 2003. Dynamics and plasticity of stimulus-selective persistent activity in cortical network models. Cereb. Cortex 13, 1151–1161.

Compte, A., Constantinidis, C., Tegnér, J., Raghavachari, S., Chafee, M., Goldman-Rakic, P., Wang, X.-J., 2003. Temporally irregular mnemonic persistent activity in prefrontal neurons of monkeys during a delayed response task. J. Neurophysiol. 90, 3441–3454.

Egorov, A.V., Hamam, B.N., Fransen, E., Hasselmo, M.E., Alonso, A.A., 2002. Graded persistent activity in entorhinal cortex neurons. Nature 420, 173–178.

Feller, W., 1967. An Introduction to Probability Theory and its Applications, third ed. Wiley, New York.

Frank, L.M., Brown, E.N., 2003. Persistent activity and memory in the entorhinal cortex. Trends Neurosci. 26, 400–401.

Hopfield, J.J., 1982. Neural networks and physical systems with emergent collective computational abilities. Proc. Natl. Acad. Sci. U.S.A. 79, 2554–2558.

Kryukov, V.I., Borisyuk, G.N., Borisyuk, R.M., Kirillov, A.B., Kovalenko, E.I., 1990. Metastable and unstable states in the brain. In: Dobrushin, R.L., Kryukov, V.I., Toom, A.L. (Eds.), Stochastic Cellular Systems: Ergodicity, Memory, Morphogenesis. Manchester University Press, pp. 225–358.

Lindner, B., Schimansky-Geier, L., Longtin, A., 2002. Maximizing spike train coherence or incoherence in the leaky integrate-and-fire model. Phys. Rev. E 66, 031916.

Massimini, M., Ferrarelli, F., Huber, R., Esser, S.K., Singh, H., Tononi, G., 2005. Breakdown of cortical effective connectivity during sleep. Science 309, 2228–2232.

McCormick, D., Shu, Y., Hasenstaub, A., Sanchez-Vives, M., Badoual, M., Bal, T., 2003. Persistent cortical activity: mechanism of generation and effects on neuronal excitability. Cereb. Cortex 13, 1219–1231.

Pikovsky, A., Kurths, J., 1997. Coherence resonance in a noise-driven excitable system. Phys. Rev. Lett. 78, 775–778.

Roberts, A., Soffe, S.R., Perrins, R., 1997. Neurons, Networks and Motor Behavior. The MIT Press, pp. 83–89 (Chapter 7).

Tabak, J., Rinzel, J., O'Donovan, M., 2001. The role of activity-dependent network depression in the expression and self-regulation of spontaneous activity in the developing spinal cord. J. Neurosci. 21, 8966–8978.

Taube, J.S., Bassett, J., 2003. Persistent neural activity in head direction cells. Cereb. Cortex 13, 1162–1172.

Tononi, G.G., Cirelli, C., 2003. Sleep and synaptic homeostasis: a hypothesis. Brain Res. Bull. 62, 143–150.

Neural Development

BioMed Central

Research article

Open Access

Axon and dendrite geography predict the specificity of synaptic connections in a functioning spinal cord network

Wen-Chang Li[1], Tom Cooke[2], Bart Sautois[3], Stephen R Soffe[1], Roman Borisyuk[2] and Alan Roberts*[1]

Address: [1]School of Biological Sciences, University of Bristol, Woodland Road, Bristol BS8 1UG, UK, [2]Centre for Theoretical and Computational Neuroscience, University of Plymouth, Plymouth PL4 8AA, UK and [3]Department of Applied Mathematics and Computer Science, Ghent University, Krijgslaan 281-S9, B-9000 Ghent, Belgium

Email: Wen-Chang Li - wenchang.li@bristol.ac.uk; Tom Cooke - tom.cooke@plymouth.ac.uk; Bart Sautois - bart.sautois@ugent.be; Stephen R Soffe - s.r.soffe@bristol.ac.uk; Roman Borisyuk - R.Borisyuk@plymouth.ac.uk; Alan Roberts* - a.roberts@bristol.ac.uk

* Corresponding author

Published: 10 September 2007

Neural Development 2007, 2:17 doi:10.1186/1749-8104-2-17

Received: 11 May 2007
Accepted: 10 September 2007

This article is available from: http://www.neuraldevelopment.com/content/2/1/17

Abstract

Background: How specific are the synaptic connections formed as neuronal networks develop and can simple rules account for the formation of functioning circuits? These questions are assessed in the spinal circuits controlling swimming in hatchling frog tadpoles. This is possible because detailed information is now available on the identity and synaptic connections of the main types of neuron.

Results: The probabilities of synapses between 7 types of identified spinal neuron were measured directly by making electrical recordings from 500 pairs of neurons. For the same neuron types, the dorso-ventral distributions of axons and dendrites were measured and then used to calculate the probabilities that axons would encounter particular dendrites and so potentially form synaptic connections. Surprisingly, synapses were found between all types of neuron but contact probabilities could be predicted simply by the anatomical overlap of their axons and dendrites. These results suggested that synapse formation may not require axons to recognise specific, correct dendrites. To test the plausibility of simpler hypotheses, we first made computational models that were able to generate longitudinal axon growth paths and reproduce the axon distribution patterns and synaptic contact probabilities found in the spinal cord. To test if probabilistic rules could produce functioning spinal networks, we then made realistic computational models of spinal cord neurons, giving them established cell-specific properties and connecting them into networks using the contact probabilities we had determined. A majority of these networks produced robust swimming activity.

Conclusion: Simple factors such as morphogen gradients controlling dorso-ventral soma, dendrite and axon positions may sufficiently constrain the synaptic connections made between different types of neuron as the spinal cord first develops and allow functional networks to form. Our analysis implies that detailed cellular recognition between spinal neuron types may not be necessary for the reliable formation of functional networks to generate early behaviour like swimming.

Background

To function properly, nervous systems rely on highly specific synaptic connections between neurons. This specificity is achieved during development by many mechanisms, for example, correct neuronal specification and differentiation, axon path finding, cell recognition and synapse conditioning by neuronal activities. At the core of this, what are the rules that ensure that appropriate and specific synaptic connections are made as neuronal circuits develop? This is one of the most intensively studied areas of developmental neuroscience and has generated an extensive body of knowledge on the chemical cues that control the assembly of neuronal circuits in the central nervous system (CNS) [1-6]. The vertebrate spinal cord provides a simple example where chemical morphogens released from the dorsal roof plate (bone morphogenetic protein) and ventral floor plate (sonic hedgehog (Shh)) form dorso-ventral molecular gradients. These initially control the fate of differentiating neurons to establish a dorso-ventral series of longitudinal columns of distinct neurons on each side (Figure 1c) [7,8]. Once a cell has acquired a specific neuronal fate, the next step is to grow an axon from the neuron soma. The factors controlling the directions of outgrowth are beginning to be

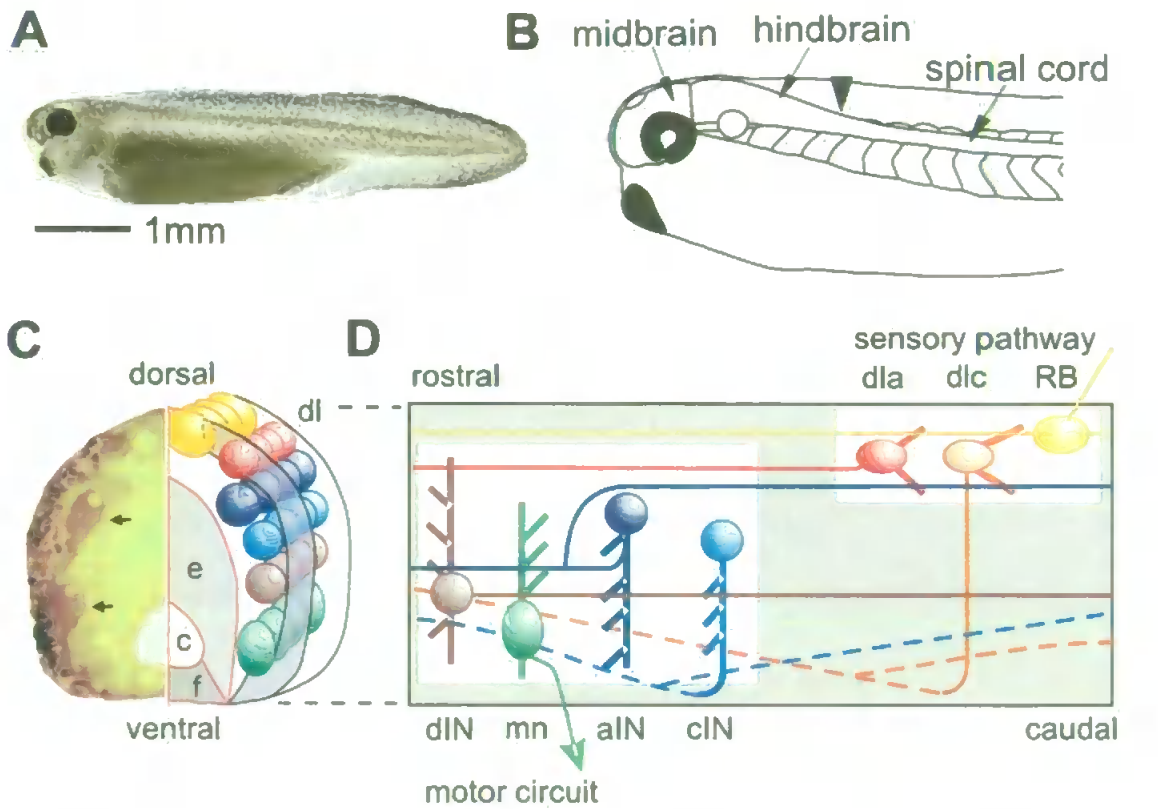

Figure 1
Hatchling *Xenopus* tadpole, nervous system and neurons. **(a)** Photograph of tadpole at stage 37/38. **(b)** The main parts of the CNS with arrowhead at hindbrain/spinal cord border. **(c)** Transverse section of the spinal cord with the left side stained to show glycine immunoreactive cell bodies (arrows) and axons (in the marginal zone). Diagrammatic right side shows the main regions: neural canal (c) bounded by ventral floor plate (f) and ependymal cell layer (e); lateral marginal zone of axons (mauve), layer of differentiated neuron cell bodies arranged in longitudinal columns (coloured circles) lying inside the marginal zone except in dorso-lateral (dl) and dorsal positions. **(d)** Diagrammatic view of the spinal cord seen from the left side, showing characteristic position and features of seven different neuron types. Each has a soma (solid ellipse), dendrites (thick lines) and axon(s) (thin lines). Commissural axons projecting on the opposite right side are dashed. See the text for details.

revealed [9]. Remarkably, the same morphogen gradients that control cell fates can also influence axon growth. For example, the Shh gradient can attract some axons to grow ventrally and cross to the opposite side [10]. After crossing, these axons are transformed and no longer attracted to the ventral floor plate [11-13]. They then turn to grow longitudinally [14], either towards the head or the tail, or they branch to grow in both directions. In all parts of the CNS such early patterns of growth by pioneer axons, controlled by chemical morphogens, lay down a basic scaffold of axon tracts that can be followed by later axons and in this way help to direct their growth [15]. Once the axons have grown to approximately the 'correct' area, they start to make connections (synapses) with the branched dendrites emerging from the cell bodies of other neurons.

We aim to answer two questions about the formation of synaptic connections. Our first question is: how accurate and specific are the synaptic connections formed during early stages of development within the CNS? Once axons have reached a suitable area to make synapses, cellular recognition processes [16] and activity-dependent mechanisms [17-20] may be needed to ensure that appropriate synaptic connections are made. However, our second question is: can simple factors, such as the broad geographical distributions of axons and dendrites, themselves generate sufficient specificity in synaptic connections to ensure the development of functional neuronal circuits?

To investigate the specificity of early synapse formation, we need to examine connections between identified neuron types in a functioning neuronal network. Very few vertebrate networks are simple enough to allow this; an exception is the developing spinal cord of the newly hatched clawed toad (*Xenopus laevis*) tadpole. Like the developing zebrafish [21,22], this spinal cord contains less than 2,000 neurons divided into very few types (approximately ten) yet it allows simple reflexes and swimming. In *Xenopus*, whole-cell recordings from pairs of spinal neurons under visual control have allowed us to build a remarkably full picture of the morphology, properties, synaptic connections and functions of the neurons and networks controlling swimming behaviour [23-28]. This detailed knowledge of the anatomy and function of different types of spinal neurons in developing *Xenopus* embryos provides a remarkable opportunity to use the whole-cell recording method to examine large numbers of synaptic connections between different types of identified spinal neuron to assess the specificity of the connections between them.

Our direct examination of synaptic connections between spinal neurons shows that connections are widespread and non-specific. We therefore examine the anatomy to see whether some very simple factors, like the different dorso-ventral distributions of the axons and dendrites of different neuron types, are sufficient to predict the connectivity found physiologically. We then use modelling to ask whether simple rules can reproduce longitudinal axon growth paths, and whether network models of the spinal circuits can produce swimming activity when synaptic connections are determined by simple probabilistic rules. Overall, our results show that it is possible that the first, pioneer neuronal networks formed in the spinal cord could be generated without specific neuron-to-neuron recognition mechanisms playing a necessary role in determining synaptic connectivity.

Results

Neuron types in the hatchling tadpole spinal cord

The two day old, hatchling *Xenopus* tadpole is 5 mm long (Figure 1a,b). The eyes are not yet functioning but the brain and spinal cord contain differentiated neurons. The spinal cord is a simple tube (approximately 0.1 mm diameter) with a central neural canal formed by ependymal cells and the ventral floor plate (Figure 1c). On each side lies a layer of nerve cells or neurons loosely organized into longitudinal columns. The neurons project processes into a superficial zone of longitudinal axons either directly or by first growing ventrally across the floor plate to the other side and then turning or branching longitudinally. As in all vertebrates, newly formed neurons are positioned in a dorsal to ventral sequence: sensory neurons; sensory interneurons; other interneurons; motoneurons. Unlike adult vertebrates, the young tadpole spinal cord has remarkably few types of spinal neuron, possibly less than ten. In this paper we consider seven types of spinal neuron involved in swimming (Figure 1d) with anatomy shown by dye filling and where the synapses made onto other spinal neurons have been defined by electrical recordings from pairs of individual neurons [29] (see also below). All synapses are made directly from longitudinal axons as they pass small processes emerging from the neurons called dendrites that protrude towards the side of the spinal cord.

Evidence from recordings on synaptic connections between neuron types

To investigate the specificity of synaptic connections between the seven different types of spinal neuron, we used the whole-cell patch method to make current clamp recordings from over 500 pairs of neurons located 0.5 to 3 mm from the midbrain and usually recorded less than 0.3 mm apart. By injecting current into each neuron to evoke an action potential, we could see if a short-latency post-synaptic excitation or inhibition was present in the other neuron. After recording, the animals were fixed, the CNS removed and the anatomy of the recorded neurons revealed by neurobiotin staining. Only those pairs with clear anatomical identification and where the axon of at

least one neuron was seen to have a possible contact point onto the dendrites of the other neuron were included in the analysis. Clearly, it was critical that we should know that the connections were monosynaptic. Synapses in the young tadpole can be unreliable, so standard tests for monosynaptic connections, involving high frequency following of presynatic spikes, were not possible. We therefore based our conclusions on measurements of latency combined with anatomy. The young tadpole has fine unmyelinated axons that conduct action potentials relatively slowly (approximately 0.3 m s^{-1}) [30] and latencies depend on the distance between the neurons [28]. Most recordings were from pairs <0.3 mm apart and had latencies of <3 ms. Latencies up to 3.6 ms were found only with larger separations, up to 0.7 mm. These latency measurements are in complete accordance with our earlier studies of monosynaptic connections [31]. For known disynaptic pathways in the tadpole [25,26], typical latencies are at least 6 ms for equivalent separations, making it highly unlikely that the connections we report here were disynaptic. This direct evidence for connections was supported by observing synaptic potentials produced by stimulating sensory neurons in the skin or occurring during swimming.

Rohon-Beard neuron synapses

Dorsal Rohon-Beard (RB) neurons are sensory, innervate the skin and respond to touch. Their central axons ascend and descend to excite other neurons by release of glutamate to activate α-amino-3-hydroxy-5-methyl-4-isoxazolepropionate (AMPAR) and *N*-methyl-D-aspartate receptors (NMDAR) [32,33,25]. In paired recordings where there is a direct synaptic connection, RB action potentials evoked by injected current lead to large excitatory postsynaptic potentials (EPSPs; 3.4–25.4 mV) at short and constant latencies (1.4–3.4 ms) [25,26]. Figure 2 shows examples of how synaptic connections were determined. In the first case, when the RB is stimulated, an ascending interneuron (aIN) is excited. In the second, the RB excites a commissural interneuron (cIN) and excitation can be blocked by glutamate receptor antagonists. Recordings from 132 pairs of neurons showed that the probability of finding synapses from RBs to dorsolateral commissural interneurons (dlcs) and dorsolateral ascending interneurons (dlas) is higher than from RBs to aINs and cINs (Table 1).

The inaccessibility of more ventral descending interneurons (dINs) and motoneurons (mns) prevented paired recordings with RBs, so we electrically stimulated RB neurites in the skin. EPSPs with short and constant latencies (<6 ms), indicating direct connections, were found in 2/10 dINs and 1/12 mns.

Dorsolateral commissural interneuron synapses

Dlcs are sensory pathway interneurons excited by sensory RB neurons. They release glutamate to excite contralateral neurons via AMPARs and NMDARs. They mediate a flexion reflex and initiate swimming activity when the skin is stimulated [25]. Paired recordings showed that dlcs can directly excite all four types of neuron (aIN, cIN, dIN and mn; Table 1) that are active in swimming and called central pattern generator (CPG) neurons. Rather surprisingly, whole-cell recordings from 17 dlcs showed that 10 received EPSPs following contralateral skin stimulation (Figure 3a). The longer latencies of these EPSPs (7–14 ms) suggested that they were not direct but could originate from dlcs excited by skin stimulation on the opposite side of the body.

Dorsolateral ascending interneuron synapses

Dlas are sensory pathway interneurons like dlcs that relay excitation from sensory RB neurons to more rostral ipsilateral CPG neurons [26]. Paired recordings and EPSP timing analyses showed that dlas could directly excite all types of CPG neurons (Table 1) [26]. In 2/11 paired recordings, dlas also excited dlcs (Figure 2g).

Ascending interneuron synapses

AINs release glycine and have a broad dorsal-ventral distribution. They inhibit neurons on the same side in both *Xenopus* tadpole and developing zebrafish spinal cord [23,34]. Paired recordings made between aINs and other ipsilateral neurons showed that aINs directly inhibited all types of neurons (Table 1).

Because aINs are active during swimming, they produce inhibition in neurons on the same side early in each swimming cycle [23,28]. Early cycle inhibitory postsynaptic potentials (IPSPs) in RB neurons during swimming are very rare but were seen in 3/136 RB neurons (Figure 3b). This connection was confirmed in 1/15 paired recordings between aINs and RBs (Figure 3c). Since RB neurons do not usually have dendrites, these synapses may be onto presynaptic regions of synapses made by RB axons that would need to be close to the soma for any PSP to be recorded.

Commissural interneuron synapses

CINs are a middle dorso-ventral group of glycinergic neurons that produce mid-cycle inhibition of CPG neurons on the opposite side of the spinal cord [35] to organize the alternation of activity between the two sides during swimming. Since they have been studied extensively [36], we made few paired recordings and cINs were only shown to produce direct contralateral unitary IPSPs in nine cINs and one dIN (Table 1). However, a consistent picture is revealed in recordings during swimming where reliable mid-cycle IPSPs/inhibitory postsynaptic current were seen

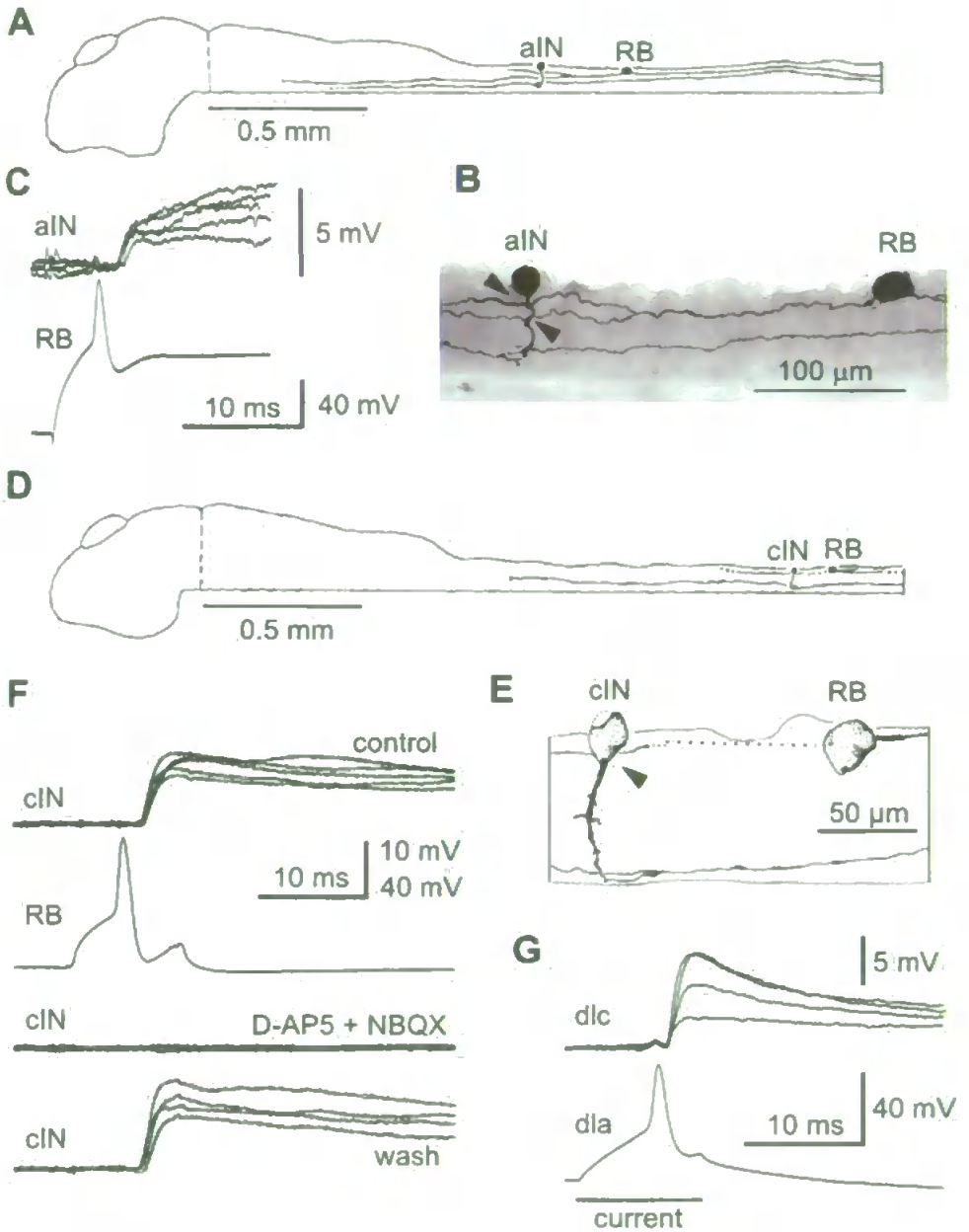

Figure 2

Recording synaptic connections. **(a-c)** RB sensory neuron excites an aIN: (a) side view of the isolated brain and spinal cord to show the location of both neurons and their axons; (b) anatomy of recorded neurons with possible synaptic contacts from RB axons onto aIN (arrowheads); (c) injection of current into RB evokes an action potential that leads to a short latency EPSP in the aIN (five traces overlapped). **(d-f)** RB excites a cIN: (d) location and (e) anatomy of RB and cIN pair; (f) current evoked RB action potentials lead to EPSPs (five traces overlapped) blocked reversibly by glutamate antagonists D-AP5 (25 μM) + NBQX (2.5 μM). **(g)** Current evoking an action potential in a dla produces short latency excitation (EPSPs) in a dlc (four traces overlapped).

Table 1: Probabilities of synaptic connections found by paired recording and data from other tests to show presence/absence of connections

	Post neuron						
Pre neuron	**RB**	**dlc**	**dla**	**aIN**	**cIN**	**dIN**	**mn**
RB ipsi	0 (0/2)	0.63 (34/54)	0.35 (6/17)	0.13 (2/15)	0.09 (4/44)	+	+
dlc contra	-	0 + (0/1)	-	0.33 (2/6)	0.43 (18/42)	0.33 (1/3)	0.46 (6/13)
dla ipsi	0 (0/17)	0.18 (2/11)	-	0.25 (2/8)	0.08 (1/12)	0 (0/2)	-
aIN ipsi	0.07 (1/15)	[0.81] (17/21)	0.38 (3/8)	0.25 (4/16)	0.15 (6/39)	0.2 (2/10)	0.33 (1/3)
cIN contra	-	0 + (0/42)	0 +	0 ++ (0/13)	0.26 (9/35)	1 ++ (1/1)	0 ++ (0/3)
dIN ipsi	-	+	0 + (0/2)	++ (6/7)*	++ (6/7)*	++ (45/62)*	++ (27/32)*

Figures in parentheses give synapses found over number of pairs tested. For each neuron type, ipsi refers to synapses made on the same side and contra refers to synapses made on the opposite side. +, rare connections inferred from other experiments; ++, common connections but no quantitative data; *, connections frequent but preliminary recordings were used to select pairs of neurons that were connected, so connection probabilities are not meaningful. Square brackets indicate an artificially high value for aIN contacts.

in all types of CPG neurons (see figure 4 in [24]). They were also present in a small proportion of recordings from dlcs [28] and dlas [26], and in 1/146 RBs (Figure 3b).

Descending interneuron synapses

DINs corelease glutamate and acetylcholine to excite other neurons via AMPAR, NMDAR and nicotinic acetylcholine receptors [31,27]. They provide ipsilateral excitation to CPG neurons during tadpole swimming [31,37]. In paired recordings, dINs were shown to directly excite all four types of CPG neurons, including other dINs (Table 1). Recordings in sensory pathway dlc and dla interneurons show that 9 of 43 dlcs and 1 of 2 dlas received weak on-cycle excitation (Figure 3d). The simplest explanation is that this excitation comes from dINs.

Overall, the results from paired recordings and other physiological recordings summarized in Table 1 reveal very widespread connectivity. Where evidence is available, neurons with dendrites (all except RBs) receive synapses from all other neuron types. This was unexpected and raised the possibility that the formation of synaptic connections in the developing spinal cord may be stochastic and not precisely determined by detailed processes of cell-to-cell recognition.

Anatomical evidence on the dorso-ventral distribution of axons and dendrites

One alternative to specific cell-cell recognition mechanisms is that axons can chemically recognise neuronal dendrites and simply make synapses with any that they contact (in transmission electron microscope studies we have found very few axon-soma synapses; A Walford and A Roberts, unpublished). If this hypothesis is correct, the probability of contact will depend mainly on the dorso-ventral distribution of axons and dendrites, since axons run along the spinal cord, rarely branch, and make synapses directly onto dendrites that they pass. We have therefore examined these distributions for six spinal neuron types in the rostral spinal cord. Dlas form a small population [26] and there were not enough examples to include them in this analysis.

Neurons for anatomical analysis were selected where the soma was in the region where our electrical recordings were made (1 to 3 mm from the midbrain; Figure 1b). Spinal interneurons were filled individually with neurobiotin using sharp micropipettes inserted from the dorsal surface of the intact cord (Figure 4a; see also [24] and [38]). The axons are all relatively straight with maximum tortuosity (actual length/straight line distance) of 1.02 (n = 6). Figure 4b uses the aINs to illustrate the dorso-ventral distributions of axons and dendrites.

The dorso-ventral range of dendrites was determined from the positions of the most ventral and dorsal dendrite for each neuron (Figure 4a,b). This range will limit the number of axons contacted. We ignore the possibility that dendrites might be unevenly distributed within this range. The dendrite dorso-ventral ranges were summed for each neuron type, except RB neurons, which do not have dendrites. For each 10% dorso-ventral position bin (spinal cord diameter is approximately 100 μm so bin width is approximately 10 μm) in the 10 μm thick marginal zone where dendrites and axons lie, we found the probability that an individual neuron of each type would have dendrites occupying that bin (Figure 5a). The dendrite distributions for neurons active during swimming (mns, aINs, cINs and dINs) were broad but all had a maximum just below the dorso-ventral midline (in the 30% or 40% bin) and fell away dorsally. In contrast, the dendrites of dlc sensory pathway interneurons had a maximum dorsally (in the 80% bin) and fell away ventrally.

We measured the dorso-ventral position of axons every 0.05 mm up to a maximum of 1 mm from the neuron soma. For each individual neuron, we pooled these measurements (discarding information about the distance

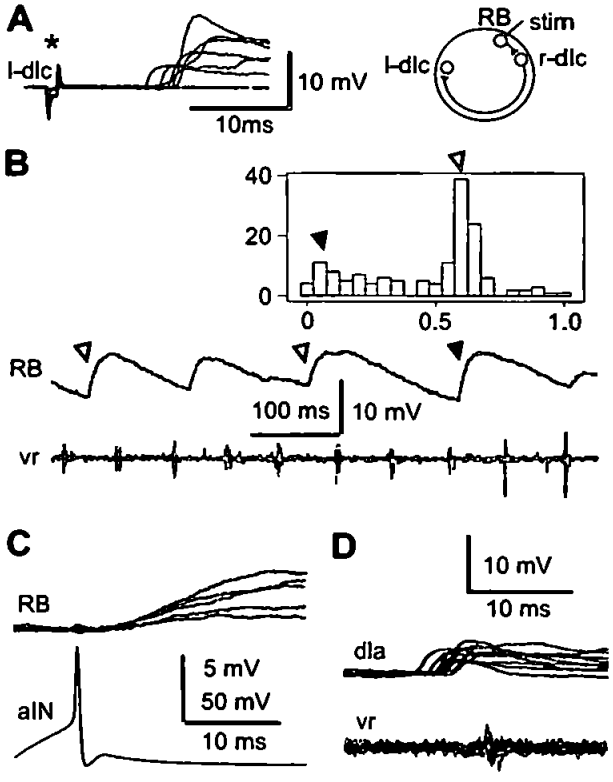

Figure 3
Unexpected synaptic connections. **(a)** In a left dlc (l-dlc) interneuron excitation is seen after variable delays as skin stimulation strength to the opposite right side increases (asterisk). The inset shows the probable pathway. **(b)** In a RB neuron, IPSPs (depolarising at resting membrane potential) occur during swimming, shown in a motor nerve recording (vr). Some IPSPs are mid-cycle (open arrowheads) and others are early-cycle (filled arrowhead). The histogram shows the phase distribution of 148 IPSPs in the swimming cycle. **(c)** Stimulating an aIN to fire an action potential leads directly to depolarising IPSPs at short latency in a RB neuron. **(d)** In a dIa, fast on-cycle EPSPs, presumed to come from dINs, are seen on 77% of cycles during swimming.

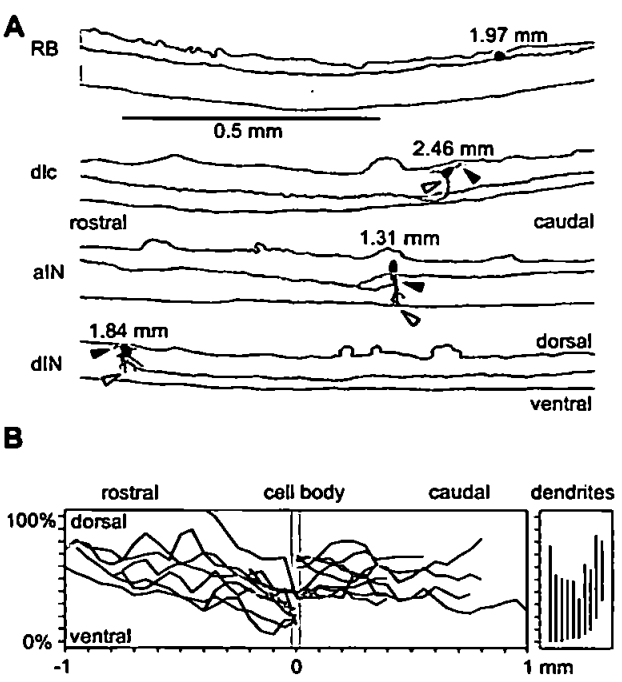

Figure 4
Dorso-ventral distribution of axons and dendrites. **(a)** Examples of neurobiotin filled neurons traced in lateral views of the spinal cord to show the dorso-ventral positions of the soma, dendrites and part of the axons. Dendrites emerge from the black soma, with the most ventral dendrite (open arrowhead) and most dorsal (black arrowhead) marked. Axons are on the same side as the soma except for dlcs where they cross ventrally then branch. Rostral to left, dorsal up. **(b)** Examples of axon trajectories of individual aINs (measured at 0.05 mm steps from the soma at 0 mm) and dorso-ventral extent of their dendrites (vertical lines at right).

from the soma and whether the axon was ascending or descending) and used them to calculate the probability of the axon occupying different dorso-ventral positions. These individual distributions were then averaged for all members of a type (Figure 5a; Table in Anatomy section of Additional file 1). The dorso-ventral axon distributions of some neurons are rather narrow. RB sensory neuron axons are dorsal (from 50% to 100%; maximum at 80%) while mns are ventral (from 10% to 30%; maximum at 20%). CINs, dINs and dlcs are all slightly biased towards ventral positions (from 10% to 60%) while inhibitory aINs have a broad axon distribution (10% to 90%; maximum at 40%).

Once the dorso-ventral distributions of axons and dendrites were established, 'contact' probabilities between axons and dendrites were calculated as follows for each pair of neuron types. The probabilities of individual axons or dendrites occupying a particular 10% dorso-ventral region were those plotted in Figure 5a. The probability that a particular pre-synaptic axon and post-synaptic dendrite would both occupy the same dorso-ventral region in the narrow marginal zone, and could therefore make contact, was simply the product of these probabilities. Overall contact probabilities between each type of neuron were then found by summing the separate probabilities for the ten dorso-ventral regions (Table 2). The contact probabilities range from 0.04 to 0.91 and relate intuitively to functions. They are higher for RB sensory neuron contacts onto sensory pathway dlcs (0.65) than onto other neurons like dINs (0.29); they are low for dlc contacts with each other

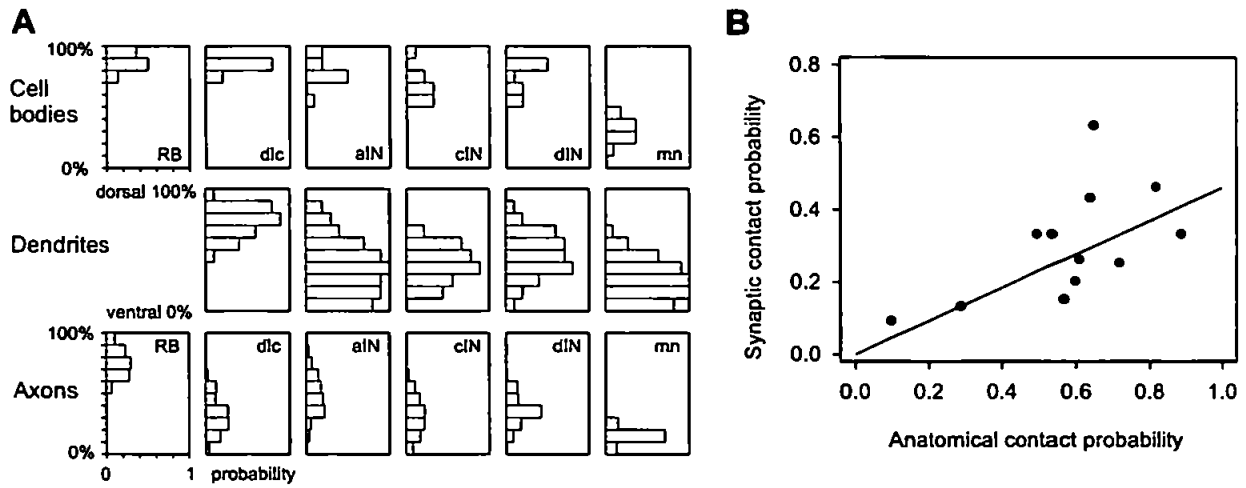

Figure 5

Axons, dendrites and synapse probabilities. **(a)** Histograms summarise dorso-ventral distribution of cell bodies, dendrites and axons of different neuron types in 10% bins where 0% is ventral and 100% dorsal edge of spinal cord. Distributions are expressed as the probability that a neuron will have a soma or dendrite in a particular dorso-ventral position. Axon distributions are expressed as the probability that a 50 μm segment of the axon from each type of neuron will lie in a particular dorso-ventral position. **(b)** Plot of synapse probability from recordings versus contact probability from anatomy for cases in bold in Table 2. Highest point (RB-dlc) was omitted in calculating regression.

Table 2: Probabilities of synapses (from Table 1) and of potential 'contacts' between axons and dendrites for each neuron type

	Dendrites				
Axons	**dlc**	**ain**	**cin**	**din**	**mn**
RB ipsi					
Synapse	**0.63**	**0.13**	**0.09**	+ (0.13)	+(0.02)
Contact	0.65	0.29	0.10	0.29	0.04
dlc contra					
Synapse	0+ (0.04)	**0.33**	**0.43**	**0.33**	**0.46**
Contact	0.08	0.89	0.64	0.54	0.82
aIN ipsi					
Synapse	(0.13)	**0.25**	**0.15**	**0.2**	**0.33**
Contact	0.28	0.72	0.57	0.60	0.50
cIN contra					
Synapse	0+ (0.04)	0++ (0.40)	**0.26**	++ (0.24)	0++ (0.37)
Contact	0.08	0.88	0.61	0.52	0.80
dIN ipsi					
Synapse	+ (0.04)	*++ (0.42)	*++ (0.34)	*++ (0.29)	*++ (0.37)
Contact	0.08	0.91	0.73	0.64	0.80
mn ipsi					
Synapse	(0.00)	(0.41)	(0.18)	(0.10)	(0.45)
Contact	0.00	0.89	0.40	0.22	0.98

Synapse probabilities in bold are those from recordings based on more random sampling. Where there are no data from recordings, estimates of synaptic contact probabilities (in parentheses) are 46% of the anatomically estimated contact probabilities. For each neuron type, ipsi refers to synapses made on the same side and contra refers to synapses made on the opposite side. +, rare connections inferred from other experiments; ++, common connections but no quantitative data; *, connections frequent but preliminary recordings were used to select pairs of neurons that were connected, so connection probabilities are not meaningful.

(0.08) but higher onto the neurons activated after skin stimulation (0.54–0.89 for aINs, cINs, dINs and mns); they are quite high for contacts between neurons active during swimming (0.5–0.91 for aIN, cIN and dIN contacts to each other and to mns).

When contact probabilities determined from anatomy were compared to synapse probabilities determined directly by electrical recording (Table 2), the two were significantly correlated for pairs where the neurons were randomly chosen for recording (bold entries in Table 2; Pearson correlation coefficient 0.593; $p = 0.042$). This significant relationship based on data from both anatomy and physiology (Figure 5b) was then used to predict the synaptic contact probability for cases with only anatomical data (Table 2). We first omitted data for contacts from RB to dlc neurons where the extensive rostro-caudal dendrites of dlc neurons are likely to result in a relatively high synaptic contact probability (see Discussion). The slope obtained by linear regression for the remaining points suggests that the probability of a real synaptic contact is around 46% of that predicted by anatomy.

We suggest on the basis of these results that during the formation of early synapses in the developing frog spinal cord, the different synapse probabilities found could depend simply on differences in the geographical distributions of axons and dendrites of different neuron types. These distributions could be sufficient to ensure, for example, that dorsal sensory RB axons synapsed mainly with dorsal sensory pathway interneurons rather than with more ventral neurons active during swimming (like mns).

Modelling axonal growth and synaptic contact probabilities

Since axons grow a considerable distance along the spinal cord (often 1 to 2 mm in a 5 mm long animal) and can wander dorsal or ventral as they grow, their pattern of growth will have a strong influence on their potential to contact dendrites of different neuron types (Figure 4a). We concluded above that synaptic contacts may depend simply on dorso-ventral axon and dendrite distribution patterns. We therefore investigated whether a simple model, without any cell-cell recognition, could generate patterns of axon growth that would reproduce the observed axon distributions and, therefore, the synaptic contact probabilities. For simplicity, we assumed that dendrites are static and passive (see Discussion).

Our computational model starts from the point when axons start to grow longitudinally (Figures 1d and 4a). This point will be determined by the position of the soma and the initial behaviour of the axon. In the case of RB neurons, the axons grow directly from the soma towards the head and tail. In most other spinal neurons the axon first grows ventrally and then turns to grow longitudinally either on the same side or after crossing ventrally to the other side. We use the experimental observations to give us starting positions and initial growth angles of axons as well as their final lengths. A repetitive process of advancing the axon 1 μm along its current growth angle and then modifying the growth angle is then applied until the predetermined rostrocaudal length of the axon is reached.

The current location and orientation of the tip of the axon (growth cone) are represented by three variables: x(t) rostrocaudal position, y(t) dorso-ventral position, and $\theta(t)$ growth angle. θ is defined as the deviation from longitudinal growth; positive values of $\theta(t)$ indicate a tendency to grow dorsally while negative values of $\theta(t)$ indicate a tendency to grow ventrally. In our first simple model just two parameters, α and γ, are defined specifically for each neuron type. The equations are:

$$x(t+1) = x(t) + \Delta\cos(\theta(t)), \quad (1)$$

$$y(t+1) = y(t) + \Delta\sin(\theta(t)), \quad (2)$$

$$\theta(t+1) = (1-\gamma)\theta(t) + \xi, \quad t = 0,1,\ldots,n-1. \quad (3)$$

where n is the length of axon; ξ is a random variable uniformly distributed in the interval $[-\alpha, \alpha]$ (α typically is about 2°-5°); and Δ is the 1 μm distance grown in each time step. The parameter γ ($0<\gamma<1$) represents the tendency of an axon to turn towards an angle of 0 degrees – in other words, the tendency of the growth cone to orient towards longitudinal growth. We use aINs to illustrate our methods. Figure 6a shows aIN axons generated by the simple model for parameter values optimized using the procedure described below together with plots of the same number of real axons. It is clear that the simple model is able to generate the descending part of aIN axon growth (right part of the plot) but fails to fit the experimental data for ascending axons. This is because the descending aIN axons are mainly short with small turning angles while the ascending aIN axons are longer with larger turning angles. When all neuron types were considered we found that if model axons had appropriate tortuosities, then their dorso-ventral distributions were too broad and they often ran into the edges of the spinal cord.

The partial failure of the simple model suggested that, in life, some factors guide axons towards a longitudinal growth path and away from the edges of the cord. We therefore examined the turning angles of real axons (between points 0.05 mm apart) and found that they depended strongly on their current angle of growth and weakly on their dorso-ventral position. This is illustrated for aINs in Figure 6b,c where both scatter plots show neg-

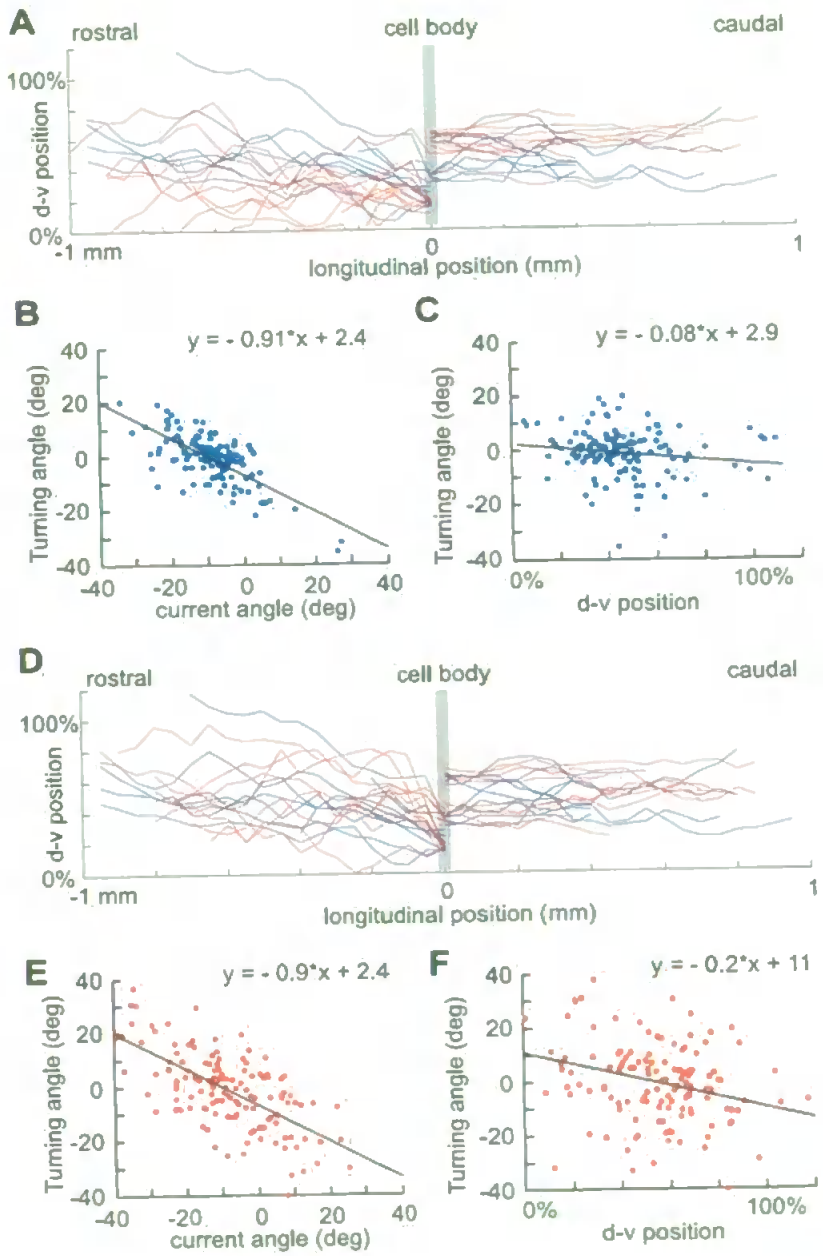

Figure 6
Modelling aIN axon growth and positional effects on axon turning angles. **(a)** aIN descending axons generated by a simple random growth model (red) fit the distribution of real descending axons (blue, to right) but model ascending axons do not match real ascending axons. **(b,c)** Real aIN ascending axon turning angles depend on the current growth angle and dorso-ventral (d-v) position. **(d)** In a model where growth angle depends on dorso-ventral position, generated aIN axons (red) match real axons (blue) closely. **(e,f)** Turning angles of modelled axons significantly match dependence of real axons on current angle and dorso-ventral position.

Table 3: Dependence of axon turning angles on current growth angle and dorso-ventral position

	Slope of turning angle versus			
Axons	**Current angle**	*P*-value	**d-v position**	*P*-value
RB				
Descending	-1.15	0	-0.53	0
Ascending	-1.09	0	-0.57	0
dlc				
Descending	-1	0	-0.16	0.2
Ascending	-0.87	0	-0.15	0.007
aIN				
Descending	-0.95	0	-0.17	0.008
Ascending	-0.91	0	-0.08	0.06
cIN				
Descending	-0.71	0	-0.31	0.003
Ascending	-0.89	0	-0.12	0.031
dIN				
Descending	-1.15	0	-0.21	0.001
mn				
Descending	-1.25	0	-0.29	0.13

P = 0 means <0.0005. d-v, dorso-ventral. Non-significant P values in bold.

ative correlations made clear by fitting the points by linear regression. For all measured neuron types the slope of the regression lines for axon turning angles were negatively dependent on current axon growth angle (-0.71 to -1.25) and dorso-ventral position (-0.08 to -0.53) (Table 3). This remarkable finding means, firstly, that the more an axon deviates from longitudinal growth the more it will turn back; secondly, the dependence of axon growth angle on dorso-ventral position means that for aIN axons, the upper and lower boundaries of the cord are repulsive.

In life many possible factors could influence axons to direct them away from edges (for example, physical barriers to growth cone extension, dorso-ventral gradients of repellent signals [38]) and guide them to a more longitudinal growth (for example, fasciculation with other longitudinal axons, longitudinal gradients of attractive or repellent signals [13]). We aimed to encapsulate the essence of such diverse mechanisms by introducing a new feature into our model: $\bar{y}$ represents the dorso-ventral position of an attractor to which axon trajectories are drawn with a strength of μ. Equations 1 and 2 are the same as above, but we replace equation 3 with:

$$\theta(t+1) = (1-\gamma)\theta(t) - \mu(y(t) - \bar{y}) + \xi, \quad t = 0,1,\ldots,n-1. \tag{4}$$

$$0 < \gamma < 1; 0 < \bar{y} < 1$$

This model contains four parameters and to specify their values we used the following optimisation procedure. For each neuron type we first pick random values of the parameters and use these to generate 70 axons. After measuring the generated axons we calculate the tortuosities and the dorso-ventral distribution of axon positions just as for the experimental data. We then consider a cost function that includes the squared differences between experimental and generated axon distributions in 10% dorso-ventral bins and the squared difference between tortuosities. Using the optimisation process (see Methods), we find parameter values that minimise the cost function and give the closest match for each type of neuron. We repeat the same procedure to get optimal parameter values for each type of neuron separately for ascending and descending axons where both exist.

The revised model was able to generate axon growth patterns very similar to those in the spinal cord (for example aINs; Figure 6d). In many cases, the optimisation procedure was able to reach very small values of the cost function; for the few cases where it did not, the generated axons were still very similar to real ones. In addition, the modelled axon growth angles showed the same dependence on current angle and dorso-ventral position as the measured axons. Just as in the real axons, scatter plots and linear regressions showed negative slopes (Figure 6e,f; Table 3).

The second revised model of axon growth establishes that axon growth paths and distributions can be generated by very simple rules based only on the initial position and growth angle of the axons. Since these modelled axon distributions closely match those measured for real axons, it

follows that their contact probabilities with dendrites will also be similar and we have confirmed this.

Can simple connection rules specify functional spinal networks?

The results from recordings, anatomy and modelling of axon growth together suggest that early spinal networks may be able to develop using very simple rules. Since different types of spinal neurons have characteristic dorsoventral positions for their cell-bodies, dendrites and axons, axons may not show any selectivity but simply synapse with a proportion of the dendrites that they contact. We therefore wanted to test if simple stochastic rules of connectivity could lead to functioning networks able to generate patterns of motor output suitable to produce swimming. Recent experiments in the immobilised hatchling *Xenopus* tadpole have shown that a very small part of the spinal cord and hindbrain, only 0.3 mm long, can generate long-lasting, alternating, swimming-like activity after a 1 ms current pulse stimulus [27]. This minimal preparation is not as reliable as more intact preparations and, as well as swimming, can also produce long-lasting rhythmic motor output that is synchronous on the left and right sides (SR Soffe, unpublished observations). Such synchronous activity has been seen in more intact tadpole preparations [39] and is a stable state in many simple reciprocal inhibitory network models [40,41]. Our aim was to use stochastic rules to build models of the minimal 0.3 mm long region of the tadpole nervous system to see whether they could produce similar rhythmic outputs, particularly swimming.

We used model neurons with just a single compartment. Specific models were used for each type of spinal neuron with membrane properties and firing characteristics based on measurements from whole-cell patch recordings [42]. For simplicity we used a single RB neuron that excited all sensory pathway dlc and dla INs on the right side. Apart from RB neurons, there were ten of each type of neuron and the broad network connections are summarised in Figure 7a. The network has left and right sides that inhibit each other reciprocally. We have shown previously in a simple model of the rhythm generating part of the tadpole spinal network (CPG), that activating left and right sides with a delay leads to alternating swimming, but when the delay is too short, synchronous activity is produced from both sides [43]. The present network model could also produce swimming or synchronous activity, probably again dependent on the exact timing of activity in the sensory pathway. In the present model, synaptic connections were probabilistic and to imitate more realistic numbers of neurons (30 of each type) each model neuron had 3 chances to make a contact. Synaptic strengths could, therefore, be 0 or 1 to 3 times the single synapse strength (see Methods). Synaptic conductances and the ratios of

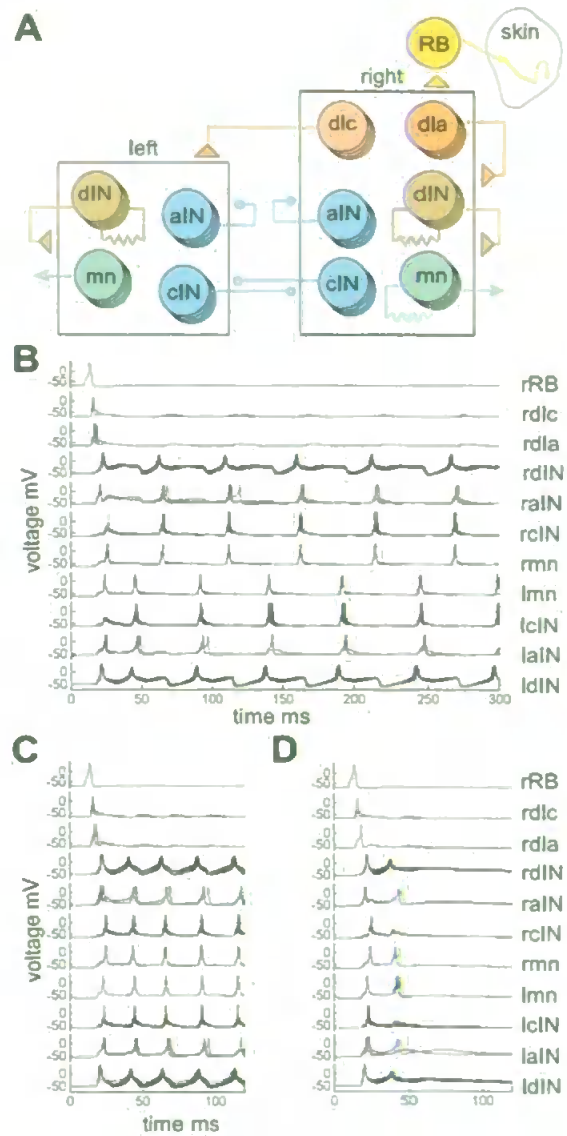

Figure 7

Model networks with probabilistic connectivity. **(a)** The network has a single sensory RB neuron exciting neurons in the right half-centre, which also has sensory pathway dlc and dla interneurons. There are ten of each neuron type in each half-centre. The broad pattern of connections is shown by the axons from groups of neurons onto the half-centres (triangles are excitatory and circles are inhibitory synapses). The actual synaptic connections are determined probabilistically for each neuron. Resistor symbols show electrically coupled neuron groups. **(b-d)** Examples of activity of selected neurons in response to a single stimulus to the sensory RB neuron for networks with connection probabilities based on experiments: (b) sustained swimming; (c) synchronous activity on each side; and (d) no long-lasting response.

NMDAR to AMPAR in glutamate synapses were specific for each type of post-synaptic neuron so that synapse properties matched those found in physiology (see Table in final Network modelling section of Additional file 1).

In the first test, 50 different networks were made where the synapse probabilities between different types of neuron were determined by those found experimentally (synapse probabilities from Table 2). The response of each network to a single stimulus to the sensory RB was then tested once. We found that 80% of these networks generated sustained activity: in 60% this was like swimming where left and right mns fired single, alternating action potentials on each cycle and the frequency was in the range of 10–30 Hz (Figure 7b); and 20% of networks produced synchronous output on each side at twice the swim frequency (Figure 7c). The remaining 20% failed to give any long lasting response to the stimulus (Figure 7d). Once initiated, swimming and synchronous activity continued indefinitely as there is no synaptic plasticity in these networks. In another 50 networks all synaptic connections were given the same contact probability, which was the average contact probability of the whole network. Swimming was never produced by these networks, even in networks where the high contact probabilities in the sensory pathway (connections from RB to dlc and dla) were restored.

We then investigated whether the particular synapse probabilities and strengths used in our first test of the model were critical to its success. Changing individual connections, especially in the sensory activation pathway, could reduce the percentage giving prolonged activity. For example, when the dlc to cIN synapse probability was reduced from 0.43 to 0.33, only 54% of networks produced prolonged activity (42% swim, 12% synchrony, n = 50). To see whether the broader pattern of synapse probabilities were important, we rounded-up all probabilities among aINs, cINs and dINs to 0.33 and found that 64% produced prolonged activity (26% swim, 38% synchrony, n = 50). These results show there is some flexibility in the values for synapse probabilities that can allow these stochastic networks to generate prolonged activity. The relatively high failure rates suggest that the sensory activation pathway is not nearly as secure in the model as in the whole animal. The reasons for this are not clear but the model network, although based on current evidence, is still unlikely to be a complete representation of the real networks.

We conclude that simple networks, where synaptic connectivity is determined by the broad dorso-ventral location pattern or geography of axons and dendrites, can generate organised swimming behaviour.

Discussion

The hatchling frog tadpole can be used to study the specificity of connections between different types of neurons because recent technical advances have made it routine to record from pairs of neurons in the spinal cord. This has allowed the networks of spinal and caudal hindbrain neurons controlling swimming to be defined in considerable detail [23,28,25,26,31,27]. It would be rash to claim that all the neurons involved have been found; on the other hand, the evidence suggests that we have now defined all the major elements in the spinal network controlling swimming. Our knowledge of the neurons and connections in this example of a functioning vertebrate circuit producing meaningful behaviour provides a unique opportunity to ask questions about how such a circuit develops. We have therefore examined synaptic connections between seven different types of neuron. This allowed us to define the synaptic contact probabilities between these different neurons (Table 1). When considered in a functional context, most connections seemed very reasonable but, to our surprise, we found evidence for almost all possible connections. These observations do not rule out specific recognition processes acting during the formation of synaptic connections. However, they raise the possibility that simpler processes that lead to some 'mistakes' still provide connections with sufficient specificity to produce a properly functional circuit.

The simpler hypothesis that we have examined is that axons can recognise and make synapses with any dendrites that they contact, so the connections formed will depend primarily on the distribution of axons and dendrites. If this is correct, then synapse formation will occur where axons and dendrites lie in the same dorso-ventral regions of the spinal cord. Given the small scale of the tadpole spinal cord, which is only about 100 μm in diameter, we have considered axons and dendrites to be within contact range if they simply lie within the same 10% dorsoventral position bins: approximately 10 μm in the <10 μm thick marginal zone of axons and dendrites. Clearly, more complex approaches are necessary in larger scale structures like the cerebral cortex [44,45]. On this basis, we therefore determined the anatomical contact probabilities of the axons and dendrites of different neuron types and compared these to the synapse probabilities determined directly by electrical recordings. The significant correlation between the two sets of probabilities suggested that synapses form in nearly 50% of cases when an axon passes through a dendritic field.

We conclude that axons make synapses with the dendrites they chance to contact rather than making synapses preferentially by recognising specific chemical markers on particular postsynaptic targets. Specific examples illustrate this. Skin sensory RB neurons drive a strong crossed exci-

tatory reflex by first exciting sensory pathway excitatory dIc interneurons with commissural axons [30]. We might predict that connections from RB neurons to reciprocal inhibitory cINs would, therefore, be inappropriate and cell recognition factors might ensure they failed to form. Yet we find that these connections do form, and at a probability predicted simply by the overlap of RB axons and cIN dendrites. On the other hand, the excitatory connections between RB neurons and dIc interneurons occur with an unusually high probability [30]. Again, this is appropriate to drive a strong contralateral reflex and we might expect that this high contact probability would result from cell recognition. Yet the high probability can be explained by the distribution of dIc dendrites: unlike most spinal neurons, where dendritic fields are very narrow longitudinally, those of dIcs are unusual in being extended along the length of the cord [46]. This gives them repeated chances to make contact with RB axons. We suggest, therefore, that contacts are determined by the geography of the spinal cord, primarily by the dorso-ventral distributions of axons and dendrites.

If the dorso-ventral distribution of axons and dendrites is an important determinant of spinal network connectivity, then what are the factors that control these distributions? Fortunately, this is a very active area of research. Different dorso-ventral distributions of axons and dendrites originate with the specification of soma positions. In the chick and mouse, a large body of work is defining the transcriptional networks that regulate the formation of an ordered dorso-ventral series of longitudinal neuron columns identified by the transcription factors that they express [47,48,7,8,49]. Fundamentally, around 12 neuron types are arranged in a consistent sequence of columns from dorsal to ventral: sensory, sensory related interneurons, motor related interneurons and mns. The same basic plan is seen in the tadpole spinal cord (Figure 1c,d). Once formed into these columns, neurons are polarized [9] and grow processes in very distinct orientations. In frogs, most grow axons ventrally (with the obvious exception of the sensory RB neurons that grow longitudinally [46]). Growth cones immediately come under the influence of attractive and repulsive chemical gradients that control their direction of growth, for example, whether they turn or grow straight across the ventral surface to the opposite side before turning [1,50,4,38,51,52]. In the tadpole all axons eventually grow in a longitudinal direction, starting in a characteristic dorso-ventral region for each neuron type. Meanwhile, dendrites grow from the soma or initial segment of the axon and, like the axons, come to lie in dorso-ventral positions characteristic for each neuron type. In contrast to extensive studies on dendrite development in brain neurons [53], there is little work on the mechanisms determining their growth in spinal neurons. Evidence from zebrafish shows that dendrites play an active role in extending very short distances (approximately 10 μm) towards longitudinal axons to form en-passant synapses [54].

To test the plausibility of the proposal that synapse formation between different neuron types in the tadpole spinal cord depends on the dorso-ventral distribution of axons and dendrites, we have used two types of modelling. Since axons grow long distances along the cord, they could wander to reach all dorso-ventral positions unless their growth is regulated. We therefore asked what kinds of growth rules were needed to reproduce the patterns of axon distribution found for different neuron types. A simple tendency to turn towards longitudinal growth could not match the real axon distributions or their active turning responses, which change with growth angle. To match the real axons we needed to add active turning towards an attractor line located at different dorso-ventral positions for each neuron type. This attractor models the complex effects of interacting attractive and repellent dorso-ventral chemical gradients that have been proposed to act on axonal growth cones in the spinal cord [4,1]. With the attractor, our simple model could reproduce real axon distributions and, by doing this, could reproduce the synaptic contact probabilities determined anatomically. (These assume that dendrite distribution is static and passive, which is almost certainly not the case.)

In our second modelling test we asked whether a functional spinal network capable of generating swimming activity could be generated simply on the basis of the synaptic contact probabilities established by our physiological and anatomical data on the different spinal neuron types. It is important to remember that in our network model, the different neuron types are not all alike but each type has their own very particular and characteristic properties [42]. Using these neurons, we show that crude probabilistic contact rules do produce networks that will generate swimming activity while networks where all neurons have the same connection patterns fail. Taken together, the modelling supports the proposal that functional circuits could be produced using simple rules. For example: excitatory dIN axons should grow tailwards, mainly in the ventral 50% of the cord and synapse with 40% to 50% of any dendrites passed; reciprocal inhibitory cINs should cross the cord ventrally, branch on the other side, grow mainly in the ventral 50% of the cord and synapse with 40% to 50% of any dendrites passed. It is important to emphasise that we are not suggesting that chemical recognition does not exist; axons need to recognise dendrites. We are suggesting that detailed cell-to-cell recognition may not be necessary to establish which connections are made in the first, functional pioneer circuits.

Conclusion

In the core, axial parts of the vertebrate nervous system, like the spinal cord and brainstem, neurons, dendrites and longitudinal axons are laid out in a dorso-ventrally ordered array on each side of the body. At early stages in development a major factor influencing primary synapse formation in such regions may be the physical proximity or separation of axons and dendrites. If axons can recognise and contact dendrites, then synapses may form. So, in the frog tadpole spinal cord, dorsally located sensory axons mainly excite the dorsal dendrites emerging from the cell bodies of dorsal sensory pathway neurons (dlcs) but the very ventral central axons of mns will virtually never contact these dendrites, so synapses will not be made. At this early, primary stage of development neurons may need only to be able to distinguish neuronal dendrites from axons and non-neuronal processes. Detailed cellular recognition and other more subtle processes to specify correct connections may, therefore, not be necessary for the formation of primary functional networks during spinal cord development. This lack of specificity could be tested if different types of spinal neurons could be marked and would form synapses in culture. Such recognition processes surely play important roles at later stages of development as connection patterns are refined [55,19].

Methods

Physiology: whole-cell patch recording

Details of the recording methods have been given recently [28]. Briefly, *Xenopus* tadpoles at stage 37/38 (Figure 1a) were anaesthetised with 0.1% MS-222 (3-aminobenzoic acid ester; Sigma, Poole, UK), immobilized in 10 μM α-bungarotoxin saline, then pinned in a bath of saline (concentrations in mM: NaCl 115, KCl 3, $CaCl_2$ 3, $NaHCO_3$ 2.4, HEPES 10, adjusted with 5 M NaOH to pH 7.4). Saline with 0 mM Mg^{2+} was used so NMDAR mediated components could be seen. Skin and muscles over the right side of the spinal cord were removed and a mid-dorsal cut made along the spinal cord to open the neurocoel. Small cuts were made in the wall of the neurocoel on the left side to expose more ventral neurons. The tadpole was then re-pinned in a small 2 ml recording chamber with saline flow of about 2 ml per minute. Exposed neuronal cell bodies were seen using a ×40 water immersion lens with bright field illumination on an upright Nikon E600FN microscope. Antagonists were applied close to the recorded neuron soma using gentle pressure to solution in a pipette with a tip diameter of 10–20 μm or dropped into a 200 μl well upstream of the recording chamber. Drugs used were NBQX (2,3-dihydroxy-6-nitro-7-sulfamoylbenzo- [*f*]quinoxaline- [*f*]quinoxaline, Tocris), D-AP5 (D-(-)-2-amino-5-phosphonopentanoicacid, Tocris), bicuculline, strychnine, tetrodotoxin, d-tubocurarine and mecamylamine (Sigma) and DHβE (dihydro-β-erythroidine; Research Biochemicals International, Natick, MA, USA).

Patch pipettes were filled with 0.1% neurobiotin and 0.1% Alexa Fluor 488 (Invitrogen, Eugene, OR, USA) in intracellular solution (concentrations in mM: K-gluconate 100, $MgCl_2$ 2, EGTA 10, HEPES 10, Na_2ATP 3, NaGTP 0.5 adjusted to pH 7.3 with KOH) and had resistances around 10 MΩ. Junction potentials were corrected before making recordings. Signals were recorded with an Axoclamp 2B in conventional bridge or continuous single electrode voltage clamp mode, acquired with Signal software through a CED 1401 Plus interface with a sampling rate of 10 kHz (Cambridge Electronic Design, Cambridge, UK). Offline analyses were made with Minitab (Minitab Ltd, Coventry, UK) and Microsoft Excel. All values are given as mean ± standard error of the mean. Experiments complied with UK Home Office regulations and received local ethical approval.

Anatomy

Neuron anatomy in *Xenopus* tadpoles at stage 37/38 was revealed by two methods. In the first method, mns were backfilled by applying fluorescein dextran to their axons in the swimming trunk muscles. After 10 minutes, muscle was removed to allow access to the side of the spinal cord and living mns observed and photographed on a Bio-Rad 500 confocal microscope with a ×40 water immersion lens [56]. In the second method, all other neurons were filled with neurobiotin through recording microelectrodes [57]. After fixing and processing, the CNS was exposed and specimens mounted on their sides between coverslips for observation, tracing with a drawing tube, or photography at ×500 on a bright field microscope [28].

Tracings of the soma, dendrites and full axonal projections were made to a scale of 0.1 mm = 50 mm. We used these scale drawings of neurons located 1 to 3 mm from the midbrain to record the dorso-ventral positions of soma, dendrites and axons for each type of neuron. The distances measured were: from the soma to the midbrain/hindbrain border; from the dorsal to ventral edge of the cord at the level of the soma; from the dorsal edge of the soma to the ventral surface of the cord; from the ventral edge of the cord to the most dorsal and most ventral dendrite. On each side of the soma, the distance of the axon from the ventral surface of the spinal cord was measured every 0.05 mm. All measurements on fixed specimens were multiplied by 1.28 to compensate for shrinkage during dehydration [24].

Modelling axon growth

The traditional approach to modelling axon growth is based on the growth cone following molecular gradients [58]. Instead, we build a simple computational model

reflecting several key attraction and repulsion processes guiding axon growth. The model includes four parameters (see equations 1, 2 and 4) that should be chosen to provide a maximum similarity between experimentally measured axons and model generated axons. Fitting the model to experimental measurements is least squares based and the similarity measure (or cost function to be minimised) contains two terms: the first term compares the distribution of model axon dorso-ventral coordinates with the distribution of experimental coordinates; the second term takes into account the extent to which the axon path is circuitous rather than direct by comparing the model and experimental tortuosities. A detailed description of the cost function to be minimized in order to find optimal parameter values is given in Additional file 1.

We run the optimization procedure for the ascending and descending axons of each neuron type. This process gives four optimal parameter values that we then use to generate biologically realistic axons with distributions of dorso-ventral coordinates and tortuosities similar to measured axon characteristics for each neuron type. We test the optimal parameter values to define the reliability of the optimization. Testing reliability is an important part of the modelling procedure because the model includes a random component in equation 4. If, for example, we generate two sets of axons using the same optimal parameters, we would like to be sure that these sets are similar. We also ensure that the properties of generated axons are not affected by 5% to 10% changes in model parameters. Optimal parameter values for each cell type, a detailed description of the testing procedure and results of testing are given in the Axon modelling section of Additional file 1.

Modelling spinal networks

Ten neurons of each type are modelled on each side [42], but at the level of connectivity each neuron represents three neurons that fire synchronously. Thus, effectively 30 neurons of each type are modelled on each side. Neurons with an ipsilateral axon connect only to ipsilateral neurons, while those with commissural axons connect only to neurons on the opposite side. After these restrictions, connections are made purely on probabilistic rules, using the contact probabilities from Table 2 ('synapse' probabilities). Since each neuron represents three synchronously firing neurons, each neuron has three chances to connect to any other neuron, where at every single attempt, there is the same probability of actual contact being established.

The connection strengths of individual synapses are primarily based on the strengths used in [42], where these strengths resulted in realistic overall conductances during swimming. These strengths had to be reduced to account for the probabilities of contact within the network, and the multiplicity of synaptic contacts between two types of neurons. The actual maximum conductances during swimming can be computed only at run-time, and vary with the connection pattern of the network, according to the probabilities of contact (the parameters used are given in a Table in the Network Modelling section of Additional file 1). Resistive electrical synapses are established between dINs and between mns with a strength of 0.3, meaning that a change of 10 mV in one neuron will cause a change of 3 mV in the other one.

Competing interests

The author(s) declare that they have no competing interests.

Authors' contributions

W-CL carried out the electrophysiology, contributed to the anatomical study and analysis of recordings. TC and RB carried out the analysis of the axon pathways and their modelling. BS carried out the network modelling. SRS participated in the design of the study and the analysis of physiology and anatomical results. AR conceived of the study, participated in its design and coordination, and was lead writer of the manuscript. All authors contributed to writing and figure preparation and have read and approved the final manuscript.

Additional material

Additional file 1

Additional material referred to in the text, in particular concerning the axon pathway modelling.

Click here for file

[http://www.biomedcentral.com/content/supplementary/1749-8104-2-17-S1.pdf]

Acknowledgements

We would like to thank Dr Stephen Eglen for advice, Drs Jon Clarke, Steve Coombes, Marc Holderied, Piers Hemsley and James Poulet for their comments on earlier versions of this paper, Jenny Maxwell and Erin Anderson for technical help, and the Wellcome Trust for financial support. Bart Sautois was a research assistant of the Research Foundation – Flanders (FWO -Vlaanderen). Roman Borisyuk was partly supported by EPSRC grant EP/D036364/1.

References

1. Dickson BJ: **Molecular Mechanisms of Axon Guidance.** *Science* 2002, **298(5600):**1959-1964.
2. Munno DW, Syed NI: **Synaptogenesis in the CNS: an odyssey from wiring together to firing together.** *J Physiol (Lond)* 2003, **552(1):**1-11.
3. Cline H: **Sperry and Hebb: oil and vinegar?** *Trends Neurosci* 2003, **26(12):**655-6661.
4. Chilton JK: **Molecular mechanisms of axon guidance.** *Dev Biol* 2006, **292:**13-124.
5. Schnorrer F, Dickson BJ: **Axon guidance: Morphogens show the way.** *Current Biology* 2004, **14:**R19 - R21.

6. Polleux F, Ince-Dunn G, Ghosh A: **Transcriptional regulation of vertebrate axon guidance and synapse formation.** *Nat Rev Neurosci* 2007, 8(5):331 -3340.
7. Helms AW, Johnson JE: **Specification of dorsal spinal cord interneurons.** *Curr Opin Neurobiol* 2003, 13(1):42-49.
8. Goulding M, Pfaff SL: **Development of circuits that generate simple rhythmic behaviors in vertebrates.** *Curr Opin Neurobiol* 2005, 15(1):14-20.
9. Calderon de Anda F, Pollarolo G, Da Silva JS, Camoletto PG, Feiguin F, Dotti CG: **Centrosome localization determines neuronal polarity.** *Nature* 2005, 436(7051):704-708.
10. Charron F, Stein E, Jeong J, McMahon AP, Tessier-Lavigne M: **The Morphogen Sonic Hedgehog Is an Axonal Chemoattractant that Collaborates with Netrin-1 in Midline Axon Guidance.** *Cell* 2003, 113(1):11 -123.
11. Moon M, Gomez TM: **Adjacent pioneer commissural interneuron growth cones switch from contact avoidance to axon fasciculation after midline crossing.** *Dev Biol* 2005, 288(2):474 -4486.
12. Shirasaki R, Murakami F: **Crossing the Floor Plate Triggers Sharp Turning of Commissural Axons.** *Dev Biol* 2001, 236(1):99 -108.
13. Lyuksyutova AI, Lu CC, Milanesio N, King LA, Guo N, Wang Y, Nathans J, Tessier-Lavigne M, Zou Y: **Anterior-Posterior Guidance of Commissural Axons by Wnt-Frizzled Signaling.** *Science* 2003, 302(5652):1984-1988.
14. Imondi R, Kaprielian Z: **Commissural axon pathfinding on the contralateral side of the floor plate: a role for B-class ephrins in specifying the dorsoventral position of longitudinally projecting commissural axons.** *Development* 2001, 128(23):4859-4871.
15. Wilson SW, Easter SS Jr.: **A Pioneering Growth Cone in the Embryonic Zebrafish Brain.** *PNAS* 1991, 88(6):2293-2296.
16. Clandinin TR, Zipursky SL: **Making Connections in the Fly Visual System.** *Neuron* 2002, 35(5):827-841.
17. Stellwagen D, Shatz CJ: **An Instructive Role for Retinal Waves in the Development of Retinogeniculate Connectivity.** *Neuron* 2002, 33(3):357-367.
18. Cang J, Renteria RC, Kaneko M, Liu X, Copenhagen DR, Stryker MP: **Development of Precise Maps in Visual Cortex Requires Patterned Spontaneous Activity in the Retina.** *Neuron* 2005, 48(5):797-809.
19. Hanson MG, Landmesser LT: **Increasing the Frequency of Spontaneous Rhythmic Activity Disrupts Pool-Specific Axon Fasciculation and Pathfinding of Embryonic Spinal Motoneurons.** *J Neurosci* 2006, 26(49):12769-12780.
20. Katz LC, Shatz CJ: **Synaptic activity and the construction of cortical circuits.** *Science* 1996, 274:1132 -11138.
21. McLean DL, Fan J, Higashijima S, Hale ME, Fetcho JR: **A topographic map of recruitment in spinal cord.** *Nature* 2007, 446(7131):71-75.
22. Higashijima SI, Schaefer M, Fetcho JR: **Neurotransmitter properties of spinal interneurons in embryonic and larval zebrafish.** *J Comp Neurol* 2004, 480(1):19-37.
23. Li WC, Higashijima S, Parry DM, Roberts A, Soffe SR: **Primitive roles for inhibitory interneurons in developing frog spinal cord.** *J Neurosci* 2004, 24(25):5840-5848.
24. Li WC, Perrins R, Soffe SR, Yoshida M, Walford A, Roberts A: **Defining classes of spinal interneuron and their axonal projections in hatchling Xenopus laevis tadpoles.** In *J Comp Neurol Volume 441*. Issue 3 United States : 2001:248-265.
25. Li WC, Soffe SR, Roberts A: **The spinal interneurons and properties of glutamatergic synapses in a primitive vertebrate cutaneous flexion reflex.** *J Neurosci* 2003, 23(27):9068-9077.
26. Li WC, Soffe SR, Roberts A: **Dorsal Spinal Interneurons Forming a Primitive, Cutaneous Sensory Pathway.** *J Neurophysiol* 2004, 92(2):895-904.
27. Li WC, Soffe SR, Wolf E, Roberts A: **Persistent Responses to Brief Stimuli: Feedback Excitation among Brainstem Neurons.** *J Neurosci* 2006, 26(15):4026-4035.
28. Li WC, Soffe SR, Roberts A: **Spinal inhibitory neurons that modulate cutaneous sensory pathways during locomotion in a simple vertebrate.** *J Neurosci* 2002, 22(24):10924-10934.
29. Roberts A: **Early functional organization of spinal neurons in developing lower vertebrates.** *Brain Res Bull* 2000, 53(5):585-593.
30. Clarke JDW, Roberts A: **Interneurones in the Xenopus embryo spinal cord: sensory excitation and activity during swimming.** In *J Physiol Volume 354*. ENGLAND ; 1984:345-362.
31. Li WC, Soffe SR, Roberts A: **Glutamate and acetylcholine corelease at developing synapses.** *PNAS* 2004, 101(43):15488-15493.
32. Clarke JDW, Hayes BP, Hunt SP, Roberts A: **Sensory physiology, anatomy and immunohistochemistry of Rohon-Beard neurones in embryos of Xenopus laevis.** In *J Physiol Volume 348*. ENGLAND ; 1984:511-525.
33. Hartenstein V: **Early pattern of neuronal differentiation in the Xenopus embryonic brainstem and spinal cord.** *J Comp Neurol* 1993, 328(2):213-231.
34. Higashijima S, Masino MA, Mandel G, Fetcho JR: **Engrailed-1 expression marks a primitive class of inhibitory spinal interneuron.** *J Neurosci* 2004, 24(25):5827-5839.
35. Dale N: **Reciprocal inhibitory interneurones in the Xenopus embryo spinal cord.** In *J Physiol Volume 363*. ENGLAND ; 1985:61-70.
36. Soffe SR, Zhao FY, Roberts A: **Functional projection distances of spinal interneurons mediating reciprocal inhibition during swimming in Xenopus tadpoles.** In *Eur J Neurosci Volume 13*. Issue 3 France ; 2001:617-627.
37. Dale N, Roberts A: **Dual component amino - acid - mediated synaptic potentials: excitatory drive for swimming in Xenopus embryos.** *J Physiol (London)* 1985, 363:35-59.
38. Bourikas D, Pekarik V, Baeriswyl T, Grunditz A, Sadhu R, Nardo M, Stoeckli ET: **Sonic hedgehog guides commissural axons along the longitudinal axis of the spinal cord.** *Nat Neurosci* 2005, 8(3):297.
39. Kahn JA, Roberts A: **The central nervous origin of the swimming motor pattern in embryos of Xenopus laevis.** In *J Exp Biol Volume 99*. ENGLAND ; 1982:185-196.
40. Wang XJ, Rinzel J: **Alternating and sychronous rhythms in reciprocally inhibitory model neurons.** *neural Comput* 1992, 4:84 -897.
41. Cymbalyuk GS, Patel GN, Calabrese RL, DeWeerth SP, Cohen AH: **Modeling Alternation to Synchrony with Inhibitory Coupling: A Neuromorphic VLSI Approach.** *Neural Computation* 2000, 12(10):2259-2278.
42. Sautois B, Soffe SR, Li WC, Roberts A: **Role of type-specific neuron properties in a spinal cord motor network .** *J computational Neuroscience* 2007, 23(1):59 -577.
43. Roberts A, Tunstall MJ: **Mutual Re-excitation with Post-Inhibitory Rebound: A Simulation Study on the Mechanisms for Locomotor Rhythm Generation in the Spinal Cord of Xenopus Embryos.** *Eur J Neurosci* 1990, 2(1):11-23.
44. Stepanyants A, Chklovskii DB: **Neurogeometry and potential synaptic connectivity.** *Trends Neurosci* 2005, 28(7):387.
45. Shepherd GMG, Stepanyants A, Bureau I, Chklovskii D, Svoboda K: **Geometric and functional organization of cortical circuits.** *Nat Neurosci* 2005, 8(6):782.
46. Roberts A, Clarke JDW: **The neuroanatomy of an amphibian embryo spinal cord.** *Phil Trans Roy Soc* 1982, 296:195-212.
47. Jessell TM: **Neuronal specification in the spinal cord: inductive signals and transcriptional codes.** *Nat Rev Genet* 2000, 1(1):20-29.
48. Lee SK, Pfaff SL: **Transcriptional networks regulating neuronal identity in the developing spinal cord.** *Nat Neurosci* 2001, 4 Suppl:1183-1191.
49. Zhuang BQ, Sockanathan S: **Dorso-ventral patterning: a view from the top .** *Current Opinion in Neurobiology* 2006, 16:20 -224.
50. Dickson BJ, Gilestro GF: **Regulation of Commissural Axon Pathfinding by Slit and its Robo Receptors.** *Annual Review of Cell and Developmental Biology* 2006, 22(1):651-675.
51. Bovolenta P, Rodriguez J, Esteve P: **Frizzled/RYK mediated signalling in axon guidance.** *Development* 2006, 133(22):4399-4408.
52. Kennedy TE, Wang H, Marshall W, Tessier-Lavigne M: **Axon Guidance by Diffusible Chemoattractants: A Gradient of Netrin Protein in the Developing Spinal Cord.** *J Neurosci* 2006, 26(34):8866-8874.
53. Cline H: **Dendritic arbor development and synaptogenesis.** *Current Opinion in Neurobiology* 2001, 11(1):118-126.
54. Jontes JD, Buchanan JA, Smith SJ: **Growth cone and dendrite dynamics in zebrafish embryos: early events in synaptogenesis imaged in vivo.** *Nat Neurosci* 2000, 3(3):231-237.

55. Seebach BS, Ziskind-Conhaim L: **Formation of transient inappropriate sensorimotor synapses in developing rat spinal cords.** *J Neurosci* 1994, 14(7):4520-4528.
56. Roberts A, Walford A, Soffe SR, Yoshida M: **Motoneurons of the axial swimming muscles in hatchling Xenopus tadpoles: features, distribution, and central synapses.** In *J Comp Neurol Volume 411*. Issue 3 UNITED STATES ; 1999:472-486.
57. Yoshida M, Roberts A, Soffe SR: **Axon projections of reciprocal inhibitory interneurons in the spinal cord of young Xenopus tadpoles and implications for the pattern of inhibition during swimming and struggling.** In *J Comp Neurol Volume 400*. Issue 4 UNITED STATES ; 1998:504-518.
58. Goodhill GJ, Gu M, Urbach JS: **Predicting axonal response to molecular gradients with a computational model of filopodial dynamics.** *Neural Computation* 2004, 16:2221 -22243.

Available online at www.sciencedirect.com
ScienceDirect
BioSystems 93 (2008) 101–114
BioSystems
www.elsevier.com/locate/biosystems

Stochasticity and functionality of neural systems: Mathematical modelling of axon growth in the spinal cord of tadpole

Roman Borisyuk [a,*], Tom Cooke [a], Alan Roberts [b]

[a] CTCN, University of Plymouth, Plymouth PL4 8AA, United Kingdom
[b] School of Biological Sciences, University of Bristol, Bristol BS8 1UG, United Kingdom

Received 23 January 2008; received in revised form 10 March 2008; accepted 20 March 2008

Abstract

In this paper we study a simple mathematical model of axon growth in the spinal cord of tadpole. Axon development is described by a system of three difference equations (the dorso-ventral and longitudinal coordinates of the growth cone and the growth angle) with stochastic components. We find optimal parameter values by fitting the model to experimentally measured characteristics of the axon and using the quadratic cost function. The fitted model generates axons for different neuron types in both ascending and descending directions which are similar to the experimentally measured axons. Studying the model of axon growth we have found the analytical solution for dynamics of the variance of the dorso-ventral coordinate and the variance of the growth angle. Formulas provide conditions for the case when the increase of the variance is limited and the analytical expression for the saturation level. It is remarkable that optimal parameters always satisfy the condition of limited variance increase. Taking into account experimental data on distribution of neuronal cell bodies along the spinal cord and dorso-ventral distribution of dendrites we generate a biologically realistic architecture of the whole tadpole spinal cord. Preliminary study of the electrophysiological properties of the model with Morris-Lecar neurons shows that the model can generate electrical activity corresponding to the experimentally observed swimming pattern activity of the tadpole in a broad range of parameter values.

Keywords: Axon growth; Computational model; Stochastic; Variance

1. Introduction

It is well known that there are many sources of noise and stochasticity in neural systems. For example, in earlier phases of development of neurons, stochasticity plays an important role and in fact controls many intracellular and extracellular developmental processes (Kaern et al., 2005). The presence of stochasticity increases the complexity of neural systems and makes their functional behaviour more diverse, complex and controllable. In this paper we model development of the neural architecture of the spinal cord of the young frog tadpole. Although the development of the tadpole spinal cord includes a variety of stochastic processes governing the assembly of the neural architecture, this neural system demonstrates extremely robust functional behaviour. In fact, the interplay between deterministic rules pre-wired in genetic instructions and stochastic processes of the growth of individual cells results in the neural circuit of the spinal cord controlling swimming.

The developing spinal cord of the hatched clawed toad (Xenopus) tadpole is a relatively simple biological system (Li et al., 2001, 2003). The spinal cord contains less than 2000 neurons divided into very few types (≈10) yet it allows simple reflexes and swimming. Experimental measurements are available to support the modelling of both the anatomy and electrophysiology of spinal circuits (Sautois et al., 2007; Li et al., 2007). Our modelling is based on experimental data collected at the Lab directed by Prof. Alan Roberts at Bristol University (Li et al., 2002, 2007). These data allow us to examine both axon growth and synaptic connections between six different types of spinal neurons.

Although there is a significant body of biological knowledge regarding the chemical cues and gradients that control the development of neuronal circuits (Dickson, 2002; Cline, 2003; Chilton., 2006; Schnorrer and Dickson, 2004; Wen and Zheng, 2006) many details of the biological mechanisms of axon growth

* Corresponding author.
E-mail addresses: rborisyuk@plymouth.ac.uk (R. Borisyuk), tcooke@plymouth.ac.uk (T. Cooke), a.roberts@bristol.ac.uk (A. Roberts).

0303-2647/$ – see front matter © 2008 Elsevier Ireland Ltd. All rights reserved.
doi:10.1016/j.biosystems.2008.03.012

are still unknown. The traditional approach to modelling axon growth is based on the idea that the growth cone follows different molecular gradients (Goodhill et al., 2004; Xu et al., 2005; Krottje et al., 2007). For example, the mathematical model presented in a recent paper (O'Toole et al., 2008) takes into account forces at the growth cone, the viscoelastic properties of the axon, and the adhesions between the axon and surrounding substrate. These three factors define whether the axon elongates by tip growth or simply by stretching. Here we do not consider the details of growth cone navigation in steep and shallow chemical gradients. Instead we build a simple mathematical model reflecting several key attraction and repulsion processes guiding axon development. Thus, our approach is to develop a mathematical model of axon growth which is as simple as possible and includes only a small number of parameters. The model should allow fitting to all available experimental measurements of axons of tadpole spinal cord: all cell types in both ascending and descending directions.

The biochemical factors controlling the direction of axon growth are beginning to be revealed (de Anda et al., 2005; Shirasaki and Murakami, 2001; Lyuksyutova et al., 2003; Moon and Gomez, 2005; Charron et al., 2003; Gomez and Zheng, 2006) and we have included in the model several basic biological rules controlling both the dorso-ventral and longitudinal positions of the growing axon. For example, some axons start to grow ventrally and cross to the opposite side. After crossing, these commissural axons are transformed and they then turn to grow longitudinally (Imondi and Kaprielian, 2001), either towards the head or the tail, or they branch to grow in both directions. Early patterns of growth by pioneer axons provide a basic scaffold of axon tracts that can be followed by later axons and in this way help to direct their growth (Wilson and Easter, 1991). Once the axons have grown to more or less the "right" area, they start to make synapses with the branched dendrites emerging from the cell bodies of other neurons.

This study of axon growth is based on a new hypothesis: there are no specific targets in this system and the axon grows according to some general gradient following rules which guide it to a particular Dorso-Ventral (D-V) region of the spinal cord (Li et al., 2007). The growing axon runs along the spinal cord (without branching) and makes synapses directly onto dendrites that it passes with some probability. More precisely: if the growing axon meets a dendrite of some other neuron allocated in the same D-V part of the spinal cord, then with some probability this axon will make a synaptic contact.

We present and study a simple mathematical model which is described by a nonlinear system of three difference equations and includes a stochastic process. Fitting the model to experimental measurements of axons allows us to find optimal parameter values for each neuron type in the spinal architecture. Using these optimal parameters, we generate a biologically realistic model of the tadpole spinal cord and test the possibility of generating electrical activity corresponding to swimming.

In Section 2 we provide a short description of the experimental measurements of axons which have been used for model development and model fitting. In Section 3 we formulate a dynamical model of axon growth which includes a stochastic process.[1] In Section 4 we study dynamical and probabilistic properties of the model to test its suitability for modelling the anatomical structure of the spinal cord. Section 5 is devoted to a description of the process of fitting the model to experimental axon measurements and finding optimal parameter values. These optimal parameters make it possible to generate a biologically realistic neural architecture of the spinal cord with the same statistical characteristics as experimentally measured axons which are described in Section 2. In Section 6 we describe a simulated neural architecture of a biologically realistic model of the whole spinal cord. In Section 7 we discuss modelling results of the anatomy of the spinal cord and the possibility that the generated neural architecture will be able to produce a swimming behaviour.

2. Description of Axon Measurements

In this Section we provide a short description of experimental measurements of axons which have been used for model development. A detailed description of experimental methods and results can be found in Li et al. (2007).

2.1. Neurons of the Spinal Cord

The 2-day old, hatchling Xenopus tadpole is 5 mm long (see Fig. 1 in publication Li et al., 2007). The spinal cord forms a simple tube ($\approx$ 0.1 mm diameter). On each side of the spinal cord lies a layer of nerve cells or neurons loosely organized into longitudinal columns. As in all vertebrates, the neurons form a dorsal to ventral sequence: sensory neurons, interneurons and motoneurons. The young tadpole spinal cord has remarkably few classes of neurons and in this paper we consider the six classes of cells: sensory and motor neurons as well as four types of interneurons.

(1) *Dorsal Rohon-Beard neurons* (*RB*) are sensory, innervate the skin and respond to touch. Their central axons ascend and descend to excite other neurons.
(2) *Motorneurons* (*MN*) have short axons which are mostly ventrally located.
(3) *Dorsolateral commissural interneurons* (*dlc*) are sensory pathway interneurons excited by sensory RB neurons. They excite contralateral neurons and initiate swimming activity when the skin is stimulated (Li et al., 2003).
(4) *Ascending interneurons* (*aIN*) have a broad dorsal-ventral distribution. They inhibit neurons on the same side and it has been found that this inhibition can affect all types of neurons.
(5) *Commissural interneurons* (*cIN*) are a middle dorso-ventral group of neurons which produce inhibition of on the oppo-

[1] Model description and some details of model fitting have been reported in additional file which can be downloaded from our open access publication (Li et al., 2007). However, for the convenience of the reader we review here this on-line publication and provide a complete description of the model and fitting technique. Section 4 on analysis of variance growth and Section 6 on reconstruction of spinal cord anatomical architecture are entirely novel.

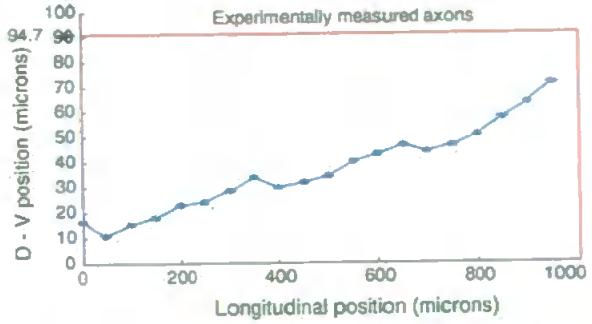

Fig. 1. An example of axon measurements for aIN ascending cell.

site side of the spinal cord (Dale, 1985) to organize the alternation of activity between the two sides during swimming.

(6) *Descending interneurons* (*dIN*) excite other neurons (Li et al., 2004, 2006). They provide ipsilateral excitation during tadpole swimming (Dale, 1985; Li et al., 2004).

All interneurons grow their axons in both ascending (from the tail to the head) and descending (from the head to the tail) directions except excitatory dIN neurons which send their axons in the descending direction only. It is likely that these connections propagate activity from the head to the tail and form the metachronal wave of the swimming pattern.

2.2. Projection of Axon Measurements

The available experimental data provide measurements of spinal cord axons for each neuron type in both descending and ascending directions when both are present. The longitudinal dimension in the model was always 1000μm however axons can be shorter or longer than this full length. Experimental measurements of dorso-ventral axon position (in micrometers) were made every 50μm. An example of a measured axon for aIN ascending cell is shown in Fig. 1. The horizontal red line ($y = 94.7\mu m$) shows the dorso-ventral height boundary of the spinal cord and the vertical red line shows the longitudinal boundary of considered spinal cord measurements.

Fig. 2 shows an example of nine experimentally measured axons for the aIN cell type in descending direction. These measurements have been used to characterize axon allocations in the dorso-ventral dimension.

The next step is the projection of axon measurements in the dorso-ventral direction. Because the boundaries of the spinal cord vary between tadpoles, we must normalize axon coordinates before projecting them. We do this by dividing both vertical and horizontal axon coordinates by the dorso-ventral height of the spinal cord (in the example shown in Fig. 1 of aIN ascending axons the height $H = 94.7\mu m$). Normalization of both coordinates allows us to keep the angular structure unchanged. Of course, after this transformation a step along the horizontal axis will be different from 50μm however all angles and proportions between horizontal and vertical sizes will not be disturbed by the normalization transformation and will be kept unchanged.

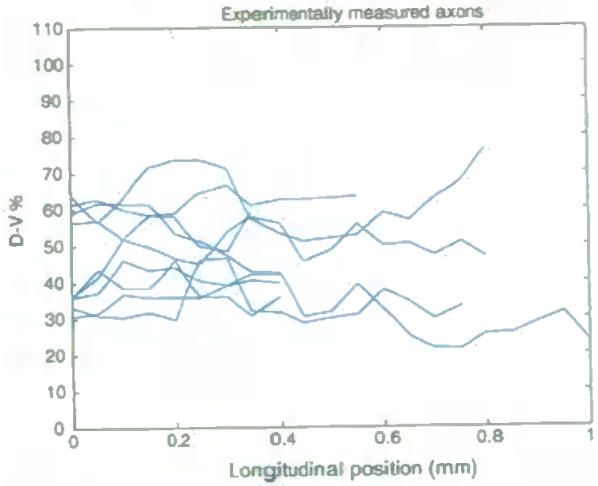

Fig. 2. Example of experimental measurements of aIN axons growing in descending direction.

After normalization we project all measured axon coordinates of this aIN ascending axon to the vertical axis and repeat this procedure for each aIN ascending axon. The total number of axon measurements is n_e ($n_e = 167$) and these data represent the dorso-ventral distribution of axon measurements in the interval [0, 100]. We divide this interval into 10 bins, count the number of measurements in each bin, and normalize it by the total number n_e to get the probability of finding an axon measurement in the bin. The resulting distribution is shown in Fig. 3. The same normalization and projection procedures have been applied to each cell type and for axons in ascending and descending directions independently and similar distributions of D-V projections have been calculated. The D-V axon distributions of some neurons are rather narrow. RB sensory neuron axons are dorsal, while motoneurons are ventral. cINs, dINs and dIcs are all slightly biased towards ventral positions. Inhibitory aINs have a broad D-V axon distribution. These D-V distributions will be used to fit the model to the experimental data (see Section 5).

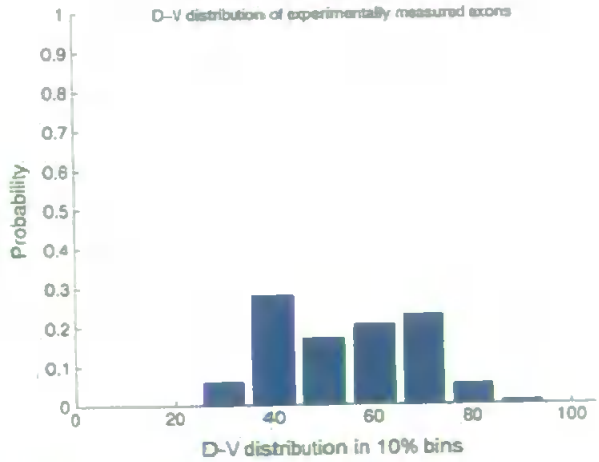

Fig. 3. Example of D–V distribution of experimental measurements of aIN axons growing in ascending direction.

2.3. Measurement of Cell Bodies and Dendrites

Similar measurements are available for D-V distribution of cell bodies and dendrites. Cell bodies are located mostly in dorsal positions except motoneurons which are located more ventrally.

The dorso-ventral range of dendrites was determined from the positions of the most ventral and dorsal dendrite for each neuron. This range will limit the number of axons contacted. We ignore the possibility that dendrites might be unevenly distributed within this range. The dendrite dorso-ventral ranges were summed for each neuron type, except RB neurons, which do not have dendrites. For each 10% dorso-ventral position bin (the spinal cord diameter is approximately 100μm so bin width is approximately 10μm) in the 10μm thick marginal zone where dendrites and axons lie, we found the probability that an individual neuron of each type would have dendrites occupying that bin. The dendrite distributions for neurons active during swimming (MNs, aINs, cINs and dINs) were broad but all had a maximum just below the dorso-ventral midline (in the 30% or 40% bin) and fell away dorsally. In contrast, the dendrites of dlc sensory pathway interneurons had a maximum dorsally (in the 80% bin) and fell away ventrally.

We will use these data regarding the distribution of cell bodies and dendrites to generate the whole neuronal architecture of the spinal cord (Section 6).

3. Model of Axon Growth

Since axons grow a considerable distance along the spinal cord (often 1–2 mm in a 5 mm long animal) and can wander dorsal or ventral as they grow, their pattern of growth will have a strong influence on their potential to contact dendrites of different neuron types. Analysing experimental data we concluded that the whole neural circuit of the spinal cord and synaptic contacts may depend simply on dorso-ventral axon and dendrite distribution patterns (Li et al., 2007). We therefore investigated whether a simple model, without any cell–cell recognition, could generate patterns of axon growth that would reproduce the observed axon distributions. For simplicity, we assumed that dendrites are static and passive.

3.1. Specification of Model Requirements and Model Variables

Our computational model of axon growth starts from the point when axons start to grow longitudinally. This point will be determined by the position of the soma and the initial behaviour of the axon. In the case of RB neurons, the axons grow directly from the soma towards the head and tail. In most other spinal neurons the axon first grows ventrally and then turns to grow longitudinally either on the same side or after crossing ventrally to the other side. We use the experimental observations to give us starting positions and initial growth angles of axons as well as their final lengths. A repetitive process of advancing the axon 1μm along its current growth angle and then modifying the growth angle is then applied until the predetermined rostrocaudal length of the axon is reached.

The current location and orientation of the tip of the axon (growth cone) are represented by three variables: x rostrocaudal position, y dorso-ventral (D-V) position, and θ growth angle. θ is defined as the deviation from longitudinal growth; positive values of θ indicate a tendency to grow dorsally while negative values of θ indicate a tendency to grow ventrally.

In the previous section we described experimental measurements which had been made for tadpoles with different spinal cord heights. To reflect that in the model, we consider axon growth in one side of the spinal cord represented as a rectangle with some height H corresponding to the dorso-ventral dimension with values randomly distributed in the range of admissible biological values (about 100μm) and fixed length $W = 1000\mu m$ corresponding to the longitudinal axis. Thus we consider the rectangle $H \times W$ and growing axons are allocated inside this field.

Developing the model equations, we implicitly assume that chemical gradients experienced by the growth cone are exponential, which for a single gradient would produce a constant rate of turning independent of the location within the gradient (but not independent of the current growth angle). The dependence of axon growth angle on dorso-ventral position (note that the dorso-ventral axis corresponds to the vertical axis (height) of the rectangle and the longitudinal location is considered to lie along the horizontal axis (length) of the rectangle) that we observe is assumed to be the consequence of interaction between at least two gradient-following processes: the noise in the axon growth angle and the tendency to grow towards some particular location. The noise component describes a random deviation of the current angle from the deterministic component and is represented by a random variable uniformly distributed in the interval $(-\alpha, \alpha)$, where parameter α defines the boundary for the angle deviation (see Fig. 4). Thus, the noise is modelled by a uniformly distributed random variable with mean equal to zero and variance equal to $\alpha^2/3$.

3.2. Mathematical Formulation

We describe the iterative process of axon growth by the system of three nonlinear difference equations. Iterations start from initial coordinates $x_0 = 0$ and some value y_0 in the rectangle $H \times W$ and initial growth angle θ_0. The values y_0 and θ_0 are

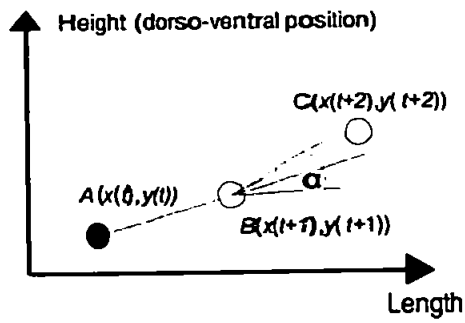

Fig. 4. The deterministic direction of growth is shown by the black line connecting point A and the yellow dot. The angle specifies boundaries of random deviation. The red line shows the chosen direction of growth for the iteration.

derived from experimental distributions of initial D-V coordinates and growth angles. The system of axon growth equations is:

$$\begin{cases} x_{n+1} = x_n + \Delta cos(\theta_n) \\ y_{n+1} = y_n + \Delta sin(\theta_n) \\ \theta_{n+1} = (1-\gamma)\theta_n + \mu(\bar{y} - y_n) + \xi \end{cases} \quad (3.1)$$

where n is the iteration number which represents the current position of the tip of the growing axon; ξ is a random variable uniformly distributed in the interval $[-\alpha, \alpha]$; (α typically is about 2–5°). Δ is the 1 μm distance grown in a single iteration. The parameter γ represents the tendency of an axon to turn towards an angle of 0°—in other words the tendency of the growth cone to orient towards longitudinal growth. If γ is zero (and $\mu = 0$ as well) then the deterministic part of the growth angle is not changed at each time step and a random deviation applies to this direction. When $0 < \gamma < 1$, the term with γ in the equation for θ will cause the angle to decay to zero. This part of the model can be justified by experimental findings which show that this orienting process towards zero angle is dependent on the current deviation from longitudinal growth—the steeper the current growth angle, the stronger the tendency to straighten towards horizontal growth. The effect of parameter γ can also be interpreted as the consequence of a longitudinal gradient-following process, which would be expected to produce the same dependence on growth cone angle.

The parameter $\bar{y}$ represents the dorso-ventral position of an attractor to which axon trajectories are drawn with a strength which can be described by parameter μ (see Eq. (3.1)). Thus, parameters μ and $\bar{y}$ characterise the interaction between two opposing gradient-following processes. The parameter $\bar{y}$ is the dorso-ventral position at which these processes effectively cancel each other out. The parameter μ represents the strength of the net attraction towards $\bar{y}$. The effects of these parameters can be interpreted as a system with two repulsive gradients, one pushing from the ventral side to the dorsal side (we know that there is some drive here at least with the commissural neurons) and one pushing from the dorsal side to the ventral direction (Li et al., 2007). The relative sensitivity of the axon to these two gradients would determine the value of the parameter $\bar{y}$ and the absolute sensitivity of the growth cone to ligands would determine the value of the parameter μ.

3.3. Discussion of Specific Features of the Model

In life, some factors guide axons towards a longitudinal growth path and away from the edges of the cord. We therefore examined the turning angles of real axons (between points 0.05 mm apart) and found that they depended strongly on their current angle of growth and weakly on their D-V position. For all measured neuron types the slope of the regression lines for axon turning angles were negatively dependent on current axon growth angle and dorso-ventral position (Li et al., 2007). This remarkable finding means firstly that the more an axon deviates from longitudinal growth the more it will turn back. Secondly, the dependence of axon growth angle on dorso-ventral position means that the upper and lower boundaries of the cord are repulsive.

There are many possible factors that could influence axons to direct them away from edges (e.g. physical barriers to growth cone extension, D-V gradients of repellant signals, Bourikas et al., 2005) and guide them to a more longitudinal growth (e.g. fasciculation with other longitudinal axons, longitudinal gradients of attractive or repellent signals, Lyuksyutova et al., 2003). In our model the essence of such diverse mechanisms is encapsulated by parameter $\bar{y}$ which represents the dorso-ventral position of an attractor to which axon trajectories are drawn with a strength of μ. This fact can be proved easily in case of the deterministic model without any stochastic component to cause deviations from the attracting level. It is important to understand the probabilistic nature of that influence and in particular whether the variance of y_n is limited or will grow to infinity with the iteration number. We will address this question in the next Section.

This model contains four parameters and to specify their values we use an optimisation procedure to fit the model to measured axon data and find optimal parameters. In Section 5 we define a cost function and describe the optimization procedure. The cost function includes the squared differences between experimental and generated axon distributions in 10% dorso-ventral bins and the squared difference between tortuosities. Optimal parameter values are found that minimise the cost function and give the closest match for each type of neuron. We repeat the same procedure to get optimal parameter values for each type of neuron separately for ascending and descending axons where both exist.

The model of axon growth establishes that axon growth paths and distributions can be generated by very simple rules based only on the initial position and growth angle of the axons. Since these modelled axon distributions closely match those measured for real axons, it follows that their contact probabilities with dendrites will also be similar and we have confirmed this (Li et al., 2007).

Also, the model was able to generate axon growth patterns very similar to those in the spinal cord. In many cases, the optimisation procedure was able to reach very small values of the cost function; for the few cases, where it did not, the generated axons were still very similar to real ones. In addition, the modelled axon growth angles showed the same dependence on current angle and D-V position as the measured axons. Just as in the real axons, scatter plots and linear regressions showed negative slopes. This significant match of model and real axons is important as these features of measured axons were not used during model development.

4. Analysis of Time Course of Variance

The model of axon growth is formed in terms of a system of three nonlinear difference equations, one of which has a stochastic term. The resulting process of axon growth is sculpted by a complicated interplay between the deterministic and stochastic components of this system of Eq. (3.1). On each time step we add a random variable, therefore, the variance of y_n grows with time and may reach large values after some number of iterations.

Thus it is important to understand how the variance of the D-V coordinate and the variance of growth angle depend on the iteration number. In particular, the important question is whether the variance is limited and saturates to some level when time tends to infinity or the variance increases without limitation. We have found an analytical solution to this problem. We only need to consider two equations for y_n and θ_n because these equations do not include x_n. In addition, we consider $\Delta = 1$ and to simplify formulas we introduce $\beta = (1 - \gamma)$. In our consideration of the model, the angle θ_n is small and we use this fact to simplify the original nonlinear model and make it linear. Thus, for study of variances we consider the following model of two linear difference equations:

$$\begin{cases} \theta_{n+1} = \beta\theta_n + \mu(\bar{y} - y_n) + \xi_{n+1} \\ y_{n+1} = y_n + \theta_n. \end{cases}$$

Denoting the constant term in the first equation by $D = \mu\bar{y}$ we have the following equations:

$$\begin{cases} \theta_{n+1} = \beta\theta_n - \mu y_n + D + \xi_{n+1} \\ y_{n+1} = \theta_n + y_n. \end{cases} \tag{4.1}$$

It is useful to convert this system of two first order difference equations into a single second-order difference equation for θ_n by excluding the variable y_n:

$$\theta_{n+1} = (\beta + 1)\theta_n - (\beta + \mu)\theta_{n-1} + (\xi_{n+1} - \xi_n).$$

Substitutions $p = \beta + 1; q = -(\beta + \mu)$ lead to the following second order linear difference equation with a stochastic term:

$$\theta_{n+1} = p\theta_n + q\theta_{n-1} + (\xi_{n+1} - \xi_n). \tag{4.2}$$

We would like to find the variance of θ_n as a function of n. First, we define initial values. Generally speaking this second order equation needs two arbitrary initial conditions. However, from a consideration of the initial conditions for system (4.1) we can find:

$$\begin{cases} y_1 = \theta_0 + y_0 \\ \theta_1 = \beta\theta_0 - \mu y_0 + D + \xi_1 \end{cases}$$

where θ_0 and y_0 are arbitrary constants. We can rewrite the second equation as $\theta_1 = A_1 + \xi_1$ where A_1 includes all non-random terms. Thus the initial conditions for (4.2) are θ_0 and $\theta_1 = A_1 + \xi_1$ where θ_0 and A_1 are arbitrary constants. Let us write several sequential solutions of (4.2):

$$\begin{aligned} \theta_0 &= A_0, \\ \theta_1 &= A_1 + \xi_1, \\ \theta_2 &= A_2 + (p - 1)\xi_1 + \xi_2, \\ \theta_3 &= A_3 + (p^2 - p + q)\xi_1 + (p - 1)\xi_2 + \xi_3, \\ \theta_4 &= A_4 + (p^3 - p^2 + 2pq - q)\xi_1 + (p^2 - p + q)\xi_2 \\ &\quad + (p - 1)\xi_3 + \xi_4, \end{aligned}$$

where A_0, A_1, ..., A_4 denote the sum of all non-random terms.

From these equations we can see that any equation includes the same terms as the previous equation (with the index of ξ increased by 1), plus one new term which is ξ with the index corresponding to the index of θ in the left hand side. Now we can write the general form of equation for θ_n. We denote the part of the equation without a random variable by A_n and we introduce coefficients B_k to give terms with ξ_k the form $B_{n-k}\xi_k$. The equation for θ_n is

$$\theta_n = A_n + B_{n-1}\xi_1 + B_{n-2}\xi_2 + \ldots + B_1\xi_{n-1} + B_0\xi_n. \tag{4.3}$$

Taking into account two sequential equations for $n = k, n = k + 1$:

$$\begin{aligned} \theta_k &= A_k + B_{k-1}\xi_1 + B_{k-2}\xi_2 + \ldots + B_1\xi_{k-1} + B_0\xi_k \\ \theta_{k+1} &= A_{k+1} + B_k\xi_1 + B_{k-1}\xi_2 + \ldots + B_1\xi_k + B_0\xi_{k+1}, \end{aligned} \tag{4.4}$$

and using the Eq. (4.2) we can write an equation for θ_{k+2} which provides an iterative formula for coefficients B_k:

$$\begin{aligned} \theta_{k+2} = p\theta_{k+1} + q\theta_k &= (pA_{k+1} + qA_k) + (pB_k + qB_{k-1})\xi_1 \\ &\quad + (pB_{k-1} + qB_{k-2})\xi_2 + \ldots + (B_2p + qB_1)\xi_{k-1} \\ &\quad + (B_1p + qB_0)\xi_k + (pB_0 - 1)\xi_{k+1} + \xi_{k+2}. \end{aligned} \tag{4.5}$$

Now we can write iterative equations for the coefficients B_k:

$$\begin{aligned} B_0 &= 1, \\ B_1 &= p - 1, \\ B_2 &= pB_1 + qB_0, \\ B_3 &= pB_2 + qB_1, \end{aligned}$$

and in the general case:

$$B_n = pB_{n-1} + qB_{n-2}. \tag{4.6}$$

Solution for the second order linear difference Eq. (4.6) with the initial conditions $B_0 = 1$, $B_1 = p - 1$ is

$$B_n = \frac{1}{\sqrt{p^2 + 4q}}[(\lambda_1 - 1)\lambda_1^n - (\lambda_2 - 1)\lambda_2^n] \tag{4.7}$$

where λ_1 and λ_2 are roots of the quadratic equation:

$$\lambda^2 - p\lambda - q = 0. \tag{4.8}$$

Let us consider the variance of both sides of the Eq. (4.3)

$$\mathrm{Var}(\theta_n) = \mathrm{Var}(\xi)[B_{n-1}^2 + B_{n-2}^2 + \ldots + B_1^2 + B_0^2]. \tag{4.9}$$

We use the formula (4.7) to substitute for the coefficients B_n in (4.9):

$$\begin{aligned} \mathrm{Var}(\theta_n) = \frac{\mathrm{Var}(\xi)}{3(p^2 + 4q)} &\Big[(\lambda_1 - 1)^2(1 + \lambda_1^2 + (\lambda_1^2)^2 + \ldots \\ &+ (\lambda_1^2)^{n-1}) + (\lambda_2 - 1)^2(1 + \lambda_2^2 + (\lambda_2^2)^2 + \ldots \\ &+ (\lambda_2^2)^{n-1}) - 2(\lambda_1 - 1)(\lambda_1 - 1)(1 + \lambda_1\lambda_2 + \ldots \\ &+ (\lambda_1\lambda_2)^{n-1})\Big]. \end{aligned}$$

Using three times the formula for summation of a geometric progression with common ratios λ_1^2, λ_2^2 and $\lambda_1\lambda_2$ and substituting $Var(\xi) = \alpha^2/3$ we have the final formula for the variance of θ_n:

$$\mathrm{Var}(\theta_n) = \frac{\alpha^2}{3(p^2+4q)} \times \left[\frac{(\lambda_1-1)^2}{1-\lambda_1^2}(1-\lambda_1^{2n}) + \frac{(\lambda_2-1)^2}{1-\lambda_2^2}(1-\lambda_2^{2n}) - \frac{2(\lambda_1-1)(\lambda_2-1)}{1-\lambda_1\lambda_2}(1-(\lambda_1\lambda_2)^n)\right].$$

If $|\lambda_1| < 1$ and $|\lambda_2| < 1$ then the variance saturates for large n and we can simplify this expression for the case $n \to \infty$:

$$\mathrm{Var}(\theta_\infty) = \frac{\alpha^2}{3(p^2+4q)}\left[\frac{(\lambda_1-1)^2}{1-\lambda_1^2} + \frac{(\lambda_2-1)^2}{1-\lambda_2^2} - \frac{2(\lambda_1-1)(\lambda_2-1)}{1-\lambda_1\lambda_2}\right].$$

An expression for the variance of y_n as a function of n can be derived using the same method we used for the variance of θ_n. Let us start from Eq. (4.1) and excluding the variable θ_n re-write the system of two first order equations as the second order linear equation for the variable y_n:

$$y_{n+1} = (\beta+1)y_n - (\beta+\mu)y_{n-1} + D + \xi_n. \tag{4.10}$$

We use the same substitutions as above $p = \beta + 1; q = -(\beta+\mu)$ and this gives the following second order linear difference equation:

$$y_{n+1} = py_n + qy_{n-1} + D + \xi_n. \tag{4.11}$$

The initial conditions for this equation are y_0 and y_1, these can be considered as arbitrary constants. Also, we represent all terms containing no random variable by arbitrary constants A_n with corresponding indexes (A_2, A_3,...). The result of the first three iterations is the following:

$$y_2 = A_2 + \xi_1,$$
$$y_3 = A_3 + p\xi_1 + \xi_2,$$
$$y_4 = A_4 + (p^2+q)\xi_1 + p\xi_2 + \xi_3.$$

Introducing coefficients B_k to give terms with ξ_k the form $B_{n-k}\xi_k$, we can write the general form of the equation:

$$y_{n+1} = A_{n+1} + B_{n-1}\xi_1 + B_{n-2}\xi_2 + \ldots + B_2\xi_{n-2} + B_1\xi_{n-1} + B_0\xi_n. \tag{4.12}$$

A consideration of cases $n = k$, $n = k+1$, and $n = k+2$ similar to that used above yields a general expression for B_{k+1}:

$$B_{k+1} = pB_k + qB_{k-1}.$$

Solving this second order linear equation with initial conditions $B_0 = 1$; $B_1 = p$ gives the following formula for B_k:

$$B_k = \frac{1}{\sqrt{p^2+4q}}(\lambda_1^{k+1} - \lambda_2^{k+1}).$$

Here λ_1 and λ_2 are the roots of quadratic Eq. (4.8).

Now we consider the variance of both sides of (4.12) and substitute the formula for B_k:

$$\mathrm{Var}(y_{n+1}) = \frac{\mathrm{Var}(\xi)}{p^2+4q^2} \times \left[(\lambda_1^n-\lambda_2^n)^2 + (\lambda_1^{n-1}-\lambda_2^{n-1})^2 + \ldots + (\lambda_1-\lambda_2)^2\right].$$

Simplifying this expression gives the following geometric progressions:

$$\mathrm{Var}(y_{n+1}) = \frac{\mathrm{Var}(\xi)}{p^2+4q} \times \left[((\lambda_1^2)^n + (\lambda_1^2)^{n-1} + \ldots + \lambda_1^2) + ((\lambda_2^2)^n + \ldots + \lambda_2^2) - 2((\lambda_1\lambda_2)^n + \ldots + (\lambda_1\lambda_2))\right].$$

Summing three geometric progressions with common ratios λ_1^2, λ_2^2, and $\lambda_1\lambda_2$ and substituting $\mathrm{Var}(\xi) = \alpha^2/3$ yields the following expression for the variance of y_n:

$$\mathrm{Var}(y_n) = \frac{\alpha^2}{3(p^2+4q)}\left[\lambda_1^2\frac{1-\lambda_1^{2n-2}}{1-\lambda_1^2} + \lambda_2^2\frac{1-\lambda_2^{2n-2}}{1-\lambda_2^2} - 2\lambda_1\lambda_2\frac{1-(\lambda_1\lambda_2)^{n-1}}{1-\lambda_1\lambda_2}\right]. \tag{4.13}$$

If $|\lambda_1| < 1$ and $|\lambda_2| < 1$ then the variance saturates for large n and the formula for the case $n \to \infty$ is

$$\mathrm{Var}(y_\infty) = \frac{\alpha^2}{3(p^2+4q)}\left[\frac{\lambda_1^2}{1-\lambda_1^2} + \frac{\lambda_2^2}{1-\lambda_2^2} - \frac{2\lambda_1\lambda_2}{1-\lambda_1\lambda_2}\right]. \tag{4.14}$$

Fig. 5 shows both analytical and computational variances versus iteration number. This figure shows the variances for aIN cells with axons growing in descending direction. Optimal parameter values (the first row in Table 1) have been calculated according to the model fitting procedure (model fitting and parameter optimisation are described in the next Section). Analytical solution for the variance of dorso-ventral coordinate y_n is shown by smooth red line calculated according to formula (4.13). This variance saturates on the level 127.5 (dotted line) and this saturation level has been calculated by using the formula (4.14). It is interesting to note that using optimal parameters for calculation of the roots of characteristic equation (4.8) gives $|\lambda_1| < 1$ and $|\lambda_2| < 1$ for all cell types in all directions. For example for aIN axons in descending direction $\lambda_1 = 0.999$ and $\lambda_2 = 0.882$.

Computational variance has been calculated according to the following procedure. First, optimal parameter values of the model have been found by nonlinear least squares fit of the model

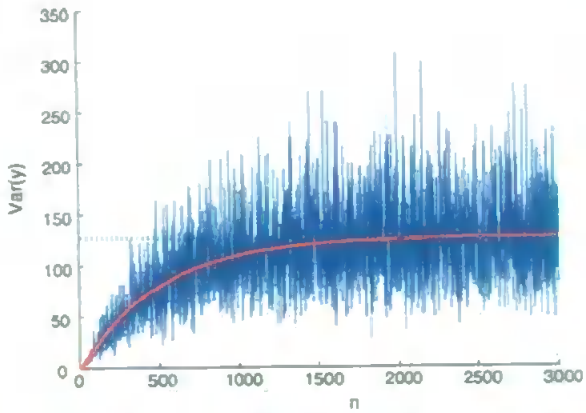

Fig. 5. Analytical and computational variances of axon D-V coordinate vs. the iteration number.

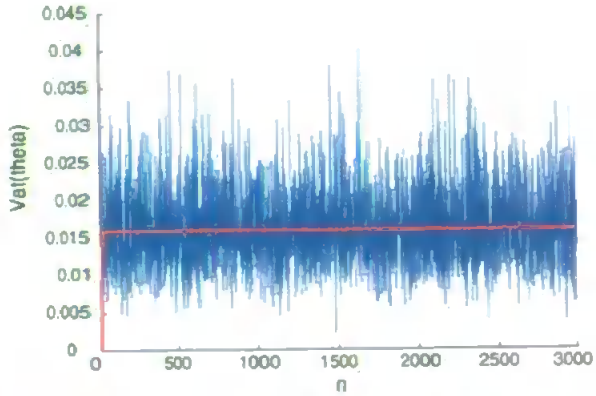

Fig. 6. Analytical and computational variances of axon growth angle vs. the iteration number.

to experimental measurements of axons. Second, using optimal parameter values we generate 200 axons starting from different initial values of the random number generator. Each axon is generated in the interval $x \in [0, n]$, $n = 2, 3, 4, \ldots, 3000$. Thus, for each iteration number n we generate a sample of D-V coordinates $y_n^1, y_n^2, \ldots, y_n^{200}$ and calculate a standard statistical estimate of the variance. It is clear from Fig. 5 that the estimate of variance varies in a wide range. Similar computations have been done for the variances of axon growth angle θ and both analytical and computational variances are shown in Fig. 6. The variance of axon growth angle saturates much faster than the variance of the D-V coordinate of the axon.

5. Fitting the Model to Experimental Measurements and Optimal Parameters

Our goal is to find model parameter values to accurately simulate an axon growth process which can generate axons that are similarly distributed in space as experimentally measured axons. Similarities are measured using a cost function with two components and the optimization procedure looks for a set of values of the four model parameters which provide a minimum of the cost function. *The first component* of the cost function takes into account similarity of distributions of axon projections in the dorso-ventral dimension. The projection procedure into 10 bins has been described above for experimental measurements and the same procedure was applied to generated axons. After that squared differences are calculated for each bin and summed. *The second component* of the cost function considers the squared difference between tortuosities of measured and generated axons. We would like the cost function to take into account the extent to which the path of the axon is circuitous rather than direct. The results from multiple model simulations suggest that tortuosity (total path length divided by straight line distance between start and end points) is an appropriate measure for this purpose. Thus, we calculate the tortuosity of each axon using the following formula:

$$T = \frac{\sum_{i=1}^{k} \sqrt{(x_i - x_{i-1})^2 + (y_i - y_{i-1})^2}}{\sqrt{(x_k - x_0)^2 + (y_k - y_0)^2}} \tag{5.1}$$

where $(x_i, y_i), i = 0, 1, \ldots, k$ are measured coordinates of the axon, and k is the number of measurements for the axon. After that we calculate the average tortuosity of experimental axons $\bar{T}^e$. The same procedure can be applied to generated axons and the average tortuosity of experimental axons is $\bar{T}^m$.

Now we would like to describe the process of axon generation. Suppose that values of the four parameters of the model are known, then we can start the process of axon generation described by the model equations above. For that we need to choose initial values for variables of the dynamical system, i.e. coordinates of the starting point of the axon (x_0, y_0) and the

Table 1
Parameters for model axon generation

	α	γ	μ	$\bar{y}$	λ_1	λ_2	Modulus
aIN des	0.104	0.119	0.0118	0.551	0.999	0.882	
aIN as	0.237	0.0881	0.0267	0.698	0.997	0.915	
cIN des	0.0538	0.0615	0.0139	0.736	0.998	0.941	
cIN as	0.0591	0.0826	0.0109	0.711	0.998	0.919	
dIN des	0.122	0.0957	0.0211	0.381	0.998	0.907	
RB des	0.117	0.0453	0.0558	0.698	0.977 + 0.0067i	0.977−0.0067i	0.977
RB as	0.122	0.0432	0.0500	0.792	0.978 + 0.0057i	0.978 −0.0057i	0.978
dlc des	0.142	0.09200	0.0411	0.412	0.995	0.913	
dlc as	0.114	0.115	0.0179	0.650	0.998	0.887	
MN	0.105	0.417	0.0282	0.176	0.999	0.583	

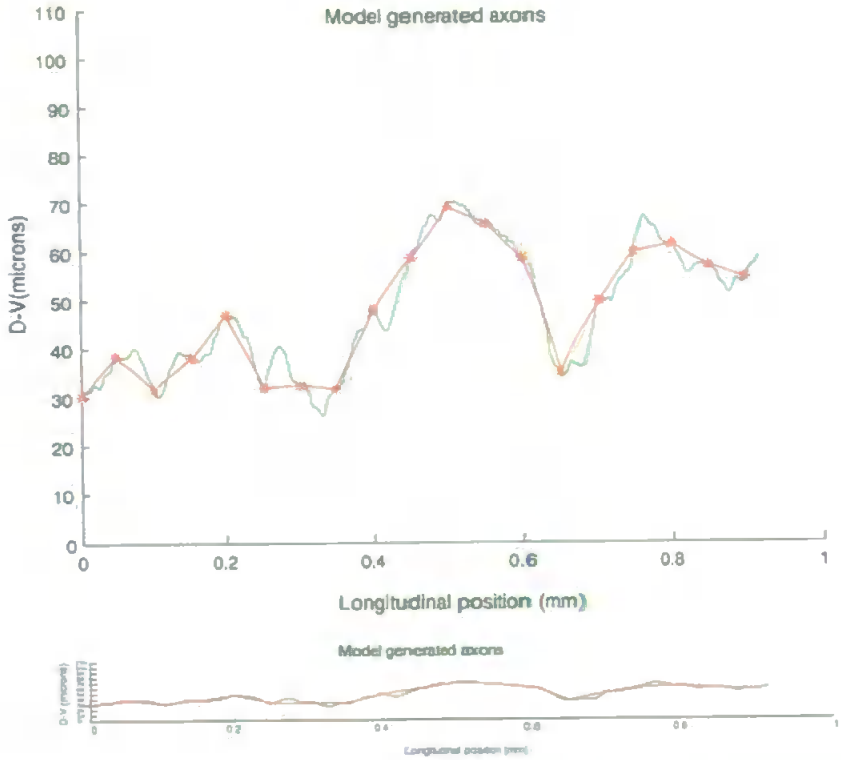

Fig. 7. Example of generated axon for optimal parameter values of aIN ascending neuron type. Green line shows generated axon and red line shows approximation with 50μm sampling along the horizontal axis. Lower panel shows the same axon with proportional axes; almost invisible axis marks and labels are the same as in the upper panel.

initial growth angle θ_0. Also, we need to fix the length of the generated axon.

For generation of all axons we choose the same initial point in the horizontal axis: $x_0 = 0$. To choose the initial value of the vertical coordinate, we first calculate the sample distribution (10 bins for 0–100 interval) of normalised initial vertical coordinates of all experimentally measured axons and generate a random number *ran* according to this distribution, thus, $y_0 = ran$. After that, to choose the initial angle, we consider the bin of distribution where the value of *ran* is and study initial angles $\eta_1, \eta_2, \ldots, \eta_q$ of axons which have the vertical coordinate of their starting point in this bin. We generate a uniformly distributed random angle η in the interval $\min(\eta_1, \eta_2, \ldots, \eta_q)$, $\max(\eta_1, \eta_2, \ldots, \eta_q)$ and the initial growth angle $\theta_0 = \eta$. Similarly, for the axon length we build the distribution of experimental axon length and generate the random number according to this distribution. Also, we use the same procedure to generate the dorso-ventral height of the spinal cord: we build the distribution of experimentally measured dorso-ventral heights and generate the random number (*ran-height*) according to this distribution; thus, we have chosen the rectangle (*ran-height* ·1000) where all model generated axons will be allocated, i.e. we use the same rectangle to generate several axons and allocate them to the same rectangle.

After fixing all initial values and axon lengths we run iterations and generate an axon. For axon generation we use step $\Delta = 1\mu m$. To get generated axon data similar to the experimental measurements we sample model axon coordinates every 50μm and use these sampled data for the following procedures: projection of axons, building D-V distribution, calculation of tortuosity, etc. Fig. 7 shows an example of a generated model axon for the optimal parameter values fitted to aIN ascending experimental measurements (the second row of Table 1). Green line shows generated model axon with 1μm step, markers show measurements at 50μm steps along the horizontal axis, the same sampling as in experiments. The lower panel of Fig. 7 shows the same generated axon in the "correct" scale where vertical and horizontal axes are proportional and angles are not distorted.

It is important to note that the procedure for choosing initial values and axon length involves generating random numbers. This means that repetition of the same procedure will result in the generation of a different axon with different initial values and a different length. Thus, we repeat this procedure r times ($r = 70$), generate r axons allocated inside the same rectangle, and calculate the dorso-ventral distribution (10 bins for [0, ... interval) of all vertical coordinates of all generated axons. This distribution we denote by $(y_1^m, y_2^m, \ldots, y_{10}^m)$, and the total number of coordinates used for calculation of the distribution is n_m (index m here means 'model'). Also, for each model axon we calculate the tortuosity and find the average tortuosity of generated axons $\bar{T}^m$.

Now we can define the cost function which includes both similarity of distributions and similarity of tortuosities. To measure similarities of distributions we use a sum of squared differences

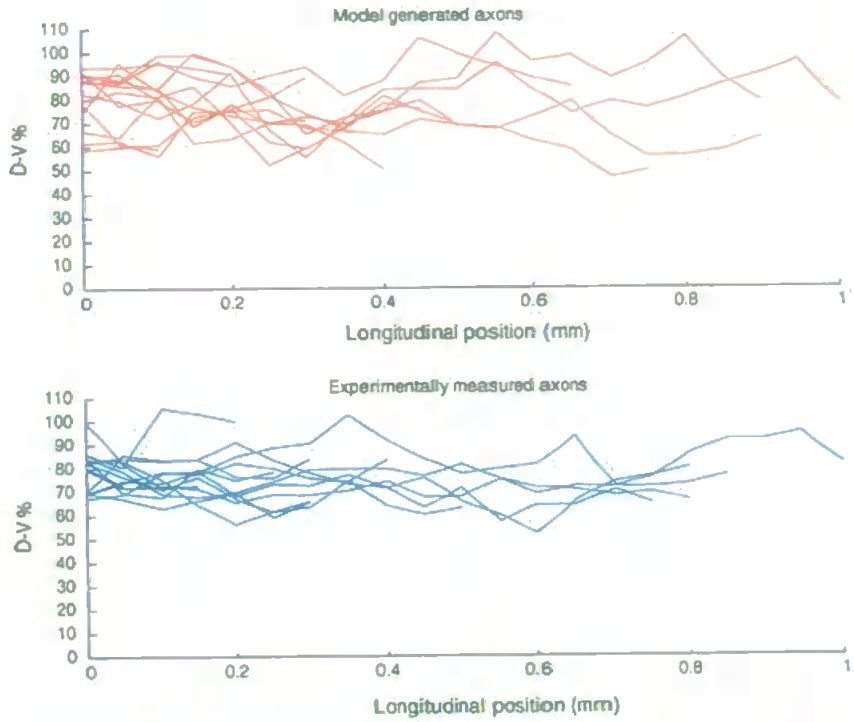

Fig. 8. An example of axons generated by model for RB cells in ascending direction (upper panel) and experimentally measured axons (lower panel). Average model tortuosity $\bar{T}^{m} = 1.01$. Average experimental tortuosity $\bar{T}^{e} = 1.009$.

between experimental and modelled distributions. To make a guess about possible values of such a sum, we would like to use normalization which is traditionally used in statistics for the one-tailed goodness of fit χ^2-test (Kendall et al., 1999). Thus, the first term of the cost function is

$$f_\chi = \sum_{i=1}^{10} \frac{(y_i^e - y_i^m)^2}{y_i^e n_e + y_i^m n_m} \tag{5.2}$$

where y_i^e, y_i^m are projection counters for the ith bin for experimental and model results respectively, $i = 1, 2, \ldots, 10$, n_e and n_m represent the numbers of measured axon points for experiment and model, respectively.

It is known in statistics that the 5% critical value with 9 d.f. for the one-tailed χ^2-test is 16.9. Thus, this value can serve as guidance for understanding the scale of cost function values and judging the quality of the optimization process.

The second term of the cost function is the squared difference between average experimental tortuosity $\bar{T}^e$ and average model tortuosity $\bar{T}^m$. The two terms of the cost function have very different scales and to balance them we consider a weight coefficient w which makes these terms consistent with each other and causes both of them to have values of the same order of magnitude. Thus, the final expression for the cost function is

$$f_{cost} = f_\chi + w(\bar{T}^e - \bar{T}^m)^2, \quad \text{where} \quad w = 10^5 \tag{5.3}$$

The cost function is based on the standard approach of nonlinear least squares and belongs to the class of nonlinear regression models (Seber and Wild, 2003). It is worth noting that the cost function includes a stochastic component, therefore, repeated calculation for the same parameter values will always result in different values of the cost function. Thus, gradient based methods are not appropriate for optimization because they usually require the cost function to be smooth which it is not true in this case. We use the Nelder-Mead simplex method, which can be used to minimize a non-smooth cost function, even if it includes a stochastic component (Lagarias et al., 1998). More sophisticated statistical procedures could also be examined (Stoyan et al., 1995).

It is important to note that the result of the optimization procedure is a random variable. This means that if we have found a set of optimal parameter values and use them to calculate the cost function several times, we will get different cost function values, because the random number generator will start from different initial values resulting in generation of different axons. The optimization procedure was run for each cell type and separately for their descending and ascending axons. The best values of model parameters are summarised in Table 1. Also, the table shows the roots of quadratic equation (4.8) which have been used in formulas for dynamics of variances. All roots are positive and less than one. Only in the case of RB cells (both ascending and descending) the roots are complex conjugates with module less than one. This fact means that for all cell types in both directions the variance of D-V coordinate is limited and asymptotically approaches the saturation level. The variance for growth angle also saturates with increase of iteration number.

An example of generated and measured axons for the case of RB cells with axons in ascending direction is shown in Fig. 8.

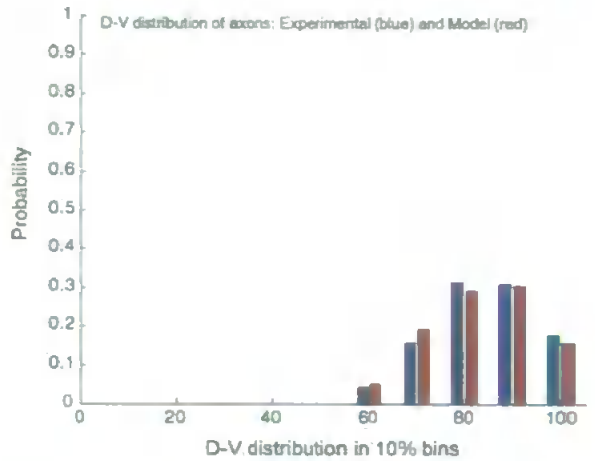

Fig. 9. Comparing the dorso-ventral distributions of model axons (red) and experimental axons (blue).

Average tortuosities for generated and measured axons are given in the caption. Fig. 9 shows distributions of dorso-ventral coordinates of experimental and generated axons.

6. Spinal Cord Network Reconstruction

Having developed a model of axon growth that produces axons that approximate those observed in the tadpole, we can now use this model to generate a reconstruction of the tadpole spinal cord. This model allows us to make some general predictions about how connectivity varies with longitudinal distance and will be used as the basis for an electrophysiological model of the network. The generated anatomical architecture allows us to substitute a neuronal model of spike generation and provides all necessary connections and synapses between different cells.

We consider a 2000 μm section of spinal cord. This section contains 6 cell types, the density of which is equivalent to 7 cells of each type per 100 μm section of spinal cord. This is a very approximate figure provided by experimental measurements (Li et al., 2007). This gives a total of 840 neurons of 6 types; 140 neurons labelled by 1 (cell type #1), 140 neurons labelled by 2(cell type #2), and so on. These neurons are allocated uniformly with spacing $\delta = (2000/840)\mu$m, in the order 1–6 and there are 140 repetitions of this sequence. Then the distribution is randomized by randomly picking a cell and swapping it with its immediate neighbour to the right, repeating this process many times. As a result of applying this permutation process, all the cell types become uniformly distributed over the length of the spinal cord. This process captures the known anatomical property that cells of the same type tend not to appear very close to each other, but avoid the artificial situation of a perfectly regularly laid out spinal cord.

We have experimental data for each cell giving the ventral and dorsal extents (v, d), $v < d$ of the dendritic field for each cell, i.e. for each cell we know that the dendrite is distributed between two values v and d ($v < y < d$), where y describes the D-V coordinate of the dendrite. Experimental measurements do not provide information about the shape of the distribution inside the (v, d) interval. We consider the distribution of the bivariate random variable $\eta = (v, d)$ where the ventral extent is v and the dorsal extent is d. Each component of this bivariate random variable is distributed in the interval [0, 100]μm and the bivariate random variable η is distributed in a triangle with two perpendicular sides of 100 μm. Using experimental measurements of dendrites for each cell type, we approximate the bivariate probability density function of the random variable η by a table of size 10×10. We divide the interval [0, 100]μm by 10 bins and calculate a two dimensional histogram for the (v, d) distribution from experimental measures. Thus, each entry contains the probability of finding the ventral and dorsal dendrite extents inside the corresponding square (10% 2D bin) of the histogram. In this table, cells under the diagonal contain estimates of probabilities, but cells above the diagonal are zero, because the dorsal extent cannot be lower than the ventral extent. These 2D histograms have been calculated for each type of cell and they have been used to determine ventral and dorsal extents of dendrites which have been generated at random according to the corresponding table.

Having determined which 2D 10% bin the dorsal and ventral extent will fall into, the actual values of dorsal and ventral extents are uniformly and independently distributed within this 2D bin. We repeat this procedure to adjust D-V coordinates of dendritic extents for each neuron. We represent the dendrite by a bar with width 1 μm in the longitudinal direction and the dorso-ventral extent of this bar is randomly generated on the basis of the two dimensional distribution for this particular cell type.

At this point, all 840 cells are allocated in their proper longitudinal and dorso-ventral positions, meaning that the distribution corresponds to the experimental distribution and the longitudinal positions are uniformly distributed for all cells.

We now apply the following procedure for each cell:

(1) Generate a random initial angle and position using the procedure detailed above.
(2) Generate a length for the axon taken from the experimental distribution of axon lengths.
(3) Grow the axon to the determined length using the algorithm detailed above. When the path of the axon intersects with the bar representing the dendritic field of a cell, produce a synapse with probability P_{syn} (i.e. generate the random variable x uniformly distributed in [0, 1] and if $x < P_{syn}$ then generate a synapse). If a synapse was produced then any subsequent intersection between the axon and this particular dendritic field will be ignored. So it is not possible that one presynaptic neuron will make two or more synapses onto the same postsynaptic cell. Experimental evidence from electrophysiological studies indicates that $P_{syn} \approx 0.3$.

Fig. 10 shows a fragment of the generated anatomical neural circuit of the whole tadpole spinal cord. Each cell type is represented by a separate colour: red colour corresponds to RB cells; green dlc cells; blue to aIN cells; magenta to cIN cells; brown to dIN cells; and black to motor neurons (MN). These colours are used to represent axons, dendrites, initial branching point of axons, and synapses (which have the same colour as the

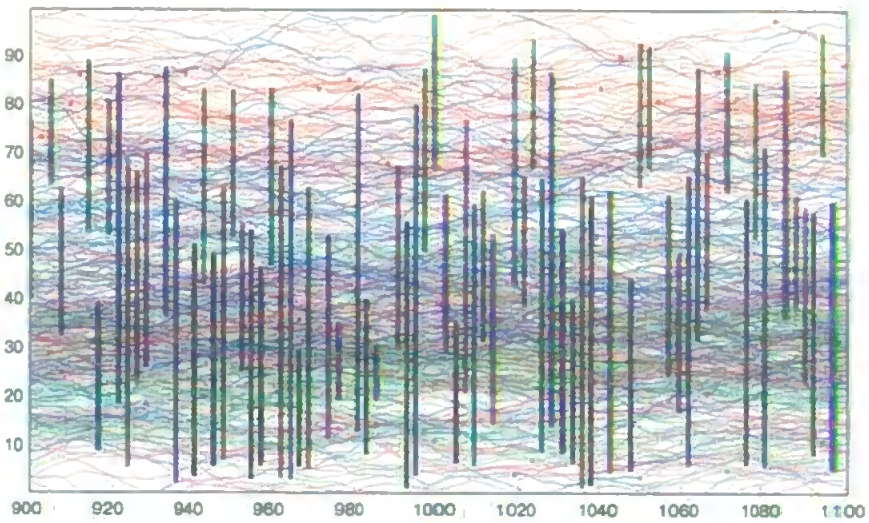

Fig. 10. Generated anatomical neural circuit of spinal cord. Each cell type is represented by a separate colour: red colour corresponds to RB cells; green dlc cells; blue to aIN cells; magenta to cIN cells; brown to dIN cells; and black to motor neurons (MN). These colours are used to represent axons, dendrites, initial branching point of axons, and synapses (which have the same colour as the presynaptic cell).

presynaptic cell). The dendrite is represented by a vertical bar and the synapse is shown by a circle. The colour of the circle relates to the presynaptic neuron, for example, a blue circle on a brown vertical bar represents a synaptic connection from an aIN cell to the dendrite of a dIN cell. The axon branch point is represented by a square. In some cases this square will be inside the dendritic bar but in other cases it will be located outside of the bar but in all cases the longitudinal position will be the same as the longitudinal coordinate of the neuron. RB neurons are represented only by their axons because they have no dendrites—they are sensory neurons that respond to skin stimulation.

Fig. 11 shows a zoomed view of the generated spinal cord extracted from Fig. 10. A squared region of the size 30μm ×30μm has been taken from the middle section of the dorso-ventral axis. Many synaptic connections (coloured circles) can be seen in this figure.

From this generated neural architecture, a complete description of the connectivity of the spinal cord has been produced which may be used as the basis for electrophysiological modelling of swimming activity.

7. Discussion

To the best of our knowledge, for the first time a complete biologically realistic neural circuit of the tadpole spinal cord has been generated. This model has great potential for further investigation (also, this model can be used for educational purposes). For example, probabilities of synaptic contacts between cells of different types can be calculated from the generated architecture and compared with experimentally measured probabilities of synaptic contacts between the same cells. Indeed, this comparison reveals that the probabilities of synaptic contacts

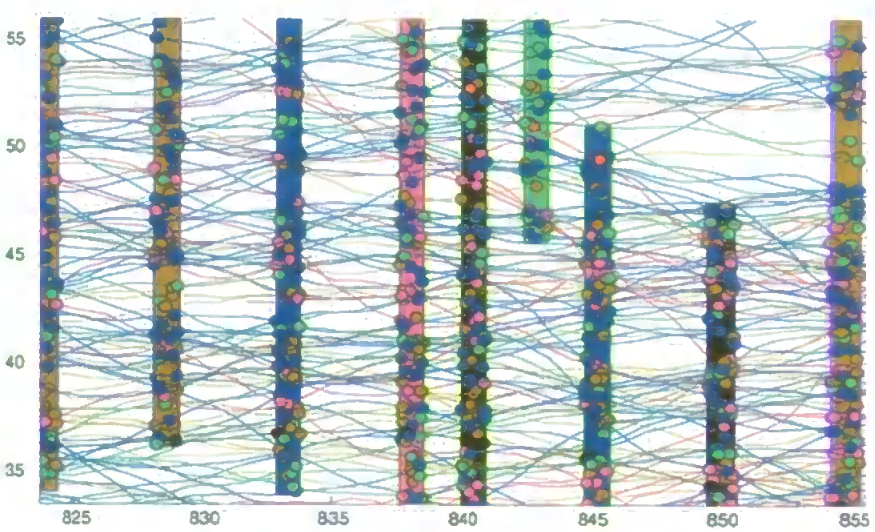

Fig. 11. Fragment of generated anatomical neural circuit of spinal cord extracted from the previous figure. The colour coding is the same as in the previous figure.

for the generated architecture correspond well to experimental measurements.

Combined with an advanced visualization system, the anatomical model could be used to demonstrate many interesting properties of spinal architecture. For example, for each neuron we can find and visualize all incoming connections. Identification of incoming connections is crucial for the development of a model of electrical activity and the study of the functionality of this neural architecture.

The spinal cord reconstruction provides information about longitudinal and Dorso-Ventral positions of each neuron, allocation of its dendritic field, coordinates of its axon and all afferent and efferent synaptic connections. Thus, the complete anatomical description of neural architecture of the spinal cord is achieved. Due to stochasticity in the model of axon growth, the neural architecture is not unique and starting from different initial states of the random number generator we can generate a number of anatomical circuits of the spinal cord. All these architectures will be similar in the sense that they have the same statistical characteristics as experimental measurements.

Now, a very intriguing question arises about the functionality of these neural networks. Can this neural network produce a specific pattern of neural activity corresponding to the swimming pattern given that some spiking neural model has been used to describe the activity of each element of the anatomical architecture? How reliable and stable is this swimming-like pattern under variation of model parameters? What fraction of generated neural architectures will be able to swim? Should the connection strengths be adjusted according to some learning rule or can the spinal cord model generate swimming for randomly chosen parameter values? Detailed answers to these questions and a complete description of the spinal cord model with spike generating elements will be given in a separate publication which is under preparation. Here we would like to report our preliminary result: the generated realistic anatomical model can swim. To obtain this result we have used Morris-Lecar spiking neurons connected according to the generated anatomical architecture. Simulations of the neural network of Morris-Lecar neurons with randomly distributed connection strengths show that the model of spinal cord demonstrates a stable swimming pattern within a broad range of parameter values.

Acknowledgments

RB work was supported in part by the UK EPSRC (Grant EP/D036364/1) and by the Russian Foundation of Basic Research (Grant 07-01-00218).

References

Bourikas, D., Pekarik, V., Baeriswyl, T., Grunditz, A., Sadhu, R., Nard, M., Stoeckli, E.T., 2005. Sonic hedgehog guides commissural axons along the longitudinal axis of the spinal cord. Nat. Neurosci. 8 (3), 297–304, URL: http://dx.doi.org/10.1038/nn1396.

Charron, F., Stein, E., Jeong, J., McMahon, A.P., Tessier-Lavigne, M., 2003. The morphogen sonic hedgehog is an axonal chemoattractant that collaborates with netrin-1 in midline axon guidance. Cell 113 (1), 11–23.

Chilton, J.K., 2006. Molecular mechanisms of axon guidance. Dev. Biol. 292 (1), 13–24, URL: http://dx.doi.org/10.1016/j.ydbio.2005.12.048.

Cline, H., 2003. Sperry and hebb: oil and vinegar? Trends Neurosci. 26 (12), 655–661.

Dale, N., 1985. Reciprocal inhibitory interneurones in the xenopus embryo spinal cord. J. Physiol. 363, 61–70.

de Anda, F.C., Pollarolo, G., Silva, J.S.D., Camoletto, P.G., Feiguin, F., Dotti, C.G., 2005. Centrosome localization determines neuronal polarity. Nature 436 (7051), 704–708, URL: http://dx.doi.org/10.1038/nature03811.

Dickson, B.J., 2002. Molecular mechanisms of axon guidance. Science 298 (5600), 1959–1964, URL: http://dx.doi.org/10.1126/science.1072165.

Gomez, T., Zheng, J., 2006. The molecular basis for calcium-dependent axon pathfinding. Nat. Rev. Neurosci. 7 (2), 115–125, URL: PM:12804694.

Goodhill, G.J., Gu, M., Urbach, J.S., 2004. Predicting axonal response to molecular gradients with a computational model of filopodial dynamics. Neural Comput. 16 (11), 2221–2243, URL: http://dx.doi.org/10.1162/0899766041941934.

Imondi, R., Kaprielian, Z., 2001. Commissural axon pathfinding on the contralateral side of the floor plate: a role for b-class ephrins in specifying the dorsoventral position of longitudinally projecting commissural axons. Development 128 (23), 4859–4871.

Kaern, M., Elston, T.C., Blake, W.J., Collins, J.J., 2005. Stochasticity in gene expression: from theories to phenotypes. Nat. Rev. Genet. 6 (1), 451–464.

Kendall, M., Stuart, A., Ord, K., Arnold, S., 1999. Kendall's Advanced Theory of Statistics: Volume 2A —Classical Inference and the Linear Model, 6th ed. A Hodder Arnold Publication.

Krottje, J.K., van Ooyen, A., 2007. A mathematical framework for modeling axon guidance. Bull. Math Biol. 69 (1), 3–31, URL: http://dx.doi.org/10.1007/s11538-006-9142-4.

Lagarias, J.C., Reeds, J.A., Wright, M.H., Wright, P.E., 1998. Convergence properties of the Nelder-Mead simplex algorithm in low dimensions. SIAM J. Optim. 9, 112–147, URL: http://citeseer.ist.psu.edu/lagarias96convergence.html.

Li, W.C., Perrins, R., Soffe, S.R., Yoshida, M., Walford, A., Roberts, A., 2001. Defining classes of spinal interneuron and their axonal projections in hatchling xenopus laevis tadpoles. J. Comp. Neurol. 441 (3), 248–265.

Li, W.-C., Soffe, S.R., Roberts, A., 2002. Spinal inhibitory neurons that modulate cutaneous sensory pathways during locomotion in a simple vertebrate. J. Neurosci. 22 (24), 10924–10934.

Li, W.-C., Soffe, S.R., Roberts, A., 2003. The spinal interneurons and properties of glutamatergic synapses in a primitive vertebrate cutaneous flexion reflex. J. Neurosci. 23 (27), 9068–9077.

Li, W.-C., Soffe, S.R., Roberts, A., 2004. Dorsal spinal interneurons forming a primitive, cutaneous sensory pathway. J. Neurophysiol. 92 (2), 895–904, URL: http://dx.doi.org/10.1152/jn.00024.2004.

Li, W.-C., Soffe, S.R., Wolf, E., Roberts, A., 2006. Persistent responses to brief stimuli: feedback excitation among brainstem neurons. J. Neurosci. 26 (15), 4026–4035, URL: http://dx.doi.org/10.1523/JNEUROSCI.4727-05.2006.

Li, W.C., Cooke, T., Sautois, B., Soffe, S.R., Borisyuk, R., Roberts, A., 2007. Axon and dendrite geography predict the specificity of synaptic connections in a functioning spinal cord network. Neural Dev. 2 (17), 1–18.

Lyuksyutova, A.I., Lu, C.-C., Milanesio, N., King, L.A., Guo, N., Wang, Y., Nathans, J., Tessier-Lavigne, M., Zou, Y., 2003. Anterior-posterior guidance of commissural axons by wnt-frizzled signalling. Science 302 (5652), 1984–1988, URL: http://dx.doi.org/10.1126/science.1089610.

Moon, M.-S., Gomez, T.M., 2005. Adjacent pioneer commissural interneuron growth cones switch from contact avoidance to axon fasciculation after midline crossing. Dev. Biol. 288 (2), 474–486, URL: http://dx.doi.org/10.1016/j.ydbio.2005.09.049.

O'Toole, M., Lamoureux, P., Miller, K., 2008. A physical model of axonal elongation: force, viscosity, and adhesions govern the mode of outgrowth. Biophys. J. 1 (2) (Epub ahead of print, January 2008, URL PM:14638388).

Sautois, B., Soffe, S., Li, W.-C., Roberts, A., 2007. Role of type-specific neuron properties in a spinal cord motor network. J. Comput. Neurosci. 23, 59–77, URL: http://dx.doi.org/10.1007/s10827-006-0019-1.

Schnorrer, F., Dickson, B.J., 2004. Axon guidance: morphogens show the way. Curr. Biol. 14 (1), R19–R21.

Seber, G., Wild, C., 2003. Nonlinear Regression. Wiley.

Shirasaki, R., Murakami, F., 2001. Crossing the floor plate triggers sharp turning of commissural axons. Dev. Biol. 236 (1), 99–108, URL: http://dx.doi.org/10.1006/dbio.2001.0321.

Stoyan, D., Kendall, W., Mecke, J., 1995. Stochastic Geometry and its Applications. John Wiley and Sons.

Wen, Z., Zheng, J., 2006. Directional guidance of nerve growth cones. Curr. Opin. Neurobiol. 16 (1), 52–58, URL: PM:11826054.

Wilson, S.W., Easter, S.S., 1991. A pioneering growth cone in the embryonic zebrafish brain. Proc. Natl. Acad. Sci. U.S.A. 88 (6), 2293–2296.

Xu, J., Rosoff, W., Urbach, J., Goodhill, G., 2005. Adaptation is not required to explain the long-term response of axons to molecular gradients. Development 132 (20), 4545–4552.